Doctoral Dissertation

Doctoral Program in Chemical Engineering (37th Cycle)

Spectroscopic Techniques as PAT monitoring Tools for the Development of Biopharmaceutical Product Processes

By

Ambra Massei

Supervisors:

Prof. D. Fissore, Supervisor

Doctoral Examination Committee:

Prof. L. Capozzi, Referee, Lancaster University

Prof. W. Friess, Ludwig-Maximilians-Universität München

Politecnico di Torino,

Novembre 2024

Declaration

I hereby declare that, the contents and the organization of this dissertation constitute my own original work and does not compromise in any way the rights of third parties, including those relating to the security of personal data.

November 2024

Ambra Massei

Acknowledgment

The financial support and contribution of Merck Serono SpA, Guidonia Montecelio (Roma), is gratefully appreciated and acknowledged.

Table of contents

1. Biopharmaceutical Products: Process Development and Manufacturing 1

1.1 The launch of a biopharmaceutical drug product 1

1.2 Process validation: from process development to commercial production 3

1.3 Stage 1 – Process Design 5

1.4 Protein stability and denaturation phenomena occurring in biopharmaceutical processes 7

1.4.1 Physical degradation 8

1.4.2 Chemical degradation 9

1.4.3 Impact of degradation mechanisms on safety, efficacy and stability of the drug product 10

1.5 Fill and finish process of a liquid/freeze-dried drug product 10

1.6 Freeze-drying process: an in-depth focus for solid formulations 11

1.6.1 Freeze-dryer instrumentation 12

1.6.2 Freeze-drying process 13

1.6.3 Freeze-drying process monitoring 15

1.6.4 Product temperature monitoring 17

1.7 Stress factors and CQAs potentially impacted in each DP manufacturing process step 18

1.8 Measurement of Critical Quality Attributes in manufacturing process 22

1.8.1 Conventional analytical techniques currently employed in biopharmaceutical industry 22

1.8.2 The need for Process Analytical Technology (PAT) in biopharmaceutical industry 23

1.9 Motivation of the work 24

2. Spectroscopic methods as PAT monitoring tools in pharmaceutical field 26

2.1 NIR spectroscopy 27

2.1.1 Fundamentals of NIR-theory 27

2.1.2 Instrumentation 28
2.1.3 NIRS application in the pharmaceutical field 29
2.2 Raman spectroscopy 31
2.2.1 Fundamentals of Raman theory 31
2.2.2 Mathematical description of Raman scattering 33
2.2.3 Instrumentation 35
2.2.4 Raman application in the pharmaceutical field 39
2.3 Data-based models in pharmaceutical field 42
2.3.1 Why multivariate data analysis is needed in pharmaceutical field? 42
2.3.2 Spectra data processing 44
2.3.3 Preprocessing techniques 45
2.3.4 Principal Component Analysis: Theory 46
2.3.5 Partial Least Squares Regression: Theory 47
2.3.6 Artificial Neural Network: Theory 49
2.3.7 Performance Evaluation 50
2.3.8 Multivariate Control Charts 51
3. MATERIALS & EQUIPMENT 53
3.1 Materials 53
3.2 Equipment 54
3.2.8 Karl-Fischer titration analysis 59
4. Determination of formulated-related CQAs of drugs 60
4.1 Introduction 60
4.2 Case-study 64
4.3 Data processing 66
4.4 Results 70
4.5 Highlights 78
5. Assessing Critical Quality Attributes in Biopharmaceuticals during Process Development and Manufacturing: Effects of Denaturation and Dilution processes 80

5.1 Introduction 80
5.2 Case-study 81
5.3 Data processing 83
5.4 Results 85
5.4.1 Protein degradation related CQAs: aggregation, fragmentation and oxidation level 85
5.4.2 Product composition related CQAs: protein, methionine and PS20 concentration 91
5.4.3 Real case-study: application on the freeze-dried mAb 98
5.5 Highlights 99
6. Estimation of residual moisture in freeze-dried products 101
6.1 Introduction 101
6.2 Case-study 102
6.3 Data processing 104
6.3.1 Analysis of the NIR spectra 104
6.3.2 Models' development and comparison 106
6.4 Results 108
6.4.1 Model S6 109
6.4.2 Ad-hoc models 114
6.4.3 Global model 115
6.4.4 Effect of training set size on the performances 117
6.4.5 Real-case study: prediction of RM in DP 119
6.5 Highlights 121
7. In-line monitoring of filtration, compounding, and freeze-drying step 123
7.1 Introduction 123
7.2 Case-study 1: NIR spectroscopy 124
7.2.1 Experiments for multivariate statistical process control 124
7.2.2 Experiments for quantification of residual moisture in-line 125

7.3 Case-study 2: Raman spectroscopy 125
7.3.1 Experiments for filtration monitoring..... 125
7.3.2 Experiments for dilution monitoring 126
7.4 Results..... 127
7.4.1 NIR spectroscopy – multivariate statistical process control..... 127
7.4.2 NIR spectroscopy – RM trend by PLS 131
7.4.3 Raman spectroscopy – filtration & dilution 134
7.5 Highlights..... 135
8. Conclusions 137
8.1.1 Off-line Raman applications..... 137
8.1.2 Off-line NIR applications 139
8.1.3 In-line Raman applications..... 139
8.1.4 In-line / At-line NIR applications..... 140
8.1.5 Applicability and future challenges..... 140

List of Figures

Figure 1: The three pillars of drug production: research, development, and approval ... 1
Figure 2: From process map to preliminary process control strategy: The evolution of process design in stage 1 activities..... 5
Figure 3: Step-by-step process for the manufacturing of liquid or lyophilized drugs: from drug substance to final product packaging 11
Figure 4: Freeze-dryer instrumentation..... 12
Figure 5: Change in water phase diagram during freeze-drying process steps..... 13
Figure 6: Various applications of Process Analytical Technology (PAT): on-line, in-line, at-line, and off-line 23
Figure 7: NIR instrumentation 28
Figure 8: Raman and Rayleigh scattering 31
Figure 9: Diagram of Rayleigh and Raman scattering processes..... 32
Figure 10: Instrumentation for Raman spectroscopy 35
Figure 11: Diagram of a dispersive Raman spectrometer (a) and FT-Raman spectrometer

(b) 36
Figure 12: Michelson interferometer 38
Figure 13: Data analysis workflow for processing NIR/Raman spectra in pharmaceutical applications. 44
Figure 14: Lyostar 3 freeze-dryer with the NIR flange highlighted. 54
Figure 15: Lyostar 3 freeze-dryer equipped with the plastic bag isolator to deal with toxic compounds. 55
Figure 16: Raman flow cell used for in-line measurements installed in the GPD department of Guidonia Montecelio Merck site 56
Figure 17: NIR spectrometer while analyzing a sample. 56
Figure 18: Schematic representation of the workflow to follow to distinguish among different stress conditions or dilutions occurred into biopharmaceutical products during manufacturing steps. 64
Figure 19: Raw Raman spectra of (a) dilutions performed on formulation 2 samples; and (b) thermal stress performed on formulation 1 samples. 66
Figure 20: Pre-processed Raman spectra of formulation 1 and formulation 2 samples in the fingerprint region colored according to the different types of samples, as clearly detailed in the legend in the right upper part of the graph. 67
Figure 21: Pre-processed Raman spectra of formulation 1 and formulation 2 samples in the entire Raman shift region colored according to the different types of samples, as clearly detailed in the legend in the right upper part of the graph. 68
Figure 22: Cumulative variance as a function of the number of components in case of PCA model developed on the entire dataset. 69
Figure 23: Scores Plot of the entire dataset in the Raman shift range 150-3425 cm^{-1}. In graph (a) the scores are displayed in the plane described by the 1st and 2nd PC, while in graph (b) the plane described by the 1st and 3rd PC is reported. 71
Figure 24: Loadings plots for the first three principal components reporting (a) PC1, (b) PC2 and (c) PC3. The data were processed using the single PCA model developed on the entire Raman shift range. 72
Figure 25: Scores plot of PCA model developed on the entire range for (a) calibration dataset and (b) prediction dataset for mAb samples colored according to the type of stress, as reported in the legend. 73
Figure 26: Hotelling's T2 graph for the prediction dataset made up of mAb samples, colored according to the type of stress. 74

Figure 27: Projection scores plot for formulation 3 using the PCA developed using the mAb dataset. 75
Figure 28: Scores plot of PCA model developed only on the thermal stressed samples. The scores are displayed in the plane described by (a) the 1st and 2nd PCs and (b) the 2nd and 3rd PCs. The groupings according to the exposure duration to the stress are obtained, ... 76
Figure 29: The loadings plot was generated by the PCA model exclusively trained on thermally stressed samples categorized by the type of stress, specifically: (a) lowest stress exposure time; (b) moderate stress exposure time; and (c) highest stress exposure time. 77
Figure 30: Loadings plot from the PLS decomposition of the dataset for (a) high HMW% and (b) low HMW%, covering the Raman shift range of 600-3000 cm^{-1}. The loadings for the first latent variable (LV) used in model development are presented. 86
Figure 31: Parity diagrams comparing the measured HMW (%) to the predicted HMW (%) are presented for thermally stressed samples. These diagrams are derived from the calibration (a, c) and prediction (b, d) datasets, covering both high (a, b) and low (c, d) values, processed using a PLS model across the full Raman shift range of 600-3000 cm^{-1}. 87
Figure 32: Relationship between the Coefficient of Variation calculated for (a) high HMW(%) and (b) low HMW(%)as a function of the corresponding measured HMW% values is reported. The black dots indicate the calibration samples, while the grey dots represent the prediction samples. The horizontal line at 10% denotes the threshold permitted according to the validation report of the reference method. 88
Figure 33: Parity diagrams comparing the measured HMW (%) to the predicted HMW (%) are presented for the calibration (a,c) and prediction sets (b,d) of thermally stressed samples, focusing on both high HMW values (a,b) and low HMW values (c,d). These diagrams were generated using a PLS model applied to the reduced Raman shift ranges (RR1 and RR2), specifically 1200-1600 cm^{-1} and 1200-1900 cm^{-1}, respectively. 89
Figure 34: Parity diagrams comparing the measured LMW (%) to the predicted LMW (%) are presented, derived from the prediction set (a) processed using the PLS model across the full Raman shift range (600-3000 cm^{-1}). Figure 3b illustrates the relationship between the Coefficient of Variation for both sets, with the calibration set shown in black and the prediction set in grey, plotted against the LMW% measured by the reference analytical technique. The grey line at 15% indicates the allowable threshold for this

critical quality attribute (CQA)..... 90
Figure 35: The loadings plot from the PLS decomposition of the dataset is presented for (a) high protein content, (b) methionine content, and (c) Polysorbate 20 (PS20) content across the Raman shift range of 600-3000 cm^{-1}. The loadings for the first latent variable (LV) utilized in the model development are displayed. 92
Figure 36: Parity diagrams comparing the measured Protein, Methionine, and PS20 content to the predicted values are presented, derived from the calibration (a, c, e) and prediction (b, d, f) sets of diluted samples processed using the PLS model across the full Raman shift range (600-3000 cm^{-1}). Specifically, graphs (a) and (b) correspond to high Protein content values, (c) and (d) pertain to Methionine content, and (e) and (f) relate to PS20 content. 94
Figure 37: The acceptance criteria are presented as the Coefficient of Variation or the ratio between the minimum and maximum concentrations of PS20, plotted against the measured concentrations of: (a) high Protein content, (b) Methionine, and (c) PS20 for the data processed in the reduced ranges RR3, RR4, and RR5. 95
Figure 38: The acceptance criteria are presented as the Coefficient of Variation or the ratio between the minimum and maximum concentrations of PS20, plotted against the measured concentrations of: (a) high Protein content, (b) Methionine, and (c) PS20 for the data processed across the entire ranges. 95
Figure 39: The loadings plot from the PLS decomposition of the low protein content dataset is displayed across the Raman shift range of 600-3000 cm^{-1}. This plot illustrates the loadings for the first latent variable (LV) used in the development of the models. . 96
Figure 40: Parity diagram relating the low protein content measured vs low protein content predicted, obtained using the calibration set processed by PLS model on the entire range of Raman shift (600-3000 cm^{-1}). 97
Figure 41: Equivalence test results obtained by processing the data using Minitab software for: (a) high HMW%, (b) LMW%, (c) Methionine concentration samples and (d) high Protein content. 97
Figure 42: The acceptance criteria are presented as the Coefficient of Variation plotted against the measured aggregation level by SE-HPLC for the data processed across the entire ranges using the Model 2..... 98
Figure 43: Spectra of sucrose and trehalose-based formulations after SNV pretreatments. In orange, the sucrose-based solutions at different concentrations are reported: (a) S6, (b) S3 and (c) S9, while in violet (d) the T6 dataset is shown. 105

Figure 44: Spectra of arginine-based formulations after SNV pretreatments: (a) SA05, (b) SA1 and (c) SA3 dataset. 105
Figure 45: Parity diagrams comparing the RM measured (%) and the RM calculated obtained using the linear regression (b) and the neural network (a) models for dataset S6 for SR..... 110
Figure 46: Parity diagrams (a, b) for the SA05 dataset, comparing the measured RM (%) with the calculated RM (%), along with absolute error plots (c, d). These results were obtained using the linear regression (b, d) and neural network (a, c) models developed with the S6 dataset for the SR wavelength range. 110
Figure 47: Parity diagrams (a, b) for the SA1 dataset, illustrating the comparison between the measured RM (%) and the calculated RM (%), as well as absolute error plots (c, d). These results were derived from the linear regression (b, d) and neural network (a, c) models developed using the S6 dataset for the SR wavelength range..... 111
Figure 48: Comparison between the absolute error plots obtained for SA3 dataset in case of linear regression (b) and neural network (a) models developed with S6 database are used for SR. 112
Figure 49: Absolute error plots of dataset S3 (a,b) and S9 (c,d) obtained using the linear regression (b,d) and the neural network (a, c) models developed using dataset S6 for SR. 113
Figure 50: Parity diagrams of dataset T6 comparing the RM measured (%) and the RM calculated obtained using the linear regression (b) and the neural network (a) models developed using dataset S6 for SR. 113
Figure 51: Parity diagrams of dataset SA05 (a,b), SA1 (c,d) and SA3 (e,f) comparing the RM measured (%) and the RM calculated (%),obtained using the linear regression (a,c,e) and the neural network (b,d,f) models developed using datasets of arginine-sucrose mixtures for SR..... 115
Figure 52: Parity plot using T6 dataset processing by PLS model in the SR..... 120
Figure 53: Absolute error plots for RM estimation of drug product processing the data by PLS model developed on T6 dataset for both SR (a) and WR (b). 120
Figure 54: Setup of Raman spectroscopy for filtration monitoring 125
Figure 55: Setup of Raman spectroscopy for filtration monitoring..... 126
Figure 56: Scores plot relating the first two principal components of the NIR spectra acquired in-line during the freeze-drying process. Data were processed by PCA in the range 7400 – 4230 cm-1. The data are colored respectively in black or grey for reference

cycle 1 and 2. 128
Figure 57: Hotelling's T2 plot (a,b) and DModX Weighted Residual plot (c,d) as a function of observations in the case of reference cycles. In black the reference cycle 1 is reported (a,c), while in grey the reference cycle 2 (b,d). 129
Figure 58: Hotelling's T2 plot as a function of observations in the case of fault cycle. 130
Figure 59: Parity diagram plot relating the measured RM values by KF in the y-axis as a function of the RM predicted by PLS model in the x-axis. 131
Figure 60: Graphs (a), (c) and (e) depicts the trend of residual moisture predicted by PLS model as a function of drying time respectively in case of reference cycle 1, reference cycle 2 and fault cycle. In the graphs (b), (d) and (f) the corresponding Pirani/Baratron ratio for the three cases are reported. 133
Figure 61: Protein content trend during (a) filtration and (b) dilution step. The in-line Raman acquisitions were processed using the PLS model developed off-line and denoted as Model 4. 134

List of Tables

Table 1: Impact of process parameters and stress factors on Critical Quality Attributes (CQAs) at different Drug Product (DP) manufacturing process steps 18
Table 2: Critical Quality Attributes (CQAs) with corresponding conventional analytical techniques and analysis durations. 22
Table 3: Number of samples for each case study considered in the work. The formulation used for each case is also reported. 65
Table 4: Raman parameters used for each case-study. 82
Table 5: Critical Quality Attributes considered in the different treatments the samples were subjected to, together with the analytical reference method and the relative acceptance criteria. 82
Table 6: Total number of samples considered and division of the dataset into calibration and validation set. Moreover, the Raman shift explored for each CQA are also reported. 84
Table 7: Performance metrics of the models created and the validation conducted in the aggregation level case study are detailed. Additionally, the model type, the critical quality attributes (CQA) examined, the Raman shift range, and the latent variables are specified. 87

Table 8: Performance metrics of the models developed, and the validation conducted in the case study for the fragmentation level are detailed. Additionally, the model type, the Raman shift range, and the latent variables are specified..... 90
Table 9: The performance metrics of the models developed, and the validation conducted in the case study for product composition are detailed. Additionally, the model type, Raman shift range, and latent variables are specified. 91
Table 10: Acceptance criteria in terms of CV% obtained in the freeze-dried Formulation 1 samples. The PLS model developed using two different pretreatments are reported: 1st derivative + SG filter and MSC + SG filter..... 99
Table 11: Type and number of samples generated for the case-study..... 103
Table 12: Process conditions of the freeze-drying cycle for producing other samples to be added to the dataset by Bobba et al. [187]..... 103
Table 13: RMSE calculated for Model S6 and the Global Model within the wavelength ranges of SR or WR, utilizing either the linear model (LR) or the neural network (NN). 108
Table 14: RMSE calculated for the LR and NN models in the context of ad hoc models for arginine-sucrose and trehalose formulations. All reported results were derived from SR. 109
Table 15: Impact of training set size on model performance. The first row indicates the type of model utilized, while the second row presents the percentage of the available dataset (ranging from 40% to 60%) allocated for training purposes. All values in the table represent the RMSE corresponding to each dataset for the specified training set sizes. The results are provided for the SR wavelength range. 118
Table 16: Different dilutions performed by adding placebo in the formulation to explore a wide range of concentration levels. 126
Table 17: Comparison of endpoint estimated by PLS model and Pirani/Baratron ratio for the reference cycles and fault one. The relative error was also reported..... 133

List of Symbols

A_j	Absorbance at the jth wavelength scanned
B	Regression matrix
D	Number of molecules per cubic centimeter
d	Groove spacing

dz	Path length of the laser in the sample
E	Electric field
E	Residual matrix from PCA decomposition
F	Residual matrix from PLS decomposition
I_R	Raman intensity
I	Number of samples
J	Number of variables for each spectrum
M_{cal}	Number of observations in the training set
M_{val}	Number of observations in the test set
N_p	Native protein
N	Number of atoms
n	Order of diffraction
$out_j^{(r)}$	output of thej^{th}neuron in the *r* layer
$out_i^{(r-1)}$	output of the i^{th} neuron in the *r-1* layer
P	Induced polarization
Q^2	Coefficient of Determination for test set
Q	Loading matrix from PLS decomposition
Q	Normal vibrational mode
Q_0	Amplitude of Q
R^2	Coefficient of Determination for training set
s_j	Signal collected at the j^{th} wavelength scanned
X	Irreversible denaturation
X	Generic spectra dataset
$\boldsymbol{X_{new}}$	Generic spectra dataset of a new observation
T	Transmitted light
T	Score matrix from PCA decomposition
t	Time
U	Score matrix from PLS decomposition
U	Denatured protein
V	Loading matrix from PCA decomposition

$\mathbf{W}$	Weight matrix from PLS decomposition
$\mathbf{Y}$	Vector of the attribute
$\mathbf{Y_{pred}}$	Vector of attribute predicted by the model
y_i^{cal}	General attribute measured by traditional method for *i*-th sample of the training set
$y_{pred,i}^{cal}$	General attribute predicted by the model for *i*-th sample of the training set
y_i^{val}	General attribute measured by traditional method for *i*-th sample of the test set
$y_{pred,i}^{val}$	General attribute predicted by the model for *i*-th sample of the test set
$\overline{y^{cal}}$	Mean of observed values in the training set
$\overline{y^{val}}$	Mean of observed values in the validation set

Greeks

α	Polarizability
β_n	Generic angle at which constructive interference occurs
λ	Wavelength of the light
μ	Constant parameter
ν	Frequency of the light
$\bar{\nu}$	Wavenumber
ν_0	Laser frequency
σ_j	Cross section at the wavenumber j

List of Abbreviations

ANN	Artificial Neural Network
API	Active Pharmaceutical Ingredient
CCD	Charge Coupled Device
CGE	Capillary Gel Electrophoresis
CQA	Critical Quality Attribute
CV	Coefficient of Variation
CPP	Critical Process Parameters
CPV	Continued Process Verification

DS	Drug Substance
DSC	Differential Scanning Calorimetry
DoE	Design of Experiments
DP	Drug Product
ELSD	Evaporative Light Scattering Detector
EMA	European Medicines Agency
EPO	Erythropoietin
ER	Entire Range
FBG	Fiber Bragg Grating
FDA	Food and Drug Administration
FDM	Freeze-dry Microscope
FIT	Filter Integrity Test
GaAs	Gallium Arsenide
GMP	Good Manufacturing Practice
HGH	Human Growth Hormone
HMW	High Molecular Weight
InGaAs	Indium Gallium Arsenide
IR	Infrared
KF	Karl Fischer
LDH	Lactate Dehydrogenase
LED	Light Emitting Diodes
LMW	Low Molecular Weight
LV	Latent Variables
mAb	Monoclonal Antibody
MSC	Multiplicative Scatter Correction
MSPC	Multivariate Statistical Process Control
MVDA	Multivariate Data Analysis
NIPALS	Nonlinear Iterative Partial Least Squares
NIR	Near Infrared
NMR	Nuclear Magnetic Resonance
NOC	Normal Operating Conditions

R&D	Research and Development
RM	Residual Moisture
OD	Optical Density
OFS	Optical Fiber Sensors
OOS	Out-of-Specification
PAT	Process Analytical Technology
PC	Principal Components
PCA	Principal Component Analysis
PCR	Planned Characterization Range
pCPP	potential Critical Process Parameters
PES	Polyester
PLS	Partial Least Squares
PLS-DA	Partial Least Squares-Discriminant Analysis
PP	Process Parameters
PPQ	Process Performance Qualification
PS	Polysorbate
PVDF	Polyvinylidene Fluoride
PRT	Pressure Rise Test
RMSEC	Root Mean Square Error of Calibration
RMSECV	Root Mean Square Error of Cross Validation
RMSEP	Root Mean Square Error of Prediction
RP-HPLC	Reverse Phase - High Performance Liquid Chromatography
RP-UPLC	Reverse Phase - Ultra Performance Liquid Chromatography
RR	Reduced Range
RTD	Resistance Thermal Detectors
SD	Standard Deviation
SE-HPLC	Size Exclusion – High Performance Liquid Chromatography
SG	Savitzky-Golay
SIMCA	Soft Independent Modelling of Class Analogy
SNV	Standard Normal Variate
SOP	Standard Operating Procedure

SVR	Support Vector Regression
QbD	Quality by Design
QbT	Quality by Testing
TDLAS	Tunable Diode Laser Absorption Spectroscopy
UV-Vis	Ultaviolet-Visibile
WFI	Water for Injection
VPHP	Vapour Phase Hydrogen Peroxide

CHAPTER 1

1. Biopharmaceutical Products: Process Development and Manufacturing

1.1 The launch of a biopharmaceutical drug product

Biopharmaceuticals represent a category of therapeutic products derived from living organisms, typically produced through biotechnological processes. The research conducted within the biopharmaceutical industry is pivotal for the advancement of new medicines, thereby contributing to innovative treatments. (Jameel, Skoug, & Nesbitt, 2020) In fact, these products serve a critical role in the management and prevention of various medical conditions, including chronic diseases and cancer. Biopharmaceuticals encompass a diverse array of substances, such as monoclonal antibodies, hormones, vaccines, gene therapies and recombinant proteins. For instance, monoclonal antibodies are artificially produced molecules engineered to replicate the immune system's capacity to combat harmful pathogens.

The introduction of new biological entities is an expensive endeavor, typically spanning an average period of 12-13 years from the identification of the new active substance. (Warne & Mahler, 2018)

Figure 1 summarized up all the necessary steps to produce a biological drug. (EFFPIA, 2021)

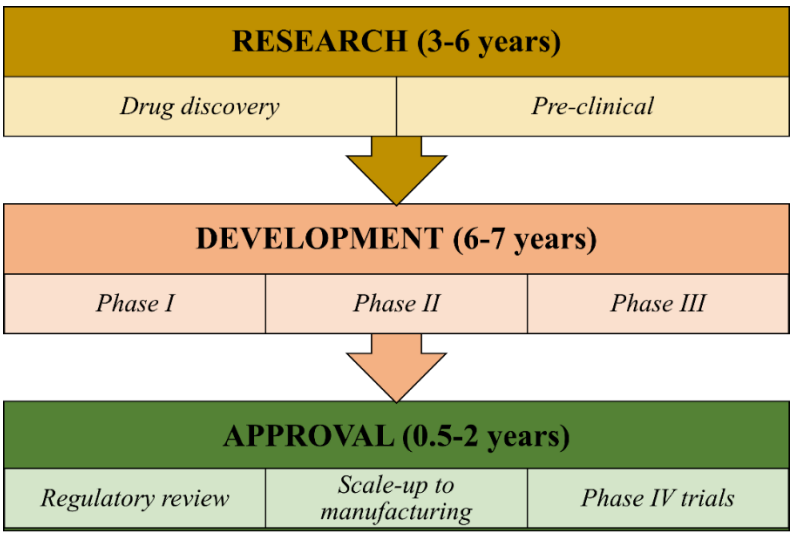

Figure 1: The three pillars of drug production: research, development, and approval

The development of a new biologic drug typically progresses through three different

stages:

- *Research phase*: the first stage involves the discovery and exploration of potential biologic drugs, which entails the identification of a biological target (like a protein or gene) and the development of a molecule capable of interacting with it. Researchers typically identify one promising compound from a pool of 5000-10000 screened candidates.
- *Development phase*: three different phases are encompassed in this stage. Clinical trials on humans are carried out. During this stage, the product and the process to manufacture are designed. In phase I the investigational compound is administered to a group of 20-100 volunteers to assess its safety, dosage range, and to identify potential side effects. In phase II, the group of volunteers is typically of 100-500 patients, who have the condition the drug is intended to treat. Then, in phase III, the biologic drug is tested in an even larger group of patients, equal to 1000-5000, to further evaluate its effectiveness and compare it to existing treatment options. The probability of passing to the next step in Phase III is low and equal to about 30%.
- *Approval phase*: upon successful completion of Phase III trials and the demonstration of safety and efficacy, the process development and transition to the manufacturing scale for final validation undergo thorough assessment. Then, a submission for approval is done to regulatory authorities, who may require up to 2 years to review it and decide whether to grant authorization for commercial purposes.

The expense associated to the introduction of a new product into the market has been projected to steadily rise. Deloitte's estimation indicates a 76% increase from 2013 to 2023, attributed to the growing complexity of product and process development (Deloitte, 2023). In this framework, pharmaceutical companies are encouraged to focus on reducing R&D costs by minimizing product launch timelines and modernizing scale-up and manufacturing methodologies.

In the recent years, regulatory authorities have promoted the adoption of new technologies to enhance pharmaceutical development and manufacturing. Notably, the FDA released the *Pharmaceutical cGMPs for the 21st Century: A Risk-Based Approach* (Food and Drug Administration, 2002) in 2002, and the *PAT – A Framework for Innovative Pharmaceutical Development Manufacturing and Quality Assurance* in 2004. (Food and

Drug Administration, 2004) This innovative approach introduces the concept of *Quality-by-Design* (QbD) which emphasizes embedding product quality within the production process rather than solely testing it at the end of manufacturing. This approach emphasizes in-depth analysis of manufacturing processes and the design of control systems to ensure product quality. QbD promotes defect prevention rather than correction after production, on the contrary of the *Quality-by-Testing* (QbT) approach. It relies primarily on the final product control through testing and analysis. This approach focuses on sampling and post-production testing to verify product compliance with quality standards. (Lawrence, et al., 2014) (Pramod, Tahir, Charoo, Ansari, & Ali, 2016) (Horst, Turimella, Metsers, & Zwiers, 2021)

Moreover, the regulatory authorities are being encouraging the introduction of consistent pharmaceutical processes following the "six sigma quality approach". It is a data-driven approach that looks for the reduction of process variation and the improvement of quality. To achieve these standards, novel technologies are needed in pharmaceutical landscapes according to the Emerging Technology Program. (Food and Drug Administration, 2017) (O'Connor, Yu, & Lee, 2016)

1.2 Process validation: from process development to commercial production

Process validation is an ongoing and integral part of all stages of drug development, ensuring that production processes consistently yield safe and effective drugs in accordance with quality standards. It plays a crucial role in several key phases. During the product development phase, process validation may begin with the development of pilot production processes and the establishment of critical process parameters. Throughout the clinical trial phases, process validation may be further refined based on the obtained results. Any change to the production process may require a new validation phase to guarantee product quality. Upon successful completion of the clinical trial phases and acquisition of the necessary regulatory approvals, process validation becomes essential to ensure that the commercial production of the drug adheres to the required quality standards and consistently delivers a safe and effective product over time. (European Medicines Agency, 2016)

Prior to the commercial distribution of any batch intended for patient treatment, a high level of confidence in the performance of the manufacturing process must be established, demonstrating its consistent production of the desired drug product meeting predefined quality standards. This assurance should be derived from objective data and from studies

conducted at laboratory, pilot and/or commercial scale. In essence, the aim of process validation is to prove that a comprehensive understanding of the product and process ensures that the manufacturing process consistently delivers a product within specified parameters. (Cartwright & Matthews, 2010)

In accordance with FDA guideline, process validation consists of three stages:

- Stage 1 – Process Design: the primary objective of the stage is to develop a process suitable for regular manufacturing, ensuring the continuous delivery of a product with the intended quality attributes. The second goal is to gain process understanding through a comprehensive evaluation of the linkages between process parameters and the quality attributes of the product. Understanding and knowledge of the process form the foundation for establishing a strategy for process control for each unit operation and the overall process. (Burdick, et al., 2017)
- Stage 2 – Process Qualification: the assessment of the process design aims to ascertain its capability for consistent commercial manufacturing. According to the FDA guidance *Process Validation: General Principles and Practices*, the Process Performance Qualification (PPQ) campaign is conducted to verify that the commercial manufacturing process is under control. (Food and Drug Administration, 2011) (Ding, et al., 2020) (Jameel F. , 2023) In other words, in this step, manufacturing campaigns are conducted to confirm that the process operates as intended and can reliably produce consistent results that comply with the required standards. Critical process variables are identified and controlled to ensure that any variations do not compromise the quality of the final product.
- Stage 3 – Continued Process Verification: during this phase, there is an ongoing assessment to ensure that the process maintains a state of control throughout commercial manufacturing. (Mahar & Verma, 2014) (Dobbins, et al., 2017)

The process of product development inherently entails a reduction in uncertainties as knowledge grows throughout the development stages. These uncertainties, stemming from the lack of information and understanding, have the capacity to negatively impact product quality and, consequently, pose risks to patient safety. Therefore, an assessment of these uncertainties, the associated issues to product quality, and their relationship to patient well-being is necessary to ensure that development is guided by proactive decision-making. (Hulbert, Feely, Inman, & Johnson, 2008)

Quality risk management, as described in ICH Q9, is "*a systematic process for identification, assessment, control, communication and review of the risks to the quality of drug products across the product lifecycle*". When applied with the concepts described in ICH Q8(R2), ICH Q10 and ICH Q11 the development of a product is based upon a systematic, scientific knowledge and risk-based approach which designs quality into the product, instead of depending on final product testing, according to the QbD initiative. (ICH Q8(R2), 2009) (ICH Q10, 2015) (ICH Q11, 2012)

1.3 Stage 1 – Process Design

One of the most critical stages of the process validation package is the Stage 1 – Process Design, whose main steps are summarized in ***Figure 2***:

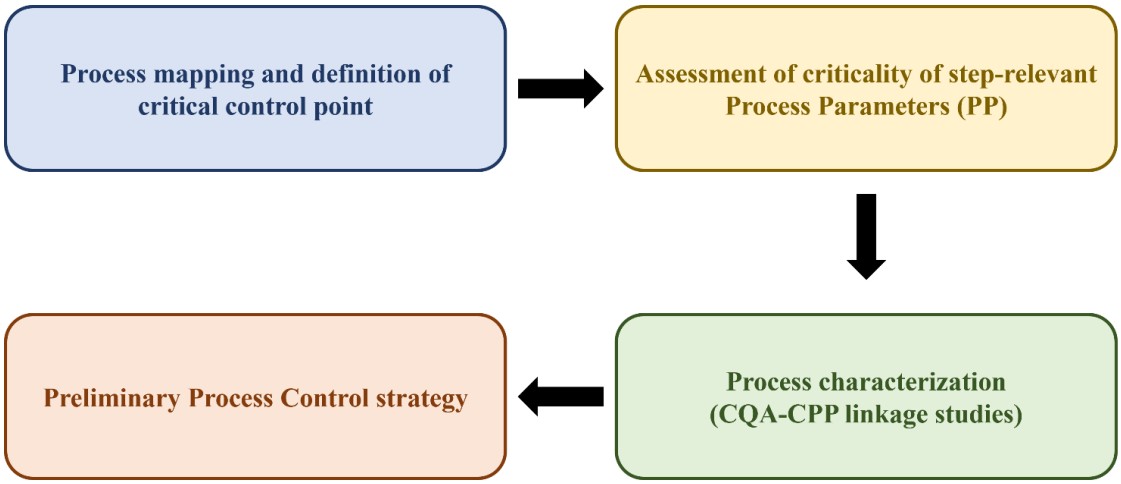

Figure 2: From process map to preliminary process control strategy: The evolution of process design in stage 1 activities

The process design commences with process mapping, a document that the R&D site receives from the manufacturing site that enumerates all critical control points and process elements to be considered.

Then, the critical process parameters (CPP), having an impact on the product CQAs, must be identified, monitored and controlled to guarantee the required product quality according to ICH Q8(R2). (ICH Q8(R2), 2009) An extremely high number of process parameters govern the manufacturing process of biotechnological products. However, experimentally testing all of these parameters to discern their effective impact on a CQA is not practically feasible. As a result, the scope of process parameters for experimental evaluation in the context of manufacturing process characterization needs to be narrowed down and focused on key management outputs. Therefore, potential critical process parameters (pCPP) that may influence any CQA are identified using a risk assessment

tool that combines prior knowledge from process development, clinical manufacturing data of the product of interest, relevant literature, and scientific expertise. (Kroll, Hofer, Ulonska, Kager, & Herwig, 2017) This methodology assesses, within a planned characterization range (PCR), the potential severity and uncertainty of impact of each process parameter on any unit operation relevant CQA. The PCR is a pre-defined range derived from an extension of the normal operating conditions (NOC). For the non-pCPPs a non-criticality range is established. Any non-CPP may become critical when it deviates outside of its non-criticality range. The criticality assessment yields a detailed list of all potential CPPs per unit operation and their respective PCR and non-criticality range. Additionally, it provides a list of relevant CQAs for each unit operation. (Gorsky, 2020)

Upon completion of the pCPP risk assessment, process characterization activities are essential to enhance the understanding of each unit operation and establish critical process parameters along with their acceptable ranges. The FDA process validation guidance states: "*Designing an efficient process with an effective process control approach is dependent on the process knowledge and understanding obtained. Design of experiment studies can help develop process knowledge by revealing relationships, including multivariate interactions, between the variable inputs (e.g., component characteristics or process parameters) and the resulting outputs (e.g., in-process material, intermediates, or the final product). Risk analysis tools can be used to screen potential variables for DOE studies to minimize the total number of experiments conducted while maximizing knowledge gained. The results of DOE studies can provide justification for establishing ranges of incoming component quality, equipment parameters, and in-process material quality attributes*". (Food and Drug Administration, 2011)

During process characterization activities, studies are performed at laboratory and pilot scale to evaluate the impact of variations of one or a combination of pCPPs on any unit operation-relevant CQAs and within PCR. Scale-down models must be developed in this phase to represent the entire unit operation by miniaturization from large scale. (Zahel, et al., 2017) The goal of process characterization is:

- To experimentally determine the relationships between process parameters and unit operation-relevant CQAs.
- To confirm or refute the criticality of process parameters.
- To determine the acceptable ranges of CPPs.
- To demonstrate process robustness through worst-case studies and excursion

studies.

After the process characterization has been conducted, a preliminary process control strategy is suggested to the manufacturing site. It is a deliberate set of controls that guarantees process performance and product quality. The controls include the process inputs (process parameters) and the process outputs (CQAs) related to drug product manufacturing processes, the equipment operating conditions and the related approaches and frequency of monitoring and regulation. It ensures to keep the manufacturing process under a state of control, i.e. the capacity of the process to withstand typical process and equipment fluctuations without adverse effects on product quality. (Lim, Sundaram, Sreedhara, & Lim, 2015)

Moreover, before starting with the process development phase, it is necessary to recognize the stability-indicating CQAs to determine the stability profile of a biotech product. The identification of the stability-indicating CQAs is performed based on prior knowledge and dedicated stress and stability studies to understand the degradation pathways. (Scott & Ritter, 2021) At the end of this kind of studies, the specific stability profile is obtained for the dedicated product. For the monoclonal antibodies, the CQAs usually considered are Low Molecular Weights (LMW) and High Molecular Weights (HMW) species, oxidation level and deamidation. Therefore, when evaluating the stability of the antibodies under long-term and accelerated conditions, it is mandatory to monitor these CQAs. (ICH Q6B, 1999) In fact, forced degradation studies are always conducted in biopharmaceutical field to support the development of mAb products. The understanding of product degradation mechanisms and the establishment of methods for stability indication to enable the monitoring of degradation are of paramount significance. (Nowak, et al., 2017) Commonly employed stress conditions encompass elevated temperature, freeze-thaw cycles, agitation, high and low pH, exposure to light, oxidation, and glycation. While these conditions are relatively severe compared to real-world storage and accelerated stability conditions, they can yield significant degradation trends and degradation products within a brief timeframe. The most encountered degradation mechanisms for mAbs are aggregation, fragmentation, deamidation, and oxidation. (Nowak, et al., 2017)

1.4 Protein stability and denaturation phenomena occurring in biopharmaceutical processes

Degradation mechanisms, mentioned in Section 1.3, could impact the protein stability, which is characterized as the difference between the free energy of the native protein and

that of the unfolded one. In the simplest case, a two-state reversible denaturation can be assumed:

$$N_p \leftrightarrow U$$

where N_p is the native protein and U the denatured one. The three-dimensional structure and biological activity characterize the folded protein. When the protein is denatured, there is a loss of biological activity. Even small alterations in the protein structure can significantly impact the stability. Protein stability can also be defined in terms or irreversible loss in activity that follows chemical and physical reactions of the folded or unfolded protein. Some examples of inactivation can include deamidation of amide side chains, methionine or tryptophan oxidation, aggregation, or surface adsorption. When irreversible reactions are kinetically favored in the unfolded protein, the description becomes:

$$N_p \rightarrow U \rightarrow X$$

where X does not readily revert to U and cannot refold by alternative pathways under favorable solution conditions. (Ahern & Manning, 1996)

The susceptibility of the molecule to the external factors experienced throughout its life cycle, including manufacturing, shelf life and administration, is assessed by examining its degradation route and rate. (Luo, et al., 2011) The observed degradation can be categorized in physical or chemical degradation. (Krause & Sahin, 2019)

1.4.1 Physical degradation

The main mechanism of physical degradation arises from the self-association of protein species or aggregation. Preserving the overall fold (secondary and tertiary structure) is essential to achieve the desired drug product properties. In typical conditions, monomeric species remain in their folded state due to the energy barrier that prevents the protein from adopting an aggregation-prone state. (De Simone, et al., 2011) In stressed conditions (i.e. exposure to high temperature environment), the flexibility of the protein conformation increases, potentially leading to conformational changes, such as modifications in secondary and tertiary structure, or reversible protein denaturation, involving the cooperative loss of higher-ordered structure. (Vermeer & Norde, 2000) This process may result in the partial exposure of buried, mainly hydrophobic amino acid residues to the surrounding aqueous solvent. Subsequently, the modified protein molecules may intermolecularly associate to reduce the unfavorable exposure of hydrophobic amino acid

residues to the solvent. (Jameel, Skoug, & Nesbitt, 2020)

For a monoclonal antibody, the aggregation process progresses through the following intermediate phases:

- Protein unfolding: disturbance of the energy barrier equilibrium to favor partially unfolded states. (Roberts, 2007)
- Protein association: interaction between aggregation-prone regions of the unfolded monomers (modulated by hydrophobicity or charge). (Weiss 4th, Young, & Roberts, 2009)
- Nucleation: structural rearrangements to promote secondary/tertiary structure changes. (Telikepalli, et al., 2014)

Since most of the aggregation process in unfolding-driven, understanding the factors that contribute to the conformational stability is essential. Therefore, the aggregation process must be under control since it is linked to the immunogenicity, that refers to the likelihood of a protein biotherapeutic to trigger unfavorable, harmful immune responses against itself. (Dobson, 2021)

1.4.2 Chemical degradation

One of the primary chemical degradation pathways induced by high temperatures is the fragmentation resulting from the cleavage of peptide bonds. Fragmentation of antibody is primarily induced by non-enzymatic reactions. The main fragmentation sites are in the hinge region and the domain-domain interfaces. (Cordoba, Shyong, Breen, & Harris, 2005) Cleavage between aspartate and proline in the CH2 domain induces aggregation. (Van Buren, Rehder, Gadgil, Matsumura, & Jacob, 2009)

Monoclonal antibodies are regularly subjected to oxidizing surroundings, which encompass dissolved oxygen, atmospheric oxygen, and free radicals. Forced oxidation is employed to investigate residues susceptible to oxidation and to ascertain the practical impact of this degradation pathway, such as the oxidation of a residue in the CDR which may affect binding and potency. The most common method involves incubating recombinant mAb with hydrogen peroxide. (Bertolotti-Ciarlet, et al., 2009) The major degradation product of forced oxidation is oxidation of methionine residues to create methionine sulfoxide and methionine sulfone. Research has shown that one methionine residue in the CH2 domain (Met252) and another in the CH3 domain (Met428) are the most vulnerable to oxidation due to their high levels of surface exposure. (Liu, et al.,

2008) (Lu, Gaza-Bulseco, & Zhou, 2009) (Chumsae, Gaza-Bulseco, Sun, & Li, 2007)

1.4.3 Impact of degradation mechanisms on safety, efficacy and stability of the drug product

Degradation mechanisms, such as aggregation, fragmentation or oxidation, can significantly impact the safety, efficacy and stability of a drug product.

Indeed, aggregated, or fragmented drug molecules can give immune responses in patients, leading to adverse effects. Aggregates may be recognized as foreign by the immune system, potentially resulting in allergic reactions or other immunogenic responses. Oxidative degradation can lead to the formation of secondary byoproducts that may pose safety risks. This can compromise patient safety and lead to health complications. Oxidative

Also, the therapeutic effectiveness of a drug can be diminished by aggregation or fragmentation. Aggregated molecules may have altered pharmacokinetics, affecting their absorption, distribution, metabolism, and excretion. Additionally, fragmentation and oxidation can lead to the formation of inactive or less active species or can modify the chemical structure of the API, reducing the overall potency of the drug and its ability to achieve the desired therapeutic effect.

Furthermore, as deeply discussed above, aggregation and fragmentation can adversely affect the physical and chemical stability of a drug product. Aggregates may precipitate out of solution, leading to inconsistent dosing and product loss. Fragmentation and oxidation can result in the degradation of API, leading to reduced shelf life and necessitating more stringent storage conditions. Overall, these changes can compromise the integrity of the drug product over time.

1.5 Fill and finish process of a liquid/freeze-dried drug product

To gain a comprehensive understanding of where changes in Critical Quality Attributes (CQAs) may occur within the product, it is essential to describe the fill and finish process of a drug product. The typical liquid and freeze-dried drug product (DP) manufacturing process, evaluated during process characterization activities, is reported in ***Figure 3***. It involves all the steps, including the preparation, filling and packaging of the final drug product. (Das, et al., 2021) Throughout the fill and finish process, adherence to Good Manufacturing Practices (GMP) and other regulatory standards is essential to ensure the safety, efficacy, and quality of the biopharmaceutical product.

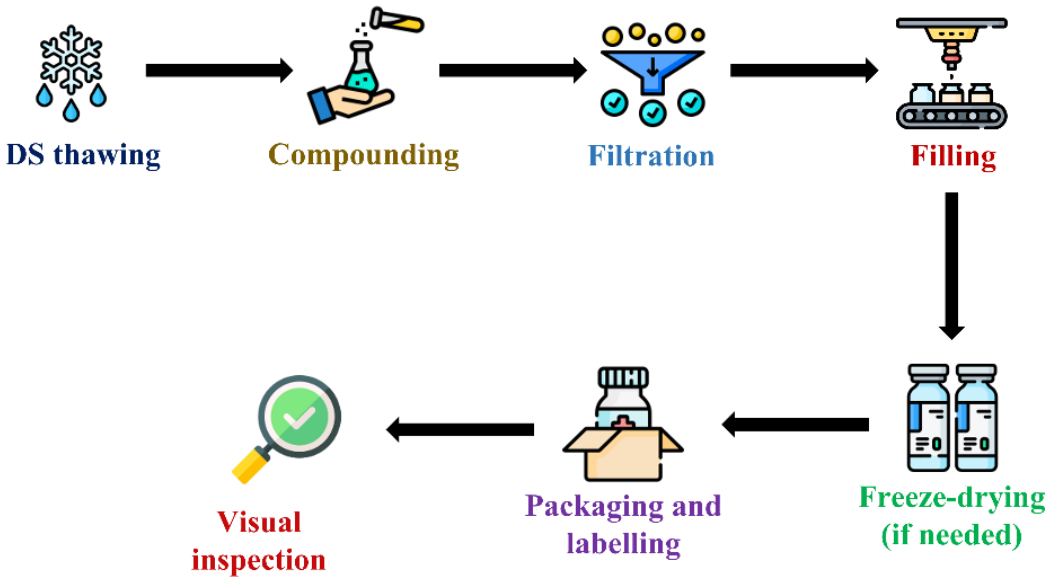

***Figure 3**:* Step-by-step process for the manufacturing of liquid or lyophilized drugs: from drug substance to final product packaging

Biopharmaceuticals are often frozen in bulk to minimize degradation of the active pharmaceutical ingredient (API), allowing for storage and transport minimizing the microbial growth. Therefore, the first stage of a manufacturing process is the thawing of the drug substance (DS). Mixing the bulk solution may involve integrating suitable excipients to achieve the final formulation and creating a buffer or diluent to modify the protein concentration in the bulk solution. The subsequent phases involve sterile filtration, followed by aseptic filling into a primary packaging container and sealing. The subsequent procedures vary based on the physical forms of the drug product:

- If the final DP is a liquid in a vial/cartridges/syringes, the containers are stoppered and capped;
- If the final DP is freeze-dried, the vials will be partially sealed and placed into a freeze-dryer. After the freeze-drying process concludes, the containers are sealed and transferred to a capping station to finalize the sealing process.

The sealed DP containers, both for liquid and freeze-dried DP, are subjected to the visual inspection step, labelling and secondary packaging operations, transportation and storage. (Patro, Freund, & Chang , 2002)

1.6 Freeze-drying process: an in-depth focus for solid formulations

Biopharmaceuticals are composed of proteins, which are often not stable in liquid phase and tend to degrade over time. Therefore, the freeze-drying is a vital stage in numerous drug manufacturing processes, as it ensures long-term stability of formulation containing

the active pharmaceutical ingredient (API). Around 46% of biopharmaceutical dosage forms sanctioned by Food and Drug Administration (FDA) from 2003 to 2011 are produced via freeze-drying. The freeze-drying process combines many advantages, such as it slows down the kinetics of chemical and physical degradation reactions and it also guarantees the sterility conditions. Moreover, the low operating temperatures render this method especially appropriate for heat-sensitive products, such as pharmaceuticals. In addition, the high specificity surface of the product allows for quick and easy reconstitution. (Fissore D. , 2013)

1.6.1 Freeze-dryer instrumentation

Freeze-drying involves eliminating the water content in a product through sublimation, transforming the ice into vapor by operating at low pressure and temperature. A highly porous structure is obtained, that can be rehydrated by the addition of the liquid.

Figure 4 illustrates the typical configuration of a freeze-dryer:

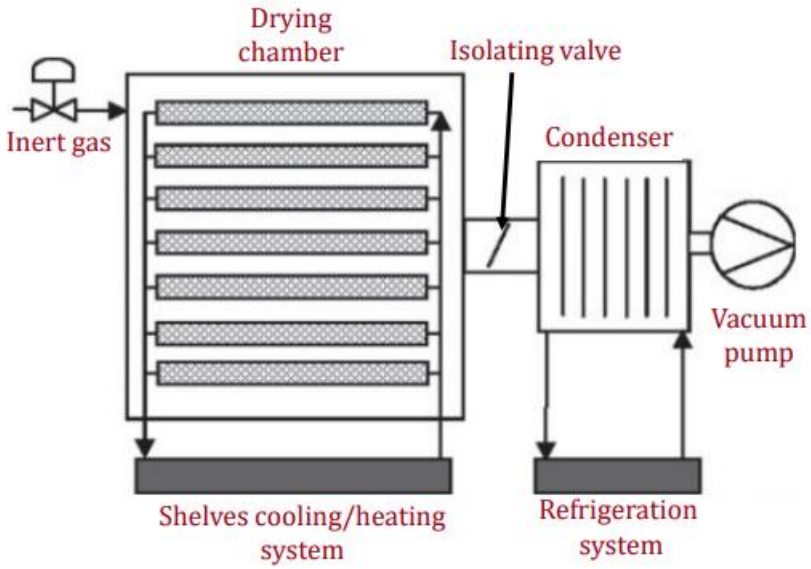

Figure 4: Freeze-dryer instrumentation

All freeze-dryers are characterized by a drying chamber, where there is a channel through which a temperature-controlled heat transfer fluid pass. Product containers are placed on the shelves inside the chambers and held in place by a metal frame. The drying chamber is connected, via a duct, to the condenser. Here there is a surface cooled to about -80°C. The solvent separated as vapor, in contact with the cold surface, will tend to freeze. The isolation valve in the duct is closed during the freezing phase and opens only during the drying phases to create vacuum in the chamber. The condenser is connected to the vacuum pump that separates the incondensable gases. The vacuum pump is essential to achieve

the desired pressure value. The maintenance of the pressure at its setpoint value may be guaranteed by the introduction of a suitable quantity of inert gas, often nitrogen, into the chamber. Inert gas is also added at the end of the process to re-pressurize the system so that product discharge can take place. (Fissore D. , 2013)

1.6.2 Freeze-drying process

Figure 5 shows the phase diagram of water and the physical transformation occurring during a freeze-drying cycle.

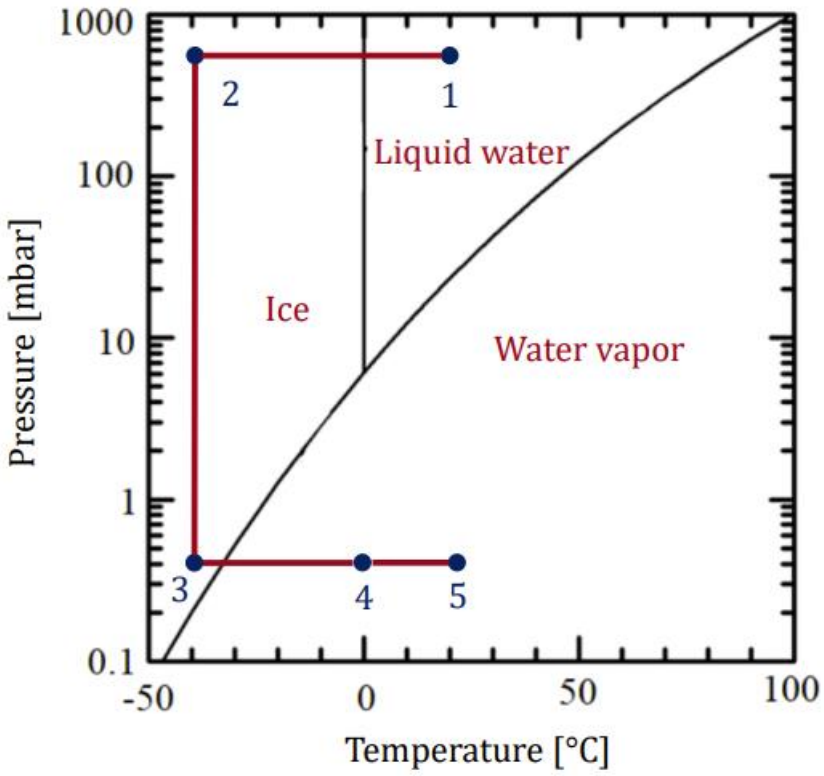

Figure 5: Change in water phase diagram during freeze-drying process steps

Three different phases characterize the freeze-drying process: freezing, primary drying and secondary drying.

The process starts with a liquid solution (1) that contains the solvent, usually water, with the API and some excipients that may be needed to protect the active molecule. During the *freezing* step (1→2) most of the solvent, the free water, is turned into ice by lowering the temperature of the process fluid up to -40/-50°C. A fraction of water, the bound water, is incorporated into the frozen product and remains unfrozen. Freezing includes two main steps:

- Nucleation, so the formation of the first stable nuclei of water;

- Growth, so the aggregation of nuclei that grow forming crystals of ice.

Nucleation temperature and cooling rate affect the characteristics of the frozen product and, therefore, the duration of primary drying. In fact, the sublimation left spaces empty, called pores, through which the vapor flows. This determines the resistance to the mass transfer, of relevant importance in the drying steps. The lower the nucleation temperature, the higher the number of stable nuclei formed. This results in the average dimension of the ice crystals. This also has a bearing on reconstitution times, as it changes the specific area that the dried solid will offer to the solvent. (Oddone, Barresi, & Pisano, 2017)

In the freezing step the formulation undergoes to a serious of stresses. Therefore, excipients are introduced to stabilize the protein molecule. Crystalline excipients will tend to form a eutectic mixture and are characterized by the melting temperature. Amorphous excipients, on the other hand, are characterized by the glass transition temperature that marks the transition from a rigid to an amorphous/viscous state. These temperatures are evaluated by Differential Scanning Calorimetry (DSC) or cryo-microscopy and they are essential for selecting the operative conditions of the primary drying step.

After the freezing is completed, the phase 2→3 corresponds to the achievement of the desired vacuum level at constant temperature. It is essential to operate sufficiently below the triple point of water. Then, there is the *primary drying* phase (3→4), the most critical and time expensive phase. The chamber pressure and the shelf temperature must be modulated according to the formulation. The product temperature should be many degrees below a limit product temperature to reach a dried product with good appearance. Primary drying is normally conducted under high vacuum conditions at 5-30 Pa and a product temperature around -35/-15°C. By lowering the pressure in the system, the solvent in the form of ice crystals will begin to sublimate, transforming into vapor. This conversion will result in a reduction in product temperature. Due to the endothermicity of the sublimation process, the temperature of the shelf is slightly increased up to 0/5°C. During sublimation, dried product (cake) appears on top of the solution and approaches the bottom of the vial.

The main significant problem during a freeze-drying process is that, under same drying conditions (pressure and shelf temperature), the vials in the batch will behave differently depending on their position. (Barresi, Pisano, Rasetto , & Fissore, 2010) The most investigated vials are the peripheric and the central ones. In particular, the central vials will be shielded from the radiation of the surrounding vials and, therefore, will have a

zero contribution of radiation on the side wall. On the other hand, the peripherical ones receive more heat by radiation from the side walls. Therefore, they have more risk of overheating, but will take much lower to complete the drying process. According to this phenomenon, the drying time is defined based on the information of the central vials which, taking the longest time, are the ones that determine the duration of the cycle. On the contrary, the product temperature is defined according to the information of the peripherical vials. (Pisano, Fissore, & Barresi, 2011) (Pisano, Fissore, & Barresi, 2011)

At the conclusion of primary drying, all ice has been removed by sublimation. However, by measuring the residual solvent concentration in the product, it is possible to observe that the amount of water may be too high, up to 20%. The water can no longer be removed by sublimation because it is no longer in the form of crystals, and it is required a more intense heating to promote water desorption. Therefore, *secondary drying* is performed (4→5), during which the product temperature increases up to 10-30°C under the same vacuum conditions of primary drying. (Fissore, Pisano, & Barresi, 2011)

1.6.3 Freeze-drying process monitoring

Determining the extent of primary drying is fundamental for the success of the entire process. In fact, it is necessary to guarantee the complete removal of ice and ensure that the residual water content is sufficiently low to prevent collapse during secondary drying or to avoid unnecessarily prolonging the process. (Fissore & McCoy, 2018)

One of the methods proposed in literature consists of calculating the ratio between the pressure measured by a thermoconductive (Pirani) sensor and the one obtained from a capacitive (Baratron) sensor. The latter measures the actual pressure of the freeze-dryer chamber, while the measure obtained through the Pirani sensor is influenced by the composition of the gas. At the beginning of the process only air is present in the chamber. Throughout primary drying, the gas in the chamber predominantly comprises water vapor, as its molar flow experiences a substantial increase. Following the conclusion of primary drying, the gas composition shifts, and nitrogen, introduced for pressure control, becomes more prevalent. Currently the Pirani/Baratron ratio decreases when ice sublimation is no longer occurring, until it asymptotically tends to 1, index of the end of this stage. (Patel, Doen, & Pikal, 2010)

Another common method used to identify the ending point of the primary drying is the TDLAS (Tunable Diode Laser Absorption Spectroscopy). It allows direct measurement of the water vapor concentration in the duct linking the condenser and the drying chamber.

A decrease in concentration indicates a change in composition and, therefore, the conclusion of the sublimation process. (Sharma, Kessler, Bogner, Thakur, & Pikal, 2019)

Another method described in this work is the Pressure Rise Test (PRT), which involves conducting a pressure increase test. The valve that separates the drying chamber from the condenser is closed. So, the drying chamber is isolated for a certain period and the speed of pressure rise is measured. If this pressure increase over time corresponds to the increase in pressure induced by gas infiltration, from the external environment into the equipment, then the primary drying phase can be deemed completed. If, on the other hand, the pressure increase is greater than that attributable to equipment leakage, then it can be deduced that there is some extra gas accumulating in the drying chamber. This is related to the generation of steam produced by the ice sublimation process. (Fissore, Pisano, & Barresi, 2011)

The endpoint of primary drying may also be identified by analyzing the response from the thermocouples in the product, provided that the vials with the thermocouples accurately represent the entire batch. (Patel, Doen, & Pikal, 2010) The temperature of the product nearing the shelf temperature set point is often regarded as an indicator of the conclusion of primary drying. However, it has to be considered that the monitored vials may not accurately represent the entire batch. Therefore, primary drying times derived from product thermocouples may be significantly skewed, with the actual primary drying duration likely being much longer, particularly in manufacturing contexts. Furthermore, edge vials, where thermocouples are typically positioned during the manufacturing process, tend to dry more quickly than center vials due to side radiation effects from the chamber walls and door. (Rambhatla & Pikal, 2003) To address this bias, a soak period of 10–20% is generally added to the primary drying time once the thermocouple vials reach the shelf temperature; however, the actual time required may vary significantly, potentially being shorter or longer than anticipated. (Tang & Pikal, 2004)

Another indicator of the primary drying endpoint is the condenser pressure. (Patel, Doen, & Pikal, 2010) During this phase, most of the gas within the chamber consists of water vapor. Due to the high total vapor flux, a significant pressure difference develops between the chamber and the condenser to facilitate the removal of water. However, once primary drying concludes, the difference in pressure decreases, leading to an increase in the condenser pressure, while chamber pressure remains constant. The condenser pressure primarily reflects the partial pressure of nitrogen present. The nitrogen bleed serves to

maintain the chamber pressure at the desired set point. The initial increase in condenser pressure indicates that sublimation is essentially complete, as the primary mass transfer phase of the process has largely concluded. (Pikal, Roy, & Shah, 1984)

A moisture sensor can be installed in a freeze-dryer to monitor the residual moisture content in the product. These sensors operate by measuring the dew point and are capable of detecting liquid or ice in quantities as low as 1%. Consequently, a noticeable decline in the dew point signifies the transition from solid ice to vapor. (Millrock Technology, 2016)

1.6.4 Product temperature monitoring

Product temperature can be measured using thermocouples or resistance thermal detectors (RTD). The thermocouples are commonly employed in laboratory scale freeze-dryers, whereas RTDs are predominantly used in manufacturing freeze-dryers due to the possibility of being sterilized. However, the size of RTDs may impact measurement accuracy. (Fissore, Pisano, & Barresi, 2017) Additionally, when using thermocouples, selecting tin wires allows for a small sensing tip, facilitating precise temperature measurements and improved positioning within the batch. Nevertheless, this approach renders the measurements highly sensitive to the exact placement, where even minor deviations can significantly affect accuracy. Conversely, a larger sensing device measures a broader section of the product, yielding an average value that, while less precise, is more robust. (Presser, 2003)

Also, optical fiber sensors (OFSs) have recently been proposed for monitoring product temperature during the freeze-drying process. The sensing element consists of a fiber Bragg grating (FBG), which features periodic variations in refractive index. Since the refractive indices of FBGs are temperature-dependent, the measured reflection correlates with the local temperature. OFSs can facilitate invasive monitoring by immersing the fiber within the product, allowing for the measurement of a three-dimensional temperature profile through a helical arrangement. Alternatively, they can be used non-invasively by integrating the fiber into the vial's bottom. These sensors are steam-sterilizable and have demonstrated greater sensitivity, faster response times, and improved resolution compared to thermocouples. (Kasper, Wiggenhorn, Resch, & Friess, 2013)

Another category of devices used for temperature monitoring involves the use of remote interrogation system (TEMPRIS) sensors. They work as passive transponders, deriving

energy from an electromagnetic field, which eliminates the need for wired connections. However, the freeze-dryer must be appropriately equipped to ensure that the sensors can be adequately irradiated in all relevant positions. A significant drawback of TEMPRIS is the considerable size of the device, which adversely impacts both the freezing and drying processes. Specifically, if the sensor is fully immersed, the height of the filled volume increases substantially, resulting in the measuring tip being positioned at the bottom of the vial. (Schneid & Gieseler, 2008)

1.7 Stress factors and CQAs potentially impacted in each DP manufacturing process step

The fill and finish process involves different unit operations, which must be investigated during the process characterization, to comprehend the stresses involved and the risk factors associated with each process stage. The stressors experienced during each unit operation in drug product manufacturing, the process parameters involved, and the typical drug product CQAs that may be affected are documented in ***Table 1*****.**

Table 1: Impact of process parameters and stress factors on Critical Quality Attributes (CQAs) at different Drug Product (DP) manufacturing process steps

Manufacturing Process Steps	***Process Parameters***	***Stress Factors***	***CQAs Potentially Impacted***
DS thawing	Thawing time and temperature, contact time with container	Cryoconcentration Interfacial stress	HMW, LMW, sub-visible particles, excipient/protein content
DP compounding	Mixing time and speed, contact time with vessel	Shear stress, interfacial stress, inhomogeneity	HMW, LMW particle formation, excipient/protein content, turbidity
DP filtration	Filter type, filtration ratio, static contact time with filter, filtration pressure	Protein/excipient adsorption	Protein/excipient concentration, particle formation
DP filling	Filling speed, filling pump type, filling needle size,	Interfacial stress, shear stress, drying on needle	HMW, LMW, particle formation
DP freeze-drying	Shelf temperature, chamber pressure, heating/cooling rate, drying times	Interfacial stress, cryoconcentration, excipient crystallization	HMW, residual moisture, cake collapse, oxidation, reconstitution time, protein content
Visual inspection	Room temperature and light intensity, step duration	Light stress, thermal stress and material compatibility	HMW, oxidation, LMW, protein/excipient content

The DS thawing process can potentially impact protein stability due to the heterogeneous distribution of protein and solute, leading to the formation of aggregates. Slow thawing rates can exacerbate this issue, as small ice crystals grow into larger ones, intensifying

the recrystallization process. This phenomenon exerts interfacial tension or shear on the protein at the ice-liquid interface, resulting in damage. Consequently, slow thawing may lead to reduced protein activity recovery, making fast thawing the recommended approach. Therefore, DS thawing is carried out under defined conditions of temperature and thawing rate. (Rodrigues, Miller , Glass, Singh, & Johnston , 2011) To replicate the behavior observed at the manufacturing scale without subjecting the molecule to undue stress, thawing experiments are conducted at the laboratory scale using the same temperature vs. time profile applied at the manufacturing level. Additionally, the contact time of DS with the container is maintained. Aggregation and protein/excipient contents can be significantly affected at this stage. Therefore, during process characterization activities, they are consistently evaluated using chromatographic techniques to ensure that thawing has no adverse effects on the molecule. (Lashmar, Vanderburgh, & Little, 2007)

Mixing is a crucial unit operation that takes place at various stages in the production process and must be executed with minimal influence on protein stability. Typically, the DS pooling and all the excipients are homogenized within a vessel container. The formation of aggregates/particles is the main modification that can occur during mixing steps. (Patel, Kothari, Tunga, Ritter, & Tunga , 2011) Protein aggregation mechanisms are primarily associated with foaming, resulting in a notable rise in the air-liquid interface to which proteins have a tendency to adhere, causing structural alterations and the development of aggregates that may return to the bulk solution. (Maa & Hsu, 1997) The parameters that can be adjusted to prevent or minimize foaming are the mixing time and speed. To subject the molecule to the same stress as at the manufacturing scale, the impeller tip speed is typically maintained at an equal level in both cases. (Deshmukh & Ogunyankin, 2020) Moreover. in the compounding phase, it is essential to achieve the target concentration in the formulated drug product according to the specified requirements. Before proceeding with subsequent stages, it is crucial to ensure that homogeneity conditions are met within the vessel where the preparation takes place. Consequently, the evaluation of drug and excipient concentrations is always performed. (Duerkop, Berger, Durauer, & Junbauer, 2018)

The injection of protein drug products requires their sterility. The sensitivity of proteins to heat prevents the use of heat sterilization, making sterile filtration the preferred technique for eliminating microorganisms. The filtration procedure, encompassing the filters utilized and other materials that encounter the product, should be suitable for the

drug product without exerting a notable influence on drug product CQAs. (Allmendinger, Mueller, Huwyler, Mahler, & Fischer, 2015) Key considerations involve the possibility of protein or excipient adherence to the filter membrane and the discharge of extractables and leachables into the drug product formulation. As filters themselves can shed particles, an initial flush volume may be employed before using them for the filtration of the DP solution to minimize the presence of shed particles. (Liu, Randolph, & Carpenter, 2012) Dilution of DP filtered at the beginning of filtration can occur due to the residual Water for Injection (WFI) in the filter after filter integrity test (FIT) pre-use. Therefore, during the filtration step, it is imperative to monitor the drug/excipient content to assess the presence of absorption or dilution effects.

Filter membranes usually have a pore dimension equal to 0.22 µm and are made of a hydrophilic material, mainly PVDF or PES. Proteins, as amphiphilic molecules, tend to adhere to interfaces, such as the filter membrane material. Although this can result in protein loss, the minimal quantities of adhered protein generally do not impact the protein dosage. However, the adhered protein may undergo structural modifications and aggregation, potentially leading to the release of misfolded and aggregated protein into the solution. (Allmendinger, Mueller, Huwyler, Mahler, & Fischer, 2015) The sizing of plant-scale filters and the determination of the maximum filterable volume are established through laboratory-scale experiments, maintaining the same filter membrane material. Additionally, various static contact time experiments are typically conducted to simulate the possibility of a stop during the manufacturing process. (Rajniak, et al., 2008)

As previously mentioned, the sterile formulation is dispensed into primary containers, such as glass vials, syringes, and cartridges. This unit operation can expose the protein to various contact surfaces and shear stresses. The filling process involves the use of different rotatory pumps, which may create air-liquid interfaces capable of inducing protein denaturation. Moreover, the protein solution may be exposed to high shear force and interact with different contact surfaces of the containers, potentially leading to foreign particle introduction and protein aggregation, which could pose immunogenicity risks. (Her, et al., 2020) Experiments are typically conducted at the pilot plant scale, paying careful attention to maintain a constant shear rate in the needle between the two scales. (Jameel, Undey, Kovach, & Tanglertpaibul, 2015)

Biopharmaceuticals are prone to degradation and often exhibit instability in the liquid phase. Therefore, freeze-drying may be employed to remove water from the product,

thereby enhancing stability for long-term storage and transportation. (ICH-Endorsed Guide for ICH Q8/Q9/Q10 Implementation, 2011) Each step of the freeze-drying process can introduce stresses that can influence the physical stability of the product, potentially inducing the formation of aggregates. Moreover, also chemical degradation, such as oxidation or deamidation, can occur during lyophilization. (Remmele, Krishnan, & Callahan, 2012) Therefore, it is strongly recommended to monitor the residual biological activity at the end of a freeze-drying cycle, ensuring that it remains sufficiently high, and to assess the reconstitution time, which should be rapid. (Tang & Pikal, 2004) The most important CQA to monitor is the residual moisture (RM), as it significantly influences the stability of the API. In fact, an excess of residual moisture acts as a plasticizer, lowering the glass transition temperature (Tg) of the drug product formulation, thus increasing mobility and susceptibility to degradation pathways. Conversely, the residual moisture content must not be too low, as water is essential for maintaining the native structure of the protein. (Mensik, Frijlink, van der Voort Maarschalk, & Hinrichs, 2017) Another crucial aspect of the freeze-drying process is to prevent collapse during primary and secondary drying, as this can potentially lead to stability issues. (Patel, et al., 2017) The product quality risk related to the freeze-drying can be reduced through the optimization of a freeze-drying cycle. To do this, a deeper understanding of the process is mandatory. (Fissore, Pisano, & Barresi, 2011) Therefore, some tools like Differential Scanning Calorimetry (DSC) and Freeze-dry Microscope (FDM) are already used to assess Tg' and collapse temperature.

The final step involves a visual inspection of the packaged biopharmaceutical products, ensuring adherence to quality standards and the absence of defects or visible issues. Automated systems are frequently utilized to improve the efficiency and precision of the visual inspection process. It is imperative to control the light intensity, temperature, and duration to avoid any impact on the oxidation level, sub-visible particles, and overall appearance of the product.

As deeply discussed above, during each of the process step, it is important to keep under control different process parameters, can have an impact on the denaturation phenomena occurring in a drug product. The use of Process Analytical Technologies (PAT) for the monitoring of the different CQAs in the process steps could speed up the development and enhance the process understanding. (Fissore D. , Pisano, Velardi, & Barresi, 2009)

1.8 Measurement of Critical Quality Attributes in manufacturing process

To monitor the evolution of product quality throughout the fill and finish process, it is mandatory to measure its CQAs to understand the entity of the stress during each DP unit operation.

1.8.1 Conventional analytical techniques currently employed in biopharmaceutical industry

The conventional analytical techniques, currently used in pharmaceutical industries and reported in ***Table 2***, are often destructive and time-consuming for the operators who perform the analysis. This result in an economic loss for the company income, since the samples analyzed are wasted.

Table 2: Critical Quality Attributes (CQAs) with corresponding conventional analytical techniques and analysis durations

CQA to be monitored	***Conventional analytical technique***	***Duration of analysis****
High Molecular Weights (HMW)	Size Exclusion – High Performance Liquid Chromatography (SE-HPLC)	5 days
Low Molecular Weights (LMW)	Capillary Gel Electrophoresis (CGE)	5 days
Oxidation Level	Reverse Phase - Ultra Performance Liquid Chromatography (RP-UPLC)	5 days
Protein content	Solo VPE	1 day
Methionine Content	Reverse Phase - High Performance Liquid Chromatography (RP-HPLC)	5 days
Polysorbate 20 Content	Reverse Phase - High Performance Liquid Chromatography (RP-HPLC)	5 days
Residual Moisture	Karl-Fischer Titration (KF)	2 days

* the duration here reported refer to all the activities related to the analysis: from the solution preparation, analytical run, test duration, cleaning of the equipment and data evaluation

Moreover, some conventional methods, like chromatography, may be complex, demanding highly skilled operators and extensive training, thereby increasing the time and cost associated to the analysis. This can lead also to potential human error occurring during sample preparation. Additionally, the conventional analytical techniques do not match with the concept of QbD approach since they allow only the testing of the product at the end of the manufacturing process.

1.8.2 The need for Process Analytical Technology (PAT) in biopharmaceutical industry

To enhance pharmaceutical development and manufacturing, regulatory authorities have promoted the adoption of new technologies in recent years, as deeply described in Section 1.2. According to the QbD approach, it would be optimal to monitor these CQAs in real-time during the process, allowing for a deeper understanding and an intervention in case of issues. Moreover, this could speed-up the time-to-market launch of a new product, since all the process development and validation phases will be more efficient, lead the company to be more competitive with respect to the others.

These aims can be reached using the Process Analytical Technology (PAT). The PAT is a system for "designing, analyzing, and controlling manufacturing through timely measurements of critical quality and performance attributes of raw and in-process materials and processes, with the goal of ensuring final product quality." (Food and Drug Administration, 2004)

Figure 6 shows all the possible applications of a PAT tool in a process stream and laboratory environments.

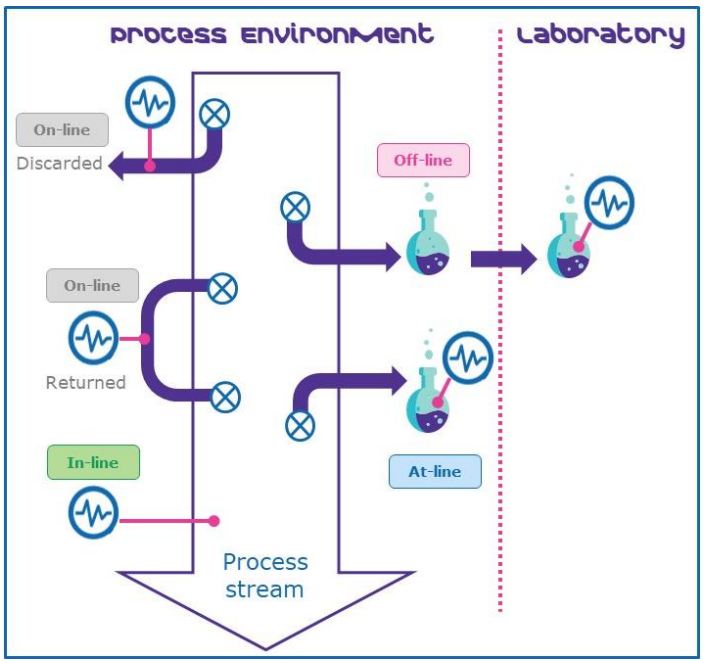

Figure 6: Various applications of Process Analytical Technology (PAT): on-line, in-line, at-line, and off-line

The PAT tools can be used in four different modalities:

- *Off-line*: off-line measurements involve taking samples outside the manufacturing process and the analysis is performed in a laboratory setting. They are mostly used for more comprehensive and detailed analyses. Samples are collected, transported to

a laboratory, and subjected to a range of analytical techniques. While not as immediate as in-line or on-line approaches, off-line methos provide a thorough understanding of product quality.

- *At-line*: at-line measurements involve taking samples from the manufacturing process, but the analysis is performed in a separate location, near to the process stream. This allows for periodic monitoring of critical parameters. Samples are collected and analyzed in a controlled environment, providing valuable data to assess and adjust the manufacturing process as needed.
- *In-line*: in-line measurements are taken directly within the manufacturing process, in real-time, without the need of removing samples from process stream. This allows for continuous manufacturing and immediate adjustments to ensure product quality.
- *On-line*: on-line measurements are conducted in real-time, but the analysis is performed slightly away from the manufacturing process. In this case, the sample can be discarded or returned to the process stream.

1.9 Motivation of the work

Monitoring the drug product CQAs impacted by the process steps involved in process development and manufacturing is fundamental to guarantee the product quality. As mentioned above, the implementation of PAT in pharmaceutical development aims to improve product quality, reduce costs, enhance process understanding, and promote a culture of continuous improvement and innovation according to QbD approach.

In this framework, NIR and Raman spectroscopy serve as potent, non-invasive tools suitable for characterizing the DP process development and expediting the technology transfer to manufacturing sites. As such, at-line and in-line applications have been devised and presented in this Thesis, with the goal of significantly enhancing process comprehension.

Chapter 2 delineates the working principles of the most prominent PAT tools in pharmaceutical field, spectroscopy techniques, specifically NIR and Raman spectroscopy.

Chapter 3 provides details on the equipment, experimental setup, and procedures used in this Thesis.

Chapter 4 and Chapter 5 pertain to the qualitative and quantitative at-line applications of Raman spectroscopy, with the objective of predicting various protein-related CQAs at different stages of the manufacturing process, including compounding, filtration, and

visual inspection of a liquid mAb product. Specifically, assessments were conducted on high molecular weights, low molecular weights, and protein/excipient contents. Furthermore, the chapter delves into the application of the developed model to the freeze-dried mAb, demonstrating that the freeze-drying process did not impact the aggregation level.

Chapter 6 focuses on the quantification of RM following the freeze-drying process, which constitutes one of the final stages in manufacturing solid products. A key enhancement involved the implementation of a neural network to minimize the experimental effort required for model generalization. Initially, the model developed for a specific surrogate product was tested on various products to assess its robustness and its performances were compared with a linear model. Subsequently, a significant innovation in this approach was the evaluation of the model developed for the surrogate to predict the RM of an actual drug product. Thus, minimal experimental effort and cost are required to develop these methods.

Chapter 7 explores the at-line and in-line application of the models developed off-line. Specifically, this chapter discusses the use of NIR spectroscopy for the freeze-drying process monitoring, highlighting its potential to enhance process understanding and control. By concentrating on the drying phases, NIR spectroscopy facilitated insights into physicochemical changes occurring in the formulation and helped identify deviations from standard operating conditions that could affect product quality. The need for a forecasting procedure to estimate the behavior of new cycles based on limited observations is acknowledged and currently under investigation. Moreover, the residual moisture trend and the endpoint of drying phases was assessed using PLS sensor and compared with Pirani-Baratron methods, demonstrating the reliability of the PLS model in monitoring the drying phases in real-time. The second part of the chapter presents two in-line Raman applications for monitoring protein content during filtration and dilution processes. The results obtained from the PLS model aligned well with the expected behavior of the drug product under investigation. These in-line applications are valuable for process characterization, serving as alternatives to traditional methods and providing real-time data availability.

Finally, Chapter 8 is focused on remarkable conclusions and perspectives for future developments of this work.

CHAPTER 2

2. Spectroscopic methods as PAT monitoring tools in pharmaceutical field

Within the biopharmaceutical field, there is a raising interest in spectroscopic techniques, such as Near-Infrared Spectroscopy (NIR) and Raman spectroscopy, among the available PAT techniques. (Pieters, De Beer, & Vander Heyden, 2012) (De Beer, et al., 2011) These non-invasive techniques, in fact, provide direct monitoring of product characteristics, focusing on the current state of the product and enabling the direct assessment of its quality. (Bai, Nayar, Carpenter, & Manning , 2005) These two complementary spectroscopic techniques are based on distinct working principles: NIR relies on the absorption of near-infrared energy by the product; while Raman is based on the scattering of a laser beam induced by the product structure. (De Beer, et al., 2009) As a result, both techniques can provide diverse chemical information about a product. (Gerzon, Sheng, & Kirkitadze, 2022) NIR spectroscopy has been extensively investigated as a powerful tool for estimating residual moisture in freeze-dried product, both off-line and in-line. Conversely, Raman spectroscopy, being insensitive to water, has the potential to investigate the behavior of the excipients and the related CQAs, including aggregation and fragmentation level, the presence of oxidized forms, and the protein/excipients content. More details on the working principle and application of both techniques in the pharmaceutical field will be given in the following sections (see Section 2.1 and Section 2.2).

The two spectroscopic techniques can be used for two different purposes:

a) *Qualitative application:* it does not yield a precise numerical value, but offers more generalized information about certain product characteristics. Generally, qualitative applications involve comparing the product evolution during the process or between samples processed in different batches to identify any potential changes with respect to the reference sample or process (calibration phase). Therefore, a qualitative approach typically needs the use of a statistical method. It can be applied during CPV to monitor and control the process performance over time.

b) *Quantitative application:* it yields a numerical value as output that quantifies a

quality attribute of the product. The calibration phase is needed involving a reference analytical technique. The developed model can be applied to speed-up the process development phase and to monitor the CQAs during DP manufacturing process.

2.1 NIR spectroscopy

2.1.1 Fundamentals of NIR-theory

Near-Infrared (NIR) spectroscopy is a spectroscopic method that uses the near-infrared region of the electromagnetic spectrum, ranging from 780 nm to 2500 nm, corresponding to the wavenumber range 12820-3959 cm^{-1}. NIR spectroscopy entails exposing a sample to a beam of NIR energy, resulting in the absorption of a portion of this energy by the molecules, thereby elevating them to a higher vibrational state. Therefore, NIR spectroscopy centers on the vibrational transitions in molecules. The most prominent absorption bands occurring in the NIR region are associated with overtones and combinations of fundamental vibrations of -CH, -NH, -OH and -SH functional groups. Therefore, the presence of O-H groups in the molecule and its interactions with C-H groups of the excipients (such as sucrose or trehalose, commonly used in pharmaceutical formulations) enable the easy detection of water by NIR. (Reich, 2005)

The molecules absorbing NIR energy can undergo vibration in two modes, characterized by the movement of their atomic groups. The first mode involves stretching, signifying the alteration in distance between two bonded atoms along the axis of the bond. The second mode is bending, indicating a change in the bond angle. (Sandorfy, Buchet, & Lachenal, 2006)

From a mathematical perspective, NIR spectroscopy can be elucidated by the anharmonic oscillator model. In fact, the energy curve of an oscillating molecule is influenced by intramolecular interactions, resulting in non-symmetric vibrations around the equilibrium position and non-uniform spacings between energy levels, which decrease with increasing energy. (Huck, 2014) Each vibrational state corresponds to an energy level, representing a specific amount of potential energy. A notable interaction is Fermi resonance, which arises when an overtone or a combination band strongly interacts with a fundamental vibrational mode, causing alterations in the spectral characteristics and intensities in the absorption bands. (Kananenka & Skinner, 2018)

2.1.2 Instrumentation

Figure 7 illustrates the four basic components of a NIR spectrometer: a laser, a monochromator, a sample holder and a detector, allowing for transmittance or reflectance measurements. (Simpson , 2010)

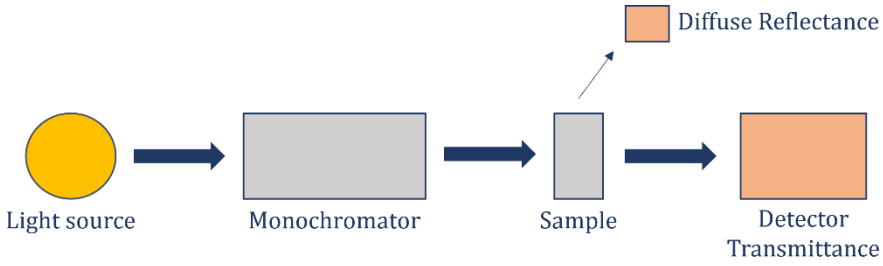

Figure 7: NIR instrumentation

- *Laser*

The light source commonly used is a tungsten halogen lamp due to its compact and durable nature in the range of radiation between 320 nm and 2500 nm. Another prevalent radiation source is the Light Emitting Diodes (LED) lamp, which are semiconductors, commonly include Gallium Arsenide (GaAs) and Indium Gallium Arsenide (InGaAs), delivering radiation up to 1700 nm. (Reich, 2005)

- *Monochromators*

They are typical systems used to select a smaller range of wavelength with respect to the one provided by the lamp. They are characterized by a dispersive element. Usually, a Fourier Transformed NIR (FT-NIR) spectrometer is used, allowing for the representation of periodic signals, the spectrum, as a Fourier series. The interferometer produces a periodic signal that is linked to the electromagnetic wave through the FT algorithm, thereby generating the spectra in the desired frequency domain. (Reich, 2005)

- *Detector*

Detector options include silicon, lead sulfide (PbS) and indium gallium arsenide (InGaAs). Silicon detectors are fast, low-noise, small and highly sensitive across the visible spectrum up to 1100 nm. PbS are slower, but widely used for their sensitivity from 1100 to 2500 nm. The InGaAs combines the speed and size attributes of the silicon detector with the wavelength range of the PbS detector. (Reich, 2005)

The detector position can be optimized to capture most of the reflected radiation from the product in case of measurements in reflectance mode. In that case, the solid sample is

exposed to the light source and the incident radiation may be absorbed or scattered by the product's particles. (Bugay & Brittain, 2006) Conversely, in transmittance measurements, the detector is aligned with the light source and the sample. (Ciurczak & Drennen, 2002) However, in all cases, the absorbance A_j is obtained at the j^{th} wavelength scanned in a logarithmic relationship of the signal collected, s_j:

$$A_j = \log \frac{1}{s_j}$$

2.1.3 NIRS application in the pharmaceutical field

In recent years, NIR spectroscopy has found extensive application in the pharmaceutical field due to its rapid analysis time and the absence of sample handling requirements, rendering it compatible with sterility issues. (Jamrogiewicz, 2012) NIR spectroscopy can be used in different steps of a pharmaceutical process, such as tableting, granulation, mixing, freeze-drying and visual inspection. (Freitas, et al., 2005) (Alcala, Blanco, Bautista, & Gonzalez, 2010) In particular, the identification of raw materials, determination of active pharmaceutical ingredients (API), particle size analysis, and assessment of residual moisture have been the subject of extensive study. (Luypaert, Massart, & Vander Heyden, 2007) However, in biotechnological field, the residual moisture (RM) is the most analyzed critical quality attributes in the drug product.

The NIR spectroscopy generate a huge dataset, made up of the spectra of the different observations analyzed. Specifically, a data matrix is collected where each row represents a sample and each column the value of absorbance at each specific wavenumber. To deal with many variables, multivariate data analysis is needed.

NIR spectroscopy has been widely investigated in combination with multivariate data analysis for the residual moisture estimation in freeze-dried products due to the strong absorbance of water in the NIR spectrum. Clavaud et al. employed statistical design of experiments (DoE) to develop a robust NIR model to assess moisture content in freeze-dried monoclonal antibody. They varied both the formulation composition and freeze-drying parameters to encompass a wide range of representative conditions. The developed NIR model was able to exclude samples exhibiting complete collapse, with moisture content higher than 6%. (Clavaud, et al., 2020) Also, Savage et al. applied the NIR model for studying the viral inactivation, which occurs at water content levels lower than the imposed threshold. (Savage, Torres, Franks, Masecar, & Hotta, 1998) Kamat et al. (Kamat, Lodder, & DeLuca, 1989) and Derksen et al. (Derksen, van de Oetelaar, & Maris,

1998) demonstrated the improved efficiency of NIR spectroscopy with respect to KF titration for residual moisture content estimation.

In the framework of QbD approach, having a tool able to follow in real-time the evolution of a specific process is highly suggested. Therefore, the possibility of using the NIR for in-line monitoring during the freeze-drying process was also explored. Rosas et al. applied NIR spectroscopy for in-line monitoring of a multi-component system during freeze-drying. They demonstrated that NIR spectroscopy proved effective even during the freezing phase, where ice typically obscures signals from other components in the spectra, by using new chemometric methods. (Rosas, et al., 2014) Moreover, the opportunity to monitor protein unfolding and its interaction with lyoprotectants during freeze-drying has been investigated by Pieters et al. (Pieters, et al., 2012) A multipoint NIR spectroscopy was proposed by Kauppinen et al. to quantify in-line residual moisture during freeze-drying. (Kauppinen, et al., 2013)

However, most of the published applications for residual moisture determination are centered on the utilization of Partial Least Squares (PLS) as a regression method in the model development phase. While it has proven to be a potent tool, it solely accounts for the linear dependence between the spectra and the residual moisture content. (Mainali, Li, Yehl, & Chetwyn, 2014) (De Beer, et al., 2013) (Grohganz, Gildemyn, Skibsted, Flink, & Rantanen, 2010) (Clavaud, et al., 2017) On the contrary, the coupling between NIR spectroscopy and machine learning tools, such as artificial neural network (ANN) or deep learning, have been mainly applied to food and agricultural field. For instance, Parastar et al. showcased the potential to differentiate fresh from thawed meat through the application of various machine learning algorithms based on NIR spectra. (Parastar, et al., 2020) Coronel-Reyes et al. utilized an artificial neural network (ANN) to ascertain the storage time of eggs at room temperature. (Coronel-Reyes, Ramirez-Morales, Fernandez-Blanco, Rivero, & Pazos, 2018) Richter et al. employed machine learning techniques to determine the geographical origin of white asparagus. (Richter, Rurik, Gurk, Kohlbacher, & Fischer, 2019) Also, Martins et al. introduced a deep learning architecture for predicting the soluble solids content of fruits. (Martins, et al., 2022) There is a scarcity of research exploring the integration of NIR spectroscopy and machine learning tools in the pharmaceutical industry. An endeavor in this direction was undertaken by Zhao et al., who developed prediction models by integrating machine learning approaches with NIR spectroscopy to enable the rapid quantification of three

active pharmaceutical ingredients. They also conducted a comparative analysis of the performance with the traditional PLS algorithm. (Zhao, Tian, Qiu, & Qu, 2021) Additionally, Akbar et al. elucidated strategies for machine learning-based mAb design, outlining the computational and experimental steps involved. (Akbar, Bashour, Rawat, Robert, & Smorodina, 2022)

2.2 Raman spectroscopy

2.2.1 Fundamentals of Raman theory

Raman spectroscopy is used to study the vibrational and rotational modes in a molecule. It is based on scattering phenomenon, that occurs due to collisions between photons and molecules, as shown in ***Figure 8.***

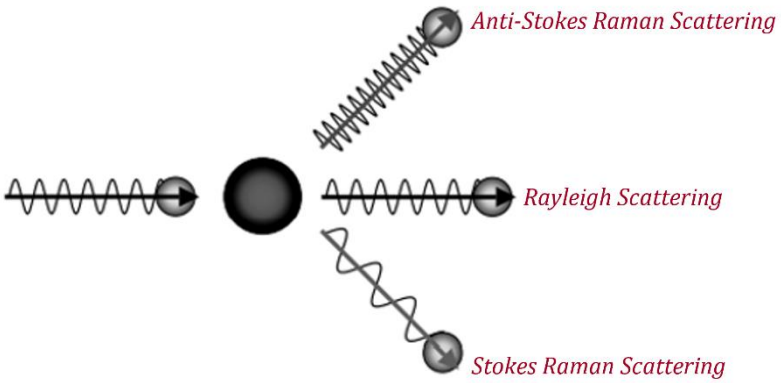

Figure 8: Raman and Rayleigh scattering

When light interacts with matter, the photons comprising the light can either be absorbed, scattered, or may not interact with the material at all. In the process of scattering, the light interacts with the molecule, causing the cloud of electrons around the nuclei to polarize and form a virtual state. As this state is transient, the photon is promptly re-radiated. (Lewis & Edwards, 2001)

The following situations can occur:

a) Rayleigh scattering: it occurs when photons do not alter their energy following collision with molecules. In essence, the photons maintain the same frequency as the incident light. This type of scattering accounts for most scattered photons and is also referred to as elastic collision. (Smith & Dent, 2019)

b) Raman scattering: it occurs when the incident photon exchanges energy with the molecule leading to the excitation of the molecule from the ground state to the virtual

energy state and the subsequent emission of another photon with a different frequency than the incident one. (Smith & Dent, 2019) As a result of the energy disparity between the original and the new state, the wavelength of the emitted photon undergoes a shift, causing the light scattering. This phenomenon is also referred to as inelastic collision. Raman scattering is a relatively weak process, with only one in every 10^6-10^8 photons undergoing Raman scattering. (Gala & Chauhan, 2015)

Two distinct situations can be discerned in Raman scattering. The incident light has a frequency equal to ν_0. If the incident photon imparts an $h\nu$ quantum of energy to the molecule, the energy of the scattered photon reduces to $h(\nu-\nu_0)$, resulting in a lower frequency (higher wavelength). This scenario is known as Stokes Raman scattering. Conversely, if the incident photon receives the $h\nu$ energy from the molecule, the energy increases to $h(\nu+\nu_0)$, causing the frequency to rise (lower wavelength). This is known as Anti-Stokes Raman scattering. (Sasic, 2008)

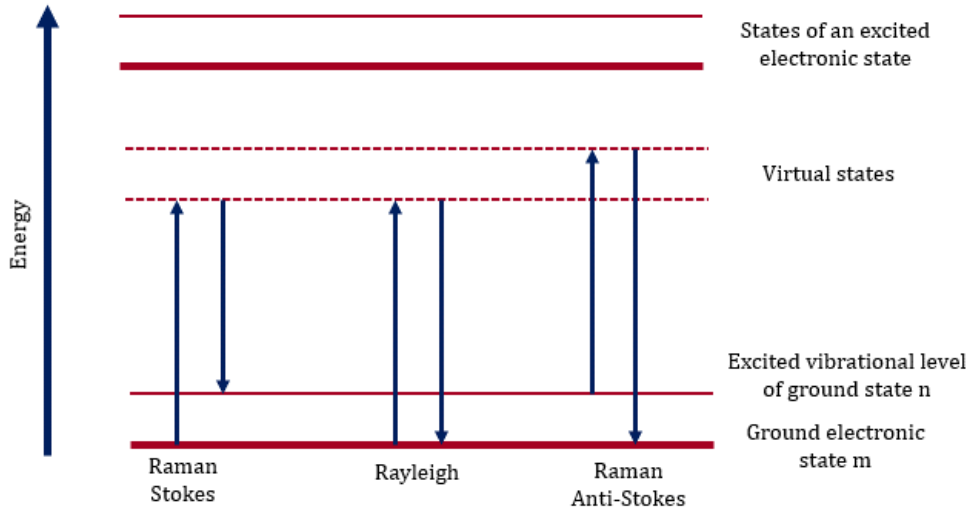

Figure 9: Diagram of Rayleigh and Raman scattering processes

Figure 9 illustrates more in detail the processes that occur for one vibration. Most molecules, at room temperature, are present in the lowest energy vibrational level m, indicated as ground electronic state. Some other molecules, due to thermal energy, are initially in the excited state, indicated by n. When the laser interacts with the electrons and causes the polarization, the formation of the virtual states, indicated in ***Figure 9*** by the dashed lines, occurs. As mentioned before, the Rayleigh process does not involve any energy change; hence, the diagram illustrates the light returning to the same original energy state. In the Raman Stokes scattering process, energy is absorbed by the molecule, resulting in a promotion to the higher energy excited vibrational state n. Conversely, in

Anti-Stokes Raman scattering, there is a scattering from the excited states n to the ground state m, involving a transfer of energy from the molecule to the scattered photon. The relative intensities of the two processes depend on the population of the various states of the molecule and on the symmetry selection rules. In particular, the weaker the population in the excited vibrational states, the weaker the anti-stokes scattering will be. (Smith & Dent, 2019)

When light interacts with matter several phenomena may occur. For instance, the sample may experience heating, or photodecomposition may occur if laser intensity is too high. Additionally, background radiation or ambient light may interfere with the measurements. Therefore, the selection of the laser wavelength is a critical consideration. Specifically, if the wavelength corresponds to an absorption band, the molecules absorb the laser light and excite towards the next state, releasing heat that is transferred to the environment. Obviously, absorption significantly interferes with the Raman effect, as the intensity of the scattered radiation is contingent on the number of incident photons reaching the analyte molecule. (Vandenabeele, 2013)

Also, fluorescence poses a significant interference when employing Raman spectroscopy. The incident laser light excites molecule to an excited state. Subsequently, through radiationless transitions, the molecule returns to a lower energy level and then to the ground electronic state by emitting radiation with lower energy than the incident laser beam. Fluorescence can be mitigated by using a different laser wavelength that avoids the excitation of the molecule. Furthermore, post-processing of the spectrum can address this issue, as the fluorescence background can be eliminated by taking the first or second derivative of the Raman spectrum. Moreover, the Raman effect is strongly influenced by the presence of ambient light, that is considered as a radiation present in the room where the measurements take place. Therefore, Raman measurements must be performed in a dark room. (Vandenabeele, 2013)

2.2.2 Mathematical description of Raman scattering

When an electromagnetic wave with frequency ν_0 radiates a molecule, a dipole moment P is induced. This means that the electric field E changes the distribution of electrons within the molecule. The strength of the induced polarization, P, is expressed as:

$$P = \alpha E \quad (1)$$

The parameter α is the electric *polarizability,* indicating how easily the electron cloud is

distorted. It consists of a constant term α_0 and an additional term that varies with molecular vibration, as reported in Eq. 3. The molecular vibrations are described as combinations of normal modes ($3N-6$ for a molecule with *N* atoms). (Sasic, 2008) The normal coordinate indicating the vibrational displacement is given by Eq. 2:

$$Q = Q_0 \cos 2\pi\nu t \tag{2}$$

where Q is the normal vibrational mode, Q_0 is the amplitude of Q and t is the time. Therefore, the polarizability becomes:

$$\alpha = \alpha_0 + \left(\frac{\partial\alpha}{\partial Q}\right)_0 Q = \alpha_0 + \left(\frac{\partial\alpha}{\partial Q}\right)_0 Q_0 \cos 2\pi\nu t \tag{3}$$

By substituting Eq. 3 and 2 in Eq. 1, the dipole moment *P* can be expressed as:

$$P = \underbrace{\alpha_0 E_0 \cos 2\pi\nu_0 t}_{\text{Rayleigh Scattering}} + \underbrace{\frac{1}{2}\left(\frac{\partial\alpha}{\partial Q}\right)_0 Q_0 E_0 \{\cos 2\pi(\nu_0+\nu)t + \cos 2\pi(\nu_0-\nu)t\}}_{\text{Raman Scattering}} \tag{4}$$

In Eq. 4 it is clearly visible that light will be scattered at three frequencies. The first term is the Rayleigh scattering, representing a component of *P* that vibrates at ν_0, the same frequency of the incident light. The second term pertains to Raman scattering and consists of vibrations occurring at two different frequencies, $\nu_0 \pm \nu$. According to this, the factor $\left(\frac{\partial\alpha}{\partial Q}\right)_0$ must not be zero for Raman scattering to occur. (McCreery, 2000) This statement is the basis of the *selection rule* for Raman scattering, indicating that a molecule is Raman-active if the change in polarizability occurs during its normal modes. Quantum mechanics is essential for determining the normal modes of complex molecules for which a change in polarizability occurs. (De Beer, et al., 2011)

Raman intensity I_R is reported in Eq. 5 as:

$$I_R = \mu(\nu_0 \pm \nu)^4 \alpha^2 Q^2 \tag{5}$$

where ν_0 is the laser frequency, ν is the frequency of light and μ is a constant parameter. Raman intensity varies with the fourth power of the frequency of the scattered light. Usually, this equation is expressed as a function of the wavenumbers, as reported in Eq. 6:

$$I_R = \mu'(\bar{\nu_0} \pm \bar{\nu})^4 \alpha^2 Q^2 \tag{6}$$

The wavenumbers, in reciprocal centimeters, are reported as $\bar{\nu}$. The parameter μ' is a

constant.

Raman efficiency of a scatterer is characterized by the *cross section*, σ, that is proportional to the probability of an incident photon being scattered as a Raman-shifted photon. It is related to the absorption coefficient in Beer's law and its unit is $cm^2/molecule$. The cross section is the most influent parameter on Raman intensity, described by Eq. 7:

$$I_R = I_0 \sigma_j D dz \tag{7}$$

where I_R and I_0 are respectively the Raman intensity and the laser intensity. D is the number of molecules per cubic centimeter, dz is the path length of the laser in the sample and σ_j is the cross section at the wavenumber j. More details about the mathematical derivations are provided in literature reviews. (McCreery, 2000) (Sasic, 2008)

2.2.3 Instrumentation

Figure 10 illustrates the four basic components of a Raman spectrometer: a laser, an optical sampling system, a wavelength separator, and a detector. The optical sampling system includes a source to illuminate the sample with laser light and another one to collect the Raman scatter for input to the spectrometer. Usually, in on-line industrial settings, fiber optics are used to optically interface the laser and the spectrometer. (Lewis & Edwards, 2001)

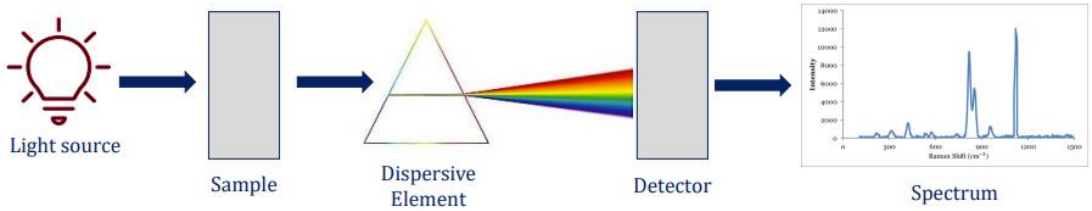

Figure 10: Instrumentation for Raman spectroscopy

- *Laser*

Due to the low fraction of scattered photons in a Raman experiment, a high-intensity monochromatic source is required, the *laser*. The selection of the laser is critical and is contingent upon the specific application. Typically, when the probability of fluorescence is high, NIR lasers are the preferred excitation source. The most practical option is to utilize lines in the 780 nm region from a diode laser, which is based on optical emission from semiconductor junctions. (Sasic, 2008) In FT-instruments, it is advantageous to

utilize the Nd:YAG laser, which emits a 1064 nm line. The laser source must meet some characteristics, such as frequency stability, narrow bandwidth, few sidebands and low divergence. (McCreery, 2000)

- *Spectrometer*

The basic components of a dispersive spectrograph are an input aperture, an input collimator, a grating and an output collimator. Light enters through the input aperture, which spatially localize it. Then, it is collimated by the input collimator before being directed to the grating, where it is dispersed into its constituent wavelengths. The dispersed light is then sent to the detector by the output collimator. (Lewis & Edwards, 2001) The main types of spectrometers available on the market are the *dispersive spectrometers*, which use a grating for the separation of the light into its components; and *Fourier-transform* (FT) *Raman spectrometers*, which employ a Michelson interferometer for this purpose. (Vandenabeele, 2013)

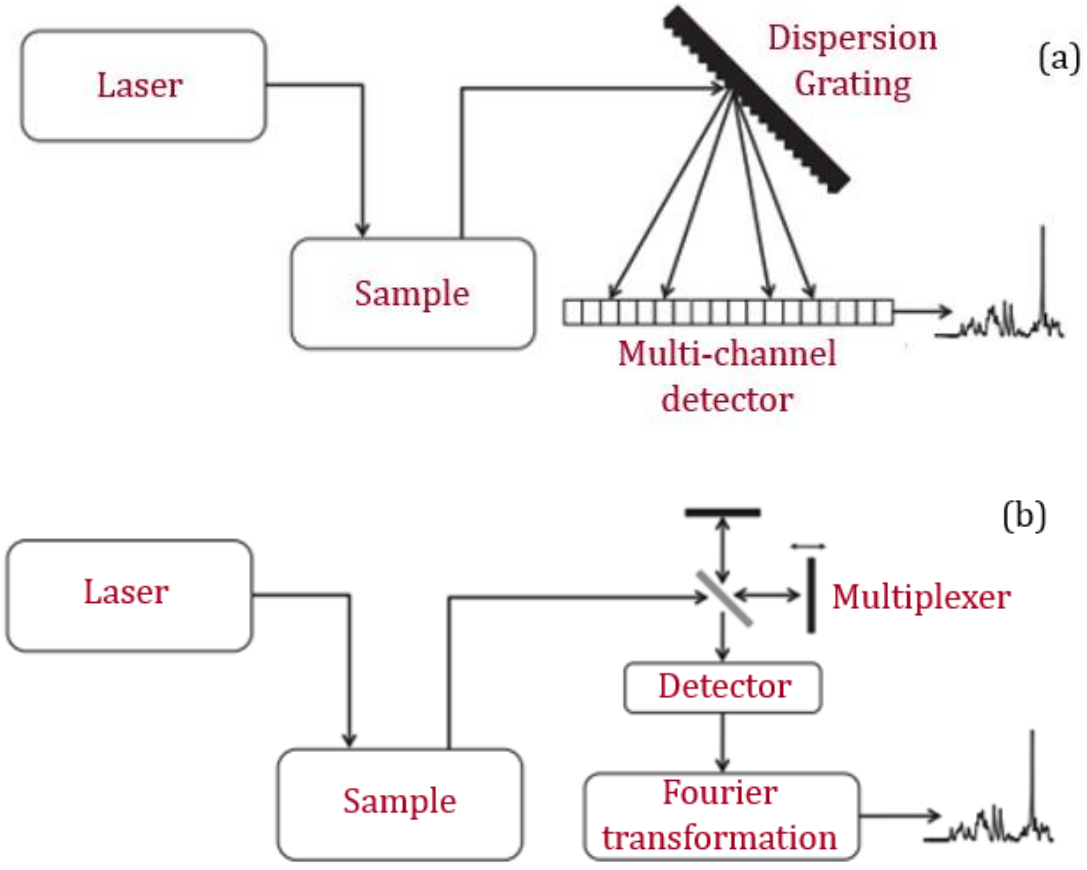

Figure 11: Diagram of a dispersive Raman spectrometer (a) and FT-Raman spectrometer (b)

Figure 11 shows the general scheme of a dispersive Raman spectrometer (a) and of a FT-Raman (b). In both scenarios, the incident laser is focused into the sample through focusing optics, and the scattered radiation is gathered and directed to the wavelength separator. The latter facilitates the separation of the scattered light based on wavenumbers, resulting in the generation of the Raman spectrum. Subsequently, the spectrum is detected by a detector device and transmitted to the computer for processing. (Smith & Dent, 2019)

The dispersive spectrometers operate by diffracting the scattered radiation using a *grating*. The grating can be conceptualized as a linear repetition of reflecting elements, with inter-element distances comparable to the wavelength of the light being dispersed. The primary function of the is to diffract the light at an angle α. For monochromatic light, constructive interference occurs under different angles β_n, according to Eq. 12:

$$n \cdot \lambda = d \cdot (\sin\alpha - \sin\beta) \tag{12}$$

The angles β_n depends on the angle of incidence, the wavelength of the light λ and the groove spacing d of the grating. The integer n is called the order of diffraction. It appears evident that under zero-order conditions $(n = 0)$ the grating acts as a mirror. By rotating the grating, it is possible to select the wavelength range that reaches the detector. (Vandenabeele, 2013)

One significant factor contributing to the substantial expansion of Raman applications in analytical problem-solving is the advent of *multi-channel spectrometers*, resulting in reduced acquisition time. The multi-channel detector, as shown in ***Figure 11a***, has the capability to simultaneously monitor numerous wavelengths by employing multiple detectors operating in parallel, thereby enabling faster spectrum acquisition compared to a single scanning. A prevalent example is a grating-based dispersive spectrograph with a CCD at its focal plane. Usually, several filters are integrated into the system, given that the intensity of the source is considerably stronger than that of Raman scatter. (McCreery, 2000)

In contrast to their counterparts, non-dispersive Raman spectrometers involve FT modulation of the signal and do not entail the physical separation of the wavenumbers. The central component of the FT-Raman spectrometer is the *Michelson interferometer,* which is depicted in ***Figure 12.*** (Sasic, 2008)

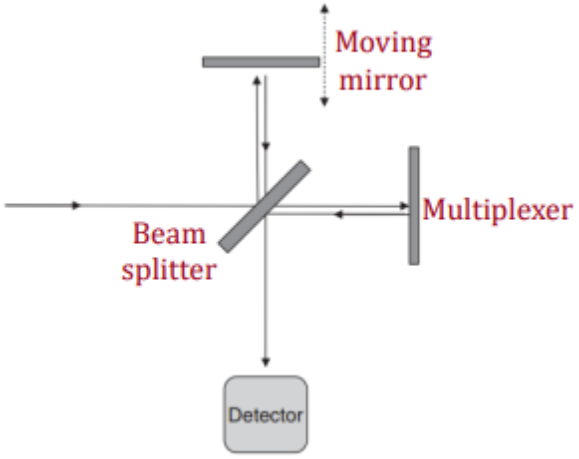

Figure 12: Michelson interferometer

The Michelson interferometer comprises a beam splitter, a moving mirror and a multiplexer or fixed mirror. The light beam is divided into two equal parts, both of which strike the mirror and are directed to the beam splitter, where they are combined and then sent to the detector. Light of different wavelengths is introduced to the interferometer, generating a fringe pattern for all wavelengths present in the spectrum. These patterns are overlaid and detected by the detector, resulting in the acquisition of the interferogram. To obtain a Raman spectrum, the inverse Fourier-transformation is applied to the interferogram. Unlike the dispersive spectrometer, the multiplex spectrometer does not separate the different wavelengths scattered by the sample, but rather modulates them at frequencies dependent on their wavelengths. The outcome is a single beam containing all wavelengths of interest, detected by a single detector, as shown in ***Figure 11b***. (Vandenabeele, 2013)

- *Detector*

The choice of the detector is crucial since it is imperative to have a sensitive and low-noise detector. Two are the most important specifications of a detector:

- *Quantum efficiency, Q*: probability that a photon striking the detector generates an electronically measurable signal. In other words, they are the photoelectrons generated per Raman photon. This value must be high.
- *Dark Signal*: the average generation rate of electrons when the detector is not exposed to light. This value must be minimized.

The most commonly used detector in Raman spectroscopy is the *Charge-Coupled-Device (CCD),* which operates across a broad wavelength range of 400-100 nm. It boasts high quantum efficiency, low dark noise and an extended detector lifetime. They are produced

from silicon and register Raman signal through the generation of electron-hole by photons with sufficient energy. A CCD camera is composed of horizontal pixels, corresponding to the wavenumber axis, and vertical pixels, which represent the intensity of the Raman signal. However, CCD detectors are not sensitive in the infrared region (1100-1700 nm), an area explored by FT-Raman instruments. Therefore, semi-conductor detectors with a small band gap are suitable in this context. (Lewis & Edwards, 2001) (Vandenabeele, 2013)

- *Optics*

Raman instruments incorporate optical components, such as *filters*, to direct the laser light to the sample and the scattered light to the Raman spectrometer. Light transmission often occurs through *glass fibers*, leveraging the principle of total reflection against the fiber walls. When selecting the fiber material, it is crucial to avoid those with numerous -OH functional groups to prevent light adsorption. The diameter of the glass fiber determines the amount of light that can be transmitted through the cable. Additionally, optical fibers can produce a fluorescence signal, necessitating the use of filters to mitigate or eliminate these signals. Filters play also a critical role in suppressing the Rayleigh signal, given the inherently weak nature of the Raman effect.

A generic filter is characterized by the optical density (*O.D.*):

$$O.D. = -\log(\%T) \tag{13}$$

where $\%T$ represents the percentage of the transmitted light. The higher the optical density, the more the filter blocks the light. (Vandenabeele, 2013)

2.2.4 Raman application in the pharmaceutical field

In the last decades, Raman spectroscopy emerged as one of the most promising tools for non-destructive and fast characterization of the pharmaceutical processes. (Nagy, et al., 2018) (Wei, et al., 2022) Raman spectroscopy popularity is increasing due to its numerous advantages. The analytical flexibility of Raman molecular spectroscopic techniques enables the examination of a broad range of transparent, opaque, and colored samples, including solids, semi-solids, suspensions, and solutions. (Smith & Dent, 2019)

As Raman spectroscopy is a scattering technique, it does not require a reference light path, rendering it suitable for remote analyses through the application of fiber optics. The minimal sample handling and the ability analyze polymer containers are anticipated to result in numerous quality control applications. Moreover, water and carbon dioxide

vapors exhibit weak scattering, obviating the need for special accessories when measuring the active pharmaceutical ingredient in aqueous solution. This represents a significant advantage over NIR spectroscopy, making the two techniques as complementary. (Paudel, Raijada, & Rantanen, 2015)

Nowadays, there is a major interest within the pharmaceutical industry to move from traditional batch processes towards continuous processes. In this framework, NIR and Raman spectroscopy are potential PAT tool, allowing rapid and non-destructive measurements without sample preparations. Furthermore, probes coupled to the spectrometers by fiber optics cables can be implemented directly into the production line, allowing continuous real-time measurements. However, as NIR spectroscopy, Raman spectroscopy needs multivariate data analysis to deal with the big dataset generated from the measurements. (De Beer, et al., 2011)

As an example, Raman spectroscopy was used to monitor *real-time* the freeze-drying process of a simple mannitol solution. De Beer et al. (De Beer, et al., 2007) and Romero-Torres et al. (Romero-Torres, Wikstrom, Grant, & Taylor, 2007) found that Raman spectroscopy was able to monitor the mannitol solid state, the process step end points (freezing and primary drying) and the physical phenomena occurring during freeze-drying. They demonstrated that by directly focusing the Raman probe on the top surface of the product from above at a specific angle, the glass vial did not interfere with the Raman signal. Also, the complementarity of Raman and NIR spectroscopy during primary drying was shown by De Beer et al. by building non-contact probes into the freeze-dryer chamber. (De Beer, et al., 2009) Raman spectroscopy proved to be an excellent tool for polymorphic transformation monitoring during the freeze-drying process. Since water and ice produce weak signals in Raman spectra, NIR spectroscopy was able to in-line monitor water and ice behavior during the process.

The development and optimization of freeze-drying cycles are pivotal stages in the process development of biopharmaceuticals. Access to tools that enable time and resource savings would substantially enhance competitiveness in the market. Hence, De Beer et al. (De Beer, et al., 2011) used a 2-level fractional factorial screening design, coupled with NIR and Raman spectroscopy, to investigate the effect of formulation and process variables on critical responses in freeze-drying. They found that the onset of ice crystallization was influenced by the freezing rate, and the introduction of an annealing step caused earlier mannitol crystallization. The study identified optimal operating

conditions leading to the desired response, resulting in the shortest freeze-drying process possible, with the same results as a traditional approach but using fewer experiments. Also, Raman spectroscopy was exploited to identify a new method to prepare drug nanocrystals by de Waard et al. (de Waard, et al., 2010) They used in-line Raman measurements to identify the critical steps that determine the final size of fenofibrate crystals in solution.

Understanding the structural alterations that occur during the freeze-drying process is crucial for ensuring the stability and efficacy of protein-based drugs and biopharmaceutical products. (Koenig, 2005) (McAvan, et al., 2020) The traditional methods to monitor the evolution of denaturation involves the use of analytical time-consuming techniques. However, protein conformational changes during freeze-drying process were studied by Pieters et al. (Pieters, et al., 2013) on lactate dehydrogenase (LDH) by monitoring the Raman band associated to the protein's backbone conformations: the amide I (peak at 1665 cm^{-1}) and the amide III (peak at 1200-1320 cm^{-1}). By constructing a PLS-DA model, they were able to discriminate between native-like and non-native conformational states of proteins. Moreover, Nitika et al. (Nitika, Chhabra, & Rathore, 2021) developed a PLS to predict the protein aggregation in freeze-dried biotherapeutic products, using erythropoietin (EPO) and human growth hormone (HGH). Also, Ettah et al. (Ettah & Ashton, 2018) and Gomez et al. (Gomez de la Cuesta, Goodacre, & Ashton, 2014) have reported the feasibility of Raman spectroscopy for monitoring antibody aggregation in drug product development. In fact, Raman spectroscopy provided dynamic information about secondary and tertiary structure and aggregation mechanisms. (Ettah & Ashton, 2018)

Raman spectroscopy has been investigated during the blending process, a critical operation of the manufacturing process since it is useful to guarantee homogeneity in the final products. Vergote et al. analyzed a binary mixture of diltiazem pellets and paraffinic wax beads during the blending process. They used the mean square of differences between two consecutive spectra to identify the endpoint of mixing. (Vergote, et al., 2004) A Soft Independent Modelling of Class Analogy (SIMCA) model was reported by De Beer et al. to determine the homogeneity of blends in-line and real-time using the combination of Raman spectroscopy and fiber optical immersion probes. They demonstrated the ability of Raman spectroscopy to monitor in-line the blending process of an aqueous suspension and its API (dilitiazem hydrochloride) concentration. They also

used NIR spectroscopy to check if the two different techniques resulted in similar process endpoints. (De Beer, et al., 2008)

Another step often applied to produce pharmaceutical solids is granulation, where the powder particles are mixed with a granulation liquid that compounds them. The feasibility of Raman spectroscopy during high shear wet granulation was reported by Wikström et al. (Wikström, Marsac, & Taylor, 2005) (Wikström, Carroll, & Taylor, 2008)

Also, in the field of tableting, Raman spectroscopy has been widely studied. Thanks to its high speed of analysis, it would be possible to analyze a remarkably high number of tablets with respect to the traditional off-line techniques (e.g. HPLC). Applications for the quantification of active compounds in dosage forms were reported by Rantanen et al. (Rantanen, 2007) and Kontoyannis et al. (Kontoyannis, 1995)

Raman spectroscopy has also been proved as a consistent tool for *coating* applications. (Romero-Torres, Perez-Ramos, Morris, & Grant, 2005) For instance, Muller et al. used Raman spectroscopy for in-line monitoring of an active coating process, leading to a quantification of the API contained in the coating layer. (Muller, Knop, Thies, Uerpmann, & Kleinebudde, 2010)

One of the most crucial aspects in the Raman spectroscopy measurements is the interference with the glass vial. In this framework, Lee et al. demonstrated a scheme reducing the co-presenting glass background in the sample spectra. (Lee, et al., 2021)

2.3 Data-based models in pharmaceutical field

2.3.1 Why multivariate data analysis is needed in pharmaceutical field?

The pharmaceutical industry is characterized by the complexity of its manufacturing processes and the stringent regulatory requirements to ensure the quality, safety, and efficacy of pharmaceutical products. In this context, the application of Multivariate Data Analysis (MVDA) plays a pivotal role in addressing the challenges associated with process monitoring, optimization, and quality control. MVDA allows for the simultaneous examination of multiple variables, providing a holistic perspective on the relationships within complex datasets. (Ferreira & Tobyn , 2014)

The motivation to apply MVDA in the pharmaceutical industry, especially within the PAT framework, stems from the industry's increasing focus on achieving continuous improvement, real-time monitoring, and enhanced process understanding. Traditional quality control methods, which often involve univariate analyses, may fall short in

capturing the intricate interdependencies and variations present in pharmaceutical processes. MVDA, on the other hand, enables the exploration of complex datasets, uncovering patterns, correlations, and trends that might otherwise remain hidden. MVDA, when integrated into PAT, allows for the monitoring of critical process parameters in real-time, facilitating early detection of deviations and enabling prompt corrective actions. This not only enhances the overall efficiency of pharmaceutical processes but also contributes to the reduction of waste, cost, and the potential for batch failures. (Yu, et al., 2014)

Furthermore, regulatory bodies, including the U.S. Food and Drug Administration (FDA) and the European Medicines Agency (EMA), emphasize the importance of utilizing advanced analytical techniques, such as MVDA, to ensure the robustness and reliability of pharmaceutical manufacturing processes. (Prmod, Tahir, Charoo, Ansari, & Ali , 2016)

Indeed, the coupling of PAT tools and multivariate data analysis would be very useful in the pharmaceutical landscape for a dual purpose:

- During Stage 1 – Process Design, establishing relationships among various variables, process conditions, and product quality would enhance process monitoring according to QbD perspective. This approach promises significant time and resource savings, effectively addressing the limitations of offline analytical techniques, which entail manual sampling and destructive methods. Regression algorithms, encompassing both linear and nonlinear methods such as PLS or artificial neural networks, can be utilized to quantify the impact on different critical quality attributes (CQAs) at each stage of the drug product manufacturing process. (Rajalahti & Kvalheim, 2011) Furthermore, integrating modeling into pharmaceutical processes will expedite the scaling-up process from pilot trials to manufacturing environments, resulting in accelerated product development and market entry.
- During Stage 3 – Continued Process Verification, the implementation of statistical process control to monitor the ongoing performance of the processes over time is essential to validate that the process is consistently maintaining a state of statistical control. This state of control is deemed to be present when specific product or process variables consistently align with their target values. This approach enables the identification of any incident with an assignable cause, facilitating the implementation of sustained enhancements in the process and

product quality. PCA models can be utilized for this objective, establishing a reference model derived from historical data collected under normal conditions and comparing future behavior against it. The new multivariate observations can be projected into the developed plane defined by the PCA. (MacGregor & Kourti, 1995)

2.3.2 Spectra data processing

Spectroscopic techniques, such as infrared (IR), ultraviolet-visible (UV-Vis), nuclear magnetic resonance (NMR) and Raman spectroscopy, generate high-dimensional datasets with huge number of variables representing spectral intensities at different wavelengths or frequencies. MVDA coupled with spectroscopy help to extract meaningful information from the spectra, enabling more effective decision-making.

The general data analysis workflow is shown in ***Figure 13***.

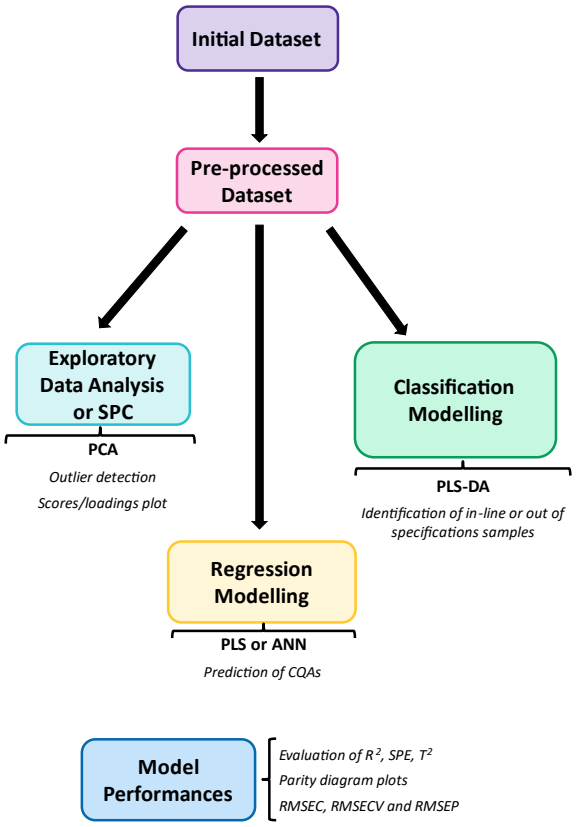

Figure 13: Data analysis workflow for processing NIR/Raman spectra in pharmaceutical applications.

The initial phase involves acquiring the raw data (initial dataset) from the analytical instrument. Subsequently, the pre-processing step is focused on highlighting useful information from the raw instrumental data removing the noise of measurement. Once the data are prepared for modeling, a crucial step is the implementation of Principal

Component Analysis (PCA). PCA serves to unveil latent information and relationships among the samples in the dataset, constituting an unsupervised exploratory phase. Subsequent procedural steps are contingent upon the specific objectives of the study and typically involve the construction of predictive models using supervised methods. (Massart, et al., 1998)

The two primary categories of predictive modelling consist of regression and classification, as outlined below:

1) If the aim is to quantify a variable, such as water content, the aggregation/fragmentation/oxidation level or the protein/excipients content in a drug product, a regression model is required. The widely utilized method for this purpose is Partial Least Squares (PLS) regression. In cases where the relationship among the variables under investigation is non-linear or when a huge number of samples is available, alternative tools such as artificial neural networks (ANN) or support vector regression (SVR) can be employed.
2) If the objective is to classify the samples in a dataset based on their class membership, a classification analysis is necessary. The most used method for this purpose is Partial Least Squares-Discriminant Analysis (PLS-DA).

In the following paragraphs, a detailed explanation on each section of the workflow will be reported.

2.3.3 Preprocessing techniques

The goal of preprocessing is to enhance the signal-to-noise ratio, correct baseline distortions, and mitigate diverse sources of interference or variability in the data. Preprocessing is essential to ensure accurate and meaningful interpretation of the intrinsic chemical or physical information within the spectra. (Rinnan, et al., 2009)

Due to the working principle of NIR spectrometer, different physical and chemical phenomena can lead to deviations from the linear relationship described by Beer's law. Therefore, noise and offsets can appear in the spectra. Therefore, an essential preprocessing technique employed in NIR spectroscopy is the Standard Normal Variate (SNV), which is a row-wise method used to emphasize the true differences between samples. It involves two main steps:

- Centering: each spectral data point's mean value is subtracted from the data point, effectively centering the data around zero to mitigate baseline shifts.

- Scaling: The centered data is subsequently divided by the standard deviation of the spectral data points, thereby standardizing intensity variations.

Through the application of SNV, unrelated variations are minimized, enabling a more focused analysis of the true spectral features associated with the sample's properties. (Amigo, 2021)

In Raman spectroscopy, instead, the derivative techniques are often involved to enhance spectral features, reduce baseline effects, and highlight small spectra changes. Nonetheless, derivatives have the potential to magnify noise, necessitating appropriate smoothing measures. The Savitzky-Golay (SG) filter is frequently employed to eliminate random noise and fluctuations while retaining critical spectral features. This method encompasses the fitting of a polynomial to small, overlapping data subsets, with the polynomial coefficients utilized for smoothing. A window of specified size traverses the data, and a polynomial is fitted to the data within each window. The determination of the window size dictates the number of data points encompassed in each local polynomial fit. Smoothed values are computed using the convolution operation based on the polynomial coefficients, requiring the specification of the polynomial's degree. (Chen, et al., 2022)

Multiplicative Scatter Correction (MSC) is another method frequently employed when dealing with scattering effects due to variations in particle size, sample opacity, sampling packing density or sample placement. (Geladi, Macdougall, & Martens, 1985) This preprocessing technique attempts to remove offset and row magnitude variability leading to diminish the signal related to scattering artifacts. (Zhi-xiang, Zenq-qiang, Hui, & Hong-fu, 2016)

2.3.4 Principal Component Analysis: Theory

Principal Component Analysis (PCA) is a bilinear decomposition and projection techniques designed to condense huge amount of data into a limited set of parameters known as principal components (PCs) or latent variables. These components capture the levels, differences, and similarities among the samples and the variables comprising the modeled data. This process involves a linear transformation that preserves data variance and enforces orthogonality of the latent variables. The fundamental assumption is that the systems are indirectly observable, meaning that the relevant, data-influencing phenomena are concealed and not directly measurable or observable, hence the term latent variables. Once uncovered, principal component (PCs) can be represented through scatter plots in a Euclidean plane. (Esbensen & Geladi, 2009)

Usually, a spectral dataset is collected in a matrix **X** with dimension *I x J,* where *I* represent the number of samples and *J* the variables for each spectrum. PCA decomposes the data matrix as follows:

$$\mathbf{X} = \mathbf{T} \cdot \mathbf{V}^{\mathrm{T}} + \mathbf{E} \quad (14)$$

The number of components, significantly fewer than the number of original variables *J,* is denoted as *A.* The score matrix, **T**, has dimension *M x A* and contains the orthogonal score vectors*,* each representing the projections of the original samples on the new PC space. These scores can be observed in the score plot. Conversely, the loading matrix, **V**, has dimension *A x J* and signifies the impact of each original variable on the PCs, enabling an assessment of the correlation structure among the variables via loading plots. The matrix **E** has the same dimension of **X** denotes the error matrix, capturing the unexplained portion of the data within the model. It comprises the residuals, signifying the distance between the observations and their projections onto the new space. Precisely, the decomposition endeavors to minimize this matrix to achieve the optimal representation in the PC space. In such a way, the variance among the data is maximized. (Davies, 2005)

The pivotal aspect in constructing a PCA model lies in the selection of the number of PCs. Typically, the plot depicting cumulative variance as a function of the number of components is utilized for this determination. Generally, a few components that correspond to 80-90% of the accounted variance are chosen. (Li Vigni, Durante, & Cocchi, 2013)

2.3.5 Partial Least Squares Regression: Theory

The essence of PLS lies in its ability to capture the maximum covariance between input variables, the data matrix **X**, and the response variables, the vector of attributes **Y**, through a latent variable approach, conversely to PCA that was focused on the variance maximization. By extracting latent factors, PLS reduces the dimensionality of the dataset while preserving the essential information for predictive modeling. Therefore, the new reference system is described by *N* latent variables.

Similarly, to PCA, the PLS performs a linear decomposition of both **X** and **Y** in the new space. The **X** matrix is decomposed as explicated for PCA, while **Y** is decomposed as follows:

$$\mathbf{Y} = \mathbf{U} \cdot \mathbf{Q}^{\mathrm{T}} + \mathbf{F} \quad (15)$$

U, Q and **F** represent respectively the scores, the loadings and the residuals matrix. The

scores matrix, **T**, is estimated through the matrix of weights, **W:**

$$\mathbf{T} = \mathbf{XW}(\mathbf{V^T W})^{-1} = \mathbf{XW}^* \quad (16)$$

The Nonlinear Iterative Partial Least Squares (NIPALS) algorithm can be used to calculate the weights, as deeply detailed in literature works. (Wold, Nonlinear partial least squares modelling II. Spline inner relation, 1992)

Following the computation of the weight matrix, the regression matrix **B** is derived through the linear combination of the weights and the loading matrix of **Y**. Subsequently, the attributes ($\mathbf{Y_{pred}}$) of the new samples ($\mathbf{X_{new}}$) can be computed:

$$\mathbf{B} = \mathbf{W}^* \cdot \mathbf{Q}^{\mathrm{T}} \quad (17)$$

$$\mathbf{Y_{pred}} = \mathbf{B} \cdot \mathbf{X_{new}} \quad (18)$$

The development of a PLS model involve two phases: calibration and validation. The performances of both steps are evaluated to assess the overall performance of the model. During the development of the model, often cross-validation is performed to assess model performance more robustly. In *k*-fold cross-validation, used in this study, the dataset was divided into *k* subsets (folds) in a random way, and the model was trained and tested *k* times, with each fold serving as the testing set exactly once.

The model performances were assessed by calculating the root mean square error of calibration (RMSEC), prediction (RMSEP) and cross-validation (RMSECV). The RMSE provides a measure of the average prediction error, reflecting the dispersion between predicted and actual values, and can be calculated using the following equations. Also, the coefficient of determination R^2 and Q^2 allows to visually define the performances of the model.

$$\mathrm{RMSEC} = \sqrt{\frac{\sum_{i=1}^{M_{cal}} \left(y_i^{cal} - y_{pred,i}^{cal}\right)^2}{M^{cal}}} \quad (19)$$

$$\mathrm{RMSEP} = \sqrt{\frac{\sum_{i=1}^{M_{val}} \left(y_i^{val} - y_{pred,i}^{val}\right)^2}{M^{val}}} \quad (20)$$

$$R^2 = 1 - \frac{\sum_{i=1}^{M_{cal}} \left(y_i^{cal} - y_{pred,i}^{cal}\right)^2}{\sum_{i=1}^{M_{cal}} \left(y_i^{cal} - \overline{y^{cal}}\right)^2} \quad (21)$$

$$Q^2 = 1 - \frac{\sum_{i=1}^{M_{val}} \left(y_i^{val} - y_{pred,i}^{val}\right)^2}{\sum_{i=1}^{M_{val}} \left(y_i^{val} - \overline{y^{val}}\right)^2} \quad (22)$$

where $M_{cal}$and M_{val} represent the number of observations in the training and in the test set, respectively. Moreover, y_i^{cal} and $y_{pred,i}^{cal}$ refer to the *i*-th sample of the training set, respectively measured by traditional methods and predicted by the model; while $y_i^{val}$and $y_{pred,i}^{val}$ refer to the *i*-th sample of the test set, respectively measured by traditional methods and predicted by the model. The mean of the observed values of the dependent variable in the training and test set are respectively reported as $\overline{y^{cal}}$ and $\overline{y^{val}}$.

The RMSEC measures the average prediction error within the same dataset that was used to calibrate the model. A low RMSEC indicates better model calibration and a closer fit of the model to the calibration data. RMSEP assesses the predictive performance of the model on a dataset that was not used during the model calibration. It represents the average prediction error for new, unseen data. A low RMSEP indicates better predictive accuracy, suggesting that the model generalizes well to new data. As with RMSEC and RMSEP, a low RMSECV indicates better model performance. Cross-validation provides a more robust estimate of the model's predictive ability, as it evaluates the model across multiple subsets of the data. Ideally, the values of RMSE must be aligned with expectations, i.e. analytical variability. Instead, R^2 coefficient represents the proportion of the total variation in the dependent variable that is explained by the independent variables in the model. A high R^2 and Q^2 values indicate a better fit of the model to the data.

2.3.6 Artificial Neural Network: Theory

Artificial neural networks (ANN), commonly referred to as neural networks, are integral to the field of machine learning and form the foundation of deep learning. (Goodfellow, Bengio, & Courville, 2016) The primary limitation of linear models lies in addressing nonlinear problems characterized by highly diverse input features. Neural networks serve as a potent solution to surmount this challenge. Their architectures draw inspiration from the human brain, emulating the intricate interactions among biological neurons. (Albon, 2018)

A neural network comprises interconnected neurons that establish relationships between the inputs and the desired outputs. (IBM) It is distinguished by three primary components: the input layer, one or more hidden layers, and the output layer. Conceptually, it represents a generalization of linear models, engaging in multiple stages of processing to arrive at a decision. Each layer consists of a specific number of nodes or neurons, each

with an associated weight. (Muller & Guido, 2016)

The input layer is characterized by a quantity of neurons equivalent to the number of inputs. The determination of the number of neurons in the hidden layer has to be achieved following a trial-and-error approach, as no specific guidelines govern this selection. The output layer is composed of a single neuron, given the regression nature of the task, which aimed to determine the residual moisture content in the final product.

The input layer values are aggregated and transmitted to each neuron within the subsequent hidden layer. Within this layer, all inputs are individually multiplied by their corresponding weights and then aggregated. These weights aid the network in discerning the variables that significantly influence the output. To enhance the model's capabilities beyond those of a linear model, a nonlinear function, known as an activation function, is applied to the result. Subsequently, the outcome is utilized in the weighted sum computation that generates the output. This mechanism enables neural networks to learn far more intricate functions than a linear model could. Common activation functions include logistic regression, the rectified linear unit, and the hyperbolic tangent. Literature indicates that logistic regression is predominantly employed for classification tasks. (Geron, 2019)

Neural networks models have a lot of coefficients (weights and bias) to learn with respect to the linear model: one between every input and every hidden layer and one between every neuron in the hidden layer and the output. The output of each neuron in each hidden layer is given by:

$$out_j^{(r)} = f(b_{r-1} + \sum_{i=1}^{n_r-1} w_{i,j}^{(r-1)} out_i^{(r-1)}) \quad (24)$$

The initial term, $out_j^{(r)}$, signifies the output of thej^{th}neuron in the r layer, while $out_i^{(r-1)}$ denotes the output of the i^{th} neuron in the preceding layer. The weights are reported as $w_{i,j}$ and pertain to the neuron of the preceding layer. The activation function is represented by *f.* (Marcato, Boccardo, & Marchisio, 2021)

2.3.7 Performance Evaluation

Each analytical technique is subjected to specific uncertainty, as outlined in validation reports provided by the company. Analytical variability is an inherent aspect encountered during experimental testing, which can affect both the reproducibility and accuracy of the results. It is crucial to understand and manage these sources of variability to ensure the

robustness of the measurements and facilitate a critical discussion of the results generated by the models. The primary sources of variability during measurement can be attributed to instrumental factors, sample preparation, operator or data processing.

A parameter used to quantify the precision of a technique is the Coefficient of Variation (CV). This metric evaluates the degree of variation in results obtained from multiple measurements. It is calculated as the ratio of the standard deviation to the mean, expressed as a percentage, as reported in Equation 23:

$$\text{CV}\ (\%) = \frac{\text{standard devation}}{\text{mean}} \cdot 100 \qquad (23)$$

A lower coefficient of variation indicates superior precision, signifying that the measurements are more consistent and less influenced by random variation. Conversely, a higher coefficient of variation reflects diminished precision and increased variability in the measurements.

Moreover, based on ICH-Q5E guideline, a comparability study must be conducted to show the equivalence between two methods. (EMA, 2005) The equivalence test is the available statistical approach applied to demonstrate similarity between analytical results. (Minitab, s.d.) The equivalence limits are set by the software knowing the standard deviation (*SD*) of the reference method, as $\pm 3 \cdot SD$. The confidence interval of the average difference between results are calculated and compared to the defined equivalence limits. (Schepers & Watzig, 2006)

Two separate null hypotheses are defined:

- *the average difference is greater than or equal to the upper limit of equivalence;*
- *the average difference is less than or equal to the lower limit of equivalence.*

If both null hypotheses are rejected, the average difference falls within the equivalence interval and, consequently, equivalence between the two methods is claimed.

2.3.8 Multivariate Control Charts

In the previous paragraphs, the tools for quantitative applications were deeply described. Here, the multivariate data analysis tools necessary for qualitative evaluation are reported.

The application of multivariate data analysis techniques for process monitoring is named multivariate statistical process control (MSPC). To deploy an MSPC model based on latent variable methods, it is essential to optimize the strategy using historical data containing faults to ensure that the model can detect potential disturbances. The efficacy

of the monitoring model should be assessed in comparison with the established monitoring routine, and both should be operated concurrently for a period to evaluate their effectiveness. During monitoring, the collected data are projected onto the model to identify deviations, abrupt changes, and gradual process drifts, by building multivariate control charts. (Kresta, MacGregor, & Marlin, 1991) One of the most used methods is PCA based on the evaluation of statistics Hotelling's T^2 and the Distance to the Model (DModX). The Hotelling's T^2 plot illustrates the distance from the origin in the score space for each designated observation. A substantial T^2 value for a specific observation, i.e., a value significantly exceeding the critical limits, signifies that the observation is distant from the others within the specified range of components in the score-space. Hence, this is likely to be an outlier. The Hotelling's T^2 for observation *i,* based on *A* components is:

$$T_i^2 = \sum_{a=1}^{A} \frac{t_{i,a}^2}{s_{ta}^2} \tag{25}$$

where s_{ta}^2 represents the variance related to the *a-th* PC and $t_{i,a}$ is the *a-th* score vector.

On the other hand, the *DModX* indicates the distance from the model plane at which the observation is situated. In other words, it indicates the residual standard deviation between the data and the PC model. When these residuals are large, this indicates an abnormal behavior in the process. Specifically, observations with a DMod larger than the critical calculated value (*DCrit*) are outliers. This indicates that these observations are different from the normal observations with respect to the correlation structure of the variables.

To track the progression of new observations, the tolerance limits for the control charts are typically computed using tolerance intervals of the mean ±3 times the standard deviation, considering the 95% and 99% values as the confidence interval. (SIMCA Sartorius, 2020)

CHAPTER 3

3. MATERIALS & EQUIPMENT

3.1 Materials

Different products were involved in the present Thesis to investigate different CQAs and evaluate the impact of the process steps.

Specifically:

- Model formulations characterized by different percentage of sucrose/trehalose and arginine in water were freeze-dried to develop regression models aiming to quantify the residual moisture starting from NIR spectra. Sucrose and arginine were provided by Merck Life Science (Darmstadt, Germany), while trehalose by Sigma-Aldrich (Saint Louis, USA). Ultra-pure water was supplied by a Millipore water system (IQ 7000, Merck Millipore, Burlington, USA). More details will be given in Section 6.2.
- A monoclonal antibody, provided by Merck Serono S.p.A. Rome – Italy (an affiliate of Merck KGaA, Darmstadt, Germany), was used as model protein to study the different CQAs related to product degradation and composition by means of Raman spectra. Two different presentations of the same mAb, named in this Thesis as "*formulation 1*" and "*formulation 2*", were used to conduct the experiments. Both formulations contain different excipients, including L-Histidine buffer, trehalose diihydrate, L-Methionine, sodium chloride and polysorbate 20. The pH of the two formulations is 5.5 ± 0.5. The only two differences lie in the API concentration, which is higher in *formulation 2*, and in the presence of arginine in *formulation 2* compared to *formulation 1*.
- A hormone, provided by Merck Serono S.p.A. Rome – Italy (an affiliate of Merck KGaA, Darmstadt, Germany), was used for proving model generalization to a different formulation composition. It is named as *"formulation 3"* in the present Thesis. The *Formulation 3* is different from the mAb since it is characterized by the presence of sucrose as principal excipient (instead of trehalose), Poloxamer 188, L-Methionine, $Na_2HPO_4 \cdot 2H_2O$, $NaH_2PO_4 \cdot H_2O$, and the meta cresol (absent in the other formulations). The pH of this formulation is 7.0 ± 0.1.

All the experimental part, in terms of stress explored and dilutions performed to explore a wide range of the CQAs under investigation, will be explained in detail in the following Chapters.

3.2 Equipment

All the experimental activities were carried out in the site of Merck Serono S.p.A. at Guidonia Montecelio (Italy).

3.2.1 Freeze-dryer Equipment

A lab-scale freeze-dryer, the Lyostar 3 (SP Scientific, Warminster, USA) with four shelves with area equal to 0.43 m^2, was employed to perform the freeze-drying cycles (***Figure 14***). The freeze-dryer was outfitted with a capacitance manometer and a Pirani gauge for pressure monitoring, along with a nitrogen gas flux for pressure control. Thermocouples were positioned at the vial bottoms to monitor the temperature profiles within the product. Additionally, the Lyostar 3 chamber featured a specially designed flange to accommodate the introduction of the NIR probe for in-line spectral acquisition, as shown in ***Figure 14***.

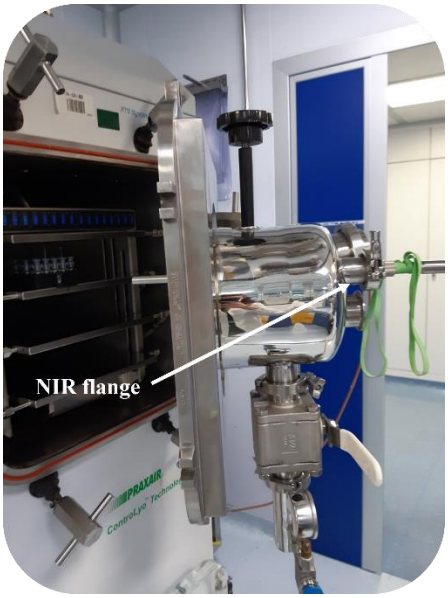

Figure 14: Lyostar 3 freeze-dryer with the NIR flange highlighted.

According to the company's internal classification, *Formulation 1* was deemed a toxic compound and required special precautions during freeze-drying. Therefore, to freeze-dry toxic compounds, a plastic bag is needed to protect the operator, as reported in ***Figure 15***.

Figure 15: Lyostar 3 freeze-dryer equipped with the plastic bag isolator to deal with toxic compounds.

3.2.2 Raman Equipment

Raman spectra acquisitions were performed using a Raman RXN2 intstrument (Kaiser Optics, Ann Arbor, MI, USA) equipped with a 785 nm excitation laser source. The power was set at its maximum output, 400 mW. An immersible contact probe was used for both measurements of liquid formulation and freeze-dried product (after reconstitution). Spectra were acquired in the range 150-3425 cm^{-1} with a 4 cm^{-1} resolution. Aluminum foils were used to protect samples from light preventing interference. The exposure length and the number of scans to be used were optimized to reach the best compromise between the signal and the noise for each CQA to be investigated. More details are found in Chapter 4 and Chapter 5.

For the in-line measurements, a flow assembly CYA680 (Kaiser Optics, Ann Arbor, MI, USA) was used, as shown in ***Figure 16***. The flow cell was connected through piping of the correct dimensions to the tank filled with the drug product. In the following Chapters a more detailed explanation will be given on the applicability of this set-up.

Figure 16: Raman flow cell used for in-line measurements installed in the GPD department of Guidonia Montecelio Merck site

3.2.3 NIR Equipment

NIR spectra were acquired using the FT NIR spectrometer (Antaris MX FT-NIR, Thermo Fischer Scientific, Waltham, USA), equipped with a halogen NIR source and an InGaAs detector. Two probes were utilized: one for collecting the spectra and the other for obtaining the blank, utilizing an external blank, as clearly visible in ***Figure 17***.

Figure 17: NIR spectrometer while analyzing a sample.

The spectra were captured in diffuse reflectance mode, covering the full available wavelength range of 10000 - 4000 cm^{-1}, with a gain of 1 and 32 scans per spectrum. To minimize noise, the final spectrum for each sample was obtained as the average of 96 scans. With these parameters, the entire acquisition process took less than 1 minute for

each sample, approximately 50 seconds. The off-line acquisition of spectra was facilitated by a polymeric block, which allowed for the placement of the blank material and the vial to be analyzed. Ensuring contact between the sample and the probe is critical to obtain high-quality spectra (***Figure 17***).

In-line acquisition was enabled by the specially designed flange installed in the freeze-dryer. The probe is inserted through the aperture, targeting a specific vial throughout the entire freeze-drying cycle with the aid of a dedicated polymeric support. (***Figure 14***). More details are found in Chapter 6.

3.2.4 Reverse-Phase High Performance Liquid Chromatography (RP-HPLC) Equipment

The excipients content, like Polysorbate 20 and methionine, were measured using a RP-HPLC system (Waters, MA, USA) coupled respectively with an Evaporative Light Scattering Detector (ELSD) and an UV detector.

In the case of methionine content, a C18 column (5 µm, 4.6 x 250 mm, Grace, Maryland, USA) was used at 40°C. Samples were loaded and a gradient elution was performed at a flow rate of 1 mL/min for 20 min. The two eluents used are a solution 0.1% of trifluoroacetic acid in water and a solution 0.079% of trifluoroacetic acid in acetonitrile. Detection was performed by monitoring UV absorbance at 234 nm. The data were processed using the Empower software (Waters). The final value of methionine content is given by the average between two dependent replicates. The range of methionine content explored is 0.22 mg/ml – 1.46 mg/ml.

For the polysorbate 20 evaluation, a Poroshell 300SB-C18 column set was used (5 µm, 2.1*75mm, Agilent, California, USA). Samples were loaded and a gradient elution was performed at a flowrate of 0.6 mL/min for 20 min. The eluents for this analysis are: milli-Q water, methanol grade 100%, acetonitrile 100% and isopropanol 100%. Detection was performed by monitoring ELS signals. The data were processed using the Empower software (Waters). The final value of protein concentration is given by the average between two independent replicates. The range of polysorbate 20 content explored is 0.22 mg/ml – 2.4 mg/ml.

3.2.5 Ultra Performance Liquid Chromatography (UPLC) Equipment

The aggregation and oxidation levels were measured using UPLC systems. Specifically, the aggregation was quantified by conducting a Size Exclusion UPLC (SE-UPLC) in an

Acquity system (Waters, MA, USA) equipped with UV detector and an Acquity UPLC BEH 200 SEC column (1.7 μm 4.6x150mm, Waters, MA, USA) was used at 30°C. Samples were loaded and isocratic elution, using a mobile phase of phosphate buffer solution, was performed at a flow rate of 0.3 mL/min for 10 min. Detection was performed by monitoring UV absorbance at 214 nm. The data were processed using the Empower software (Waters). The final value of HMW species is given by the average between two dependent replicates. The range obtained for the aggregation level is 0.44%-30%.

The oxidation level was quantified by means of RP-UPLC. An Acquity UPLC system (Waters, MA, USA) equipped with UV detector and an Acquity UPLC BEH 130 C18 column (1.7 μm 2.1x100mm, Waters, MA, USA) was used at 60°C. Samples were loaded and a gradient elution was performed at a flow rate of 0.6 mL/min for 30 min. Detection was performed by monitoring UV absorbance at 214 nm. The data were processed using the Empower software (Waters). The final value of oxidation level is given by the average between two dependent replicates. The range of oxidation level explored is 14.2%-77.4%.

3.2.6 SoloVPE UV system

Protein content of the samples was evaluated by means of the SoloVPE variable pathlength UV system (C Technologies, Inc., New Jersey, U.S.A.), using small quartz vessel with a filling volume of 120 μl. The wavelength was equal to 280 nm and the molar extinction coefficient to 1.97 mL/(mg*cm). The final value of protein concentration is given by the average between two independent replicates. The range of concentration explored is 0.11 mg/ml – 40 mg/ml.

3.2.7 Capillary Gel Electrophoresis – Sodium Dodecil Sulphate (CGE-SDS) Equipment

Protein fragmentation was quantified by means of CGE-SDS. A PA800 Plus system (AB Sciex, MA, USA) equipped with a Photodiode Array Detector (PDA) detector and a bare fused-silica capillary (50 μm I.D., 67 cm total length and 375 μm O.D, AB Sciex, MA, USA) was used to perform the analysis. The following analytical procedure was followed:

- Samples were pre-treated by adding a reducing agent, specifically 2-mercaptoethanol, to facilitate the reduction of disulfide bonds in the protein.
- The pre-treated samples were mixed to ensure uniformity and subjected to centrifugation for 1 minute. This step helped to separate any particulate from the solution, ensuring that only the desired analyte remained in the supernatant.

- Following centrifugation, samples were heated to +70°C for 10 minutes for denaturing proteins, which helped to reveal their structural characteristics and improved the resolution of the analysis.
- After the heating, samples were cooled to room temperature for 5 minutes to stabilize the proteins and, then, mixed again and centrifuged for 2 minutes.
- Finally, 95 µL of the prepared solution was transferred into the specific vials designed for the PA800 Plus system.

The data generated were analyzed using the 32 Karat software (AB Sciex, version 7.0). The final value of LMW species is given by the average between two dependent replicates. The range obtained for the fragmentation level is 4%-28%.

3.2.8 Karl-Fischer titration analysis

Residual moisture was quantified using a coulometric titrator (C30S Mettler Toledo, Columbus, USA). The following steps were conducted to perform the analysis:

- Samples were reconstituted with a mixture of formamide and methanol. Each vial was weighed before and after reconstitution to determine the weight of the sample.
- The equipment was calibrated before each session using Hydranal Water Standard as control sample to ensure accuracy and reliability of the results.
- A syringe was filled with the prepared sample solution and injected into the titration cell of the Karl Fischer titrator.
- The moisture content was calculated based on the weight of the sample and the results printed out from the titration. Each value derived from the average of two replicates.

The analytical variability of the conventional methods used are reported in **Table 10.**

CHAPTER 4

Some results presented in this Chapter have been already published in a peer-reviewed journal (Massei, Falco, & Fissore, 2024).

4. Determination of formulated-related CQAs of drugs

4.1 Introduction

Over the last three decades, there has been a notable increase in the approval of antibody-based biopharmaceutical products, establishing their leadership in the market due to their highly targeted and effective treatments for chronic diseases. (The business reasearch company) Nevertheless, the primary challenge associated with these molecules pertains to the potential degradation pathways, including aggregation, fragmentation, oxidation levels, and alterations in protein concentration. It is imperative to identify and monitor these factors to detect potentially out-of-spec products. (Shukla, et al., 2023)

Advanced solutions are necessary to monitor and quantify structural alterations in the mAb that may contribute to immunogenicity and diminished drug efficiency. (McAvan, et al., 2020)

The adoption of a suitable PAT tool can be beneficial in different stage of the pharmaceutical landscape. As an example, identification of stability indicating CQAs is a critical exercise for process and product development to establish the stability profile of a biotech product. The identification of the stability indicating CQAs is performed based on prior knowledge and dedicated stress and stability studies to understand the degradation pathways. At the end of these studies, the specific stability profile is obtained for the dedicated product (e.g. LMW, HMW, oxidation level and deamidation profile).

During the process design of a biopharmaceutical product, studies are performed at laboratory and pilot scale to evaluate the impact of the process parameters on any unit operations. These studies are performed for both drug substance and drug product manufacturing processes to demonstrate that the process delivers the expected product quality, even in case it is operated at the limits of the acceptable ranges of process parameters for the specific product. The quality of the resulting product and the performance of the process are verified by checking that all the CQAs are within the expected product specifications, as deeply discussed during Section 1.8. (Deshmukh & Ogunyankin, 2020)

In this framework, the monitoring of protein/excipient concentration as well as the HMW and LMW species is generally performed during the compounding and filtration steps. During the compounding phase, it is crucial to achieve the target concentration in the formulated drug product as per the specified requirements. Before proceeding to subsequent stages, it is essential to ensure homogeneity within the compounding vessel where the preparation takes place. (Bai, Bee, Biddlecombe, Chen, & Leach, 2012) Consequently, the evaluation of protein and excipient concentrations is always performed. Furthermore, denaturation phenomena can occur during compounding due to the shear stress the molecule is subjected to (i.e. mixing speed and the presence of interfaces). In fact, during mixing step, protein is exposed to different contact surfaces in combination with stirring process and its stability may be therefore impacted. There are also several air-liquid interfaces that can induce protein denaturation. Aggregation level is the most impacted CQA because of increasing amount of protein exposed to the hydrophobic air-liquid interface and then pulled back into the bulk. (Patel, Kothari, Tunga, Ritter, & Tunga , 2011) Minimizing foaming caused by agitation during manufacturing may be critical to prevent significant loss of protein activity and generation of HMW. Therefore, assessing the levels of aggregation and fragmentation is usually also conducted. (Bee, et al., 2009)

Additionally, during the filtration step it is mandatory to monitor the protein/excipients content to evaluate any potential absorption or dilution phenomena. (Deiringer, Leitner, & Friess, 2023) Indeed, during filtration, it is possible for the initial aliquots following the filtration process to exhibit a protein/excipient concentration that deviates from the target value due to the absorption of certain components onto the filter membrane. The filter integrity is routinely assessed by flushing it with water and subsequently drying it. Nevertheless, sometimes the filter is not completely dried, and some residues of water can remain, causing dilution in the initial product aliquots following filtration. Therefore, in this scenario as well, monitoring the protein/excipient concentration is crucial to ensure that the concentration returns to the target value for both the protein and excipients. (Allmendinger, Mueller, Huwyler, Mahler, & Fischer, 2015) (Rajniak, et al., 2008)

Moreover, during the filling and transfer process, the drug product is exposed to different shear forces and ambient light. Moreover, the pumping process may create air-liquid interfaces that can induce protein denaturation. Also, the direct interactions of the DP with contained surface and components, can affect the protein stability. As a result,

aggregation/fragmentation/oxidation levels are always monitored in this step. (Nayak, Colandene, Bradford, & Perkins, 2011)

Additionally, aseptic filling operation are often carried out under isolator technology by using Vapour Phase Hydrogen Peroxide (VPHP) as sterilizing agent due its biocidal activity. (Cheng, Zheng, & Yang, 2016) Prior to starting manufacturing operations, the isolator is decontaminated with Vaporized Hydrogen peroxide. Once the decontamination phase of the VPHP cycle is over, an aeration phase starts with the aim to rapidly decrease the vapour of hydrogen peroxide to the concentration of less than 1 ppm. However, biotech pharmaceutical compounds contain many aminoacidic residues sensitive to oxidative agent at levels of sub-ppm. (Vuylsteke, Luyckx, & de Lannoy, 2019) The DP can be exposed to VPHP in two ways:

- Filling machine materials, i.e. tubing, can adsorb VPHP during the decontamination cycle and release it in DP during a filling stop (being the DP in static contact with filling machine tubing);
- Open filled vials under isolator during a filling stop can uptake residual VPHP in the isolator environment. (Hubbard, et al., 2018)

Therefore, the VPHP can migrate into the drug product solution through diffusion into open, filled containers, due to the exposure during line interruptions or via diffusion through single-use components subjected to the decontamination process. It is essential to implement precautionary measures by thoroughly examining the impact of a line stoppage on product quality and establishing an acceptable maximum duration to mitigate the risk of product degradation. Aggregation and oxidation levels must be monitored during filling stops occurring in manufacturing environment.

Although freeze-drying is an effective way of overcoming protein instability by removal of most of the water, it can also produce instability in proteins, typically manifested by either an irreversible change in structure or greater levels of aggregation. In fact, proteins may denature due to exposure to ice-water interfaces or the formation of the freeze-concentrate, facilitating protein aggregation. Also, covalent modifications can occur due to change in pH caused by crystallization of buffer components. (Bhatnagar, Bogner, & Pikal, 2007)

Protein degradation via aggregation and oxidation can also occur during the visual inspection phase due to the sensitivity of mAb to ambient light. (Luis, Hu, Zamiri, & et al., 2018) In fact, the exposure to light can trigger a chain of biochemical events that

continue to affect the protein even after the light source is turned off. These effects depend on the amount of energy imparted to the protein and the presence of environmental oxygen. As an example, photo-oxidation is induced when a compound absorbs a certain wavelength of light, which provide energy to rise the molecule to an excited state. Then, the excited molecule can transfer that energy to molecular oxygen, converting it to reactive singlet oxygen atoms. This is the path of degradation of tryptophan, histidine and tyrosine under light in presence of oxygen. (Rathore & Rajan, 2008)

While Raman spectroscopy has been extensively used for identifying small molecule raw materials, (Soto , Meriage, Wagner, Wang, & Semin, 2021) its application in characterizing protein therapeutics has only recently gained attention. (Makki, et al., 2021) There is a small amount of research investigating the capability of Raman spectroscopy to differentiate the kind of stress impacting a given molecule. When a protein is exposed to a specific stress, it undergoes noticeable alterations in secondary and tertiary configuration. Raman spectra can offer understanding into the protein's primary structure, side-chain groups, and can be utilized to monitor and control the higher-order arrangement (α-helix, β-sheet, and random coil conformations).

The qualitative application presented in this Chapter is aimed to fully assess the Raman spectroscopy as a powerful tool to discriminate the different stresses acting on the protein. Multivariate data analysis was combined with Raman spectroscopy to investigate a monoclonal antibody, showcasing their powerful ability in discerning the type of stress impacting the molecule and on quantifying it. A forced thermal and oxidative degradation was carried out on the molecule by subjecting it for one month at 50°C and by oxidating it with hydrogen peroxide for up to 30 minutes. Moreover, dilutions were performed on the samples to discriminate different protein concentrations.

This Chapter presents a *qualitative application*, aiming to investigate the applicability of Raman spectroscopy for differentiating among the stresses and identifying the good samples, i.e., those that were either not subjected to a specific stress or met the specifications set by the company.

To develop the spectroscopic qualitative application, some steps must be performed, as reported in ***Figure 18***.

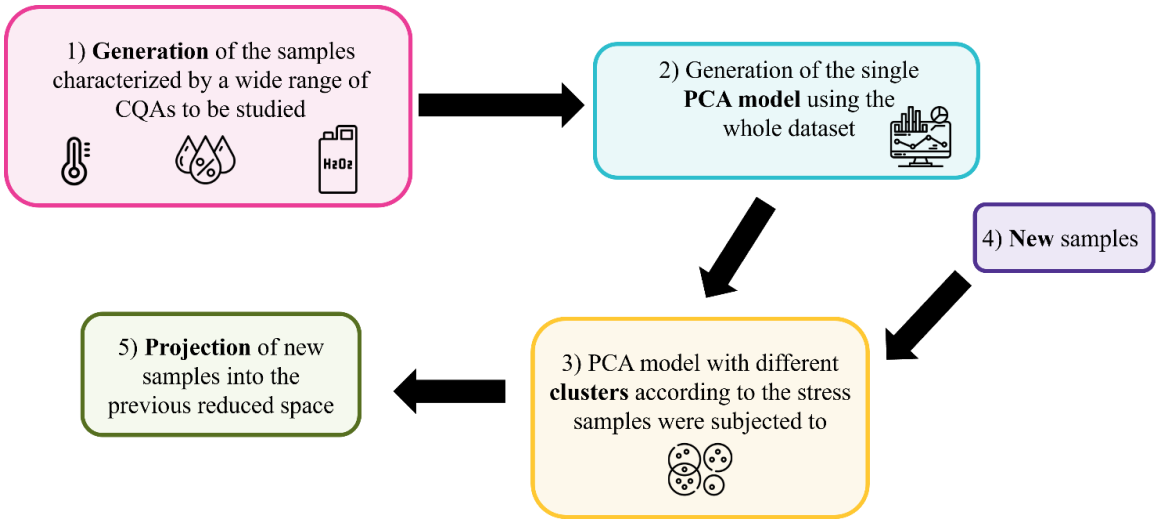

Figure 18: Schematic representation of the workflow to follow to distinguish among different stress conditions or dilutions occurred into biopharmaceutical products during manufacturing steps.

Firstly, samples must be generated to explore different stress conditions or dilution levels. Spectra of the dataset are acquired, creating the whole dataset to be analyzed as a single big data matrix used to develop the PCA model. Once the model has been obtained, check if clusters are present in the scores plot. If not, it may be that the technique used do not see any differences in the samples. If yes, it means that Raman spectroscopy is suitable for the purpose. Following, when it comes to evaluate a new sample from other samples, not included into the calibration phase, they will be projected into the previous reduced spaces, using the loadings previously found. This approach can be used for any new technology must be proved for a specific discrimination purpose. It is a significant aid for quantitative analysis since it helps you to assess if the technology works with the CQAs under investigation.

When a new sample undergoes various processing steps, it will inevitably undergo changes in its CQAs. By incorporating it into the PCA model, one can discern which CQA were impacted by the process, as well as the specific bonds and spectral regions involved. Consequently, you can determine the necessary PLS models to quantify the extent of the stress and pinpoint the region that necessitates model refinement.

4.2 Case-study

The *Formulation 1* was used as model protein and was subjected to both thermal and oxidative stresses to investigate the CQAs related to the degradation of the protein, such as HMW, LMW and oxidation level. Each sample was deliberately exposed to severe stress conditions, leading to values (e.g. high HMW% and LMW% values) that may not normally arise in real-world processes. Being more concentrated, the *Formulation 2* was

used to perform different dilutions of the drug product with placebo, leading to explore a wide range of protein concentration in the mAb ranging from 40 mg/ml to 2 mg/ml. Furthermore, *Formulation 3* was utilized as an external test set to evaluate the reliability of the developed model and its suitability for products not originally included in the calibration.

Table 3 provides an overview of the number of samples generated for each type of stress.

Table 3: Number of samples for each case study considered in the work. The formulation used for each case is also reported.

Case study	*Formulation*	*Number of samples*
No stress	*Formulation 1*	13
No stress	*Formulation 3*	55
Thermal stress (out-of-spec)	*Formulation 1*	38
Thermal stress (in-spec)	*Formulation 1*	12
Dilutions	*Formulation 2*	29
Oxidative stress	*Formulation 1*	21

The samples were labeled based on the type of stress to which they were subjected. Not all samples experienced stress; Raman spectra were also acquired for pure samples, named as "no stress" for *Formulation 1* and *Formulation 3.* All other case studies were exclusively conducted on *Formulation 1,* except for the dilutions, which were applied only to *Formulation 2*. The composition of the three formulations is reported in Chapter 3. Thermal stress led to two distinct sample groups: those out-of-specifications, identified by aggregates values exceeding 5%; and those meeting product specifications, characterized by aggregate values below 5% (in accordance with the company's standard operating procedure).

The generation of the stresses and the dilutions were performed according to the Standard Operating Procedure (SOP) and internal protocols of the company:

- Thermal stress was performed by incubating 10R vials (NBB, Schott) filled with 6 mL of *Formulation 1* based products at 50°C for a duration of one month, exceeding the standard storage condition. The stress was stopped at various time points by storing the specific sample at -80°C. Based on prior knowledge on the molecule, the thermal stress resulted in a significant increase in aggregation and fragmentation

levels, quantified using chromatography and capillary electrophoresis techniques.

- The oxidative stress was induced on products of *Formulation 1* by adding 200 µl of hydrogen peroxide for 20 minutes. Then, the stress was stopped each minute by inserting 120 mg of methionine in the sample.
- Dilutions with placebo were carried out on samples of *Formulation 2* based product, starting from a protein concentration of 40 mg/ml up to 2 mg/ml with a concentration interval of 1 mg/ml.

After the sample generation, the Raman spectra were acquired according to the setup described in Chapter 3. Each spectrum was collected using 3 scans of 45 seconds exposure time per scan.

4.3 Data processing

All the data were pretreated using the first-derivative tool as a baseline correction tool. Moreover, the smoothing step was useful to remove random noise, preserving useful spectra information. In the present case, Savitzky-Golay algorithm was used setting up a second polynomial order with a 15-window size, leading to noise reduction. Then, the pretreated data were used to develop the PCA model. As graphical outcomes, the scores and loadings plots are reported in the following discussions. All data were processed using SIMCA (Version 17.0.0.24543, Sartorius, Germany). The raw Raman spectra are shown in ***Figure 19***.

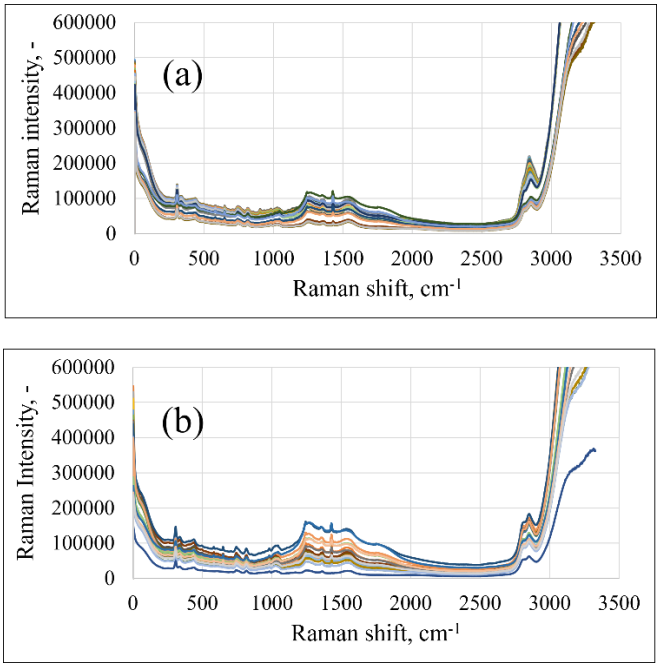

Figure 19: Raw Raman spectra of (a) dilutions performed on *formulation 2* samples; and (b) thermal stress performed on *formulation 1* samples.

To deeper understand variations in the spectra, the datasets involved in this study are reported, after pre-treatments, in ***Figure 20***, showing the zoom up to 1800 cm^{-1}, being the fingerprint region of the antibody in the Raman spectra.

The mAb, as all proteins, is characterized by hydrogen bonds between amino acids in the polypeptide chain. Raman spectroscopy, being a vibrational technique, is based on the vibrations of chemical bonds, specifically the backbone C-N, C-C and C-O bonds in proteins. Additionally, the amide bands are particularly significant in Raman spectroscopy for examining the secondary structure in proteins. In particular, the amide I band primarily originates from C=O stretching vibrations and is highly informative for analyzing the secondary structure, where distinct signals for alpha helixes, beta sheets and random coils are located.

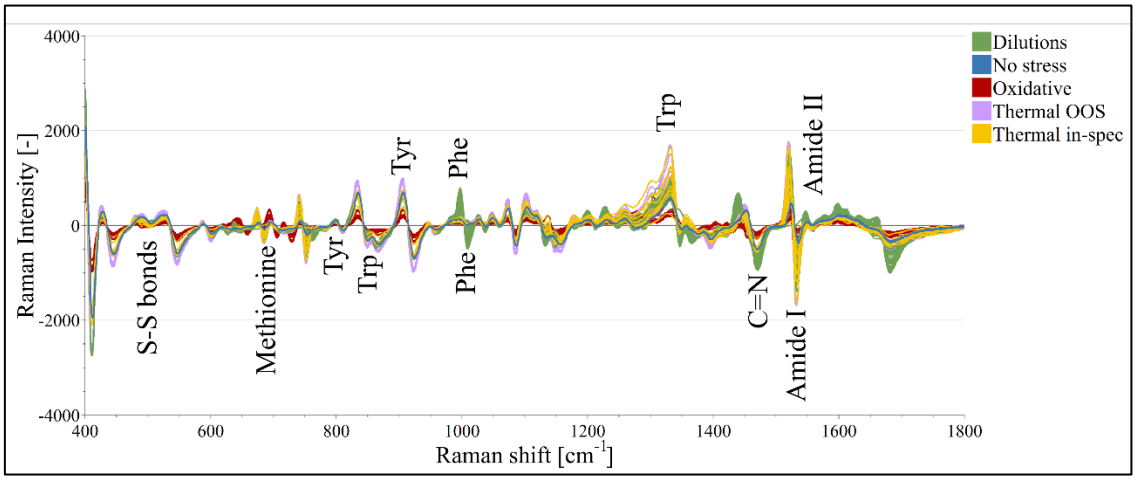

Figure 20: Pre-processed Raman spectra of *formulation 1* and *formulation 2* samples in the fingerprint region colored according to the different types of samples, as clearly detailed in the legend in the right upper part of the graph.

In a Raman spectrum, each molecule exhibits distinct peaks associated to the vibrational frequency of various functional groups. Assigning each peak in Raman spectra is challenging, but it is more common to refer to different regions or zones. As described above, the applied stresses may induce alterations in the secondary and tertiary structures of the protein, as aggregation, fragmentation and oxidation phenomena are involved. (Feidl, et al., 2019) A mAb formulation consists of protein and excipients in aqueous buffer. Therefore, the amide I ($1600 - 1700\ cm^{-1}$), II ($1500 - 1600\ cm^{-1}$) and III ($1200 - 1300\ cm^{-1}$) regions are used to characterize changes in the secondary structures of the protein, since the carbonyl (C=O) and the amine (N-H) groups of the protein contribute to hydrogen bonding in α-helix, β-sheet and random coil. (Lamsal, Harroun, Brosseau, & Gagnon, 2012) Furthermore, to stabilize the tertiary structure of the protein,

disulfide bridges and aromatic amino acids in the side chains are present, resulting in peaks in the spectra between 500 cm^{-1} and 700 cm^{-1}. The aromatic residues of amino acids produce numerous vibrational bands in the fingerprint region, such as those at 702 cm^{-1}(methionine), 835 and 850 cm^{-1} (tyrosine), 870 cm^{-1} (tryptophan), 1000 cm^{-1} and 1027 cm^{-1} (phenylalanine). The C-N stretching vibrations, in conjunction with N-H bending, are associated with the secondary structure of the protein in the region of the amide-II bond (1520 cm^{-1}). Moreover, the CH_2 bending, and CH deformation are linked to the primary structure of the protein. The peak at 1121 cm^{-1} corresponds to the C-N bond, and the one at 1454 cm^{-1} to the C-H deformation. The peaks in the amide-I region around 1680 cm^{-1} are attributed to the β-sheets. (Thiagarajan, et al., 2015) (Biancolillo & Marini, 2018)

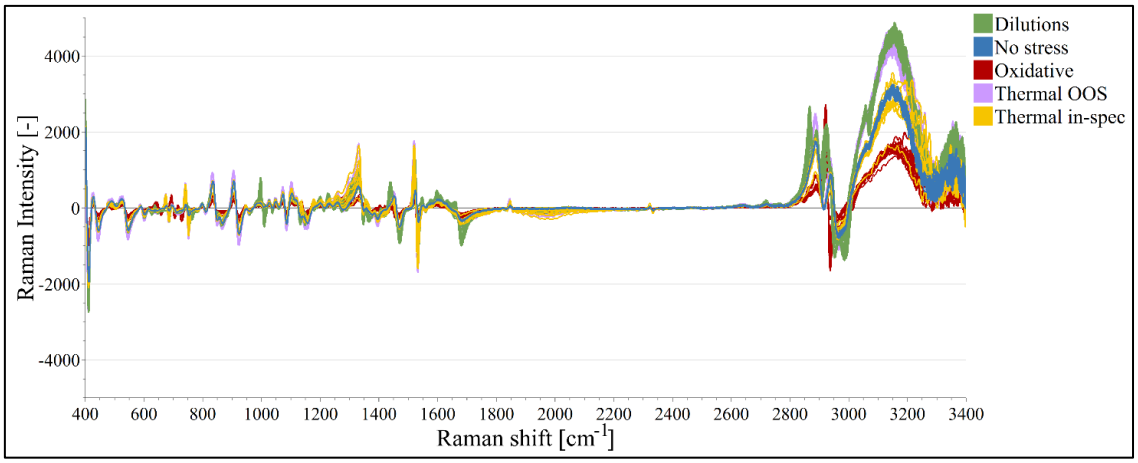

Figure 21: Pre-processed Raman spectra of *formulation 1* and *formulation 2* samples in the entire Raman shift region colored according to the different types of samples, as clearly detailed in the legend in the right upper part of the graph.

In ***Figure 21***, the pretreated spectra in the entire range of acquisition for each case-study are reported, highlighting the specific peak of O-H stretch at 3148 cm^{-1} and the C-H stretching region at around 2920 cm^{-1}.

4.3.1 PCA model development

Two different PCA models were developed using the mAb-based products: one considering the entire dataset and one by focusing only on the thermally stressed samples.

The primary objective of this Thesis was to conduct a feasibility study aimed at determining whether Raman spectroscopy was a suitable tool for distinguishing between different types of stress affecting the protein. To achieve this, the entire dataset was incorporated into the calibration phase of model development. The first three significant principal components will be detailed in the Results section, as they account for 99% of

the variance, representing most of the information contained in the data, as depicted in ***Figure 22***. A comparison between the R2X and the Q2 is reported. In particular, the R2X represents the cumulative fraction of sum of squares of the entire X explained by all extracted components; while the Q2 is the cumulative fraction of the total variation for all the x-variables for the extracted components. The more similar the two values are to each other, the more robust the developed model can be considered.

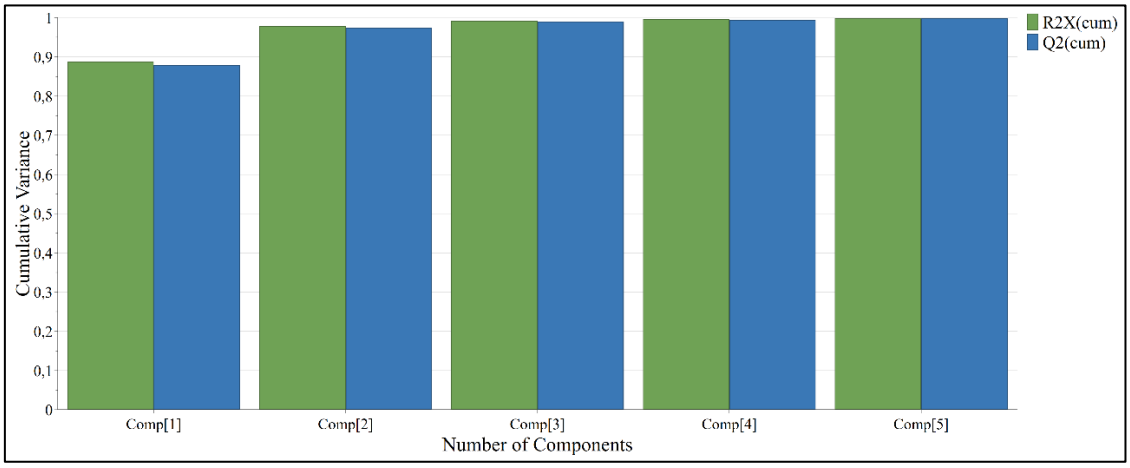

Figure 22: Cumulative variance as a function of the number of components in case of PCA model developed on the entire dataset.

Including more than three components will lead to modeling the measurement noise, without emphasizing the valuable information regarding the described phenomena.

The model mentioned above encompassed the complete dataset during the calibration phase, enabling the assessment of Raman spectroscopy's capability to differentiate the stresses experienced by the molecule. However, it did not clarify whether the model could be extended to other samples not involved in the calibration process. To address this, the dataset was divided into two segments for each stress: 2/3 of the data was utilized as the calibration set, while the remaining 1/3 was designated for prediction. The projection scores plot will be presented in the Results section.

Finally, an external validation was performed by employing the model to project a different product than the one utilized in the calibration phase into the previously reduced space. Specifically, the model, originally developed using an antibody molecule, was tested using a hormone.

To gain a more comprehensive understanding of the processes occurring during thermal stress in the protein and to identify the primary bonds involved in this phenomenon, a PCA was carried out also by focusing only on the thermally stressed samples.

4.4 Results

The interpretation of the PCA results is centered on the analysis of the scores and loadings, with a specific focus on the groupings associated with the type of stress to which the sample was exposed. Moreover, the most significant variables for each kind of stress, characterized by the highest peaks in the loadings plot will be highlighted.

4.4.1 PCA – discrimination among stresses acting on the mAb

Two different scores plot, relating PC1 vs PC2 and PC1 vs PC3, are reported respectively in ***Figure 23a*** and ***Figure 23b*****.** The PCA revealed a distinct trend in grouping based on the type of stress demonstrated by the samples (refer to the legend for interpreting the groups).

Upon closer examination of PC1 vs PC2, a distinct separation into two regions is evident: the oxidative-stressed samples are positioned in the positive PC1 range, while both the thermal-stressed out-of-specification (OOS) and diluted samples are located in the negative range. The samples labeled as "thermal in-spec" and "no stress" overlap in the central region of the plot. This serves as a successful application of the technology for the intended purpose. Specifically, the "thermal in-spec" samples experienced a lower degree of stress, resulting in HMW% and LMW% values that adhere to the specified specification limits imposed by the company for the product under investigation. From a statistical quality control perspective, it is advantageous that PCA accurately identifies these samples as closely aligning with the non-stressed ones.

Moreover, ***Figure 23b*** offers valuable insights regarding the protein concentration. Specifically, as the values of PC3 transition from negative to positive, the protein concentration in the formulation rises from 2 mg/ml up to 40 mg/ml. A link with the loadings plot shown in **Figure 24c** can be made, as deeply described below.

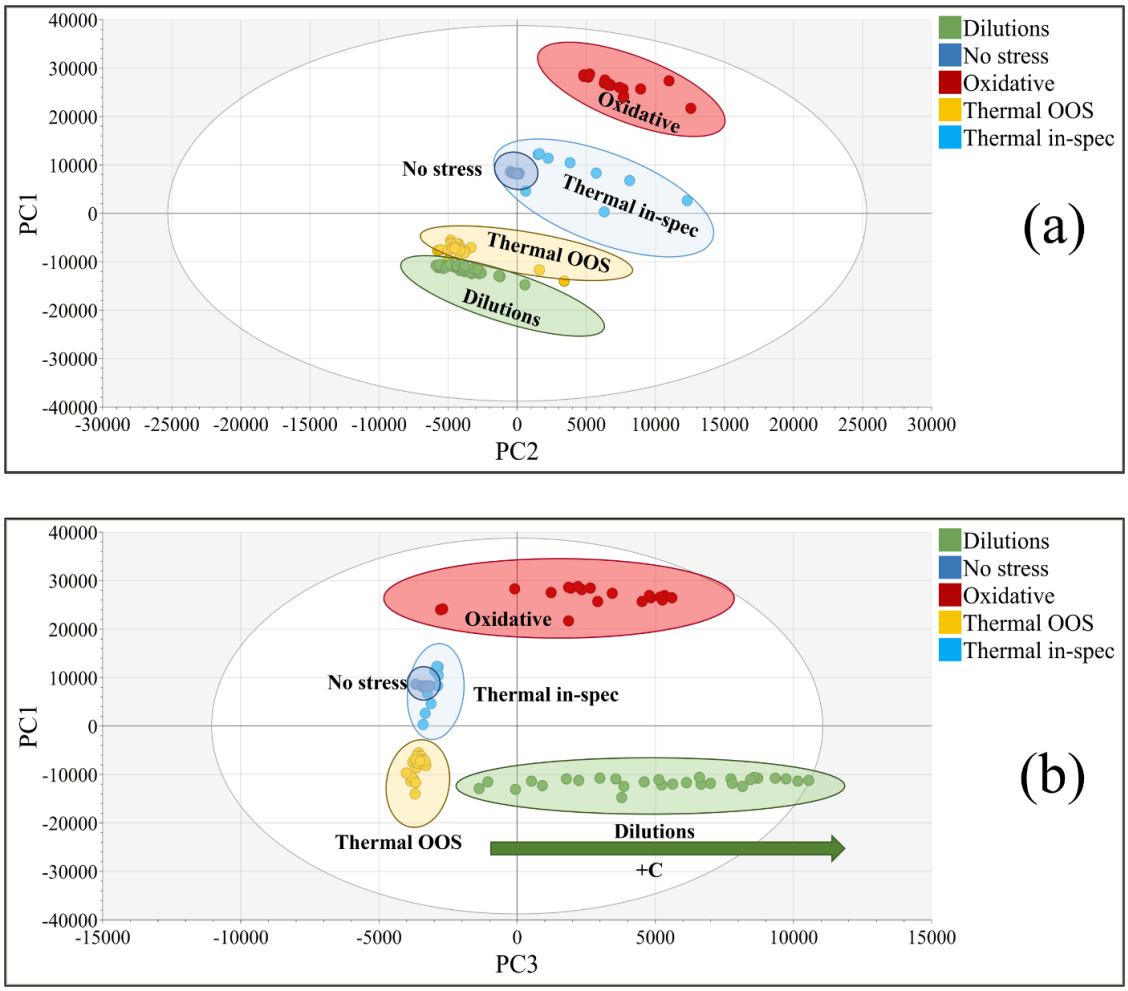

Figure 23: Scores Plot of the entire dataset in the Raman shift range 150-3425 cm^{-1}. In graph (a) the scores are displayed in the plane described by the 1st and 2nd PC, while in graph (b) the plane described by the 1st and 3rd PC is reported.

The loadings plots, depicted in ***Figure 24***, emphasize the most critical variables for each stress type, as indicated by the peaks in the loadings trend. The peaks of C-H stretching are identified are significant for distinguishing between oxidative-stressed samples and the thermal and diluted counterparts. Furthermore, variations in the fingerprint regions are observed, likely associated with structural modifications at the secondary and tertiary structure of the protein.

PC1, as shown in ***Figure 24a,*** reveals an increase in peak intensity at approximately 2800 cm^{-1} for the thermal-stressed (out of specification) and diluted samples, located within the negative PC1 values in the score plot. In the case of these two stress factors, another peak around 3000 cm^{-1}, primarily associated with O-H and C-H stretching. Furthermore, PC2, as shown in ***Figure 24b***, underscores the significance of the peak at 2800 cm^{-1} for the samples situated in the region of positive PC2 values in the scores plot. Therefore, a positive correlation was found between the oxidative stressed samples and the thermally

in-specification one: higher score values are related to an increase in the signal at 2800 cm^{-1}. Conversely, in the negative part of the scores plot, the samples are anti-correlated, meaning that the opposite occurs.

Figure 24c shows the loadings plot for PC3 and highlights that the region between 2800 and 3000 cm^{-1} contains the most significant variables for the description of the dilution process. It is reasonable to assume that as the protein content in the formulation decreases, the number of bonds between the protein itself and the excipients is likely to diminish, leading to variations in peak intensity. Particularly, the peak at around 2870 cm^{-1} exclusively appears in the diluted samples, absent in the non-stressed ones, indicating its association with the alteration in protein concentration. Additionally, variations in the amide-I bands are observed, contributing to the dilution process.

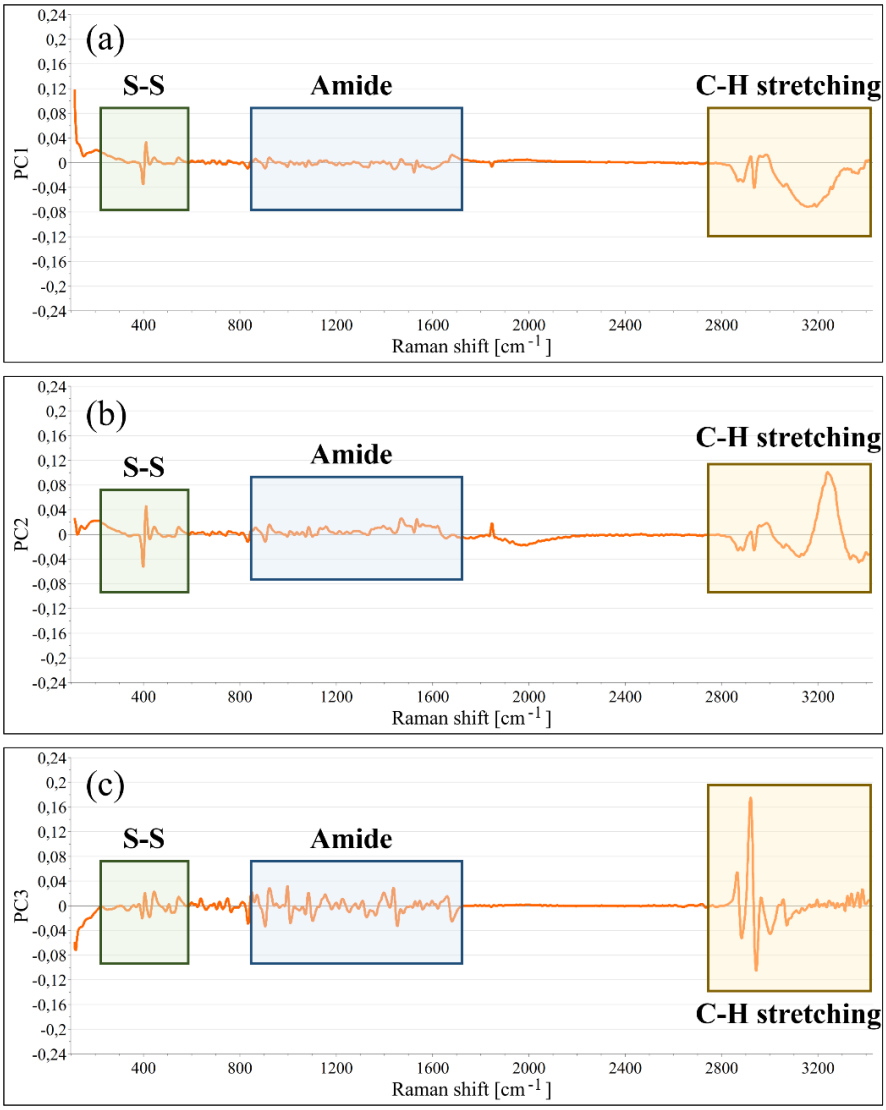

Figure 24: Loadings plots for the first three principal components reporting (a) PC1, (b) PC2 and (c) PC3. The data were processed using the single PCA model developed on the entire Raman shift range.

4.4.2 PCA – Splitting of dataset in calibration and prediction

The results reported in Section 4.4.1 refer to the PCA model developed using the whole dataset in the calibration phase. This enabled to assess the potential of Raman spectroscopy in discriminating among the stresses the protein was subjected to. To understand whether the model could be extended to other samples not involved in the calibration process, the dataset was divided as deeply reported in Section 4.3.1.

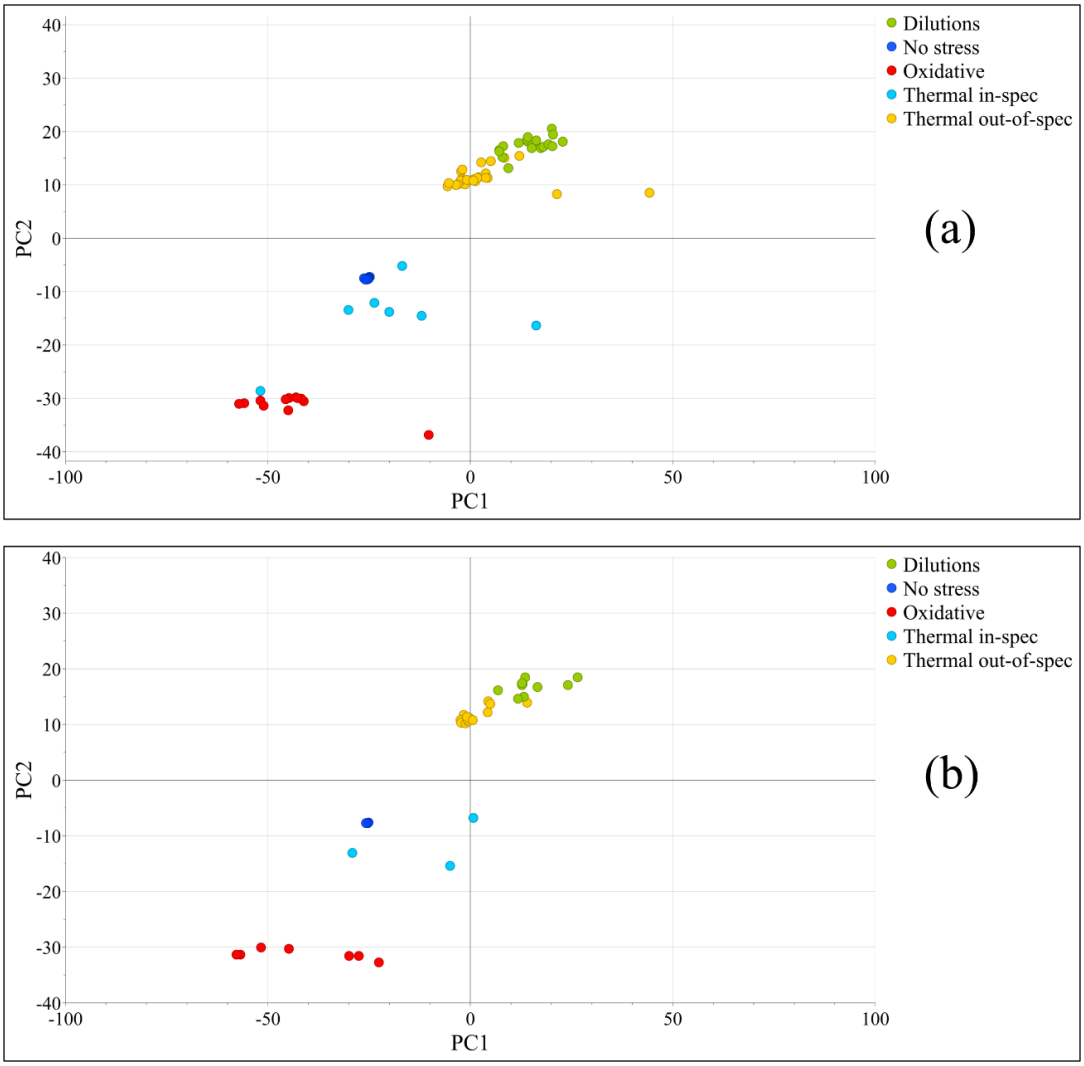

Figure 25: Scores plot of PCA model developed on the entire range for (a) calibration dataset and (b) prediction dataset for mAb samples colored according to the type of stress, as reported in the legend.

The projection scores plot, depicted in ***Figure 25***, demonstrates the model's capability to project results for new samples based only on the calibration dataset (calibration scores plot in ***Figure 25a***). Therefore, if a new sample is generated, it can be evaluated by the model to ascertain its location in the plane. Moreover, the Hotelling's T2 value as a function of the samples was reported in ***Figure 26*** for the prediction set.

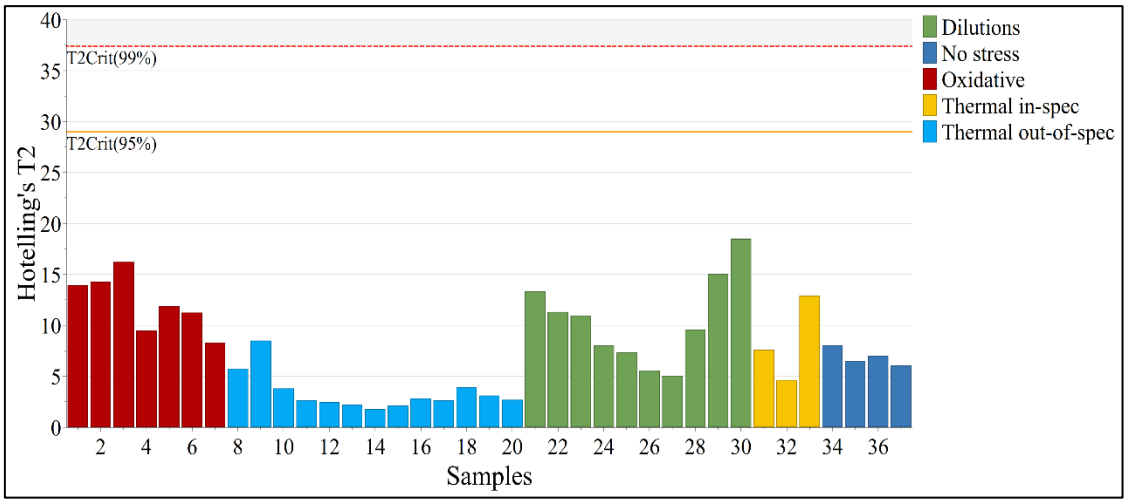

Figure 26: Hotelling's T2 graph for the prediction dataset made up of mAb samples, colored according to the type of stress.

One data point was identified as an outlier due to an issue that occurred during the acquisition of Raman spectra and was subsequently removed from the dataset. All other data points exhibited Hotelling's T2 values significantly below the control limits calculated by the model itself at the 95% and 99% of confidence level.

4.4.3 PCA – External testing using a hormone product

The model described in Section 4.4.1 was applied to project a different product in the reduced space. Specifically, the model, originally developed using the mAb products, was tested with a hormone. Although the two molecules have different structures, the bonds involved in the Raman spectra are similar. The projection score plot and Hotelling's T2 graph, shown in ***Figure 27***, confirmed the robustness of the developed model. It has to be remarked that there was only one outlier, among the 55 samples, distinguished by a notably high T2 value. The model successfully distinguished that the hormone samples were not subjected to any stress, positioning them accurately within the appropriate zone of the graph. However, to demonstrate that the model can also differentiate among various types of stress to which the hormone may be subjected, additional experimental trials must be conducted.

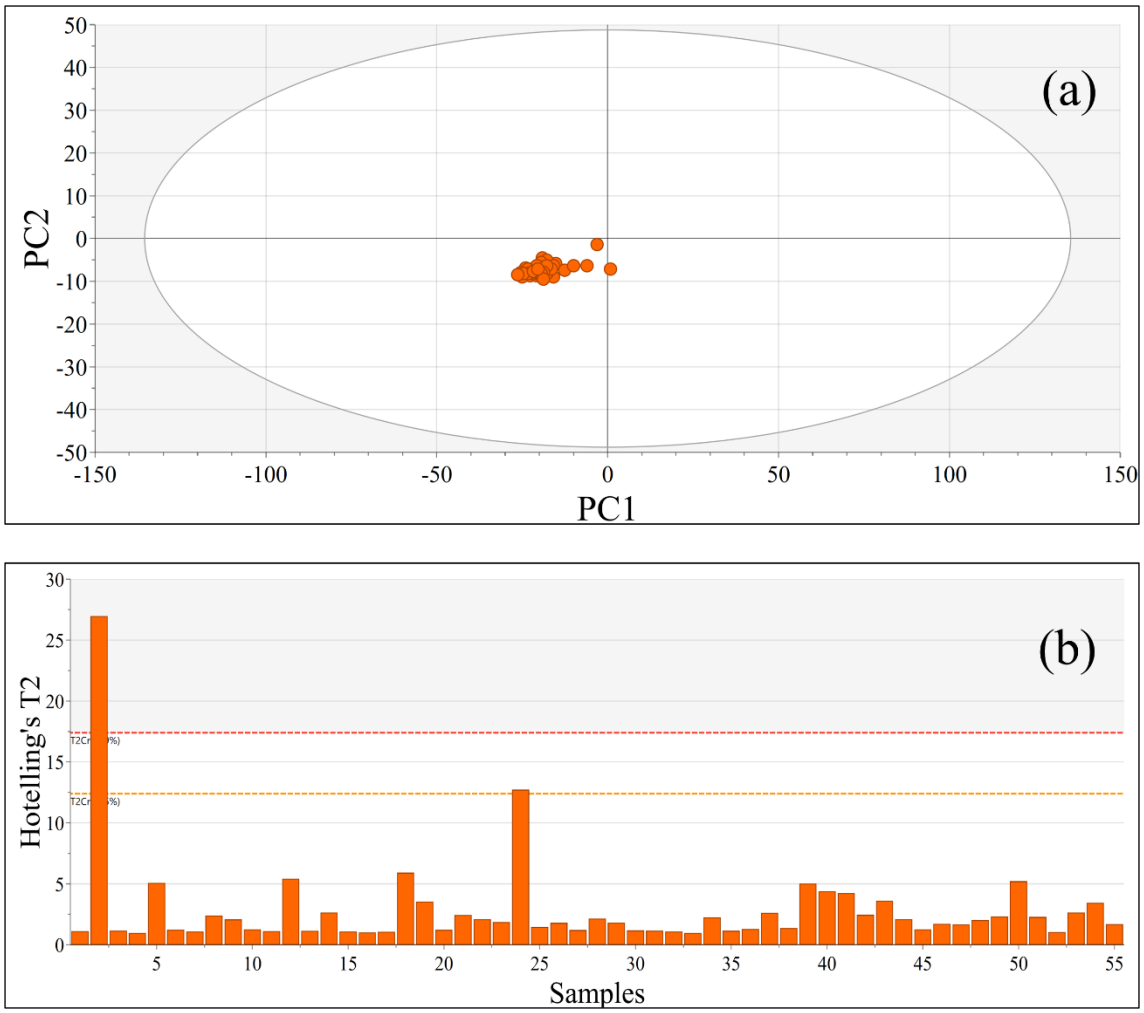

Figure 27: Projection scores plot for *formulation 3* using the PCA developed using the mAb dataset.

4.4.4 PCA only on thermal stressed samples

PCA model was also developed by considering only the thermal stressed samples to gain a deeper comprehension on which bonds are primarily involved during the thermal stress in protein formulations. This type of information cannot be obtained by using the model that incorporates all the stresses acting on the protein. In such cases, the majority of the variance is attributed to the differences among the stresses, as well as the various bonds involved depending on the applied stress. To effectively track the evolution of thermal stress, a tailored PCA is required.

The scores plot relating PC1 vs PC2, reported in ***Figure 28a***, revealed three different groups, according to the exposure duration. Samples located on the right side of the graph are associated to lowest exposure time (up to 7 days) and correspond to positive values of PC2 and negative values of PC1. Conversely, the samples with the highest exposure time are positioned on the opposite side, while the moderately stressed samples are in the central region. The two PCs account for the 94% of the variance, enabling the

classification of the samples into three distinct groups. Additionally, a discernible upward trend is noted when transitioning diagonally for the least stressed samples (from positive values of PC2 to 0) and for the most stressed ones (from negative values of PC2 to 0). On the contrary, a stochastic behavior is observed in the central portion.

By looking at the PC3, as shown in ***Figure 28b***, a trend can be observed for the middle-stressed samples. Indeed, they are arranged in order, with stress exposure increasing along the horizontal axis, transitioning from negative to positive values of PC3. This suggests that PC3 effectively delineates the increasing stress levels of the moderately stressed samples.

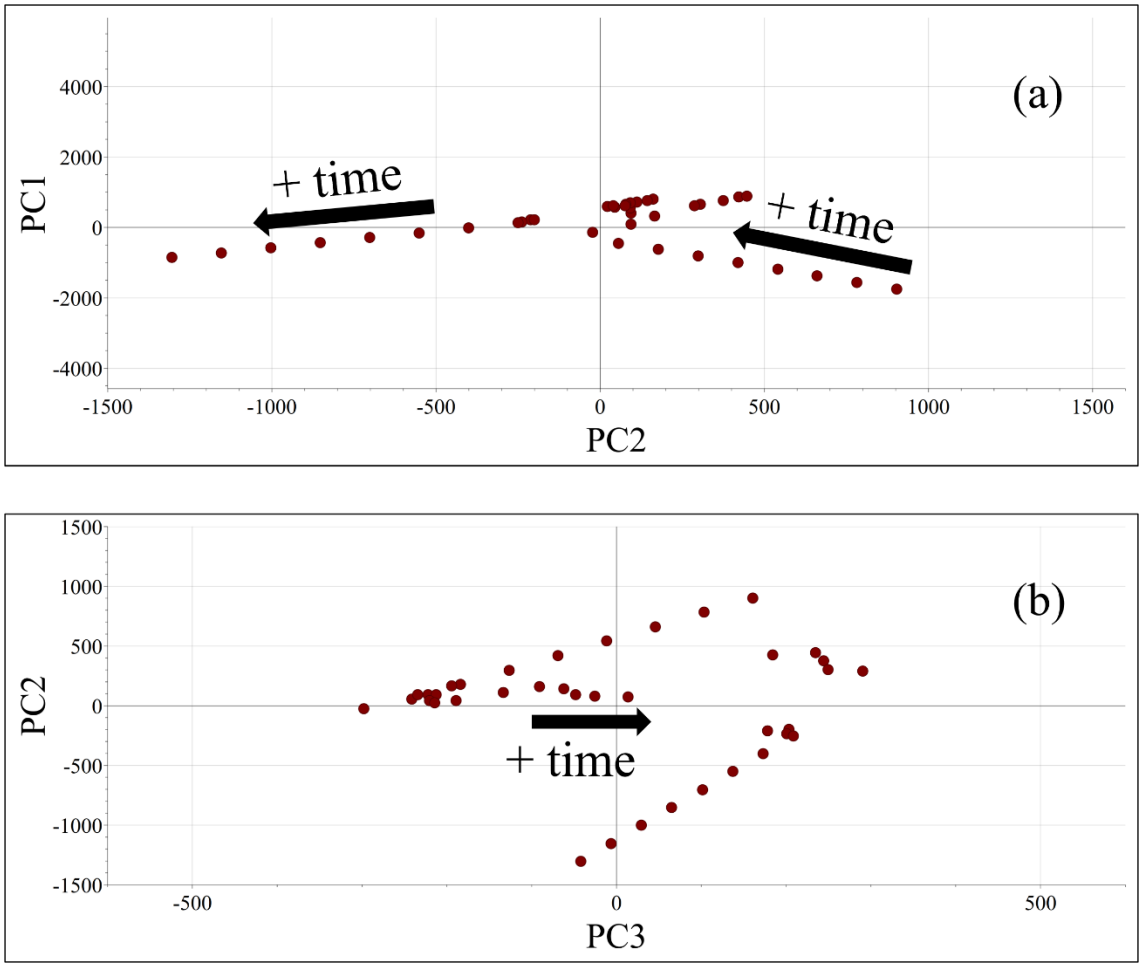

Figure 28:Scores plot of PCA model developed only on the thermal stressed samples. The scores are displayed in the plane described by (a) the 1st and 2nd PCs and (b) the 2nd and 3rd PCs. The groupings according to the exposure duration to the stress are obtained,

The interpretation of the scores plot revealed distinct spectral regions that are impacted based on the magnitude of stress. Therefore, a single PCA was carried out for each individual cluster focusing. Only PC1, which accounts for the highest variance and therefore the majority of the information in the data, was depicted in the loadings plot

(***Figure 29***) to emphasize the spectral regions that undergo changes with prolonged exposure to thermal stress.

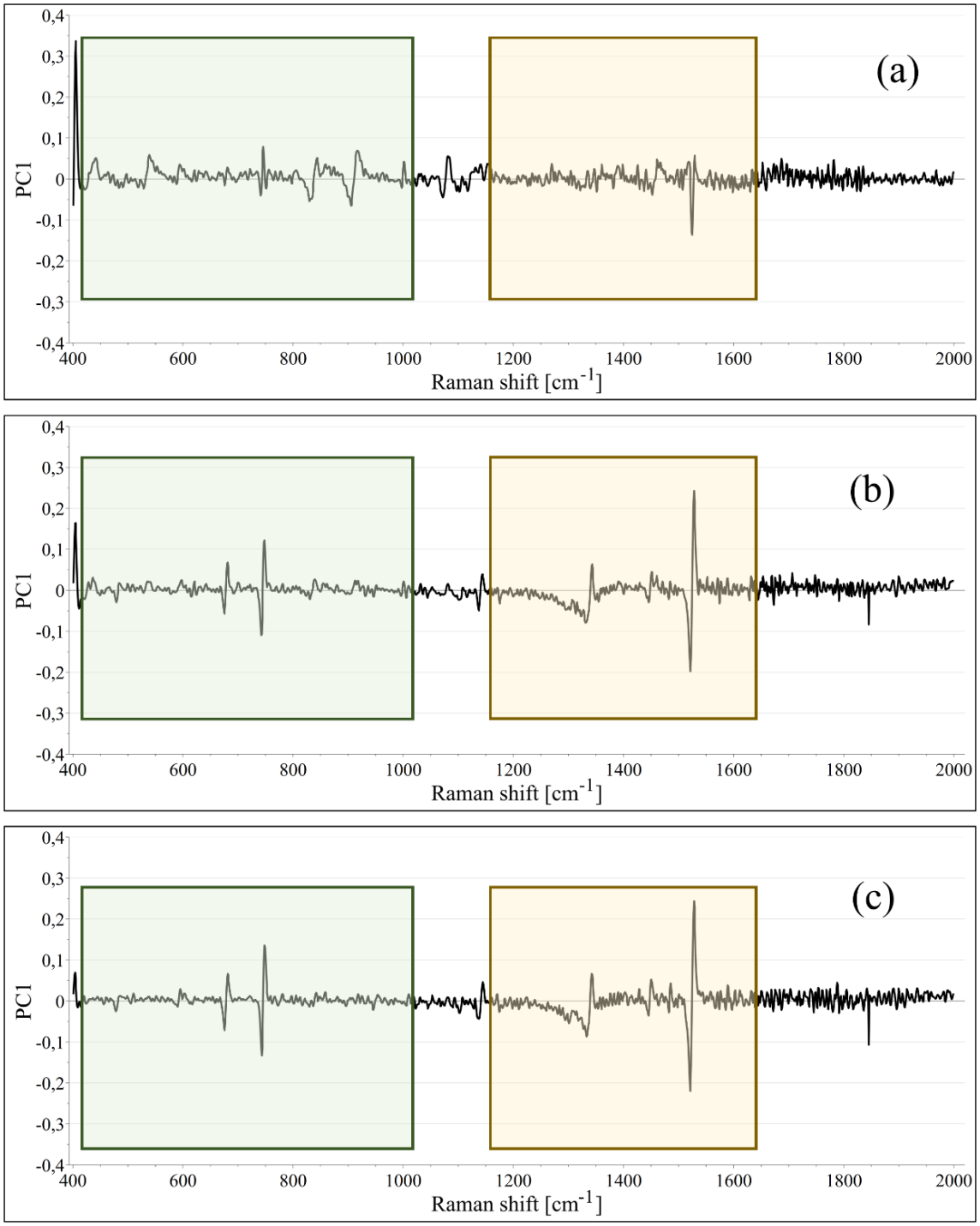

Figure 29:The loadings plot was generated by the PCA model exclusively trained on thermally stressed samples categorized by the type of stress, specifically: (a) lowest stress exposure time; (b) moderate stress exposure time; and (c) highest stress exposure time.

As indicated by the highlighted frames, the spectral regions associated with amino acid bands (Raman shift lower than 1000 cm^{-1}) exhibit a reduction in signal intensity with prolonged exposure to thermal stress. This implies that certain critical bonds may be

compromised because of aggregation and fragmentation phenomena. Moreover, as the exposure duration to thermal stress increases, it is anticipated that all associated phenomena will advance, leading to more significant alterations in the secondary and tertiary structure. This explains the observed rise in Raman signal intensity of the amide bands with increasing stress levels.

4.5 Highlights

The feasibility study shown in this Thesis successfully employed Raman spectroscopy to distinguish different types of stress affecting the protein. These stresses often occur during DP manufacturing, and it is imperative to monitor their impact on the DP quality.

Raman spectroscopy demonstrated to be a powerful tool to deal with thermal stress, oxidative stress, and dilutions. Additionally, non-stressed samples were correctly classified in a separate cluster, together with the in-specification samples, by the PCA model.

Furthermore, the methodology enabled a comprehensive analysis of samples exposed to thermal stress, allowing for the classification into three different groups according to the level of stress encountered. This highlights the strength and adaptability of Raman spectroscopy in characterizing protein stress responses. It must be highlighted that the same analysis was conducted also on the oxidative stressed samples, but no valuable insights were obtained.

The findings outlined here serve as a valuable resource for quantitative analysis. As a new sample undergoes different processing steps, it will inevitably experience alterations in its Critical Quality Attributes (CQAs). By integrating this information into the PCA model, it is possible to identify which CQAs were affected by the process step, along with the specific bonds and spectral regions involved. This approach enables the development of an appropriate PLS model to quantify the degree of stress and identify the areas requiring focused model refinement.

In the development and manufacturing of therapeutic proteins, oxidation and thermal degradation are commonly observed challenges. The susceptibility of proteins to these stressors can alter their secondary and tertiary structures, which in turn affects their stability and biological activity, potentially compromising product efficacy and patient safety. Moreover, dilutions effect can be found during compounding or filtration steps, leading to changes in protein concentration. Consequently, it is essential to monitor these stress factors and the resulting variations in different Critical Quality Attributes (CQAs)

throughout the therapeutic protein development process.

This Raman-based application would be suitable in the perspective of statistical quality control, being able to classify “good” samples from “stressed” ones. It can be implemented as an at-line tool to speed-up the stability studies and the process development and technology transfer activities. However, it must be highlighted that PCA is an unsupervised model, not allowing for a prediction of new samples in its usual understanding. Therefore, some work must be done to develop a classifier model like Partial Least Squares – Discriminant Analysis (PLS-DA) as future steps to create a predictive model based on the preliminary results obtained by the reported exploratory data analysis.

It is important to note that the excipients present in the formulation significantly influence both the development and performance of the model, as they provide specific signals in the Raman spectra. In this chapter, trehalose and sucrose were examined, as they are the most commonly used excipients in pharmaceutical formulations. Furthermore, it was found that the model developed using a formulation containing trehalose was capable of accurately predicting the non-stressed hormone presentation, which primarily consisted of sucrose. However, further investigation is required to determine whether the model can also differentiate the stresses affecting a different formulation compared to the one used during the calibration phase.

CHAPTER 5

5. Assessing Critical Quality Attributes in Biopharmaceuticals during Process Development and Manufacturing: Effects of Denaturation and Dilution processes

5.1 Introduction

The pharmaceutical industry continuously strives to improve PAT tools for the monitoring and evaluation of DP quality during both product and process development, as well as manufacturing. However, the currently used analytical techniques, such as chromatography or capillary electrophoresis, are labor-intensive and time-consuming. (McAvan, et al., 2020) (Clegg, 2020) Therefore, the adoption of spectroscopic techniques, coupled with multivariate data analysis, is crucial for enhancing efficiency and enabling cost-effective monitoring of CQAs throughout a product's lifecycle, all while ensuring the maintenance of the required product quality standards. (Food and Drug Administration, 2011) (Esmonde-White, Cuellar, & Lewis, 2022) A detailed introduction is reported in Section 4.1.

This Chapter exploits the information obtained from the qualitative analysis to develop a soft-sensor able to quantify the entity of the stress the molecule was subjected to. In fact, different PLS models were developed allowing for the evaluation of each CQAs under investigation. To develop the quantitative application, the reference techniques are needed to obtain the reference CQA values to calibrate the model.

Typically, the development of the models involves two steps:

a) Firstly, the *calibration* phase is performed aimed to find a relationship between the Raman spectra and the CQAs to be monitored, i.e. HMW, LMW, oxidation level and protein/excipients content.
b) Then, the *validation* is performed by predicting CQAs values of new samples, not included in the first phase that the model has never seen. These values must be compared with the ones measured by the reference techniques to evaluate the model's performances.

Having a PLS model able to quantify the precise value of each CQAs would significantly save time and resources, since the experimental analytical effort would be minimized.

After the PLS models were developed, a real-case study was evaluated. Specifically, *Formulation 1* was subjected to the freeze-drying process with the aim to evaluate the aggregation level and the protein content at the end of the cycle and compare the obtained values with the ones obtained for the liquid formulation. A proof of concept was carried out by comparing the results obtained by the model with the ones measured by the reference technique, showing the reliability and robustness of the soft sensor.

5.2 Case-study

Formulation 1, which is less concentrated, has also been developed in a freeze-dried forms and is suitable for evaluating denaturation phenomena, like HMW%, LMW% or oxidation levels. Conversely, *Formulation 2*, being more concentrated, was used as starting point to conduct progress dilutions and focus on the protein/excipient contents. The choice to utilize this type of formulation is based on the availability of this material within the Company. As deeply detailed in the Introduction Section, these formulations, being mAb, can be considered as worst-case formulations, since they are highly susceptible to the stresses encountered during the biopharmaceutical manufacturing.

For PLS calibration and validation, it is essential to investigate a wide range of each CQA. Consequently, dilutions of *Formulation 2* were carried out to generate multiple samples with varying concentration of protein, methionine and PS20. Specifically, two distinct ranges of protein content were investigated: a low range of 0.1-1.0 mg/ml and a high range of 1.0-40 mg/ml. Instead, methionine concentration ranged from 0.22 mg/ml – 1.46 mg/ml and PS20 content ranged from 0.22 mg/ml – 2.40 mg/ml.

The explanation of how the thermal stress was conducted is deeply described in Section 4.2. However, with that experimental set-up only high HMW% values were obtained. Therefore, to generate HMW levels between 0.44% and 1.0%, the thermal stress was interrupted every 30 minutes during the initial 8 hours of incubation at 50°C.

After each sample was generated, Raman spectra were acquired according to the setup reported in Section 3.2.2, with the Raman probe immersed in the liquid product into the vial. The Raman parameters used for each case-study are reported in ***Table 4***.

Table 4: Raman parameters used for each case-study.

Case-study	*Exposure [s]*	*Counts*
Thermal stress	50	2
Oxidative stress	50	2
Dilution (protein)	45	3
Dilution (methionine)	55	2
Dilution (PS20)	50	2

Once spectra were collected, the reference value for each CQA of each sample was measured according to the specific analytical methods and the setup described in Section 3.1 and summarized up in ***Table 5***, where the acceptance criteria were also reported according to the internal SOP provided by the company.

Table 5: Critical Quality Attributes considered in the different treatments the samples were subjected to, together with the analytical reference method and the relative acceptance criteria.

CQA	*Treatment*	*Analytical Reference Method*	*Acceptance Criteria*
Aggregation level (HMW)	Thermal stress	SE-UPLC	CV < 10%
Fragmentation level (LMW)	Thermal stress	CGE-SDS	CV < 15%
Oxidation level	Oxidative stress	RP-UPLC	CV < 15%
Protein Content	Dilution	SoloVPE	CV < 3%
Methionine Content	Dilution	RP-HPLC	CV < 3%
Polysorbate 20 Content	Dilution	RP-HPLC	$\frac{min\ CPS20}{max\ CPS20} > 78\%$

Matlab scripts were written to develop different PLS models, one for each CQA under investigation using Matlab software (R2021a, The Mathworks Inc., Natick, MA, USA). The following libraries and functions were used for model development:

- *Signal Processing Toolbox:* the function "*sgolayfilt*" was used to apply the Savitzky-Golay filter to the dataset.
- *Statistics and Machine Learning Toolbox:* the function "*plsregress*" was used to perform the PLS regression.

Firstly, the entire Raman shift range was involved. Then, reduced ranges were considered according to the signals obtained in the loading plots. Each dataset was divided into

calibration and validation set to evaluate the performances of the model by determining the root mean squared errors and the coefficient of variations. As a further confirmation, the equivalence test was conducted, using Minitab® version 21.1, as described in Section 2.3.7 to compare the model's performances with the precision of the analytical method derived from the internal validation report provided by the company.

As a graphical outcome, parity diagrams plots are shown. They relate the values of each CQA measured by the reference analytical technique as a function of the corresponding value predicted by the PLS model. The more the points are aligned with the bisector, the more the model is considered accurate. Moreover, the graph relating the coefficient of variation as a function of the CQA measured by the reference technique was reported to assess the model performances.

An additional group of freeze-dried samples, belonging to *Formulation 1,* was generated to evaluate the HMW% and protein content using the off-line developed model. This has been conducted to externally validate the model itself and show a real case-study of possible applicability.

5.3 Data processing

From a practical point of view, a Raman spectrum is characterized by many Raman intensity values, one for each acquired Raman shift. Therefore, it is challenging to analyze them by means of simple tools and multivariate data analysis is needed to consider the correlations among the variables, as deeply discussed in Section 2.3. (Wang, Muzzio, & Glasser, 2016) (Wold, 1995)

All the spectra underwent to derivative pre-treatments to improve spectral features and peak identifications. Specifically, a first-derivative was applied followed by the Savitsky-Golay smoothing filter of the first order with a window size of 15. The entire range was considered as 600-3000 cm^{-1}, since the signals at higher or lower frequencies were removed due to the noise. Also, some samples were removed due to issues occurred during spectra acquisition. Furthermore, a second derivative was conducted on the dataset; however, no improvements were observed.

For model development, the 70% of the dataset serves as calibration set and the remaining 30% was used as prediction set for internal validation purposes. A 3-fold cross-validation scheme was used in the present work to assess model performances more robustly. The number of samples, the division of the dataset into calibration and validation set, and the Raman shift considered for the development of the models are reported in ***Table 6***.

The selection of the number of latent variables for model construction was meticulously conducted by examining the percentage of variance explained. Specifically, a number of variables was chosen to ensure that at least 96% of the variance in the data was accounted for.

Then, Each PLS model was firstly developed on the entire range of Raman shift, leading to evaluate the most significant peaks for each case-study from the loadings plot. Then, a PLS model in the narrowed range was also developed for each CQA to try improving model's performances. Firstly, the calibration step was performed using the 70% of the dataset and the performance metrics, RMSEC and RMSECV, were evaluated. How much they are closer between each other, more the model is reliable and robust. Then, the 30% of the dataset was used to internally validate the model and the RMSEP was calculated. Furthermore, the coefficient of variation was calculated for each predicted sample and the equivalence test was carried out to show the equivalence between the model and the analytical technique.

Table 6: Total number of samples considered and division of the dataset into calibration and validation set. Moreover, the Raman shift explored for each CQA are also reported.

Model Type	***CQA***	***N° samples***	***Calibration set***	***Validation set***	***Raman Shift [cm^{-1}]***
Model 1	High HMW	36	26	10	600-3000 1200-1600
Model 2	Low HMW	10	8	2	600-3000 1200-1900
Model 3	LMW	36	26	10	600-3000 1200-1600
Model 4	High Protein Content	28	21	7	600-3000 2600-1000
Model 5	Low Protein Content	10	10	-	600-3000
Model 6	Methionine Content	23	17	6	600-3000 530-1530
Model 7	PS20 Content	19	13	6	600-3000 1200-1600

5.4 Results

The performances of the developed PLS models were evaluated for each specific CQA in the two different scenarios under investigation:

- Product degradation due to thermal and/or oxidative stress, leading to potential changes in the structure of the protein;
- Dilution process, leading to changes in product composition (protein and excipients content)

The interpretation of the PLS models relies on the parity diagram, which illustrates the relationship between the CQA measured by the reference technique and the CQA predicted by the PLS model. The purpose of this graph is to visually assess the alignment of the data points along the bisector; clearly, the closer the points are to the bisector, the more accurate the predictions. Additionally, the graph depicting the coefficient of variation as a function of the CQA measured by the reference technique is included to determine whether the allowable error of the model falls within the bounds of analytical variability.

5.4.1 Protein degradation related CQAs: aggregation, fragmentation and oxidation level

Thermal stress resulted in alterations to the levels of aggregation and fragmentation of the molecule, whereas oxidative stress induced variations in the oxidation state.

The aggregation mechanism leading to high percentage of HMW likely differ from those associated with low percentages. As a result, it was not feasible to create a single model that could accurately estimate the entire range of HMW% being evaluated. The different percentage of HMW in the product were intentionally generated by altering the exposure time to thermal stress, thereby achieving a broader range for this CQA. Two distinct models were developed: Model 1 addresses high HMW% levels, ranging from 5% to 30%, while Model 2 pertains to low HMW% levels, ranging from 0% to 1%. Due to logistic reasons, no points were taken in the range 1% - 5% since the sampling lied during night. The necessity for developing two different models arises from the different bonds and regions of the Raman spectra that are involved, depending on the value of HMW%, as illustrated in ***Figure 30***. Both models were initially constructed using the entire range (ER) of Raman shift values, specifically from 600 to 3000 cm^{-1}. To determine whether a more precise and accurate model could be developed by concentrating on the Raman spectral region most influenced by thermal stress, a thorough analysis was conducted to

identify the appropriate Raman shift range. Following the creation of a preliminary PLS model using the full range of 600-3000 cm^{-1} for each case, the loadings of the first latent variable—containing most of the information—were examined to pinpoint the most significant signals. These signals corresponded to the highest (either positive or negative) peaks in the loadings plot shown in ***Figure 30***. Consequently, two distinct Raman shift ranges were established, as outlined below:

- Reduced Range 1 (RR1): 1200-1600 cm^{-1}
- Reduced Range 2 (RR2): 1200-1900 cm^{-1}

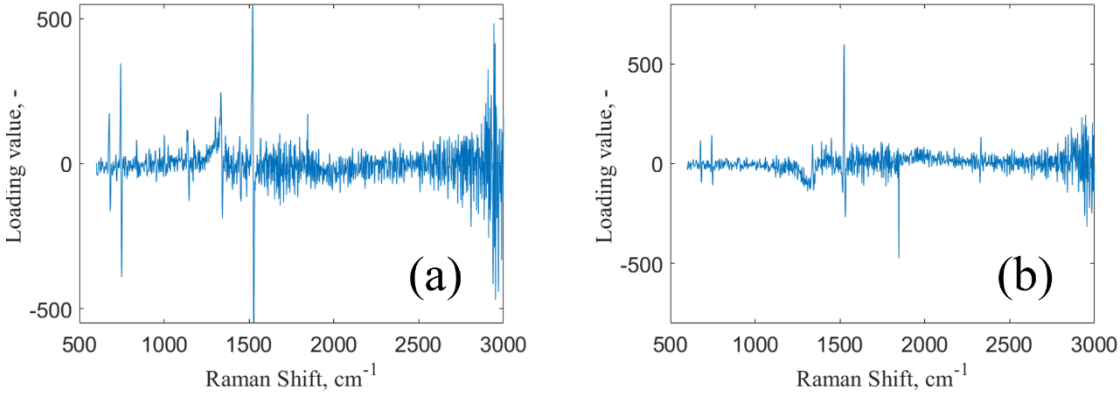

Figure 30*:* Loadings plot from the PLS decomposition of the dataset for (a) high HMW% and (b) low HMW%, covering the Raman shift range of 600-3000 cm^{-1}. The loadings for the first latent variable (LV) used in model development are presented.

By analyzing the trend of the loadings, it became evident that signals at Raman shift exceeding 2000 cm^{-1} were not particularly significant in characterizing the low HMW% dataset (***Figure 30b***). In contrast, a notable signal in the range of 2800-2900 cm^{-1} was identified as relevant for the high HMW% case (***Figure 30a***). However, the most critical peaks were observed within the amide regions, specifically between 1200-1600 cm^{-1}, which are essential for describing the phenomenon of aggregation at elevated levels. Additionally, a significant peak was detected at 1850 cm^{-1} for cases of low aggregation levels. This observation is justifiable, as the aggregation phenomenon primarily involves alterations in the secondary and tertiary structures of the molecule, with corresponding signals located in the amide regions. These regions encompass the vibrations of chemical bonds associated with the C-N, C-C, and C-O backbones in proteins. Furthermore, the C=O and N-H groups, which are crucial for hydrogen bonding in α-helices, β-sheets, and random coils, also exhibit peaks within these Raman shift ranges.

The performance parameters used to assess the aggregation levels are presented in **Table 7**. As indicated, the performance of the models evaluated in both the entire range (ER)

and Reduced Range 1 (RR1) is similar for high and low HMW% levels. Specifically, the R^2 and Q^2 values are notably high. Additionally, the RMSEC and RMSECV values are comparable, contributing to the creation of robust models. A more detailed analysis of the model performances is provided below.

Table 7: Performance metrics of the models created and the validation conducted in the aggregation level case study are detailed. Additionally, the model type, the critical quality attributes (CQA) examined, the Raman shift range, and the latent variables are specified.

Model Type	*CQA*	*Range*	*LV*	*RMSEC*	*RMSECV*	*RMSEP*	R^2	Q^2
Model 1	High HMW%	ER	4	0.587	0.801	0.629	0.994	0.991
		RR1		0.618	0.878	0.876	0.993	0.984
Model 2	Low HMW%	ER	4	0.014	0.112	0.034	0.899	0.810
		RR2		0.014	0.046	0.034	0.898	0.810

Figure 31 presents the parity plots that compare the HMW% values obtained through chromatography with those predicted by the model, for both the calibration and prediction datasets.

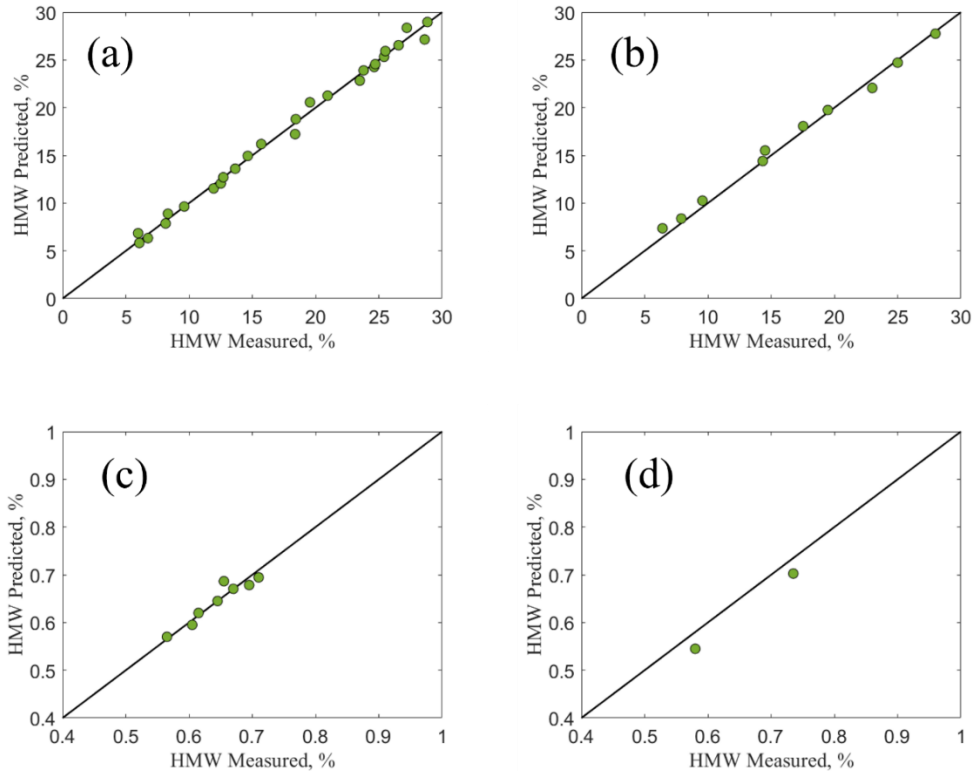

Figure 31: Parity diagrams comparing the measured HMW (%) to the predicted HMW (%) are presented for thermally stressed samples. These diagrams are derived from the calibration (a, c) and prediction (b, d) datasets, covering both high (a, b) and low (c, d) values, processed using a PLS model across the full Raman

shift range of 600-3000 cm^{-1}.

The aggregation level shows a strong correlation with the Raman spectra. For high HMW% levels, both the calibration and validation sets closely align with the data points, as illustrated in ***Figure 31 (a)*** and ***(b)***. The calibration set achieved a low RMSEC of 0.587, indicating that the developed model performed well with this dataset. In contrast, the RMSECV value of 0.801 was comparable to the calibration result, suggesting that the model may maintain good performance when applied to new samples. To further investigate this, a new set of samples was used for prediction. The resulting RMSEP and Q^2 values of 0.629 and 0.991, respectively, support this hypothesis. Notably, the RMSEP closely mirrors the values obtained during the calibration phase. Similar results were observed for low HMW% values, with an RMSEC of 0.014 and an RMSEP of 0.034.

To assess whether the predicted values align with the analytical variability of the reference method, the Coefficient of Variation (CV) was calculated for each pair of measured and predicted HMW% values. ***Figure 32*** displays the CV(%) as a function of the HMW(%) measured by chromatography for both cases. The horizontal line represents the threshold indicated in ***Table 5***, derived from the validation reports.

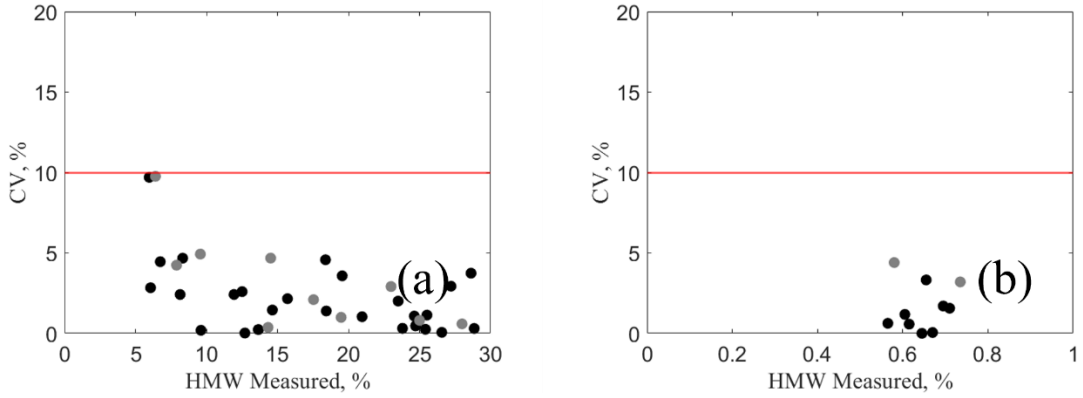

Figure 32**:** Relationship between the Coefficient of Variation calculated for (a) high HMW(%) and (b) low HMW(%)as a function of the corresponding measured HMW% values is reported. The black dots indicate the calibration samples, while the grey dots represent the prediction samples. The horizontal line at 10% denotes the threshold permitted according to the validation report of the reference method.

As shown in ***Figure 32***, all samples comply with the limits set by the company for both high and low HMW% models. The calibration set (black dots) and the validation set (grey dots) are situated below the horizontal line, which represents the acceptable limit for the analytical reference method. Consequently, both developed models are deemed robust and accurate. Additionally, differences in HMW% by 0.1% are within the error of the chromatography method and integration.

Parity diagrams in the case of reduced ranges are reported in ***Figure 33***. As shown in ***Table 7*** and illustrated in ***Figure 33a***, the performance of Model 1 within the reduced range was inferior to that of the model developed using the full range. This decline in performance may be due to a significant peak observed between 2800-2900 cm^{-1}, which played a crucial role in characterizing the phenomena. Excluding this peak likely resulted in the loss of essential information needed for accurately estimating the aggregation level. In the low HMW% dataset (***Figure 33b***), both ranges demonstrated similar performance; however, there was an improvement in the RMSECV, with values of 0.112 (ER) versus 0.046 (RR2). These RMSECV values closely resemble the RMSEC obtained in both scenarios, indicating the development of a more robust model suitable for predicting unknown and future samples. Nonetheless, an increase in the number of samples in this dataset is recommended for further evaluations.

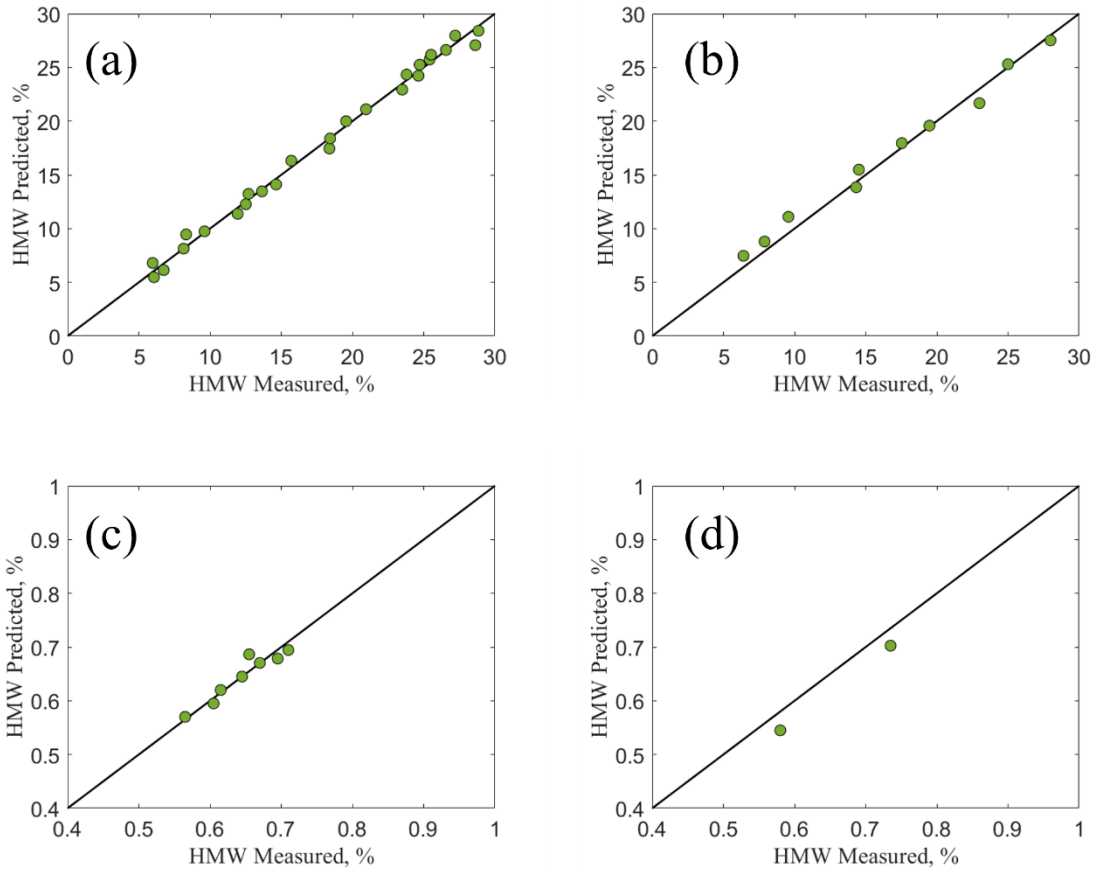

Figure 33: Parity diagrams comparing the measured HMW (%) to the predicted HMW (%) are presented for the calibration (a,c) and prediction sets (b,d) of thermally stressed samples, focusing on both high HMW values (a,b) and low HMW values (c,d). These diagrams were generated using a PLS model applied to the reduced Raman shift ranges (RR1 and RR2), specifically 1200-1600 cm^{-1} and 1200-1900 cm^{-1}, respectively.

The calibration plots confirm the good model performances since all the points lie on the bisector line. The same approach discussed was conducted for the fragmentation level

quantification, estimated through Model 3. The specific ranges investigated for LMW% quantification are the ER and RR1 ranges outlined in the aggregation level section, as supported by the loading plot, where the highest loading signal is observed around 1500 cm^{-1}, validating the reduced range RR1. A summary of the performance parameters for both models is provided in ***Table 8***.

Table 8: Performance metrics of the models developed, and the validation conducted in the case study for the fragmentation level are detailed. Additionally, the model type, the Raman shift range, and the latent variables are specified.

Model Type	*CQA*	*Range*	*LV*	*RMSEC*	*RMSECV*	*RMSEP*	*\R²*	*Q²*
Model 3	LMW%	ER	4	0.565	0.651	0.682	0.993	0.986
		RR1		0.615	0.671	0.648	0.992	0.988

The evaluation of the fragmentation level also yielded strong performance results. The RMSEC and RMSECV values were 0.565 and 0.651, respectively, as indicated in ***Table 8***. External performance metrics further validated the robustness of the developed model, resulting in an RMSEP of 0.682. ***Figure 34*** presents the parity diagram plots for the prediction set, along with a graph depicting the Coefficient of Variation as a function of the LMW% measured by capillary electrophoresis. In this instance, the threshold is set at 15%, according to the validation report of the reference method. Similar findings to those in previous cases are highlighted here.

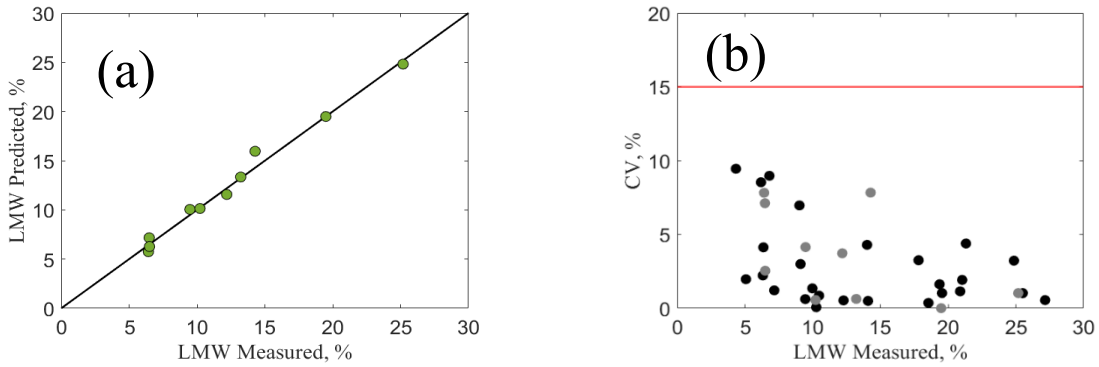

Figure 34: Parity diagrams comparing the measured LMW (%) to the predicted LMW (%) are presented, derived from the prediction set (a) processed using the PLS model across the full Raman shift range (600-3000 cm^{-1}). Figure 3b illustrates the relationship between the Coefficient of Variation for both sets, with the calibration set shown in black and the prediction set in grey, plotted against the LMW% measured by the reference analytical technique. The grey line at 15% indicates the allowable threshold for this critical quality attribute (CQA).

For the oxidized samples, Raman spectroscopy did not yield meaningful results, as the variations in the signals were primarily attributed to noise. Upon reviewing the spectra

resulting from oxidative stress, no clear trend was detected based on the oxidation level of each sample. Therefore, advancing with model development appeared unnecessary, as the differences observed in the spectrum were largely due to measurement noise rather than significant variability among the samples.

5.4.2 Product composition related CQAs: protein, methionine and PS20 concentration

In the present subparagraph, the evaluation of product composition concerning the concentrations of Protein, Methionine and Polysorbate 20 is reported. These critical quality attributes (CQAs) are not directly linked to the stress applied to the protein but are relevant to the dilution process that may occur during filtration or compounding. Consequently, the performance parameters estimated for these calculations are presented in **Table *9***.

Table 9: The performance metrics of the models developed, and the validation conducted in the case study for product composition are detailed. Additionally, the model type, Raman shift range, and latent variables are specified.

Model Type	*Range*	*LV*	*RMSEC*	*RMSECV*	*RMSEP*	R^2	Q^2
Model 4	ER	3	0.509	0.632	0.815	0.997	0.990
	RR3		0.460	0.895	0.865	0.997	0.992
Model 5	ER	3	0.101	0.505	-	0.944	-
Model 6	ER	6	0.035	0.049	0.039	0.992	0.975
	RR4		0.035	0.046	0.042	0.992	0.974
Model 7	ER	4	0.161	0.183	0.103	0.928	0.783
	RR5		0.163	0.050	0.091	0.934	0.971

The protein content dataset was divided into two groups: low protein content values ranging from 0.1 mg/ml to 1 mg/ml and high protein content values from 1 mg/ml to 40 mg/ml. Two distinct models were developed: Model 4 corresponds to high protein content values, while Model 5 pertains to low protein content values. Additionally, Model 6 and Model 7 are focused on estimating Methionine and Polysorbate 20 concentrations, respectively. Initially, all PLS models were created using the entire Raman shift range (ER) of 600-3000 cm^{-1}.

In this instance, the appropriate range for model development was also examined. Following a preliminary PLS analysis across the full range of 600-3000 cm^{-1} for each case, the loadings for this composition were analyzed to identify the most significant

signals, which corresponded to the highest (either positive or negative) peaks in the loadings plot shown in ***Figure 35***.

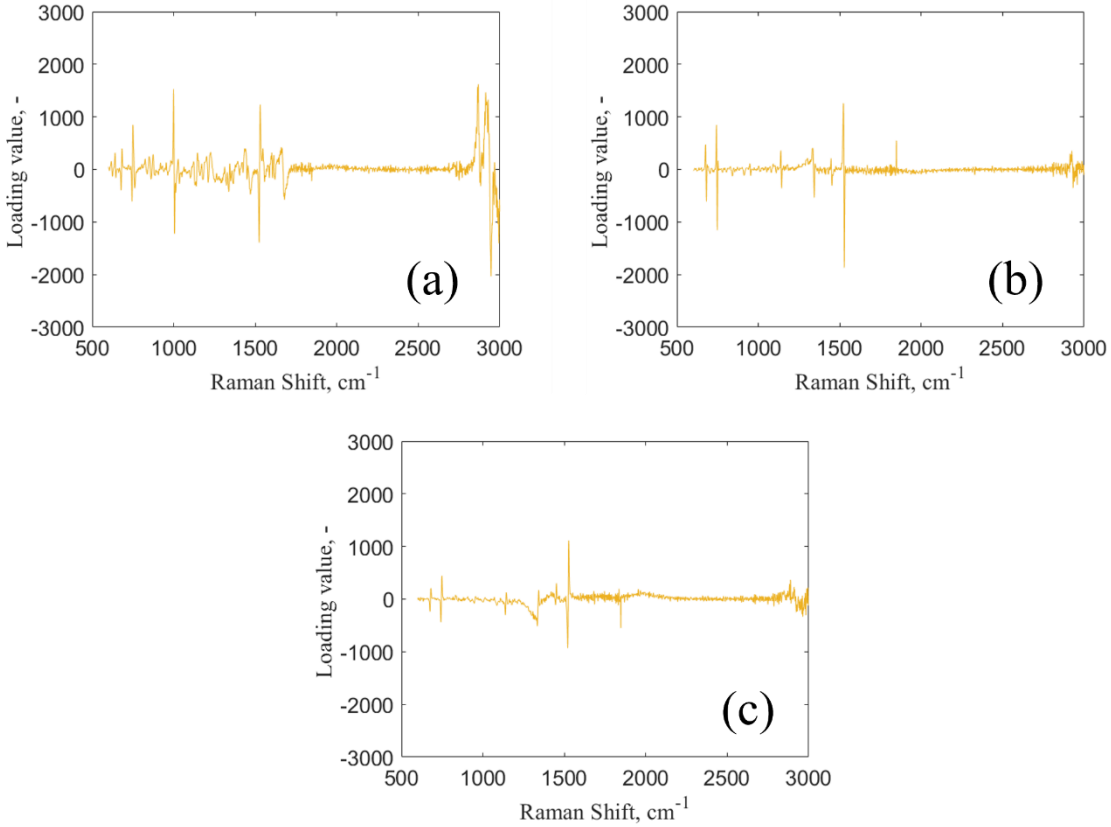

Figure 35: The loadings plot from the PLS decomposition of the dataset is presented for (a) high protein content, (b) methionine content, and (c) Polysorbate 20 (PS20) content across the Raman shift range of 600-3000 cm^{-1}. The loadings for the first latent variable (LV) utilized in the model development are displayed.

The specific ranges explored for the case-study of product composition are named as in the following list:

- Reduced Range 3 (RR3): 2600-3100 cm^{-1};
- Reduced Range 4 (RR4): 520-1530 cm^{-1}.
- Reduced Range 5 (RR5): 1200-1600 cm^{-1}.

The regions of the Raman spectra relevant to each case study vary depending on the dataset being analyzed. For high protein content values (***Figure 35a***), the most significant signals are observed around 2800-3000 cm^{-1}, associated with the C-H stretching of the molecule. A decreasing trend in peak intensity is noted as protein concentration decreases, a finding corroborated by Massei et al (Massei, Falco, & Fissore, 2024). Additionally, signals at 1000 and 1500 cm^{-1} are also influential, linked to C-N bonds and the amide II region, respectively. This latter region contains typical bonds of the protein's secondary

structure, specifically the carbonyl (C=O) and amine (N-H) groups.

In ***Figure 35b***, the key Raman shifts for estimating Methionine content are highlighted. The highest loading value is found around 1500 cm^{-1}, corresponding to CH_2 and S-CH_3 bending vibrations. Peaks in the range of 700-800 cm^{-1}, associated with C-S stretching vibrations, also contribute significantly to the analysis. Furthermore, C-N and C-C stretching vibrations are emphasized in the region between 1000 and 1400 cm^{-1}.

For Polysorbate 20 (PS20) content, ***Figure 35c*** identifies the Raman shift around 1500 cm^{-1} as the most significant, primarily related to CH_2 bending vibrations. Peaks in the 1200-1300 cm^{-1} range also exhibit high loading values, primarily associated with C-H bending vibrations. At higher Raman shifts, the trend of the loadings appears flat, prompting the decision to remove this region and narrow the range to 1200-1600 cm^{-1} to enhance the performance of the model developed for PS20 estimation.

The parity plots generated using the full Raman shift range, which relate the measured high Protein, Methionine, and Polysorbate 20 content to the predicted concentration values predicted by the model, are reported in ***Figure* 36** both for the calibration and prediction set. The trends for Protein and Methionine content shown in ***Figure* 36*a***, ***40b***, ***40c***, and ***40d*** indicate a strong correlation between the measured and predicted values. This is further supported by the similar RMSEC and RMSECV values: 0.509 and 0.632 for high Protein content, and 0.035 and 0.049 for Methionine content. The robustness of these two models is also demonstrated by the RMSEP values, which are 0.815 for high Protein content and 0.039 for Methionine content. In contrast, the trend for Polysorbate 20 concentration at high values in the calibration set (***Figure* 36*e***) appeared less favorable. However, in the prediction set, the trend at high concentration values showed improvement, resulting in a commendable RMSEP value of 0.103.

For the PLS models developed on the reduced ranges, the acceptance criteria for the case study are presented in ***Figure 37***. In the context of high protein content values, a slight improvement is observed in the calibration set, with an RMSEC of 0.460 compared to 0.509 for the entire range (ER). However, there is a decline in the prediction set, where the RMSEP is 0.865 versus 0.815 for the ER.

When comparing the performance of the reduced range models to those of the entire range, as illustrated in ***Figure 38***, it is noted that one point in the calibration set reached a CV% of 19%. Nevertheless, all other points remained below the acceptance criteria, indicating that the model's performance did not surpass that of the model developed using

the full range. This may be attributed to the loadings plot shown in ***Figure 38a***, which reveals significant signals in the amide regions at Raman shifts lower than those included in the reduced range.

Similarly, for the assessment of Methionine concentration, the model evaluated within the reduced range did not yield any improvements. The RMSEC, RMSECV, and RMSEP values are nearly identical to those obtained from the entire range, as shown in **Table *9***. Additionally, ***Figure 37b*** and ***Figure 38b*** indicate comparable CV% values.

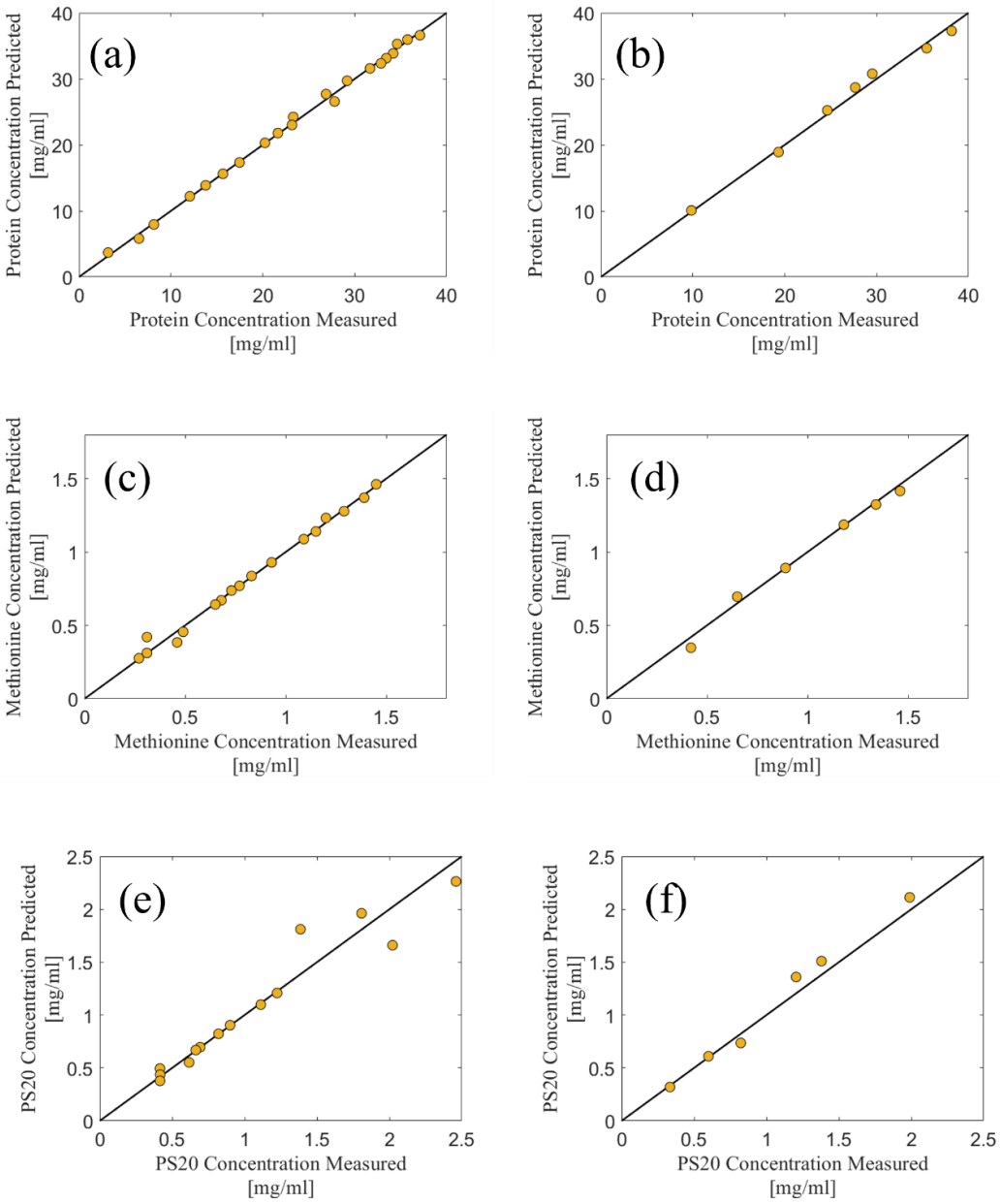

Figure 36: Parity diagrams comparing the measured Protein, Methionine, and PS20 content to the predicted values are presented, derived from the calibration (a, c, e) and prediction (b, d, f) sets of diluted samples processed using the PLS model across the full Raman shift range (600-3000 cm^{-1}). Specifically, graphs (a) and (b) correspond to high Protein content values, (c) and (d) pertain to Methionine content, and (e) and (f) relate to PS20 content.

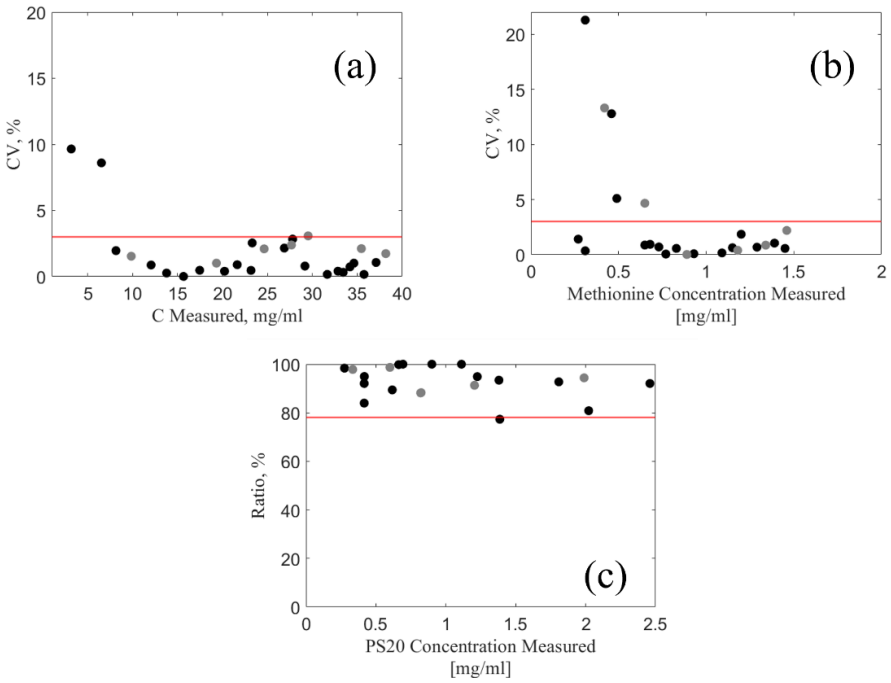

***Figure 37*:** The acceptance criteria are presented as the Coefficient of Variation or the ratio between the minimum and maximum concentrations of PS20, plotted against the measured concentrations of: (a) high Protein content, (b) Methionine, and (c) PS20 for the data processed in the reduced ranges RR3, RR4, and RR5.

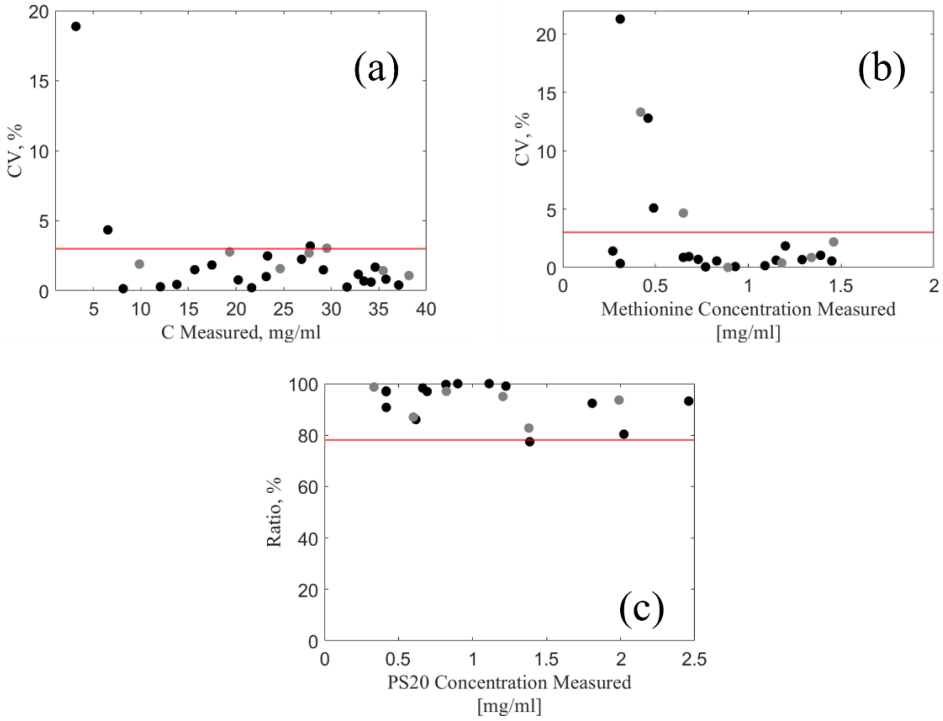

Figure 38: The acceptance criteria are presented as the Coefficient of Variation or the ratio between the minimum and maximum concentrations of PS20, plotted against the measured concentrations of: (a) high Protein content, (b) Methionine, and (c) PS20 for the data processed across the entire ranges.

In contrast, when estimating the concentration of PS20, narrowing the range of Raman shifts led to improved performance in the prediction set, with RMSECV and RMSEP

values of 0.050 and 0.091, respectively. Additionally, the Q^2 value for the reduced range surpassed that of the entire range, measuring 0.971 compared to 0.783. Consequently, a reduced model is recommended for evaluating PS20 concentration.

As previously noted, it was not feasible to create a single model for predicting Protein concentration; therefore, the dataset was divided into high and low concentration values. Analyzing the loadings plots presented in ***Figure 35a*** and ***Figure 39*** reveals that the influential signals associated with the two dilution phenomena differ. Specifically, for low protein concentrations, the signals related to C-H bonds are minimal, whereas for high concentrations, the signals with the highest loadings are the most significant.

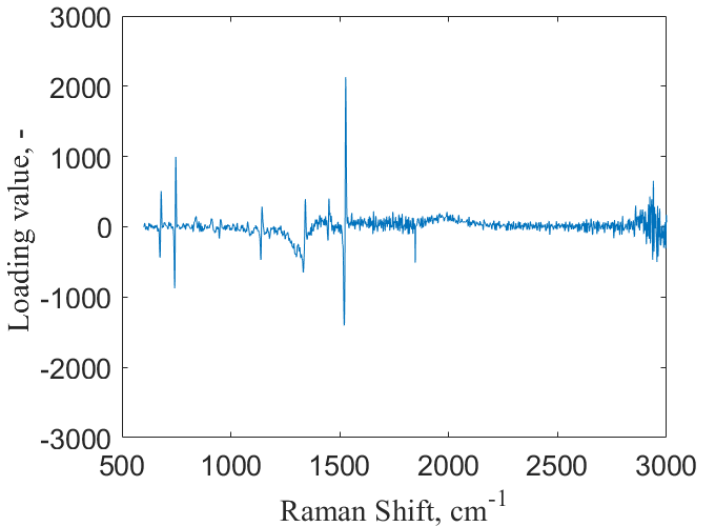

Figure 39: The loadings plot from the PLS decomposition of the low protein content dataset is displayed across the Raman shift range of 600-3000 cm^{-1}. This plot illustrates the loadings for the first latent variable (LV) used in the development of the models.

Nonetheless, a model was developed using the entire range by including all points in the calibration set, given the small size of the dataset. The resulting RMSEC and RMSECV values were 0.101 and 0.505, respectively, with the parity plot for the calibration set shown in ***Figure 40***. Additional data points within this concentration range could be collected to enhance the model's performance.

To further validate the findings, an equivalence test (t-test) was performed on samples characterized by high Protein content, high HMW%, LMW%, and Methionine concentration values, utilizing data obtained from the entire Raman shift range. Equivalence was established in all instances, as illustrated in ***Figure 41***. The confidence interval is entirely contained within the equivalence limits, allowing us to conclude that the mean of the test population is equivalent to the mean of the reference population.

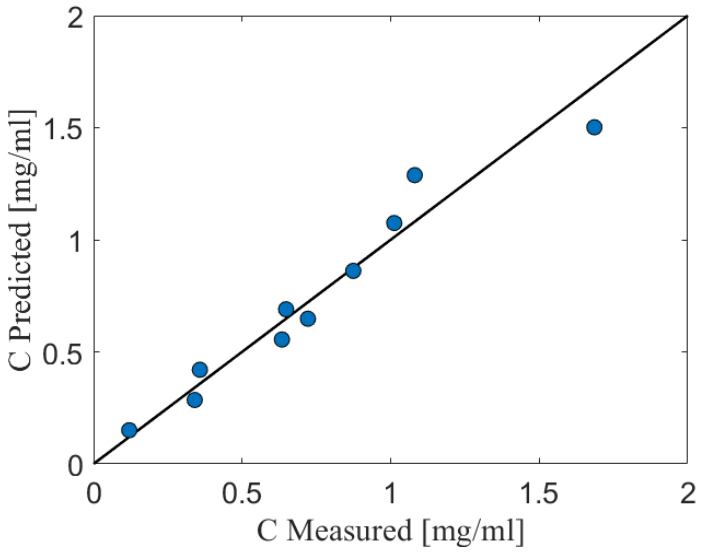

Figure 40: Parity diagram relating the low protein content measured vs low protein content predicted, obtained using the calibration set processed by PLS model on the entire range of Raman shift (600-3000 cm^{-1}).

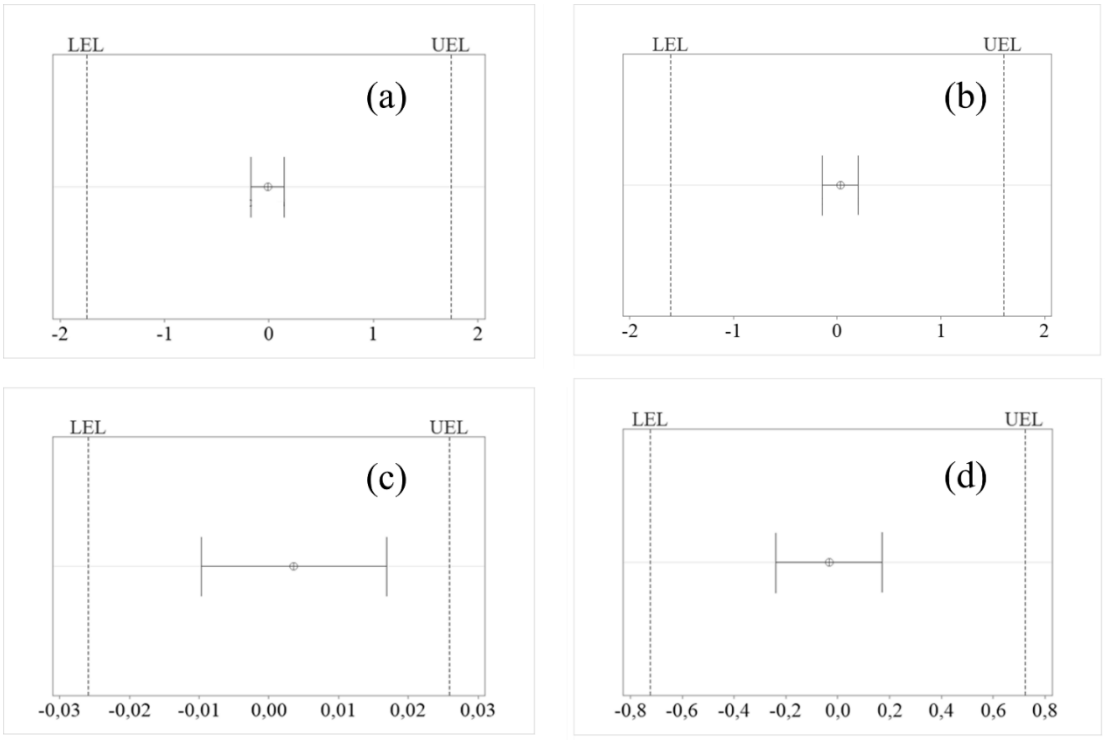

Figure 41: Equivalence test results obtained by processing the data using Minitab software for: (a) high HMW%, (b) LMW%, (c) Methionine concentration samples and (d) high Protein content.

5.4.3 Real case-study: application on the freeze-dried mAb

Model 2 was applied to the *Formulation 1* after it underwent the freeze-drying process to determine whether the process itself had an impact on the aggregation level or protein content (being the CQAs usually mostly influenced by freeze-drying). The comparison with the HMW% value measured by the SE-HPLC and the protein content measured by Solo VPE was performed to assess the precision of the model. In the case of HMW%, the same values observed for the liquid formulation prior to thermal stress were replicated. All the points were well below the specification limit imposed by the company, as shown in **Figure 42,** highlighting the robustness of the developed model.

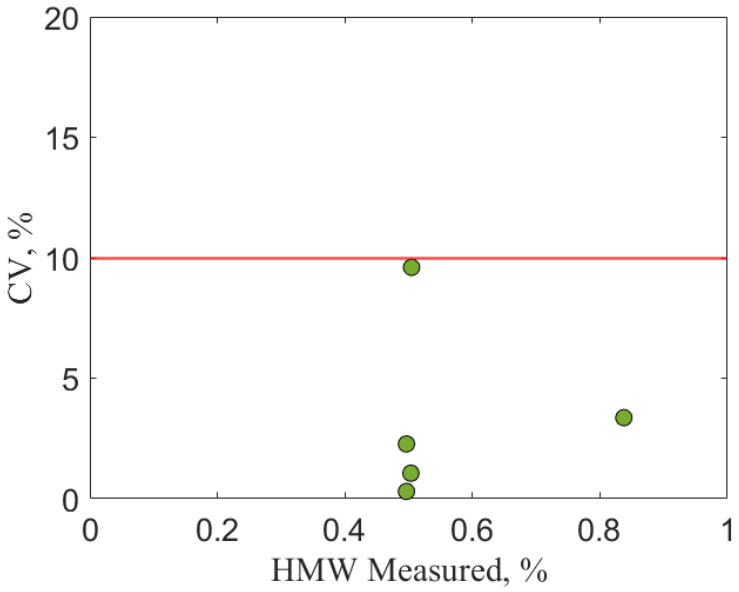

Figure 42: The acceptance criteria are presented as the Coefficient of Variation plotted against the measured aggregation level by SE-HPLC for the data processed across the entire ranges using the Model 2.

On the contrary, in case of protein content, higher errors were obtained. This could be reasonable since the model was developed on *Formulation 2* which also contains arginine inside and is more concentrated. Some improvements in the CV% calculation were made by using a Multiplicative Scatter Correction (MSC) as pretreatment. In **Table 10** the results in the two cases are reported:

Table 10: Acceptance criteria in terms of CV% obtained in the freeze-dried Formulation 1 samples. The PLS model developed using two different pretreatments are reported: 1st derivative + SG filter and MSC + SG filter.

Samples	*Protein Concentration by Solo VPE [mg/ml]*	*CV% (from 1st derivative + SG filter data)*	*CV% (from MSC + SG filter data)*
1	10.27	15.51	14.78
2	10.21	11.34	5.41
3	10.39	9.78	0.51
4	10.26	6.60	1.86
5	10.17	10.53	5.68

However, it must be remarked that the different formulation compositions can have a great impact on the values obtained and the residual error could be attributed to this.

5.5 Highlights

This PLS-based application coupled with Raman spectroscopy could be helpful to quantify CQAs of biopharmaceutical formulation in the perspective of process validation activities. Various PLS models were developed to monitor protein structural analyses, specifically focusing on aggregation and fragmentation levels, as well as product composition, including Protein, Methionine, and Polysorbate concentrations. These models were designed for potential application during the process development stage, with different Raman shift ranges considered based on the signals identified in the loadings plots. Notably, most models performed effectively when utilizing the entire Raman shift range.

The information derived from these models correlates well with conventional analytical techniques currently employed to assess the various CQAs of interest. However, the model developed for estimating oxidation levels did not yield satisfactory results, likely due to limitations in the quality of the dataset. This highlights the need for further investigation to ascertain whether Raman spectroscopy can reliably monitor oxidation phenomena.

Overall, the findings underscore the applicability and sensitivity of Raman spectroscopy in detecting structural changes resulting from the forced degradation of monoclonal antibodies (mAbs) and in analyzing product compositions in at-line applications. Raman

spectroscopy offers significant advantages over traditional methods such as chromatography and electrophoresis, particularly regarding sample preparation and the time required for analysis. This efficiency enhances analytical operations and facilitates cost-effective monitoring of CQAs throughout a product's lifecycle.

The PLS models were developed and tested using a single formulation, and their generalization to different formulations for HMW%, LMW%, methionine and PS20 was not explored in this Thesis. In contrast, the protein content model was developed using *Formulation 2* and tested with *Formulation 1,* resulting in significant prediction errors. Therefore, these findings indicate that a formulation-specific model must be established within the appropriate ranges of Raman shift. Moreover, *Model 2,* which has been developed on liquid samples from *Formulation 1,* demonstrated effective predictive capabilities for *Formulation 1* samples after they underwent the freeze-drying process. This highlights the potential to implement Raman spectroscopy following the reconstitution of freeze-dried products without necessitating additional efforts in model development.

Another noteworthy benefit of Raman spectroscopy is its ability to quantify multiple CQAs from a single spectrum, thereby significantly reducing the time needed for analytical assessments. For instance, from the single matrix obtained from thermally stressed samples, both aggregation and fragmentation levels were evaluated.

The spectral characteristics associated with these structural changes, as well as the concentrations of proteins and excipients, can be harnessed to develop in-line analytics for therapeutic mAbs, particularly in the context of Process Analytical Technology (PAT) applications. This capability could enable real-time monitoring and adjustments to the manufacturing process, ultimately enhancing product quality and consistency.

CHAPTER 6

Some results presented in this Chapter have been already published in a peer-reviewed journal (Massei, Falco, & Fissore, 2023).

6. Estimation of residual moisture in freeze-dried products

6.1 Introduction

During the fill and finish process of a solid drug, freeze-drying is a crucial step as it provides long-term stability by removing most of the water present in the product by sublimation, converting the ice into vapor, by operating at low pressure and temperature. The low operating temperatures make this process especially ideal for heat-sensitive products, such as pharmaceuticals. (Fissore D. , 2013) The residual moisture (RM) is one of the main CQA to monitor to assess the quality of the product, as described in Chapter 1. The most used method to measure RM in freeze-dried products is the Karl Fisher (KF) titration, which has a lot of disadvantages, such as it is a destructive method, so the samples analyzed are wasted, turning out as an economic loss for the company income. It is time-consuming, since handling of the sample is required, and the instrument must be calibrated before each analytical session. Moreover, safety issues for operators are not negligible, since polluting reactants (formamide and methanol) are involved (Connors, 1988) (European Pharmacopeia 8th edition, 2013)

In the perspective of PAT tools, Near-Infrared (NIR) spectroscopy was investigated a lot as one of the most powerful tools to evaluate residual moisture in freeze-dried products due to the strong absorption of water around 5150 cm^{-1}, NIR spectroscopy was widely used to evaluate RM. (Bobba, Zinfollino, & Fissore, 2022). In fact, it is a rapid, non-invasive method that requires minimal sample pretreatments. Moreover, it allows to measure the RM on majority of the vials within a batch, instead of a fraction of it, for demonstration of batch homogeneity and uniformity.

The main challenging issue is finding a reliable model that allows to evaluate the RM value from the NIR spectra. Most of the published applications for RM determination are focused on the application of Partial Least Squares (PLS) as regression method used in the model development step.

It turned out to be a powerful tool, but it considers only the linear dependence between the spectra and the residual moisture content. To address this issue and to try to improve

the accuracy of the models, machine learning tools, such as artificial neural network, could be a suitable alternative for dealing with complex data. However, the currently accepted method that respects data integrity and GMP compliance in pharmaceutical companies is the PLS regression.

In the present Thesis, a linear regression model and a neural network-based model were developed to evaluate the RM values in freeze-dried products starting from NIR spectra. The performances of the two models were compared by calculating the RMSE value and plotting the parity diagrams. The purposes of this Chapter are the followings:

- Demonstrate the feasibility of the application of neural networks for RM estimation and compare its performance to the one of the linear models.
- Prove the robustness and the ability of the neural network-based model to predict RM values of products not involved in the calibration step. The effect of reducing the size of the training step on the model performance was also investigated.
- Use the model developed on a placebo (without API) to predict the RM of a drug product with the aim of reducing experimental effort and costs associated to model development.

6.2 Case-study

Freeze-drying cycles were performed in the laboratories of the Guidonia Montecelio (Italy) site of Merck Serono S.p.A using a lab-scale freeze-drier (Lyostar3, SP Scientific, Warminster, USA). The dataset obtained by Bobba et al. [187] was enhanced by conducting additional tests under the same operating conditions. Other experimental data were sourced from the previously published study. (Bobba, Zinfollino, & Fissore, 2022) For sample preparation, seven different aqueous solutions were freeze-dried in 2R glass vials (Nuova Ompi, Piombino Dese, Italy) with a filling volume of 1 mL. The type and the number of samples are reported in **Table 11**.

Table 11: Type and number of samples generated for the case-study.

Data set	*Formulation*	*N° Samples*
S6	Sucrose 6%	91
T6	Trehalose 6%	45
S3	Sucrose 3%	63
S9	Sucrose 9%	36
SA05	Sucrose 6% + Arginine 0.5%	30
SA1	Sucrose 6% + Arginine 1%	28
SA3	Sucrose 3% + Arginine 3%	31

Vials were arranged in a honeycomb pattern and surrounded by metal frames, ensuring direct contact with the freeze-dryer shelves. The process conditions for the freeze-drying cycle were consistent with those used by Bobba et al. (Bobba, Zinfollino, & Fissore, 2022), which are detailed in ***Table 12*** for the sake of clarity.

Table 12: Process conditions of the freeze-drying cycle for producing other samples to be added to the dataset by Bobba et al. [187]

Step	*Freezing*	*Annealing*	*Primary drying*	*Secondary drying*
Rate [°C/min]	-2	-2	+2	+1
T_f [°C]	-45	-15	-25	+35
P_c [Pa]	atm	atm	5	5
Holding time [h]	6	2	30	10

After the freeze-drying cycle, to explore a wider range of moisture in the samples, different amount of water were added in the stopper of each vial, which was closed upside-down for a night, to get values of RM in the range 1% – 5%. Then, NIR spectra were acquired for each sample, according to the setup presented in Section 3.2.3. Once spectra were collected, all samples were tested by KF titrations, following the internal Standard Operative Procedure (SOP) of the company, to get the reference value of RM.

All samples presented in ***Table 11*** may be considered as products, indicating that they do not contain the API. One of the objectives of this Thesis is, in fact, to demonstrate the applicability of a surrogate-based model in a real drug product, particularly by focusing on the wavelength range specific of water component. Consequently, a new freeze-drying cycle was conducted on the *Formulation 1* product, in accordance with the company's internal recipe. Five vials were analyzed using both NIR spectroscopy and KF titration to

externally validate the robustness of the model. Given that the mAb formulation primarily consists of trehalose, a PLS model was developed on T6 dataset using SIMCA software, being GMP compliance. The choice of the PLS model with respect to ANN relies on the fact that this is accepted by the GMP compliance in the company and respects the data integrity requirements.

6.3 Data processing

The raw NIR spectra underwent to Standard Normal Variate (SNV) correction to obtain good quality spectra to be used for modeling purposes. Upon examining the full wavelength's spectra, it was observed that the trend remains constant for wavenumber values exceeding 7000 cm^{-1}. Therefore, the wavelength range used for model development was narrowed to 7000 − 4250 cm^{-1}, according to the findings of Bobba et al. However, most of the information related to water content are found in the region around 5150 cm^{-1}. (Bobba, Zinfollino, & Fissore, 2022)

6.3.1 Analysis of the NIR spectra

The spectra of the different formulations within the range related to the water signal are presented in ***Figure 43*** and ***Figure 44***. The spectra are colored according to the excipient present in the formulation: in orange all the spectra containing sucrose are reported, in violet the ones containing trehalose, while in green the mixtures arginine-sucrose are depicted.

The signals characteristics of water were detected in the O–H stretching and H–O–H bending bands at approximately 5150 cm^{-1}. Additionally, an overtone of O–H stretch was observed at around 6900 cm^{-1}. As previously mentioned, the majority of the spectral information was identified in the region between 4250 and 7000 cm^{-1}, where signals specific to the analyzed product were noted. For instance, in the range between 4000 and 4500 cm^{-1}, sucrose exhibited a peak associated with C–H stretching. A similar observation was made for trehalose. In contrast, the spectra of the sucrose-arginine mixtures indicated that as the concentration of arginine increases (expressed as a percentage of the total solid fraction), the peak in the water region diminished, while a new peak specific to arginine product emerged at around 4900 cm^{-1}, as shown in ***Figure 44c***.

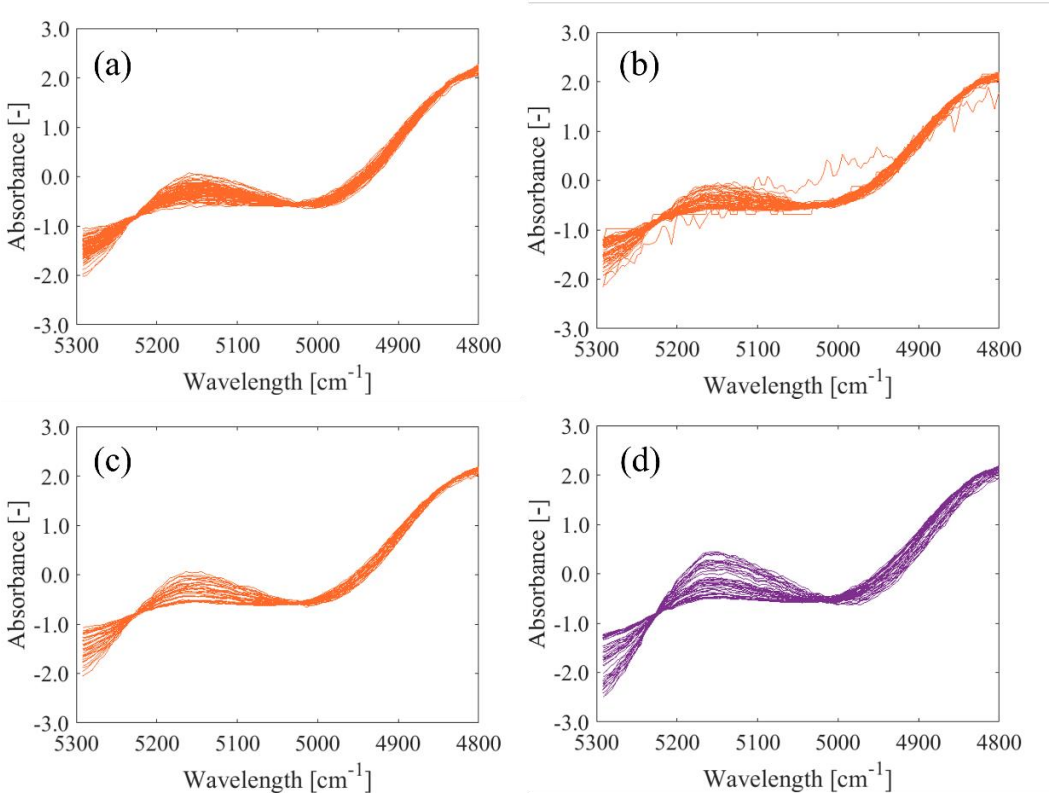

Figure 43: Spectra of sucrose and trehalose-based formulations after SNV pretreatments. In orange, the sucrose-based solutions at different concentrations are reported: (a) S6, (b) S3 and (c) S9, while in violet (d) the T6 dataset is shown.

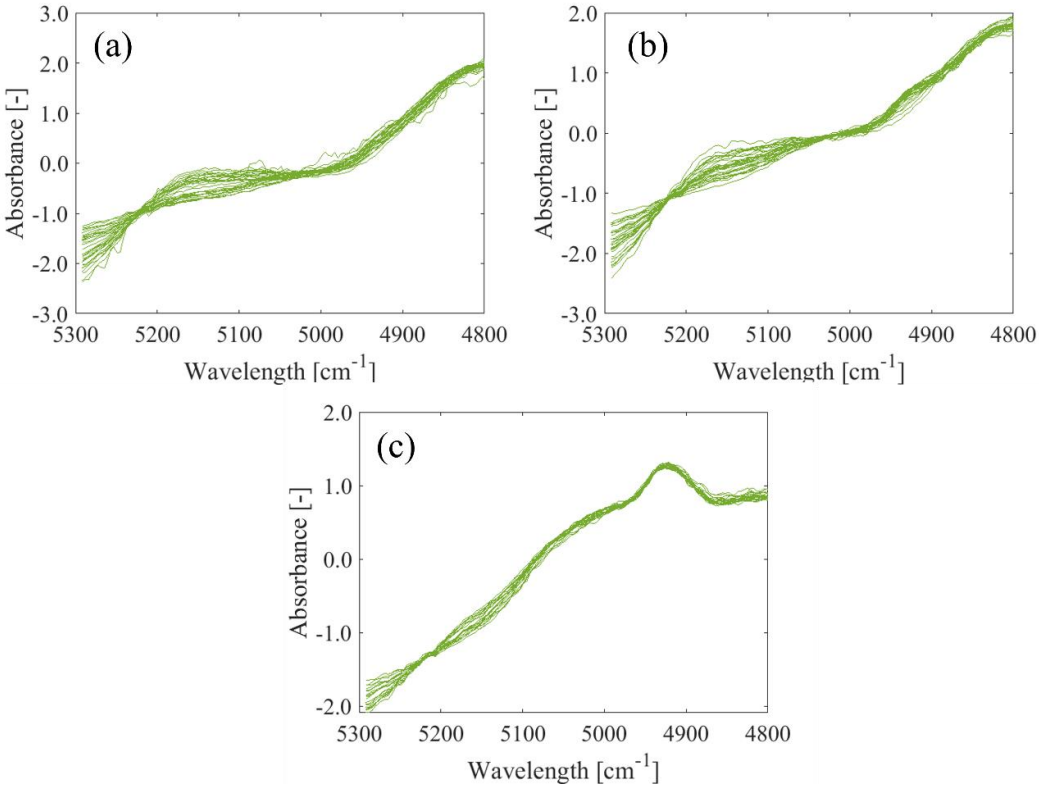

Figure 44: Spectra of arginine-based formulations after SNV pretreatments: (a) SA05, (b) SA1 and (c) SA3 dataset.

Considering all these findings, two different wavelengths ranges were examined:

- Small Range (SR): the focus was on the region 5290–4787 cm^{-1}, containing the peak of water at approximately 5150 cm^{-1}. According to previous literature works, in this way the model would me more robust since the specific peaks of products are less considered. (Bobba, Zinfollino, & Fissore, 2022)
- Wide Range (WR): the focus was on the region 7100–4250 cm^{-1}, also including the peaks characteristics of the different excipients present in the formulations.

Matlab scripts, SIMCA and Minitab software were used to process the data.

6.3.2 Models' development and comparison

The neural network was developed using Matlab (R2019b) software by exploiting the *Neural Net Fitting Toolbox* in the following steps:

- The dataset was divided into training and test set.
- The number of neurons in the hidden layer was determined through trial and error to optimize the model's performances. The optimal configuration identified was two hidden layers containing 10 and 5 neurons, respectively.
- The Levenberg-Maqruardt algorithm as training function.
- The hyperbolic tangent, defined as "*tansig",* was used as transfer function for all the hidden layers.
- A PCA was applied to the data as preprocessing technique using the command "*processpca"* and all data were normalized to fall in the range [-1,1] using the command "*mapminmax".*
- During the training phase, neural networks acquired knowledge by iteratively performing forward and backward propagation for each input variable across multiple epochs, adjusting the parameter values accordingly. The training process concluded when one of the following conditions was met: the maximum number of epochs (set equal to 1000) was reached, the performance gradient dropped below a predefined threshold, or the validation performance improved beyond the specified maximum allowable failures (set as 6).

Different models were developed:

1) *Model S6:* the reference product was considered as the dataset S6 (due to the larger amount of data available), which was used to develop and conduct an internal validation of the model. All the remaining datasets (S3, S9, SA05,

SA1, SA3 and T6) were used as external validation set. This model aimed to operate in the perspective of reducing the experimental effort and laboratory testing needed to develop it. Indeed, it would be great to obtain a model able to accurately predict values of RM of formulations not included in the calibration phase. If the spectra of the formulations are similar, this scope can be achieved. The percentages of the training set were changed during the analysis from 70 % up to 40 % to assess the robustness of the developed model.

2) *Ad – Hoc Models:* no good results were obtained using sucrose-arginine mixture as external set with the Model S6. Therefore, two ad hoc models were developed to understand if the acquired spectra were of good quality.
3) *Global Model (GM):* a single dataset, comprising a specific percentage of all available datasets, was used in the calibration phase. Additionally, in this analysis, the proportion of the training set was varied from 70 % to 40 % to assess any potential decline in performance when reducing the number of experiments needed for model development. As nonlinear tools, neural networks are particularly advantageous for managing large and diverse datasets compared to linear models.
4) *Model T6:* A PLS model was developed using T6 dataset all in the calibration phase. This model aimed to demonstrate its applicability to predict the RM of a real drug product (Formulation 1), mainly containing trehalose as excipient. This could be useful in the perspective of cost-reduction since the model could be developed using only the placebo, without consuming the API. The choice of the PLS algorithm with respect to ANN relies on the fact that PLS is accepted by regulatory authorities being included in the SIMCA software, that is GMP compliance.

For models described at bullet point 1, 2 and 3, both neural network and linear regression algorithms were developed and compared.

As a graphical outcome, the parity plots, which correlate the RM values calculated by the model (y-axis) with the RM values measured by KF (x-axis), were used to compare the performances of the models. It has been also useful to report the diagrams that correlate the absolute error (%) with the RM values measured by KF. An arbitrary threshold for this absolute error (difference between residual moisture calculated and measured by KF)

equal to 0.5 % (indicated by a black line in the following graphs) was chosen. Ideally the value of absolute error should be zero, but this is (obviously) quite impossible. Therefore, a slightly little discrepancy between the two instruments (NIR and KF) had to be set, and the value of 0.5 % was considered adequate in this study. In this framework it must be considered that also KF titration is affected by an error, that may be considered equal to 0.3 %. Therefore, when using NIRs for RM estimation we do not know if the error is due just to the ANN model or also to KF: it can be considered this occurrence by setting a lower target value of RM.

6.4 Results

The RMSE, considering both calibration and validation set, calculated for the models cited above are grouped in ***Table 13*** and ***Table 14*** will be discussed in the next sections.

Table 13: RMSE calculated for Model S6 and the Global Model within the wavelength ranges of SR or WR, utilizing either the linear model (LR) or the neural network (NN).

	Model S6 SR		***Global Model SR***		***Model S6 WR***		***Global Model WR***	
Dataset	*RMSE LR*	*RMSE NN*	*RMSE LR*	*RMSE NN*	*RMSE LR*	*RMSE NN*	*RMSE LR*	*RMSE NN*
S6	0.122	0.172	0.358	0.213	0.066	0.156	0.133	0.167
S3	0.519	0.446	0.493	0.295	0.509	0.681	0.269	0.298
S9	0.774	0.305	0.444	0.309	0.539	0.296	0.249	0.259
SA05	0.873	0.554	0.658	0.356	0.765	0.643	0.426	0.367
SA1	0.707	0.351	0.436	0.387	0.583	0.803	0.269	0.573
SA3	0.519	0.572	0.352	0.173	0.514	0.963	0.367	0.318
T6	0.334	0.199	0.325	0.181	0.773	0.338	0.283	0.249

Table 14: RMSE calculated for the LR and NN models in the context of ad hoc models for arginine-sucrose and trehalose formulations. All reported results were derived from SR.

	Ad-hoc Model for Arginine-Sucrose		***Ad-hoc Model for Trehalose***	
Dataset	*RMSE LR*	*RMSE NN*	*RMSE LR*	*RMSE NN*
SA05	0.288	0.233	-	-
SA1	0.336	0.229	-	-
SA3	0.227	0.115	-	-
T6	-	-	0.334	0.199

6.4.1 Model S6

Model S6 was developed and tested using both the SR and WR wavelength ranges. The development process involved dividing the S6 dataset into two segments: 70% was allocated as the training set (comprising 64 samples), while the remaining 30% was designated as the test set (comprising 27 samples). This division was executed to ensure that all RM values were represented in both sets. Additionally, the external datasets S3, S9, SA05, SA1, SA3 and T6 were used to assess the robustness of the model.

Figure 45 displays parity plots comparing the RM values calculated by the model as a function of those measured using the reference method, the KF titration. The upper part of the graph, on the right (***Figure 45a***), illustrates results obtained through linear model; while, on the left (***Figure 45b***), results obtained with the neural network are presented. Ideally, all points should align with the bisector, but minor deviations are acceptable due to technical limitations and model-related issues. In this case, since S6 dataset was included in the calibration step, the trend perfectly fitted the points. Also, the absolute error was calculated as the absolute difference between the calculated and the measured value of RM (in %). The red line at 0.5 % was assumed as the limit to assure the applicability of the model. Both the developed models are characterized by a very good accuracy, with 100 % of the points lying below the acceptance threshold, as deeply investigated and reported by Massei et al. (Massei, Falco, & Fissore, 2023)

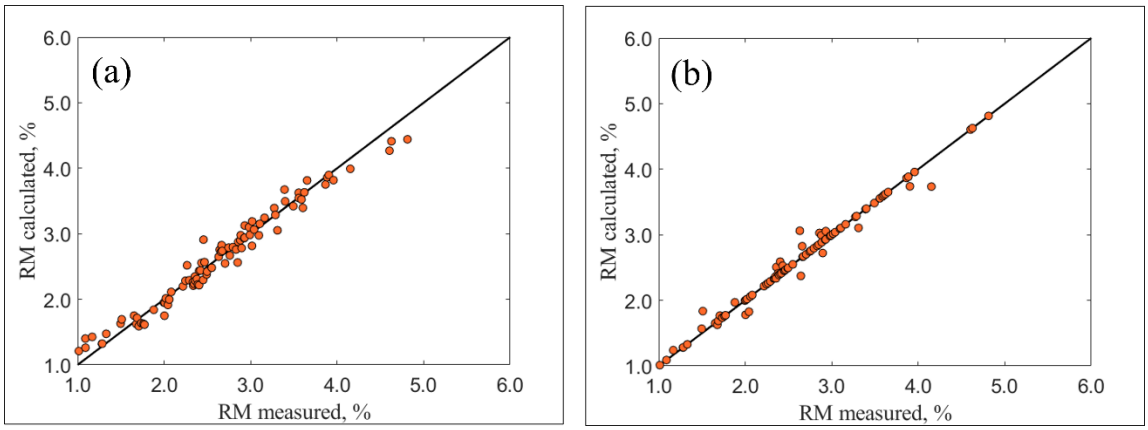

Figure 45: Parity diagrams comparing the RM measured (%) and the RM calculated obtained using the linear regression (b) and the neural network (a) models for dataset S6 for SR.

Based on the data presented in ***Table 13***, the neural network demonstrated lower RMSE values compared to the linear model for small wavelength ranges (SR). Specifically, this superior performance was evidenced by the RMSE values for the arginine-sucrose mixture: for SA05, the neural network exhibited an RMSE value of 0.554, while the linear model recorded an RMSE of 0.873; for SA1, the respective RMSE values were respectively 0.351 and 0.707. The parity diagrams and the absolute error plots are illustrated in ***Figure 46*** and ***Figure 47***.

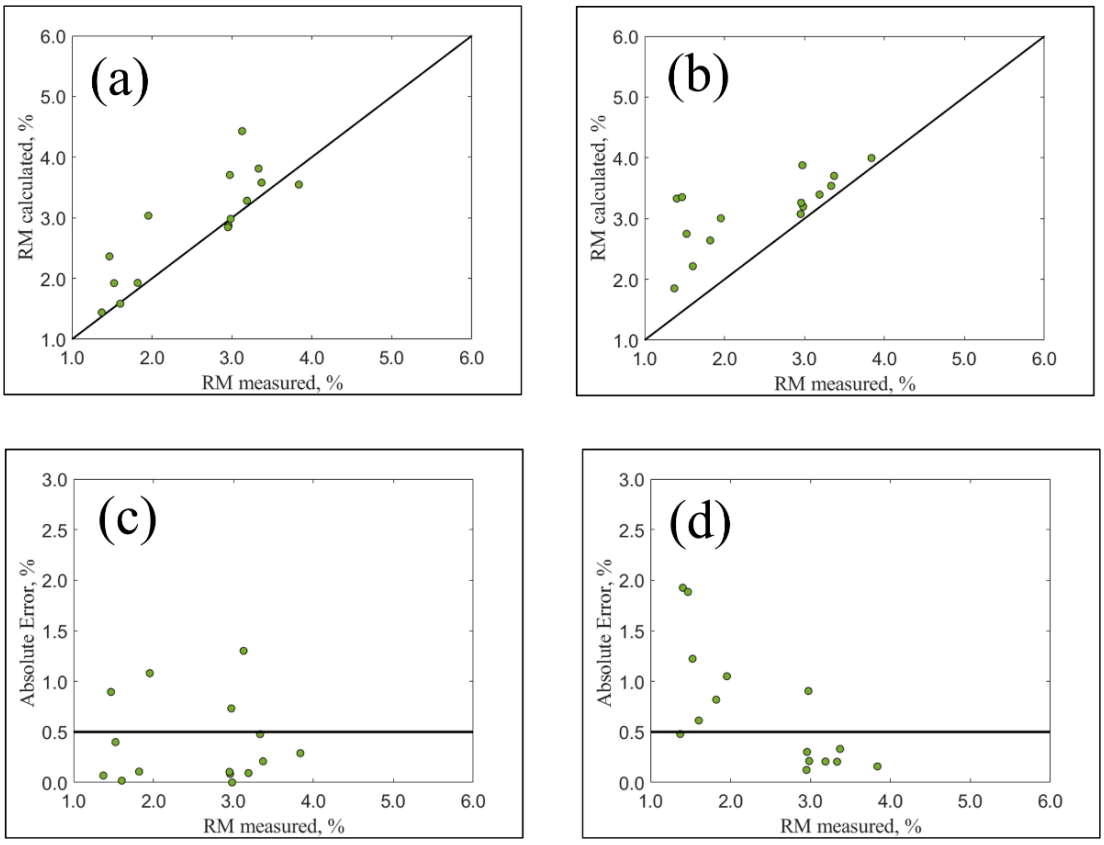

Figure 46: Parity diagrams (a, b) for the SA05 dataset, comparing the measured RM (%) with the calculated RM (%), along with absolute error plots (c, d). These results were obtained using the linear regression (b,

d) and neural network (a, c) models developed with the S6 dataset for the SR wavelength range.

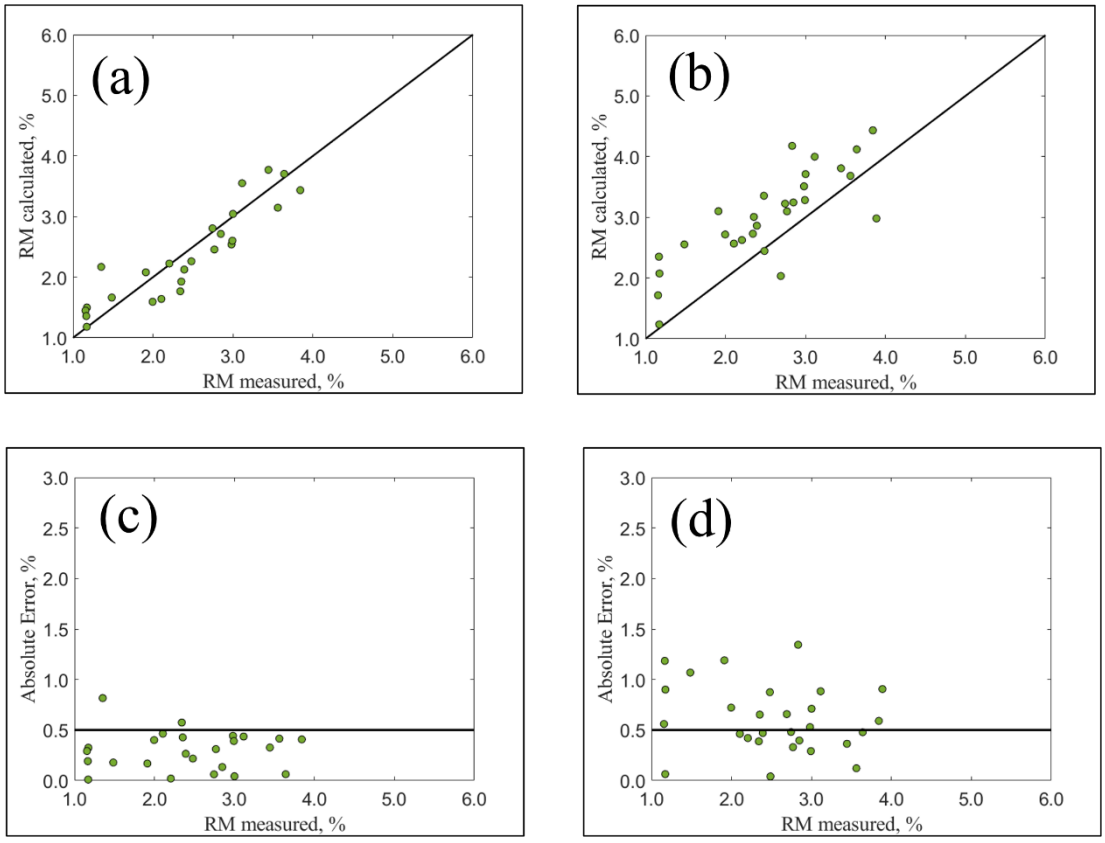

***Figure 47*: Parity diagrams (a, b) for the SA1 dataset, illustrating the comparison between the measured RM (%) and the calculated RM (%), as well as absolute error plots (c, d). These results were derived from the linear regression (b, d) and neural network (a, c) models developed using the S6 dataset for the SR wavelength range.**

For the reasons mentioned in Section 6.3.2, a RMSE value greater than 0.5 is not considered as acceptable. So, the neural network exhibited good accuracy, comparable to the intrinsic error of the analytical method. However, both algorithms, neural network and linear model, struggled to predict the SA3 dataset, which contains the highest percentage of arginine in solution (50 % of the total solid fraction), resulting in RMSE values of 0.572 and 0.519, respectively. The spectra of the sucrose solution, used for model calibration, significantly differ from those of sucrose-arginine mixture at higher concentrations. Notably, the presence of arginine resulted in the disappearance water specific peak at 5150 cm^{-1}, as illustrated in ***Figure 44***. Given that the model was evaluated in the SR wavelength range, which is sensitive to the water peak, these results were deemed reasonable. The poor performance of the models was further confirmed by the absolute error plots shown in ***Figure 48***, where almost half of the points are above the acceptance threshold (black line).

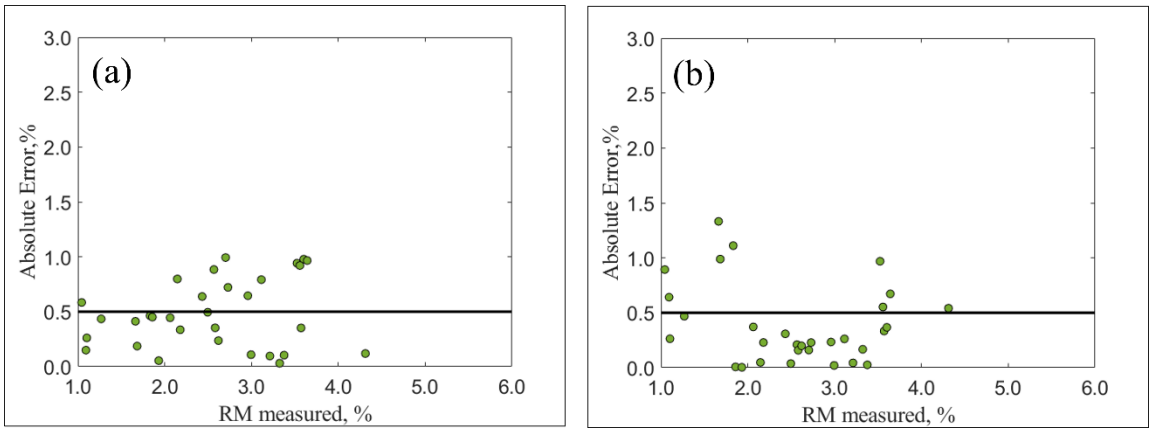

***Figure 48*:** Comparison between the absolute error plots obtained for SA3 dataset in case of linear regression (b) and neural network (a) models developed with S6 database are used for SR.

Neural network also provided a superior description of the datasets with varying sucrose percentages, specifically dataset S9 (for SR). The most significant disparity was observed in the prediction of the S9 dataset, which had the highest sucrose concentration, yielding RMSE values of 0.305 for the neural network and 0.774 for the linear model. The spectra of S6, S3 and S9 were similar, as reported in ***Figure 43***.

Nevertheless, minor differences resulting from varying sucrose concentrations in water caused the linear model to perform less effectively than the neural network. These observations were supported by the absolute error plots for S9 dataset presented in ***Figure 49c*** and ***Figure 49d.*** In the case of the neural network, only 9% of the samples surpassed the acceptance threshold (indicated by the black line), whereas for the linear regression model, 40% of the samples exceeded this threshold, indicating the linear model's limited predictive capability. For the S3 dataset the performances of the two models are comparable, as evidenced by the results reported in ***Table 13***. In fact, the calculated RMSE value for the neural network was 0.446, compared to 0.519 of the linear model.

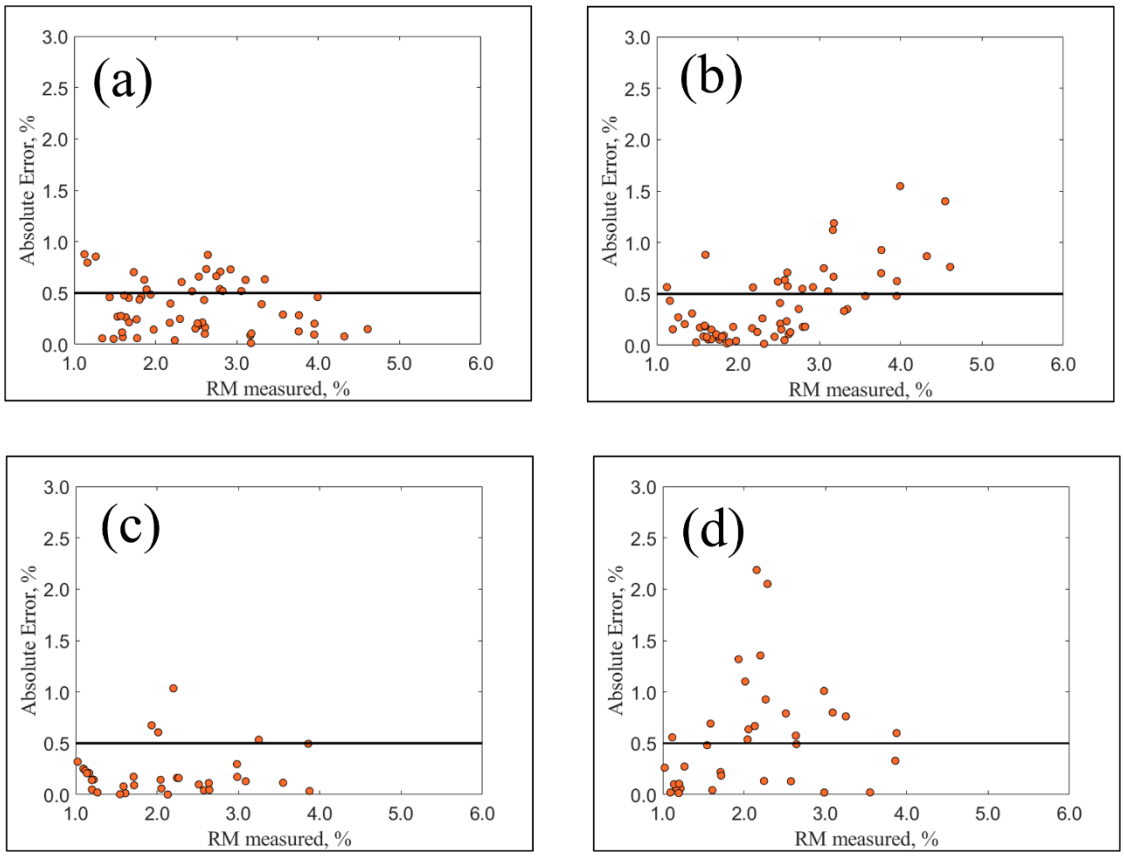

Figure 49: Absolute error plots of dataset S3 (a,b) and S9 (c,d) obtained using the linear regression (b,d) and the neural network (a, c) models developed using dataset S6 for SR.

Similar observations were made for the trehalose formulation, T6 (SR). The spectrum exhibited a shape comparable to that of the S6 dataset. Consequently, the neural network achieved an accurate RMSE value of 0.199. In contrast, the linear regression yielded a less accurate, yet still acceptable, RMSE of 0.334. The parity diagrams plots, confirming the excellent performances of both models, are presented in ***Figure 50***. Small deviations from the bisector are found at higher values of RM. This could be reasonable since the model was calibrated with only few points in that range.

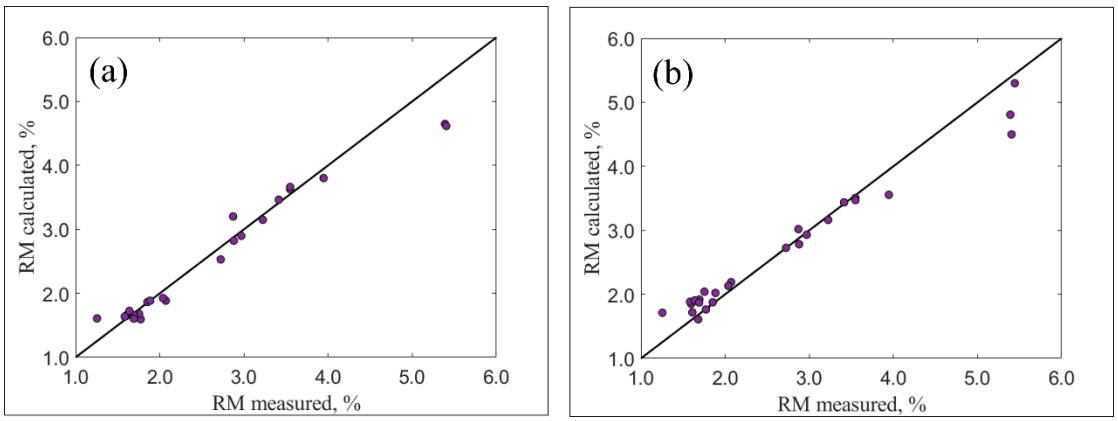

Figure 50: Parity diagrams of dataset T6 comparing the RM measured (%) and the RM calculated obtained using the linear regression (b) and the neural network (a) models developed using dataset S6 for SR.

It has to be remarked that the RMSE obtained for the trehalose formulation was slightly higher than that for the S6 dataset (which was 0.172), used during the calibration phase. This indicates that the model, calibrated solely with sucrose as the excipient, is capable of accurately predicting the RM value for a formulation containing a different excipient, such as trehalose, if the focus is done in the specific region where peaks of water are located.

The application of the model across a broader wavelength range resulted in diminished performance for the neural network, as indicated in ***Table 13***. Notably, the prediction for the S6 dataset, which was also part of the calibration phase, demonstrated good accuracy. However, for all other datasets, the RMSE values exceeded the acceptable error thresholds established by the experimental method. This outcome is deemed justifiable, as expanding the wavelength range incorporated additional peaks specific to the formulations.

6.4.2 Ad-hoc models

The unsatisfactory results obtained with Model S6 for predicting the SA3 dataset prompted the development of a specialized model for sucrose-arginine mixtures. This model was created by incorporating a specific percentage of the SA05, SA1, and SA3 datasets during the calibration phase, ensuring that all three formulations containing arginine were included in the training process. Only a narrow wavelength range was analyzed. In this instance, 70% of the dataset was designated as the training set (comprising 62 samples), while the remaining 30% served as the test set (comprising 27 samples). The results are summarized in ***Table 14.***

For the SA3 dataset, the RMSE values were 0.227 for the linear model and 0.146 for the neural network; for SA1, the values were 0.336 and 0.229, respectively, and for SA05, they were 0.287 and 0.233. The performance of the linear model and the neural network appeared to be comparable, which is reasonable given that only a limited number of samples were used in the calibration phase, and they exhibited similar spectral characteristics. The parity diagrams are presented in ***Figure 51***.

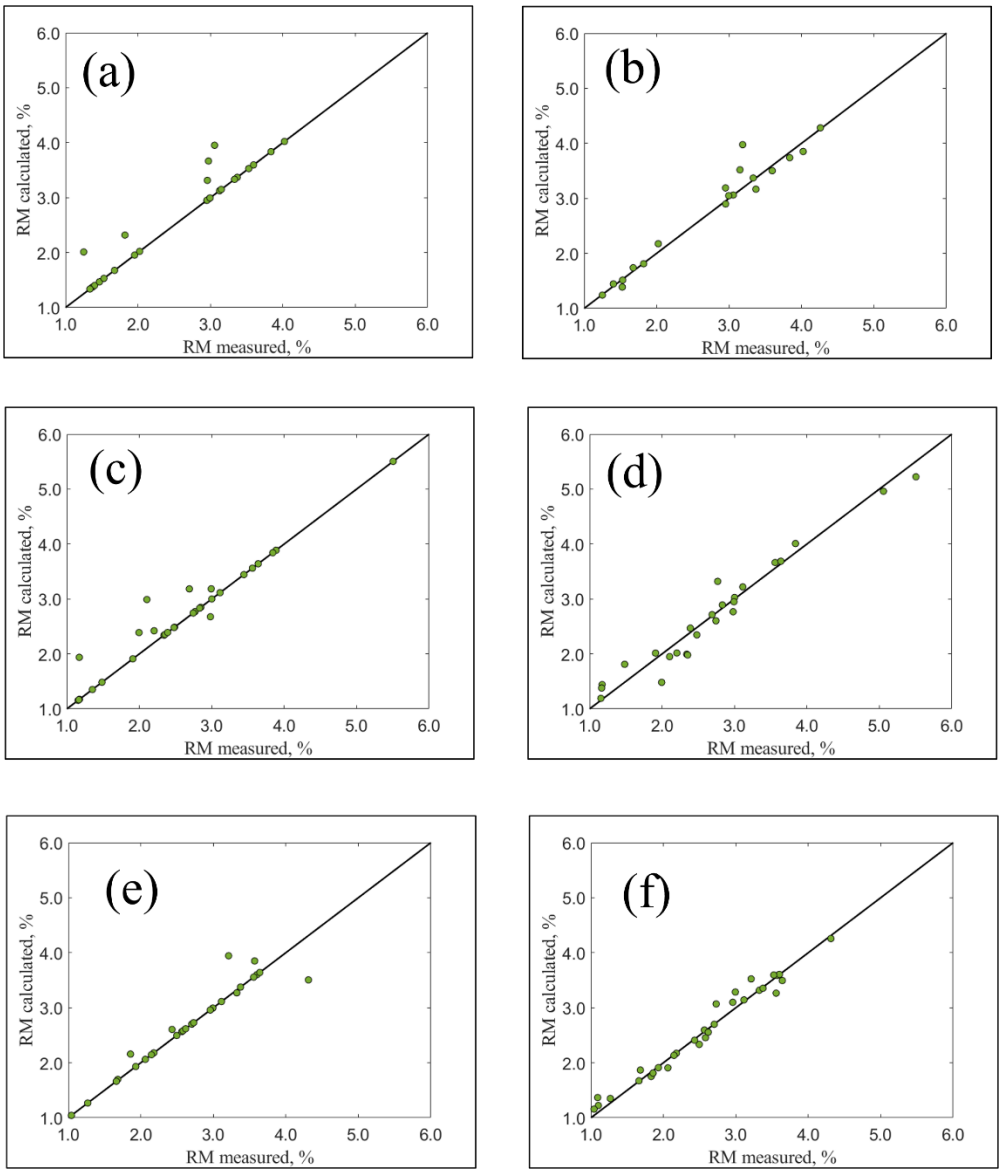

Figure 51: Parity diagrams of dataset SA05 (a,b), SA1 (c,d) and SA3 (e,f) comparing the RM measured (%) and the RM calculated (%),obtained using the linear regression (a,c,e) and the neural network (b,d,f) models developed using datasets of arginine-sucrose mixtures for SR.

An additional specialized model was developed for mixtures containing trehalose, utilizing a training set of 32 samples (70%) and a test set of 13 samples (30%). The comparison of the two models, presented in ***Table 14,*** revealed RMSE values of 0.155 for the linear model and 0.128 for the neural network, with both models demonstrating comparable performance.

6.4.3 Global model

For the evaluation of the global model, the complete dataset, which included S6, S3, S9, SA05, SA1, SA3, and T6, was divided into two distinct sets for calibration and validation. The calibration set comprised 70% of the dataset (228 samples), while the validation set accounted for the remaining 30% (97 samples).

Initially, the application of the global model was concentrated on the narrow wavelength range. It was evident that the performance of the Global Model, using the S6 dataset, was inferior to that of the initial Model S6, primarily due to a smaller percentage of the dataset being included in the calibration set to ensure homogeneity among all formulations. Homogeneity here refers to maintaining an equal representation of each formulation in the training set.

In instance, the RMSE values were 0.213 for the neural network and 0.358 for the linear model, both higher than those of the previous model (respectively 0.172 and 0.122). Conversely, the performance of S3 dataset showed an overall improvement, with RMSE values of 0.295 for the neural network and 0.493 for the linear model. For the S9 dataset, the neural network performance remained consistent, while the linear model exhibited an improvement with a RMSE value of 0.444. These results were expected, as both datasets were included in the training set for model development. However, the differences in performance between the two models were not significant. Therefore, it can be concluded that a global model is not necessary for predicting the RM values of S3 and S9, as Model S6 alone provides sufficiently high accuracy, comparable to that achieved by the global model. (Massei, Falco, & Fissore, 2023)

The scenario was notably different for the sucrose-arginine mixtures, where performance exceeded that of Model S6. The inclusion of arginine-based formulations in the training set enhanced predictions for the three datasets (SA05, SA1, and SA3) by accounting for specific peaks unique to arginine, which differ from those present in sucrose formulations. This improved performance is evidenced by the RMSE values presented in ***Table 13***, indicating that the neural network consistently yielded lower RMSE values compared to the initial model. For instance, the RMSE for SA3 was 0.173, in contrast to 0.572 for the previous model.

Thus, it may be necessary to develop a model that incorporates samples from the new formulation (containing arginine) during the training phase to address the significant variability in the spectra of the different formulations. Furthermore, the neural network proved to be more effective in managing a large input dataset and accounting for their variability when predicting RM values for freeze-dried products. All RMSE values obtained were lower than those calculated using the linear regression model, primarily due to the non-linear nature of the neural network.

The global model was additionally applied across a broader wavelength range (WR), with

the results presented in ***Table 13***. In this instance, the performance of both models appeared to be quite comparable, exhibiting similar RMSE values. All values were within the range of the intrinsic error associated with the analytical method.

6.4.4 Effect of training set size on the performances

The effect of the training set size on model performance was tested by calculating the RMSE values in each case. The results are summarized in ***Table 15***.

The RMSE values were computed for both models by varying the size of the training set, represented as a percentage of the available data, ranging from 70% to 40%. This approach facilitated the identification of potential issues related to overfitting or underfitting. The highest RMSE values were observed for the sucrose-arginine mixture, with a direct correlation indicating that an increased percentage of arginine in solution resulted in higher RMSE values. Overall, the RMSE values obtained with the linear model were consistently greater than those achieved with the neural network across all percentages used.

Table 15: Impact of training set size on model performance. The first row indicates the type of model utilized, while the second row presents the percentage of the available dataset (ranging from 40% to 60%) allocated for training purposes. All values in the table represent the RMSE corresponding to each dataset for the specified training set sizes. The results are provided for the SR wavelength range.

	Model S6 LR			***Model S6 NN***			***Global Model LR***			***Global Model NN***		
Dataset	*40%*	*50%*	*60%*	*40%*	*50%*	*60%*	*40%*	*50%*	*60%*	*40%*	*50%*	*60%*
S3	0.427	0.375	0.392	0.408	0.352	0.283	0.757	0.598	0.681	0.422	0.294	0.334
S9	0.574	0.558	0.412	0.252	0.333	0.189	0.691	0.689	0.468	0.286	0.212	0.304
SA05	0.877	0.415	0.909	0.593	0.419	0.644	0.969	0.559	0.669	0.426	0.323	0.330
SA1	1.998	0.544	0.993	0.506	0.349	1.061	1.352	0.495	0.631	0.384	0.354	0.401
SA3	0.599	1.880	1.169	0.952	0.868	1.219	1.229	0.723	0.430	0.632	0.397	0.400
T6	0.494	0.479	0.479	0.491	0.291	0.358	1.363	0.465	0.473	0.660	0.487	0.578

A detailed examination of ***Table 15*** reveals that the RMSE values remained relatively stable across the various training set sizes analyzed for the datasets S3, S9 and T6. This is a favorable outcome, as it suggests a reduction in the experimental effort required for model development. Moreover, it is an indication that no underfitting or overfitting was performed in the development of the above-mentioned models. A moderate increase in RMSE was noted for the dataset SA05, whereas a significant increase was observed for the dataset with higher percentage of arginine, so SA1 and SA3. In these instances, the RMSE values ranges from 0.6 up to 2 even with very low training set percentages. A similar trend is evident for the neural network; however, all curves are shifted downward, indicating superior performance.

A different scenario was noted for the global model presented in ***Table 15.*** In the case of the linear regression model, performance was suboptimal at 40 % of training set, exhibiting significantly high RMSE values ranging from 0.7 up to 1.4. The remaining trend was approximately stable, with minimal fluctuations for the 60 % of training set. Conversely, the neural network demonstrated improved performance, characterized by consistently low RMSE values across all percentages of the training set. This work may serve as a valuable resource for balancing model accuracy with the experimental efforts required for its development.

As noted in the previous Sections, the *Model S6* has the potential to be generalized to different formulations such as S3, S9 and T6, as the spectra of these formulations exhibit significant spectra similarity. In contrast, a higher error is observed when arginine is included in the formulation, due to its substantial influence on the shape of the NIR spectra. Nevertheless, the global model demonstrated an ability to enhance the estimation of formulations containing arginine, yielding acceptable results across all datasets under investigation.

6.4.5 Real-case study: prediction of RM in DP

One of the primary challenges encountered in model development within a pharmaceutical company is the lack of availability of drug product, along with the significant costs associated with their utilization for modeling purposes. Therefore, if a model developed using placebo data proves effective in predicting residual moisture values in the drug product, it could greatly facilitate the integration of modeling techniques into process design and validation activities. The PLS model was chosen for this purpose since it is currently the only multivariate method accepted by the company

since it is GMP compliance. Indeed, by using SIMCA software only PCA and PLS models are available for data analysis.

In ***Figure 52*** the calibration parity plot is reported using the trehalose-based formulations by directly focusing on the region where specific signals of water are located. Indeed, the *Formulation 1* drug product is mainly made up of trehalose as excipients. The similarity between the RMSEC, equal to 0.129%, and the RMSECV, equal to 0.136%, highlighted the good performances of the developed model. However, a PLS model in the WR of wavenumber was also developed to compare the prediction results.

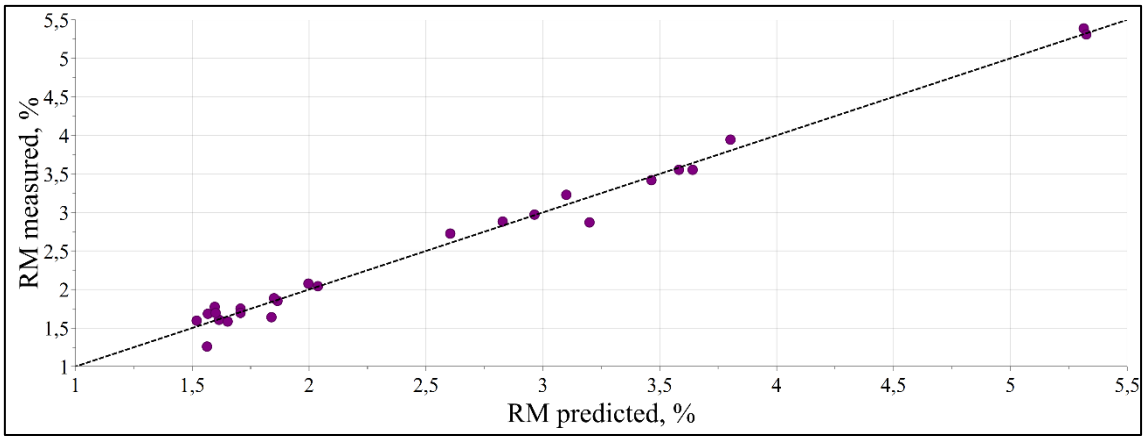

Figure 52: Parity plot using T6 dataset processing by PLS model in the SR.

The PLS developed models were used to predict ten different samples of *Formulation 1* after it has been subjected to the freeze-drying cycle. The absolute error plots are reported in **Figure 53**.

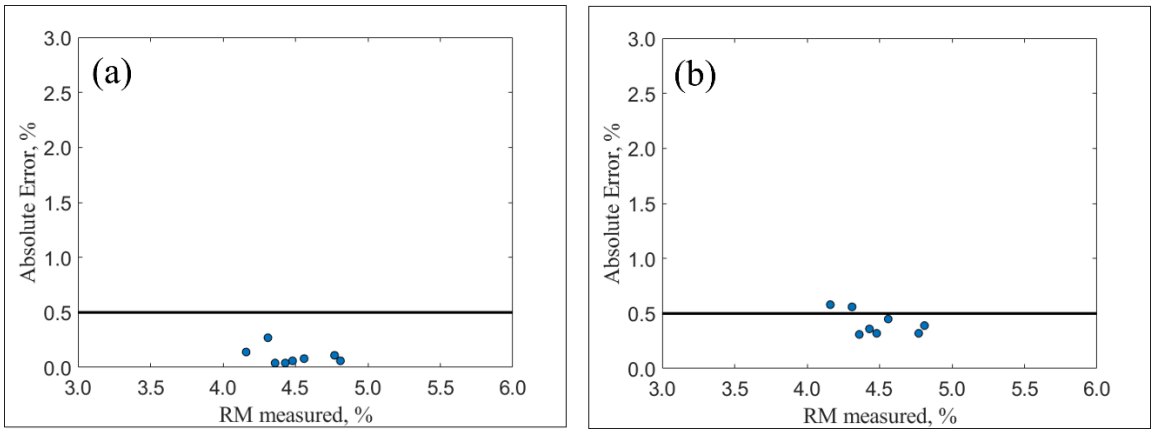

Figure 53: Absolute error plots for RM estimation of drug product processing the data by PLS model developed on T6 dataset for both SR (a) and WR (b).

Examining the graphs provides confirmation of the previously reported findings. By focusing on the water absorption bands and excluding the product-specific peaks, more

favorable results are obtained, as observed in graph (a). This represents a noteworthy achievement, as it has been demonstrated that the model developed using a surrogate product can accurately predict the RM values of a real drug product. Such accuracy enables significant savings in both resources and time during the model development process.

6.5 Highlights

In this Chapter a NIR-based application for the monitoring of the residual moisture in biopharmaceutical product has been presented.

NIR spectroscopy was coupled with machine learning techniques to quantify the residual moisture content in freeze-dried products. The first goal of the present work was the development of a model able to estimate the residual moisture in a certain reference product, the S6 dataset. Then, the robustness of this model was tested using the other different products as external validation dataset. Two different models were developed: a linear regression model and a neural network. This study clearly demonstrates that the coupling of NIR spectroscopy with chemometric techniques is a powerful tool for the quantitative prediction of RM values as an alternative to KF titration in the context of process development.

By comparing the developed models, the neural network turned out in more accurate and reliable performance than the conventional linear models. Its better performance was assessed both for the prediction of products non-involved in the calibration step and for dealing with large dataset, as in the case of global model. So, the robustness of the neural network was demonstrated with RMSE values lower than the intrinsic error of the analytical method (KF). It was assessed that the introduction of a new component, like arginine, that gives a different contribution in the analyzed spectral region, required for the development of a global model, while the product-specific model for S6 revealed accurate in the prediction of dataset containing sucrose at different percentage and trehalose (having a similar spectra).

Another remarkable aim of the present Chapter was the reduction of the experimental effort associated with the model development phase. Therefore, a PLS model was calibrated using a trehalose-based formulation and was tested to estimate the residual moisture values of a real drug product. This validation process confirmed that the NIR-based model could reliably predict the RM values of a DP, thus allowing for a cost-effective approach to model development without consuming the API. The insights

gained from this research could contribute to the replacement of KF titration with NIR spectroscopy for the monitoring of residual moisture in the Stage 1 activities in pharmaceutical company.

CHAPTER 7

Some results presented in this Chapter have been already published in a peer-reviewed journal (Massei, Falco, & Fissore, 2025).

7. In-line monitoring of filtration, compounding, and freeze-drying step

7.1 Introduction

Batch processes are widely used across different sectors, including chemical, pharmaceutical, food and biotechnology industries. Specifically, the drug product (DP) manufacturing relies on a batch process, defined by a limited duration and non-steady-state behavior. Usually, when a batch run is successfully completed during the development phase and yields a product that meets specifications, the key process variables from that run are documented in a recipe. Then, the latter is subsequently employed for future batch productions, aiming to guarantee the product quality. However, it is not always sufficient to apply a recipe-driven approach. In fact, monitoring in real-time a specific process offers numerous benefits, including reduced costs, identifying fault detection, process optimization and a deeper process understanding.

In this framework, the in-line application of NIR or Raman spectroscopy could be helpful also in different steps of DP manufacturing in the perspective of QbD approach. Indeed, it would be optimal to monitor the DP process, and the related CQAs, in real-time allowing for intervention in case of any deviations from the normal operating conditions expected.

According to the literature explored, few works have been published regarding the in-line application of NIR and Raman spectroscopy to biopharmaceutical products. As an example, Thakur et al. presented a NIR-based approach for real-time measurement of the concentration of mAb in the framework of continuous production of biopharmaceutical products. Also, De Beer et al. demonstrated the application of both NIR and Raman spectroscopy in-line to monitor the product crystallization, annealing step and the polymorph formation of intermediate and end products. (Oddone I. , 2015) (De Beer, et al., 2007)

In the present Chapter two different applications are reported:

- An in-line application of NIR is documented to investigate the system's ability to

identify possible deviations occurring during a freeze-drying cycle. Not all deviations have a great impact on the quality and lead to a rejection of the product. Therefore, it is important to evaluate the most critical quality attributes to understand it. Therefore, the RM trend was evaluated using PLS model to assess in real-time the behaviour of the formulation under investigation. Additionally, the endpoint of primary drying phase was calculated and compared with the one calculated from the Pirani-Baratron methods.

- Raman spectroscopy is reported as in-line tool for monitoring the filtration and the compounding step by focusing on the protein content behavior.

7.2 Case-study 1: NIR spectroscopy

7.2.1 Experiments for multivariate statistical process control

For the development of the statistical quality control model, 2R glass vials (Nuova Ompi, Piombino Dese, Italy) were filled with 1 mL of sucrose 5%w aqueous solution. Ultra-pure water by a Millipore water system (IQ 7000, Merck Millipore, Burlington, USA) was used for the preparation of the solution, while sucrose was supplied by Merck Life Science (Darmstadt, Germany). Three different runs were carried out in a laboratory scale freeze-dryer (Lyostar 3, SP Scientific, Warminster, USA) using the NIR in-line pointing out on a specific sample as the setup reported in Section 3.2.3. In all tests 23 vials were placed in a polymeric frame, whose side contained a carving shaped for probe positioning and keep it in contact with the monitored sample. Temperature control was performed by means of two thermocouples, while pressure monitoring was performed with a capacitance manometer and a Pirani sensor.

The normal operating conditions used for the reference freeze-drying cycles (named as *"Cycle 1"* and *"Cycle 2"* were the following:

- Freezing at -45°C for 6h (cooling/heating rate set at 2°C/min)
- Primary drying at -25°C and 5 Pa for 30h
- Secondary drying at +35°C and 5 Pa for 10h

In the fault cycle, labelled as labelled as *"Cycle 3",* shelf temperature was decreased to -15°C after 24h of drying. Then, it was restored to -25°C and hold for 30 minutes. Then, chamber pressure was gradually increased 10 Pa after other 30 minutes of drying and to 15 Pa after 20 minutes of drying. This cycle was used to prove the ability of the model to detect faults occurring during the process. In both cases, spectra were acquired in a

continuous mode each 2 minutes for the entire duration of the lyophilization cycle.

7.2.2 Experiments for quantification of residual moisture in-line

For the quantification of the trend of residual moisture, a sucrose 6%w aqueous solution (labelled as S6) was prepared. Ultra-pure water by a Millipore water system (IQ 7000, Merck Millipore, Burlington, USA) was used for the preparation of the solution, while sucrose was supplied by Merck Life Science (Darmstadt, Germany). The S6 formulation was freeze-dried into 2R glass vial (Nuova Ompi, Piombino Dese, Italy) with a filling volume of 1 mL using the reference cycle described above. For the calibration of the PLS model, a wide range of moisture in the samples is needed. Therefore, a manual humidification was carried out to obtain a RM between 0% - 5% by adding a certain amount of water into the stopper and leaving the vials in upside position over-night, leading the diffusion of water.

Then, the spectra were acquired off-line using a Fourier Transform NIR spectrometer (Antaris MX FT-NIR, Thermo Fischer Scientific, Waltham, USA) according to the setup reported in Section 3.2.3. After the acquisition of the spectra, Karl Fischer (KF) titration was performed on the samples to obtain the reference value of residual moisture. A coulometric titrator was employed (C30S Mettler Toledo, Columbus, USA) for this purpose.

7.3 Case-study 2: Raman spectroscopy

7.3.1 Experiments for filtration monitoring

The setup used for in-line monitoring of the filtration step using Raman spectroscopy is reported in ***Figure 54.***

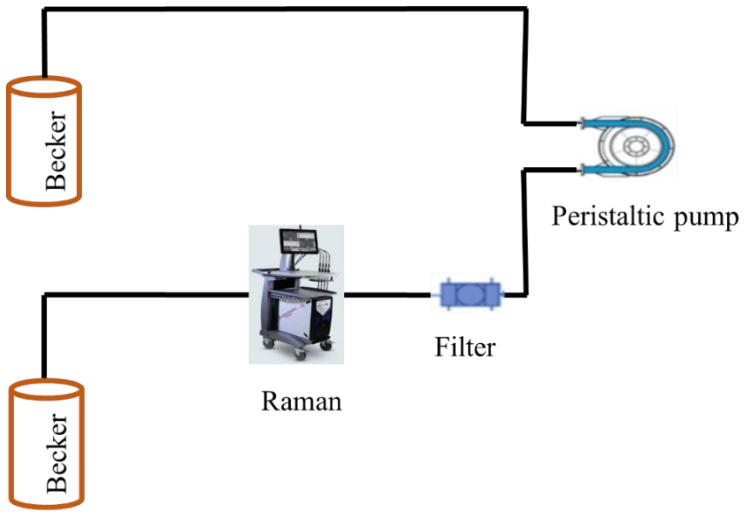

Figure 54: Setup of Raman spectroscopy for filtration monitoring

Formulation 2 was used for this scope. It was introduced into the first beaker and subsequently pumped through a peristaltic pump to the 0.22 µm filter. The filtered liquid was then analyzed in-line by the Raman flow cell, with data acquisition occurring every 10 seconds for a total duration of 5 minutes, resulting in 50 observations. The analyzed liquid was collected in a separate becker.

7.3.2 Experiments for dilution monitoring

The setup used for in-line monitoring of the filtration step using Raman spectroscopy is reported in ***Figure 55.***

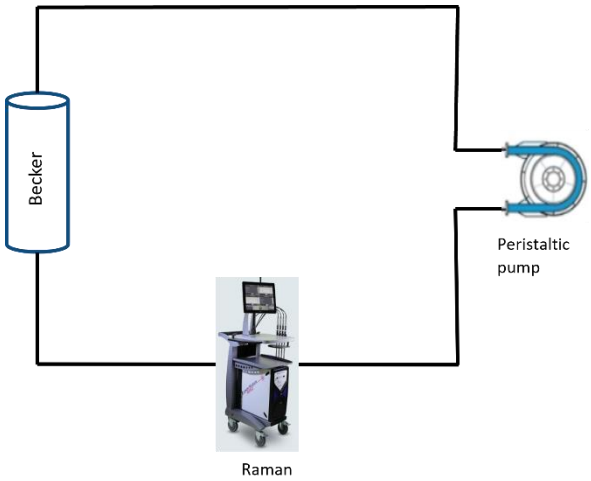

Figure 55*:* Setup of Raman spectroscopy for filtration monitoring

Different dilutions were performed in *Formulation 2* with placebo, as reported in ***Table 16,*** to explore different concentration levels.

Table 16: Different dilutions performed by adding placebo in the formulation to explore a wide range of concentration levels.

Dilution n°	***Density [g/mL]***	***Initial DP volume [mL]***	***Initial C DP [mg/mL]***	***Final C DP [mg/mL]***	***Placebo to be added [kg]***
0	1.018	100.00	40.00	35.00	14.54
1		114.29	35.00	30.00	19.39
3		160.00	25.00	20.00	40.72
4		200.00	20.00	10.00	203.60
5		400.00	10.00	5.00	407.20
6		800.00	5.00	1.00	3257.6

7.4 Results

7.4.1 NIR spectroscopy – multivariate statistical process control

The first step involved the suitability of in-line NIR spectroscopy to gain insights on the freeze-drying process. Therefore, all the spectra related to the two reference freeze-drying cycles, were subjected to SNV pretreatment, and then were analyzed by a PCA over the range 7400 - 4230 cm-1. Indeed, the behavior for higher or lower frequencies was found to be meaningless since the spectra appeared flat or too noisy. The first 2PCs of the PCA model were found the most significative since they explained more than 97% of the variance among the spectra. After performing PCA with SIMCA program, two graphs named score plot and loading plot were obtained for each principal component investigated.

In the freezing phase, the absorbance values do not exhibit significant peaks, indicating that NIR spectroscopy is less effective in this stage. This can be primarily attributed to the solidification of the formulation, which limits the interaction of NIR light with the water molecules. As a result, the spectral information gained from this phase are not useful for the aim of the analysis. During the primary drying, as deeply discussed in Section 6.3.1, a notable peak appears around 5200 cm^{-1}, corresponding to the water signal. This peak indicated the sublimation of ice and the transition of water from a solid to a vapor state. The absorbance value fluctuates significantly in this phase, reflecting the changes in moisture content as ice sublimates. Lastly, during secondary drying the same peak is present, but at a lower intensity with respect to the primary drying.

Initially, all spectra, regardless of the phase of the freeze-drying cycle, were analyzed using PCA. ***Figure 56*** shows an example of scores plot relating PC1 as a function of PC2.

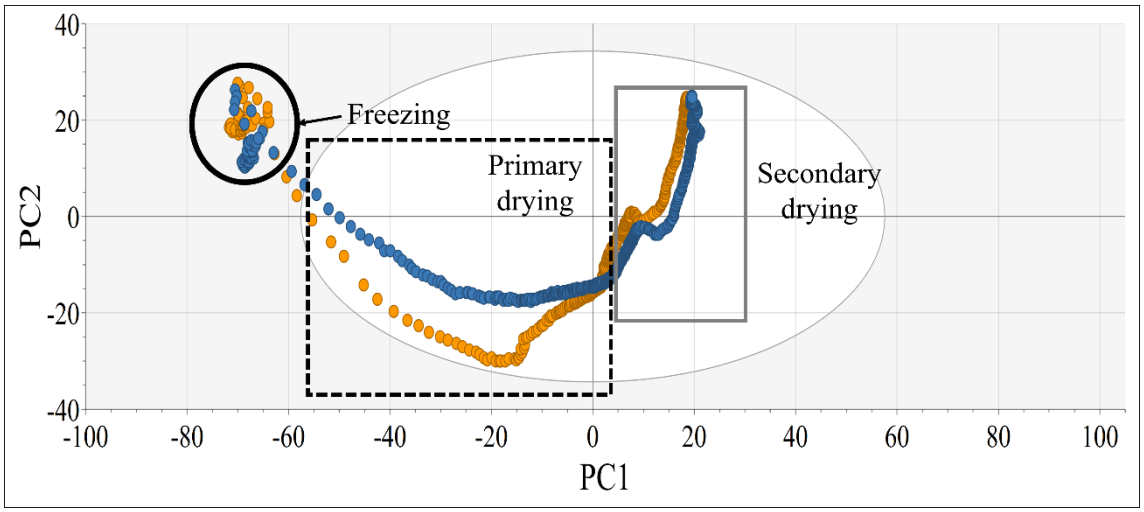

Figure 56: Scores plot relating the first two principal components of the NIR spectra acquired in-line during the freeze-drying process. Data were processed by PCA in the range 7400 – 4230 cm-1. The data are colored respectively in black or grey for reference cycle 1 and 2.

The scores plot demonstrates how samples are distributed across the first two principal components derived from the NIR spectra collected in-line during the freeze-drying process. The graph highlights three distinct regions corresponding to different phases of the process. During the freezing phase, samples are clustered randomly, as NIR spectroscopy is not particularly sensitive to this step. As the process advances to primary drying, a shift in scores occurs, reflecting changes in the material's properties as ice sublimates. Specifically, the decrease in scores along PC2 during this phase indicates a reduction in free moisture content, resulting from the transition from high water content in the frozen material to a lower water content state due to sublimation. As the primary drying phase progresses, a fraction of bound water is remained entrapped in the solid matrix, i.e. water did not crystallize during freezing, and NIR spectroscopy could be able to detect this change. An increase in PC1 was noted, indicating a shift back towards more positive values. This increase could be associated with the starting desorption of residual moisture, that is the transition to the secondary drying stage. At the end of secondary drying, where the final target value of residual moisture is obtained, positive values of PC2 are observed that could correspond to a great reduction in water content and the transition of the material to a more stable solid form. Also, in this phase, a stabilization along PC1 is seen, suggesting that the overall composition and structure of the formulation are becoming more consistent. In fact, as the drying process concludes, the distribution of the active pharmaceutical ingredient (API) and excipients becomes more uniform. This homogeneity leads to reduced variability in the spectra data, stabilizing the values along PC1. The trend is also confirmed by the behavior of the loading plot, where

the peak related to water content is negative in the loading of PC2.

Having assessed that NIR spectroscopy provides useful insights during the drying phases, the spectra of the freezing stage are removed for the subsequent analysis. Therefore, a new PCA model was developed by focusing only on the drying phases. The two control limits based on Hotelling's T2 and Distance to the Model were data-driven calculated using SIMCA software. The Hotelling's T2 is calculated by considering a confidence level equal to 95% and 99%.

Figure 57 depicts two key plots related to the analysis of two reference freeze-drying processes. The first cycle was reported in black and the second one, run under the same operating conditions, is denoted in gray for the sake of clarity.

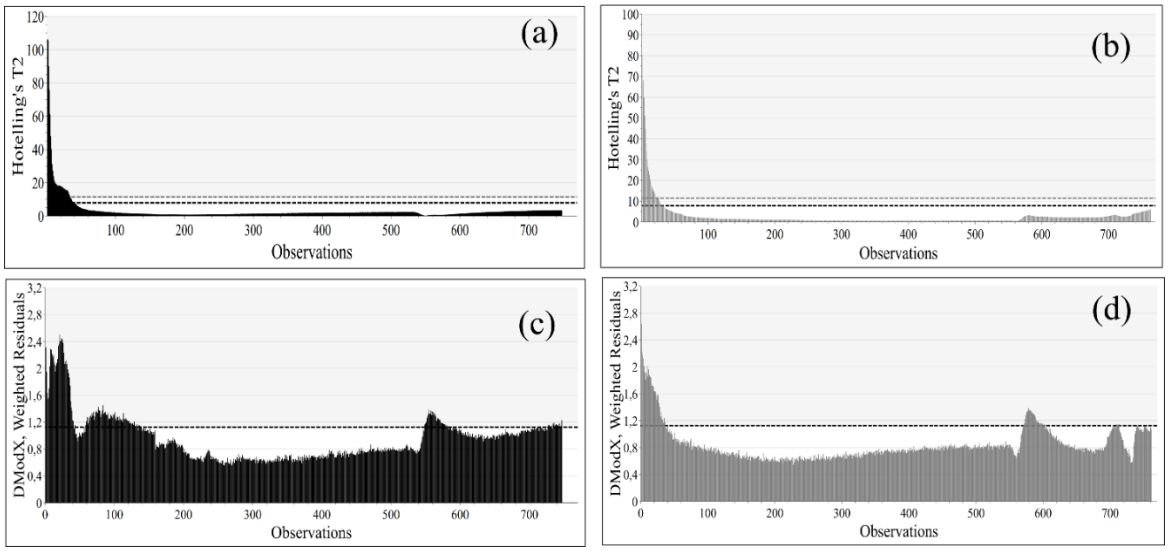

Figure 57: Hotelling's T2 plot (a,b) and DModX Weighted Residual plot (c,d) as a function of observations in the case of reference cycles. In black the reference cycle 1 is reported (a,c), while in grey the reference cycle 2 (b,d).

Figure 57a and ***57b*** show the Hotelling's T2 statistics over the observations for both processes. The black and grey dashed lines indicate respectively the critical values for T2 at 95% and 99% confidence levels. Values exceeding these limits suggest that the observations are outside the expected variability of the system. For both processes, the initial observations show high T2 values. This could be consistent with the early stages of primary drying, where rapid sublimation occurs, leading to rapid changes in the system's dynamics, which can cause significant variations in the measured parameters. In fact, in the starting instants of primary drying, temperature and pressure conditions can fluctuate significantly as the ice transitions to vapor. Therefore, these initial points above the limits can be attributed to the period in which the material is adjusting to the new

conditions. After the initial phase, T2 values for both processes drop below the 95% control limit, indicating that the processes stabilize.

The lower plot in ***Figure 57c*** and ***57d***, displays the DModX weighted residuals for both processes, measuring how far each observation deviates from the model predictions. This can be useful also to identify potential outliers in the data. The dashed line represents the critical limit. Observations exceeding this limit are considered statistically significant deviations from the expected model. Like the T2 plot, the DModX values for both processes are initially high, reflecting non-equilibrium conditions during the early drying phase. This aligns with the earlier explanation regarding the instability of the system. After the initial phase, the DModX values stabilize for both processes, indicating that they have reached a more consistent state. Some outlier observations were identified at around 550 and were critically analyzed by looking into detail at their NIR spectra. Some anomalies in the data collection process occurred during the acquisition, arising maybe from instrumental noise of measurement or external disturbances.

After having assessed this PCA model, the cycle intentionally conducted under fault conditions was projected into the existing space. By introducing these fault conditions, we aimed to challenge the robustness of the model and verify its sensitivity to deviations that may indicate potential issues in the lyophilization process. The results obtained for the Hotelling's T2 projection are reported in ***Figure 58.***

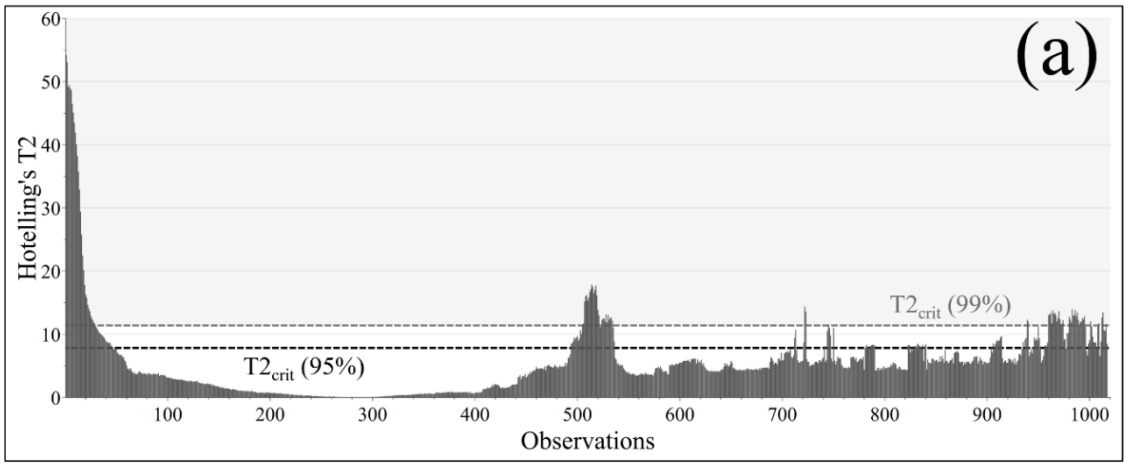

Figure 58: Hotelling's T2 plot as a function of observations in the case of fault cycle.

It is possible to notice some observations exceeding the critical limits. This is perfectly reasonable since at a time instant, corresponding to the 500 observation, the shelf temperature was increased from -25°C to -15°C. Therefore, the T2 plot can identify the

deviation from the expected process behavior. After around one hour, the process operating conditions were reported at the target one and this can be also reflected in the graph, since the subsequent points are below the critical limits calculated. However, the gradually pressure increase performed in the next time points is also detected by this chart since other points exceeding the critical limits were noticed.

7.4.2 NIR spectroscopy – RM trend by PLS

If a deviation occurs in the process, it could be helpful to evaluate the residual moisture trend to highlight if the quality of the product has been impacted or not. In this framework, the aim is to understand if the deviation occurred during the *Cycle 3* had an impact in terms of residual moisture value and primary drying duration.

Therefore, a PLS model was developed by considering the entire dataset deeply explored in previous works by Bobba et al. and Massei et al. (Bobba, Zinfollino, & Fissore, 2022) (Massei, Falco, & Fissore, 2023) In this stage, the entire dataset was used to calibrate the model, and a comparison between the RMSEC and the RMSECV was performed to evaluate the model's performance. This comparison is a crucial metric for understanding how effectively the model fits the training data in relation to its capacity to generalize to unseen data.

Figure 59 shows the parity diagram plot comparing the residual moisture measured by KF (y-axis) against the RM values predicted by the PLS model (x-axis).

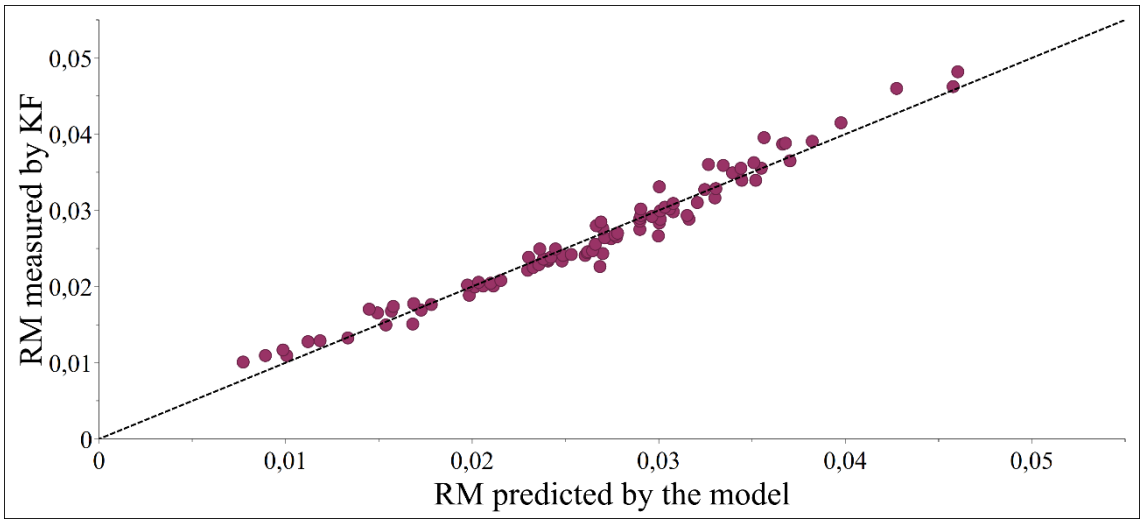

Figure 59: Parity diagram plot relating the measured RM values by KF in the y-axis as a function of the RM predicted by PLS model in the x-axis.

The closeness of the data points to the dashed bisector line suggests that the model successfully captures the relationship between the measured and predicted values. The

model demonstrates a strong fit to the calibration data, as evidenced by the low RMSEC equal to 0.152%. Also, good predictive performance is evaluated, with a RMSECV equal to 0.156%, when applied to unseen data during cross-validation. The proximity of RMSEC and RMSECV values suggests that the model can generalize well to new observations, maintaining its accuracy without being overly tailored to the specific calibration dataset.

Once the model has been developed, the in-line acquired NIR spectra served as input in the PLS model to calculate the evolution of residual moisture throughout the cycle. The aim of this step was to assess the endpoint of primary drying stage and compare it with the estimated drying time from the ratio between Pirani and Baratron profiles, as reported in ***Figure 60***.

Figure 60a, 60c and ***60e*** depict the predicted residual moisture values over time during the drying steps. In the three graphs, there is a noticeable decline in RM during the initial stages, indicating effective moisture removal. The steep drop in moisture levels suggests that the primary drying is efficiently progressing. The end point of the primary drying phase was marked in both graphs, signifying the transition to the secondary drying phase. The residual moisture trends stabilize towards the end of the drying process, indicating that the target moisture content has been achieved in all cases. Moreover, similar asymptotic values were found for the first reference cycle RM was equal to 0.60% and for the second reference cycle RM was equal to 0.68%. This was expected since the two cycles were conducted in the same operating conditions. A higher RM value was obtained for the cycle carried out in fault conditions, although in specification with the limits imposed by the company.

Figure 60b, 60d and ***60f*** illustrate the ratios of pressure measurements taken from the ratio between the Pirani and Baratron sensors over time. These graphs are helpful to assess the endpoint of the primary drying step to have a comparison with the value predicted by the PLS model. In both curves, the initial value is approximately 1.7, as the Pirani sensor measures the thermal conductivity of the gas within the drying chamber, resulting in readings that are about 60% higher than those from Baratron manometer. When the gas composition shifts from water vapor to nitrogen, the ratio Pitani/Baratron starts to decline, indicating the sublimation is occurring. The point at which this decrease starts is denoted as “onset”, while the point where the lower asymptote is reached is the known as the “offset”. Research has indicated that the onset, offset, and midpoint can serve as

indicators of drying time. (Patel, Doen, & Pikal, 2010) In the present work, the offset value has been calculated from the Pirani/Baratron ratio. **Table 17** compares the endpoints calculated using two different methods: PLS and the Pirani-Baratron ratio.

Table 17: Comparison of endpoint estimated by PLS model and Pirani/Baratron ratio for the reference cycles and fault one. The relative error was also reported.

Cycle	*Endpoint by PLS, h*	*Endpoint by Pi_Ba, h*	*Relative Error, %*
Cycle 1	21	22	4.55
Cycle 2	19	21	9.52
Cycle 3	22	23	4.35

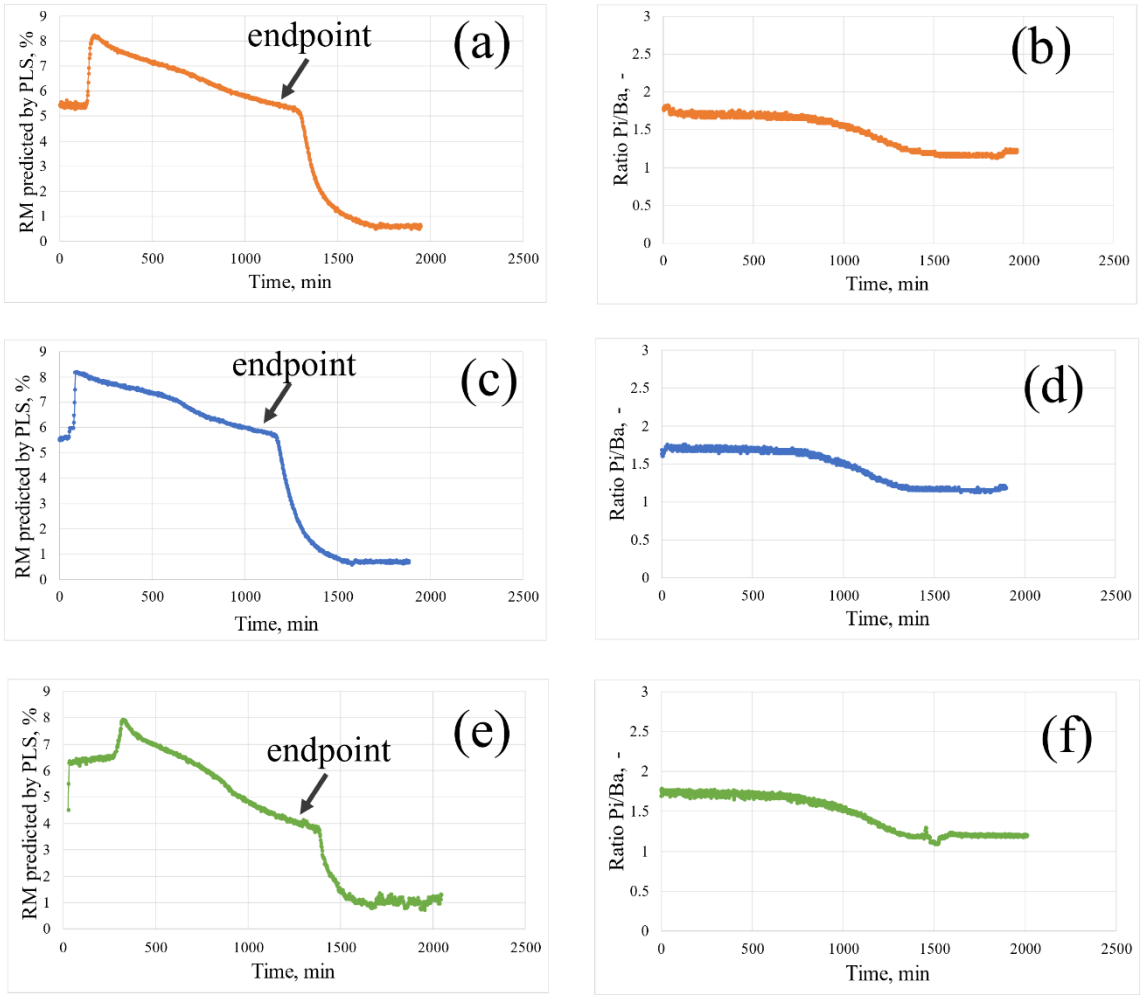

Figure 60: Graphs (a), (c) and (e) depicts the trend of residual moisture predicted by PLS model as a function of drying time respectively in case of reference cycle 1, reference cycle 2 and fault cycle. In the graphs (b), (d) and (f) the corresponding Pirani/Baratron ratio for the three cases are reported.

The primary drying endpoints obtained from both methods for each cycle are very similar, suggesting that the PLS approach produces consistent results. It is worth mentioning that

the PLS method generally estimates slightly lower endpoint values compared to the Pirani/Baratron ratio across all cycles. The close proximity of these primary drying endpoint values supports the reliability of the PLS model for monitoring the lyophilization process. Additionally, the relative error for the three cases is reported, showing optimal results with values consistently below 10%. This is entirely reasonable, as it is important to recognize that drying time values are subject to considerable uncertainty due to their determination through graphical methods.

7.4.3 Raman spectroscopy – filtration & dilution

The protein content monitoring during filtration and compounding step is a crucial factor in pharmaceutical companies to verify that the target concentration is reached after each process step. Therefore, Model 4 was used introducing a MSC as pretreatment to estimate the protein content trend using the in-line Raman acquisition.

The trend of protein content obtained in the two cases under investigation are reported in ***Figure 61***:

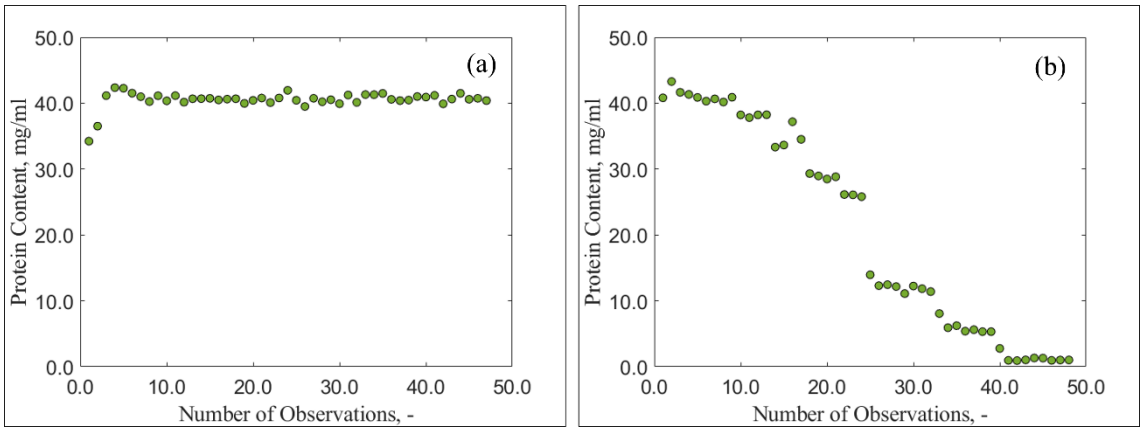

Figure 61: Protein content trend during (a) filtration and (b) dilution step. The in-line Raman acquisitions were processed using the PLS model developed off-line and denoted as Model 4.

Formulation 2 was used for the study targeting a protein concentration of 40 mg/ml. During the filtration process, the protein content trend consistently aligns with the expected target value, except for the first two observations, which recorded a value of approximately 36 mg/ml, as shown in ***Figure 61a***. This decrease is attributed to adsorption phenomena occurring at the filter membrane. Confirmation of this behavior was validated by a filtration study conducted within the company for this molecule.

Moreover, even in the case of different dilutions, the obtained protein content values are consistent with the expected theoretical values, as depicted in ***Figure 61b***.

7.5 Highlights

In the first part of the present Chapter, the application of NIR spectroscopy for at-line and in-line monitoring of the freeze-drying process is reported, emphasizing its potential for enhancing process understanding and control.

Specifically, by focusing on the drying phases, the capabilities of NIR spectroscopy can be leveraged to gain valuable insights into the physiochemical changes occurring within the formulation. Moreover, it was also possible to identify possible deviations from the normal operating conditions that may have an impact on the product quality. It has to be remarked that a forecasting procedure to estimate the behavior of a new cycle by having only very few observations is needed and it is under investigation. However, the presented application can be useful if some deviations occur at the very beginning of the process or as an at-line tool.

Once the deviation has been identified, it is necessary to assess if it had an impact or not in product quality. Therefore, the residual moisture trend was estimated using the PLS sensor, highlighting that in the present case-study the fault cycle resulted in higher RM values, but still below the specification limits imposed by the company.

Moreover, the results demonstrated that the endpoints calculated using both PLS and Pirani-Baratron methods were closely aligned, indicating the reliability of the PLS model in predicting moisture levels and to track in-line the evolution of the drying phases.

While NIR spectroscopy offers significant advantages, including non-destructive measurements and high sensitivity to moisture, it is essential to acknowledge its limitations for in-line measurements in representing batch heterogeneity due to its focus on single vial monitoring. Furthermore, the monitored vial is consistently positioned in the first row, where it is subjected to the highest heat contribution, resulting in lower residual moisture values compared to the central vials. This discrepancy could impact the endpoint determination of the freeze-drying process. Therefore, it is essential to consider and verify a safety margin during the engineering run testing, prior to PPQ. Nevertheless, for development purposes, this approach may facilitate time and resource savings in the development of freeze-drying cycles and in the technology transfer to manufacturing sites.

In the second part of the present Chapter, two in-line Raman applications were presented regarding the protein content monitoring during filtration and dilution step. The results estimated by the PLS model perfectly aligned with the expected behavior for the drug

product under study. These in-line applications can be useful in the framework of process characterization activities as replacement of traditional methods and to have real-time data availability.

The approaches here presented are highly appreciated in R&D departments where it could speed-up the process development phases and enhance process understanding for optimizing different DP manufacturing steps. However, it is important to note that manufacturing sites are still relatively hesitant to adopt this technology. While benefits of real-time monitoring and data-driven decision-making are evident, many manufacturing facilities have not yet fully integrated NIR or Raman spectroscopy into their standard procedures. This reluctance may stem from various factors, including the need for regulatory compliance, the complexity of implementing new technologies on existing qualified lines, and the necessity for staff training to ensure proper usage and interpretation of the data. As the pharmaceutical industry continues to evolve towards a more data-centric approach, it is essential to advocate for the adoption of these innovative techniques in manufacturing environments.

CHAPTER 8

8. Conclusions

This work presented some novel technologies, NIR and Raman spectroscopy, to design and optimize the process steps within the entire fill & finish manufacturing process. The research project demonstrated the ability of multivariate data analysis to deal with spectroscopic techniques to aid pharmaceutical industry in process design, control, and optimization.

In the pharmaceutical field, speeding-up process development activities and technology transfer to manufacturing sites is fundamental to fasten the time-to-market of the products in a more efficient way. Moreover, the unavailability and the cost associated to the API lead to the optimization of the process to save resources by minimizing the number of experiments and by avoiding human errors during the conventional analytical techniques.

In the perspective of the QbD approach and the PAT initiative, NIR and Raman spectroscopy demonstrated powerful abilities to replace the conventional methods currently employed to quantify the different CQAs of a biopharmaceutical product during the different DP manufacturing steps.

8.1.1 Off-line Raman applications

The feasibility study presented in Chapter 4 in this Thesis effectively demonstrated the application of Raman spectroscopy as a robust method for differentiating different type of stress that proteins may encounter during the development and manufacturing of drug products. Monitoring these stresses is crucial, as they can significantly impact the quality of the final product. The results indicate that Raman spectroscopy is a powerful analytical tool for assessing thermal stress, oxidative stress, and the effects of dilutions on proteins. Furthermore, the methodology facilitated a detailed analysis of samples subjected to thermal stress, enabling their classification into three distinct groups based on the severity of the stress experienced. It is noteworthy that a similar analysis was performed on samples subjected to oxidative stress; however, this did not yield significant insights. The application of Raman spectroscopy outlined in this study is particularly relevant from a statistical quality control perspective, as it has the potential to classify “good” samples distinct from “stressed” ones. This technique could be implemented as an at-line tool to

expedite stability studies, enhance process development, and facilitate technology transfer activities. However, it is essential to acknowledge that PCA is an unsupervised model, which does not inherently allow for the prediction of new samples in the conventional sense. Consequently, further work is required to develop a classifier model, such as Partial Least Squares – Discriminant Analysis (PLS-DA), as a future step toward creating a predictive model based on the preliminary results obtained from the exploratory data analysis presented in this Thesis.

The findings presented in Chapter 4 served as a valuable framework for conducting the quantitative analysis deeply discussed in Chapter 5. As new samples progress through various processing steps, they inevitably undergo changes in their Critical Quality Attributes (CQAs). By integrating this information into the PCA model, it becomes possible up to now to discern which CQAs have been affected by specific process steps, as well as to identify the particular bonds and spectral regions involved. However, to highlight the entity of each specific stress, different PLS models were developed to facilitate the monitoring of protein structural analyses, with a specific emphasis on assessing aggregation and fragmentation levels, as well as the composition of the product, including concentrations of Protein, Methionine, and Polysorbate. These models were strategically designed for potential implementation during the process development phase, taking into account different Raman shift ranges based on the signals identified in the loading's plots. Remarkably, most of these models demonstrated effective performance when utilizing the full range of Raman shifts. The data obtained from these PLS models exhibit a strong correlation with conventional analytical techniques that are currently employed to evaluate the various CQAs of interest.

Raman spectroscopy offers significant advantages over traditional analytical methods, such as chromatography and electrophoresis, particularly in terms of sample preparation and the time required for analysis. This increased efficiency not only enhances analytical operations but also facilitates cost-effective monitoring of CQAs throughout the product lifecycle. Another significant advantage of Raman spectroscopy is its capacity to quantify multiple CQAs from a single spectrum, which considerably reduces the time required for analytical assessments. For example, from the single matrix obtained from thermally stressed samples, both aggregation and fragmentation levels were effectively evaluated.

8.1.2 Off-line NIR applications

In Chapter 6 a novel application of NIR spectroscopy for the monitoring of residual moisture in freeze-dried product was presented. The study integrated NIR spectroscopy with advanced machine learning techniques, like artificial neural network, to quantify the residual moisture content in freeze-dried formulations. The comparison with linear models was also conducted. The primary objective of this research was to develop a robust model capable of accurately estimating the residual moisture in a specific reference product, referred to as the S6 dataset. Following the establishment of this model, its robustness was rigorously evaluated using various other products as external validation datasets. The enhanced performance of neural network was evidenced not only in its ability to predict the moisture content of products that were not included in the calibration step but also in its effectiveness when applied to large datasets, as seen in the case of the global model. However, the applicability of these tools in pharmaceutical industry is not GMP compliance, but only linear models are allowed.

Another significant aim of this Chapter was to minimize the experimental effort typically associated with the model development phase. To this end, a Partial Least Squares (PLS) model was calibrated using a trehalose-based formulation and subsequently tested for its ability to estimate the residual moisture values of an actual drug product. The validation process confirmed that the NIR-based model could reliably predict RM values in a drug product, thereby facilitating a cost-effective approach to model development that does not deplete the active pharmaceutical ingredient (API). The insights gained from this research hold the potential to contribute significantly to the replacement of KF titration with NIR spectroscopy for monitoring residual moisture during Stage 1 activities in pharmaceutical companies. This transition not only promises to enhance the efficiency of moisture monitoring processes but also supports the broader goal of advancing analytical methodologies in the biopharmaceutical industry.

8.1.3 In-line Raman applications

The spectral characteristics associated with these structural changes, along with the concentrations of proteins and excipients, were leveraged to develop in-line analytics for therapeutic mAbs, especially within the context of Process Analytical Technology (PAT) applications. The in-line Raman acquisition demonstrated outstanding performances for the protein content evaluation during filtration and compounding step.

This capability has the potential to enable real-time monitoring and adjustments to the

manufacturing process, ultimately leading to enhanced product quality and consistency. The integration of Raman spectroscopy into biopharmaceutical manufacturing processes represents a significant advancement in the field, paving the way for more efficient and reliable quality control measures that can adapt to the dynamic nature of biopharmaceutical production.

8.1.4 In-line / At-line NIR applications

NIR spectroscopy was assessed to obtain valuable insights into the physiochemical changes occurring during the freeze-drying process by using an ad-hoc probe inserted into the freeze-dryer.

This methodology enabled the identification of potential deviations from standard operating conditions that may adversely affect product quality. It is important to note that a forecasting procedure aimed at estimating the behavior of a new cycle based on limited observations is currently under investigation. Nonetheless, the application presented here proves to be beneficial, particularly in scenarios where deviations occur at the initial stages of the process or as an at-line monitoring tool. The impact of the deviation was investigated by estimating the trend of residual moisture using the PLS sensor, revealing that the fault cycle resulted in higher RM values, but remaining within the specification limits established by the company.

Furthermore, the results indicated a close alignment between the endpoints calculated using both the PLS and Pirani-Baratron methods. This correlation underscores the reliability of the PLS model in predicting moisture levels and tracking the in-line evolution of the drying phases. While NIR spectroscopy presents considerable advantages, including non-destructive measurements and high sensitivity to moisture, it is crucial to recognize its limitations in in-line measurements, particularly regarding batch heterogeneity. This limitation arises from the technique's focus on monitoring individual vials, which may not fully capture the variability present across the entire batch.

8.1.5 Applicability and future challenges

The approaches presented in this Thesis are highly valuable within R&D departments, as they have the potential to significantly accelerate the process development phases, the technology transfer to manufacturing sites and to enhance the understanding of processes. By integrating techniques such as NIR and Raman spectroscopy, R&D teams can gain real-time insights into the physicochemical properties of formulations, allowing for more

informed decision-making and optimization of different manufacturing steps. This capability not only facilitates the identification of critical process parameters but also supports the development of robust and reproducible manufacturing processes.

One of the main points to be highlighted relies on the choice between a product-specific model or a non-specific general model. The product-specific model can be finely tuned to account for the unique characteristics of a specific formulation, leading to potentially higher accuracy and reliability in predictions. For instance, as observed in Chapter 6, the inclusion of arginine in formulations significantly impacts the NIR spectra shape, suggesting that a tailored model could better capture these nuances. On the contrary, a general model can potentially be applied across multiple formulations, reducing the need for extensive retraining. However, general models may sacrifice accuracy, as they might not capture the specific interactions and characteristics of individual formulations. In pharmaceutical applications, the choice between these models should be driven by the specific context of use, balancing the need for precision against the practicality of model deployment. Implementing a framework for continuous model updates as new data becomes available, as well as incorporating a wide range of formulations during the training phase, could improve the robustness, generalization to different products and the adaptability of the model over time.

Another critical aspect to be remarked is that the manufacturing sites remain relatively hesitant to adopt these advanced technologies. While the benefits of real-time monitoring and data-driven decision-making are clear, many manufacturing facilities have yet to fully integrate NIR or Raman spectroscopy into their standard operating procedures.

This reluctance can be attributed to a variety of factors:

- One significant concern is the need for regulatory compliance; the pharmaceutical industry is heavily regulated, and any new technology must meet stringent guidelines set by regulatory agencies.
- The integration of NIR or Raman spectroscopy into existing processes requires careful validation to ensure that it complies with these regulations, which can be a time-consuming and resource-intensive endeavor.
- The complexity of implementing new technologies on existing qualified production lines poses another barrier to adoption. Manufacturing facilities often operate under established protocols that have been validated over time. Introducing new analytical methods necessitates modifications to these protocols, which can disrupt production

and require extensive testing to confirm that the changes do not adversely affect product quality.

- The successful implementation of NIR and Raman spectroscopy hinges on the necessity for staff training. Personnel must be adequately trained not only in the operation of these sophisticated instruments but also in the interpretation of the data generated. This training is crucial for ensuring that the information derived from these techniques is utilized effectively to inform process adjustments and enhance product quality.

As the pharmaceutical industry continues to evolve towards a more data-centric approach, it becomes essential to advocate for the adoption of these innovative techniques within manufacturing environments. Emphasizing the potential for improved efficiency, enhanced product quality, and the ability to make informed, real-time decisions can help to alleviate some of the hesitancies associated with the adoption of NIR and Raman spectroscopy. By fostering a culture of innovation and continuous improvement, the industry can better position itself to leverage the full benefits of these advanced analytical tools, ultimately leading to more efficient and effective manufacturing processes. This shift not only aligns with the industry's goals of ensuring product safety and efficacy but also supports the broader movement towards modernization and technological advancement in pharmaceutical manufacturing.

References

Ahern, T., & Manning, M. (1996). *Stability of Protein Pharmaceuticals. Part A: Chemical and Physical Pathways of Protein Degradation.* New York and London: Plenum Press.

Akbar, R., Bashour, H., Rawat, P., Robert, P., & Smorodina, E. (2022). Progress and challenges for the machine learning-based design of fit-for purpose monoclonal antibodies. *mAbs, 14*, 2008-2790.

Albon, C. (2018). *Machine Learning with Python Cookbook.* United States of America: O'Reilly Media Inc.

Alcala, M., Blanco, M., Bautista, M., & Gonzalez, J. (2010). On-line monitoring of a granulation process by NIR spectroscopy. *Journal of Pharmaceutical Sciences, 99*, 336-345.

Allmendinger, A., Mueller, R., Huwyler, J., Mahler, H.-C., & Fischer, S. (2015). Sterile Filtration of Highly Concentrated Protein Formulations: Impact of Protein Concentration, Formulation Composition, and Filter Material. *Journal of Pharmaceutical Sciences, 104*(10), 3319-3329. doi:https://doi.org/10.1002/jps.24561

Amigo, J. (2021). Data mining, machine learning, deep learning, chemometrics. *Brazilian Journal of Analytical Chemistry, 8*, 45-61.

Bai, G., Bee, J., Biddlecombe, J., Chen, Q., & Leach, W. (2012). Computational fluid dynamics (CFD) insights into agitation stress methods in biopharmaceutical development. *International Journal of Pharmaceutics, 423*, 264-280.

Bai, S., Nayar, R., Carpenter, J., & Manning , M. (2005). Noninvasive determination of protein conformation in the solid state using near infrared (NIR) spectroscopy. *Journal of Pharmaceutical Sciences, 94*(9), 2030-2038. doi:https://doi.org/10.1002/jps.20416

Barresi, A., Pisano, R., Rasetto , V., & Fissore, D. (2010). Model-Based Monitoring and Control of Industrial Freeze-Drying Processes: Effect of Batch Nonuniformity. *Drying Technology, 28*, 577-590.

Bee, J., Stevenson, J., Mehta, B., Svitel, J., Pollastrini, J., Platz, R., . . . Randolph, T.

(2009). Response of a Concentrated Monoclonal Antibody Formulation to High Shear. *Biotechnology Bioengineering, 103*(5), 936-943.

Bertolotti-Ciarlet, A., Wang, W., Lownes, R., Pristatsky, P., Fang, Y., McKelvey, T., . . . Vlasak, J. (2009). Impact of methionine oxidation on the binding of human IgG1 to Fc Rn and Fc gamma receptors. *Molecular Immunology, 46*(8-9), 1878-1882. doi:https://doi.org/10.1016/j.molimm.2009.02.002

Bhatnagar, B., Bogner, R., & Pikal, M. (2007). Protein stability during freezing: separation of stresses and mechanisms of protein stabilization. *Pharmaceutical Development and Technology, 12*(5), 505-523.

Biancolillo, A., & Marini, F. (2018). Chemometric Methods for Spectroscopy-Based Pharmaceutical Analysis. *Frontiers in Chemistry, 6*.

Bobba, S. (2021). *Near-Infrared Spectroscopy for Freeze-Drying: Applications for Pharmaceuticals.* PhD Thesis.

Bobba, S., Zinfollino, N., & Fissore, D. (2022). Evaluation of the Robustness of A Novel NIR-based Technique to Measure the Residual Moisture In Freeze-dried Products. *Journal of Pharmaceutical Sciences, 111*(5), 1437-1450.

Bugay, D., & Brittain, H. (2006). Infrared Absorption Spectroscopy. In *Spectroscopy of Pharmaceutical Solids* (pp. 235-269). New York: Taylor & Francis.

Burdick, R., LeBlond, D., Pfahler , L., Quiroz, J., Sidor, L., Vukovinsky, K., & Zhang, L. (2017). Process Design: Stage 1 of the FDA Process Validation Guidance. In *Statistical Applications for Chemistry, Manufacturing and Control (CMC) in the Pharmaceutical Industry* (pp. 115-154). Cham: Springer. doi:https://doi.org/10.1007/978-3-319-50186-4_3

Cartwright, A., & Matthews, B. (2010). *International Pharmaceutical Product Registration.* Boca Raton: CRC Press. doi:https://doi.org/10.3109/9781420081831

Chen, C., Chen, F., Yang, B., Zhang, K., Lv, X., & Chen, C. (2022). A novel diagnostic method: FT-IR, Raman and derivative spectroscopy fusion technology for the rapid diagnosis of renal cell carcinoma serum. *Spectrochimica Acta Part A: Molecular and Biomolecular Spectroscopy, 269*, 1386-1425.

Cheng, W., Zheng, X., & Yang, M. (2016). Hydrogen Peroxide Induced Protein

Oxidation During Storage and Lyophilization Process. *Journal of Pharmaceutical Sciences, 105*, 1837-1842.

Chumsae, C., Gaza-Bulseco, G., Sun, J., & Li, H. (2007). Comparison of methionine oxidation in thermal stability and chemically stressed samples of a fully human monoclonal antibody. *Journal of Chromatography B, 850*(1-2), 285-294. doi:https://doi.org/10.1016/j.jchromb.2006.11.050

Ciurczak, E., & Drennen, J. (2002). *Pharmaceutical and Medical Applications of Near-infrared.* New York: Marcel Dekker.

Clavaud, M., Lema-Martinez, C., Roggo, Y., Bigalke, M., Guillemain, A., Hubert, P., . . . Allmendinger, A. (2020). Near-Infrared Spectroscopy to Determine Residual Moisture in Freeze-Dried Products: Model Generation by Statistical Design of Experiments. *Journal of Pharmaceutical Sciences, 109*(1), 719-729. doi:https://doi.org/10.1016/j.xphs.2019.08.028

Clavaud, M., Roggo, Y., Degardin, K., Sacrè, P., Hubert, P., & Ziemons, E. (2017). Global regression model for residual moisture content determination using near-infrared spectroscopy. *European Journal of Pharmaceutics and Biopharmaceutics, 119*, 343-352.

Clegg, I. (2020). Process analytical technology. In *Specifications of Drug Substances and Products* (pp. 149-173). Elsevier.

Colucci, D., Fissore, D., Barresi, A., & Braatz, R. (2020). A new mathematical model for monitoring the temporal evolution of the ice crystal size distribution during freezing in pharmaceutical solutions. *European Journal of Pharmaceutics and Biopharmaceutics, 148*, 148-159. doi:https://doi.org/10.1016/j.ejpb.2020.01.004

Connors, K. (1988). The Karl-Fischer titration of water. *Drug Dev. Ind. Pharm. , 14*, 1891-1903.

Cordoba, A. J., Shyong, B.-J., Breen, D., & Harris, R. J. (2005). Non-Enzymatic hinge region fragmentation of antibodies in solution. *Journal of Chromatography B, 818*(2), 115-121. doi:http://dx.doi.org/10.1016/j.jchromb.2004.12.033

Coronel-Reyes, J., Ramirez-Morales, I., Fernandez-Blanco, E., Rivero, D., & Pazos, A. (2018). Determination of egg storage time at room temperature using a low-cost NIR spectrometer and machine learning techniques. *Computers and Electronics*

in Agriculture, 145, 1-10.

Das, T., Sreedhara, A., Colanclene, J., Chou, D., Filipe, V., Grapentin, C., . . . Jiskoot, W. (2021). Stress Factors in Protein Drug Product Manufacturing and Their Impact on Product Quality. *Journal of Pharmaceutical Sciences*, 1-19. doi:https://doi.org/10.1016/j.xphs.2021.09.030

Davies, A. (2005). Back to basics: Applications of principal component analysis. *Spectroscopy Europe, 17*(2), 30-31.

De Beer, T., Alleso, M., Goethals , F., Coppens, A., Vander Heyden, Y., Lopez De Diego, H., . . . Baeyens, W. (2007). Implementation of a Process Analytical Technology System in a Freeze-Drying Process Using Raman Spectroscopy for In-Line Process Monitoring. *Analytical Chemistry, 79*, 7992-8003.

De Beer, T., Bodson, C., Dejaegher, B., Walezak, B., Vercruysse, P., Burggraeve, A., . . . Baeyens, W. (2008). Raman Spectroscopy as a Process Analytical Technology (PAT) Tool for the In-Line Monitoring and Understanding of a Powder Blending Process. *Journal of Pharmaceutical and Biomedical Analysis, 48*, 772-779.

De Beer, T., Burggraeve, A., Fonteyene, M., Saerens, L., Remon, J., & Vervaet, C. (2011). Near infrared and Raman spectroscopy for the in-process monitoring of pharmaceutical production processes. *International Journal of Pharmaceutics, 417*, 32-47. doi:https://doi.org/10.1016/j.ijpharm.2010.12.012

De Beer, T., Hansen, L., Vander Heyden, Y., Pieters, S., Varvaet, C., Remon, J., . . . Daoussi, R. (2013). Near-infrared spectroscopy evaluation of lyophilized viral vaccine formulations. *Biotechnology Progress, 29*, 1573-1586.

De Beer, T., Vercruysse, P., Burggraeve, A., Quinten, T., Ouyang, J., Zhang, X., . . . Baeyens, W. (2009). In-line and real-time process monitoring of a freeze drying process using Raman and NIR spectroscopy as complementary process analytical technology (PAT) tools. *Journal of Pharmaceutical Sciences, 98*(9), 3430-3446. doi:https://doi.org/10.1002/jps.21633

De Beer, T., Wiggenhorn, M., Hawe, A., Kasper, J., Almeida, A., Quinten, T., . . . Remon, J. (2011). Optimization of a pharmaceutical freeze-dried product and its process using an experimental design approach and innovative process analyzers. *Talanta, 83*(5), 1623-1633. doi:https://doi.org/10.1016/j.talanta.2010.11.051

De Beer, T., Wiggenhorn, M., Veillon, R., Debacq, C., Mayeresse, Y., Moreau, B., . . . Baeyens, W. (2009). Importance of using complementary process analyzers for the process monitoring, analysis, and understanding of freeze drying. *Analytical Chemistry Journal, 81*(18), 7639-7649. doi:https://doi.org/10.1021/ac9010414

De Simone, A., Dhulesia, A., Soldi, G., Vendruscolo, M., Hsu, S.-T., Chiti, F., & Dobson, C. (2011). Experimental free energy surfaces reveal the mechanisms of maintenance of protein solubility. *Proceedings of the National Academy of Sciences , 108*(52), 21057-21062. doi:https://doi.org/10.1073%2Fpnas.1112197108

de Waard, H., De Beer, T., Hinrichs, W., Vervaet, C., Remon, J., & Frijilink, H. (2010). Controlled Crystallization of the Lipophilic Drug Fenofibrate During Freeze-Drying: Elucidation of the Mechanism by In-Line Raman Spectroscopy. *American Association of Pharmaceutical Scientists, 12*(4), 569-575. doi:https://doi.org/10.1208%2Fs12248-010-9215-z

Deiringer, N., Leitner, I., & Friess, W. (2023). Effect of Tubing Material Used in Peristaltic Pumping in Tangential Flow Filtration Processes of Biopharmaceutics on Particle Formation and Flux. *Journal of Pharmaceutical Sciences, 112*, 665-672.

Deloitte. (2023). *Measuring the return from pharmaceutical innovation - 14th edition.* Retrieved from https://www.deloitte.com/uk/en/Industries/life-sciences-health-care/research/measuring-return-from-pharmaceutical-innovation.html

Derksen, M., van de Oetelaar, P., & Maris, F. (1998). The use of near-infrared spectroscopy in the efficient prediction of a specification for the residual moisture content of a freeze-dried product. *Journal of Pharmaceutical and Biomedical Analysis, 17*(3), 473-480. doi:https://doi.org/10.1016/s0731-7085(97)00216-1

Deshmukh, S., & Ogunyankin, M. (2020). Chapet 17: Scale-Down Models for Robust Biologics Drug Product Process Development. In *Development of Biopharmaceutical Drug-Device Products* (pp. 405-429). Springer International Publishing. doi:http://dx.doi.org/10.1007/978-3-030-31415-6_17

Deshmukh, S., & Ogunyankin, M. (2020). Scale-Down Models for Robust Biologics Drug Product Process Development. In *Development of Biopharmaceutical Drug-Device Products* (pp. 405-429). Kenilworth, NJ, USA: American Association of

Pharmaceutical Scientists.

Ding, Y., Marino, M., Zen, K., Sheffer, J., Almaguer, N., Caddy, K., & Praseuth, A. (2020). Considerations for Monoclonal Antibody Bioprocess and Manufacturing Validation. *Pharmaceutical Technology, 44*(8), 31-36. Retrieved from https://www.pharmtech.com/view/kadimastem-and-pluri-enter-cell-therapy-manufacturing-deal

Dobbins, J., Pluschkell, S., Krause, P., O'Neil, J., Swann, P., & Welch, J. (2017). CMC forum: Evolution of biopharmaceutical control strategy through continued process verification. *BioProcess International, 17*. Retrieved from https://www.bioprocessintl.com/cmc-forums/cmc-forum-evolution-of-biopharmaceutical-control-strategy-through-continued-process-verification

Dobson, C. (2021). The structural basis of protein folding and its links with human disease. *Philosophical Transactions of the Royal Society of London, 356*(1406), 133-145. doi:https://doi.org/10.1098%2Frstb.2000.0758

Duerkop, M., Berger, E., Durauer, A., & Junbauer, A. (2018). Impact of cavitation, high shear stress and air/liquid interfaces on protein aggregation. *Biotechnological Journal, 13*(7), 1800-18062. doi:https://doi.org/10.1002/biot.201800062

EFFPIA. (2021). *The pharmaceutical industry: a key asset to medical progress and the European economy.* Retrieved from https://www.efpia.eu/media/602709/the-pharmaceutical-industry-in-figures-2021.pdf

EMA. (2005). *ICH Topic Q5E: Comparability of Biotechnological/Biological Products*. Retrieved from https://www.ema.europa.eu/en/documents/scientific-guideline/ich-q-5-e-comparability-biotechnologicalbiological-products-step-5_en.pdf

Esbensen, K., & Geladi, P. (2009). Principal Component Analysis: Concept, Geometrical Interpretation, Mathematical Background, Algorithms, History, Practice. *Comprehensive Chemometrics, 2*, 211-226.

Esmonde-White, K., Cuellar, M., & Lewis, I. (2022). The role of Raman spectroscopy in biopharmaceuticals from development to manufacturing. *Analytical and Bioanalytical Chemistry, 414*, 969-991.

Ettah, I., & Ashton, L. (2018). Engaging with Raman Spectroscopy to Investigate

Antibody Aggregation. *Antibodies, 7*(3), 24. doi:https://doi.org/10.3390%2Fantib7030024

European Medicines Agency. (2016). *Guideline on process validation for finished products - information and data to be provided in regulatory submissions.* Retrieved from https://www.ema.europa.eu/en/documents/scientific-guideline/guideline-process-validation-finished-products-information-and-data-be-provided-regulatory-submissions-revision-1_en.pdf

European Pharmacopeia 8th edition. (2013). Water: Semi-Micro Determination.

Feidl, F., Garbellini, S., Vogg, S., Sokolov, M., Souquet, J., Broly, H., . . . Morbidelli, M. (2019). A new flow cell and chemometric protocol for implementing in-line Raman spectroscopy in chromatography . *Biotechnology Progress, 35*, 2847.

Ferreira, A., & Tobyn , M. (2014). Multivariate analysis in the pharmaceutical industry: Enabling process understanding and improvement in the PAT and QbD era. *Pharmaceutical Development and Technology*, 1-15.

Fissore, D. (2013). Freeze Drying of Pharmaceuticals. *Encyclopedia of Pharmaceutical Science and Technology*, 1723-1737.

Fissore, D. (2013). Freeze-drying of Pharmaceuticals. In *Encyclopedia of Pharmaceutical Science and Technology* (pp. 1723-1737). Taylor & Francis. doi:http://dx.doi.org/10.1081/E-EPT4-120050278

Fissore, D., & McCoy, T. (2018). Editorial: freeze-drying and process analytical technology for pharmaceuticals. *Front. Chem., 6*, 1-2.

Fissore, D., Pisano, R., & Barresi, A. (2011). Advanced Approach to Build the Design Space for the Primary. *Journal of Pharmaceutical Sciences, 100*(11), 4922-4933. doi:10.1002/jps.22668

Fissore, D., Pisano, R., & Barresi, A. (2011). Monitoring of the secondary drying in freeze-drying of pharmaceuticals. *Journal of Pharmaceutical Sciences, 100*, 732-742.

Fissore, D., Pisano, R., & Barresi, A. (2011). On the Methods Based on the Pressure Rise Test for Monitoring a Freeze-Drying Process. *Drying Technology, 29*(1), 73-90. doi:http://dx.doi.org/10.1080/07373937.2010.482715

Fissore, D., Pisano, R., & Barresi, A. (2017). On the use of Temperature Measurement to

Monitor a Freeze-Drying Cycle for Pharmaceuticals. *Proceedings of IEEE International Instrumentation and Measurements Technology Conference.* Torino.

Fissore, D., Pisano, R., Velardi, S., & Barresi, A. (2009). PAT tools for the optimization of the freeze-drying process. *Pharmaceutical Engineering, 29*(5), 58-70.

Food and Drug Administration. (2002). *Pharmaceutical cGMPs For The 21st Century - A Risk-Based Approach.* Retrieved from https://www.pharmaceuticalonline.com/doc/pharmaceutical-cgmps-for-the-21st-century-a-r-0001

Food and Drug Administration. (2004). *PAT - A Framework for Innovative Pharmaceutical Development, Manufacturing, and Quality Assurance.* Retrieved from https://www.fda.gov/regulatory-information/search-fda-guidance-documents/pat-framework-innovative-pharmaceutical-development-manufacturing-and-quality-assurance

Food and Drug Administration. (2011). *Guidance for Industry - Process Validation: General Principles and Practices.* Retrieved from https://www.fda.gov/files/drugs/published/Process-Validation--General-Principles-and-Practices.pdf

Food and Drug Administration. (2011). *Guidance for Industry: Process validation: general principles and practices.* FDA.

Food and Drug Administration. (2017). *Advancement of Emerging Technology Applications for Pharmaceutical Innovation and Modernization Guidcande for Industry.* Retrieved from https://www.fda.gov/regulatory-information/search-fda-guidance-documents/advancement-emerging-technology-applications-pharmaceutical-innovation-and-modernization-guidance

Freitas, M., Sabadin, A., Silva, L., Gianotti, F., do Couto, D., Tonhi, E., . . . Russo, V. (2005). Prediction of drug dissolution profiles from tables using NIR diffuse reflectance spectroscopy: a rapid and nondestructive method. *Journal of Pharmaceutical and Biomedical Analysis, 39*, 17-21.

Gala, U., & Chauhan, H. (2015). Principles and applications of Raman spectroscopy in pharmaceutical drug discovery and development. *Expert Opinion on Drug Discovery, 10*(2), 187-206. doi:https://doi.org/10.1517/17460441.2015.981522

Geladi, P., Macdougall, D., & Martens, H. (1985). Linearization and Scatter-Correction for Near-Infrared Reflectance Spectra of Meat. *Applied Spectroscopy, 39*(3), 491-500.

Geron, A. (2019). *Hands-on Machine Learning with Scikit-Learn, Keras & TensorFlow - Concepts, Tools and Techniques to Build Intelligent Systems.* O'Reilly Inc.

Gerzon, G., Sheng, Y., & Kirkitadze, M. (2022). Process Analytical Technologies – Advances in bioprocess integration and future perspectives. *Journal of Pharmaceutical and Biomedical Analysis, 207*(5), 1143-11479. doi:https://doi.org/10.1016/j.jpba.2021.114379

Giordano, A., Barresi, A., & Fissore, D. (2011). On the use of mathematical models to build the design space for the primary drying phase of a pharmaceutical lyophilization process. *Journal of Pharmaceutical Sciences, 100*(1), 311-324. doi:https://doi.org/10.1002/jps.22264

Gomez de la Cuesta, R., Goodacre, R., & Ashton, L. (2014). Monitoring Antibody Aggregation in Early Drug Development Using Raman Spectroscopy and Perturbation-Correlation Moving Windows. *Analytical Chemistry, 86*(22), 11133-11140. doi:https://doi.org/10.1021/ac5038329

Goodfellow, I., Bengio, Y., & Courville, A. (2016). *Deep learning.* United States of America: Cambridge, MA: MIT Press.

Gorsky, I. (2020). *Chapter 7 - Process Validation Stage 1 - Parenteral Process Design.* (A. Press, Ed.) Downingtow, PA: A Pratical Lifecycle Approach. doi:https://doi.org/10.1016/B978-0-12-809412-9.00006-X

Grohganz, H., Gildemyn, D., Skibsted, E., Flink, J., & Rantanen, J. (2010). Towaeds a robust water content determination of freeze-dried samples by near-infrared spectroscopy. *Analitica Chimica Acta, 676*, 34-40.

Her, C., Tanenbaum, L., Bandi, S., Randolph, T., Thirumangalathu, R., Mallela, K., . . . Elias , Y. (2020). Effects of Tubing Type, Operating Parameters, and Surfactants on Particle Formation During Peristaltic Filling Pump Processing of a mAb Formulation. *Journal of Pharmaceutical Sciences, 109*(4), 1439-1448. doi:https://doi.org/10.1016/j.xphs.2020.01.009

Horst, J., Turimella, S., Metsers, F., & Zwiers, A. (2021). Implementation of Quality by

Design (QbD) Principles in Regulatory Dossiers of Medicinal Products in the European Union (EU) Between 2014 and 2019. *Therapeutic Innovation & Regulatory Science, 55*, 583-590. doi:https://doi.org/10.1007/s43441-020-00254-9

Hubbard, A., Roedl, T., Hui, A., Knueppel, S., Eppler, K., Lehnert, S., & Maa, Y. (2018). Vapor Phase Hydrogen Peroxide Decontamination or Sanitization of an Isolator for Aseptic Filling of Monoclonal Antibody Drug Product-Hydrogen Peroxide Uptake and Impact on Protein Quality. *PDA Journal of Pharmaceutical Science and Technology, 72*(4), 348-366.

Huck, C. (2014). Near-Infrared (NIR) Spectroscopy in Natural Product Research. In *Handbook of Chemical and Biological Plant Analytical Methods* (pp. 227-234). John Wiley & Sons. doi:http://dx.doi.org/10.1002/9780470027318.a9909

Hulbert, M., Feely, L., Inman, E., & Johnson, A. (2008). Risk Management in the Pharmaceutical Product Development Process. *Journal of Pharmaceutical Innovation, 3*(4), 227-248. doi:http://dx.doi.org/10.1007/s12247-008-9049-8

IBM. (n.d.). *What is a neural network?* Retrieved 2022, from https://www.ibm.com/topics/neural-networks

ICH Q10. (2015). *ICH guideline Q10 on pharmaceutical quality system.* Retrieved from https://www.ema.europa.eu/en/documents/scientific-guideline/international-conference-harmonisation-technical-requirements-registration-pharmaceuticals-human-guideline-q10-pharmaceutical-quality-system-step-5_en.pdf

ICH Q11. (2012). *Development and manufacture of drug substances (chemical entities and biotechnological/biological entities) Q11.* Retrieved from https://database.ich.org/sites/default/files/Q11%20Guideline.pdf

ICH Q6B. (1999). *Specifications: test procedures and acceptance criteria for biotechnological/biological products.* Retrieved from https://ntp.niehs.nih.gov/sites/default/files/iccvam/methods/biologics/vaccine/ich-q6b.pdf

ICH Q8(R2). (2009). *Pharmaceutical Development Q8(R2).* Retrieved from https://database.ich.org/sites/default/files/Q8_R2_Guideline.pdf

ICH-Endorsed Guide for ICH Q8/Q9/Q10 Implementation. (2011). *Quality*

Implementation Working Group Points to Consider (R2). Retrieved from https://database.ich.org/sites/default/files/Q8_Q9_Q10_Q%26As_R4_Points_to_Consider_0.pdf

Jameel, F. (2023). *Principles and Practices of Lyophilization in Product Development and Manufacturing.* Springer.

Jameel, F., Skoug, J., & Nesbitt, R. (2020). *Development of Biopharmaceutical Drug-Device Product* (Vol. 35). (Springer, Ed.) Cham, Switzerland: AAPS Advances in Pharmaceutical Sciences Series. doi:https://doi.org/10.1007/978-3-030-31415-6

Jameel, F., Undey, C., Kovach, P., & Tanglertpaibul, J. (2015). Application of QbD Elements in the Development and Scale-up of Commercial Filling Process. In *Quality by Design for Biopharmaceutical Drug Product Development* (pp. 265-302). New York: Springer. doi:https://doi.org/10.1007/978-1-4939-2316-8_13

Jamrogiewicz, M. (2012). Application of the Near-Infrared Spectroscopy in the Pharmaceutical Technology. *Journal of pharmaceutical and biomedical analysis, 66*, 1-10.

Kamat, M., Lodder, R., & DeLuca, P. (1989). Near-infrared spectroscopic determination of residual moisture in lyophilized sucrose through intact glass vials. *Pharmaceutical Research, 6*(11), 961-965. doi:https://doi.org/10.1023/a:1015997530367

Kananenka, A., & Skinner, J. (2018). Fermi resonance in OH-stretch vibrational spectroscopy of liquid water and the water hexamer. *The Journal of Chemical Physics, 148*, 24410-24417. doi:https://doi.org/10.1063/1.5037113

Kasper, J., Wiggenhorn, M., Resch, M., & Friess, W. (2013). Implementation and Evaluation of an Optical Fiber System as Novel Process Monitoring Tool During Lyophilization. *European Journal of Pharmaceutics and Biopharmaceutics, 83*(3), 449-459. doi:10.1016/j.ejpb.2012.10.009.

Kauppinen, A., Toiviainen, M., Korhonen, O., Aaltonen, J., Jarvinen, K., Paaso, J., . . . Ketolainen, J. (2013). In-Line Multipoint Near-Infrared Spectroscopy for Moisture Content Quantification during Freeze-Drying. *Analytical Chemistry, 85*(4), 2377-2384. doi:https://doi.org/10.1021/ac303403p

Koenig, J. (2005). Raman Spectroscopy of Biological Molecules: A Review. *Journal of Polymer Science Macromolecular Reviews, 39*, 510-551.

Kontoyannis, C. (1995). Quantitative Determination of CaCO3 and Glycine in Antacid Tablets by Laser Raman Spectroscopy. *Journal of Pharmaceutical and Biomedical Analysis, 13*, 73-76.

Krause, M., & Sahin, E. (2019). Chemical and physical instabilities in manufacturing and storage of therapeutic proteins. *Current Opinion in Biotechnology, 60*, 159-167. doi:https://doi.org/10.1016/j.copbio.2019.01.014

Kresta, J., MacGregor, J., & Marlin, T. (1991). Multivariate statistical monitoring of process operating performances. *Canadian Journal of Chemical Engineering, 69*, 35-47.

Kroll, P., Hofer, A., Ulonska, S., Kager, J., & Herwig, C. (2017). Model-Based Methods in the Biopharmaceutical Process Lifecycle. *Pharmaceutical Research, 34*(12), 2596-2613. doi:https://doi.org/10.1007%2Fs11095-017-2308-y

Lamsal, R., Harroun, S., Brosseau, C., & Gagnon, G. (2012). Use of surface enhanced Raman spectroscopy for studying fouling on nanofiltration membrane. *Separation and Purification Technology, 96*, 7-11.

Lashmar, U., Vanderburgh, M., & Little, S. (2007). *Bulk Freeze-Thawing of Macromolecules.* Retrieved from https://shop.sartorius.com/medias/Bulk-Freeze-Thawing-of-Macromolecules-published-in-BioProcess-technical.pdf?context=bWFzdGVyfGRvY3VtZW50c3w5NjY1MDF8YXBwbGljYXRpb24vcGRmfGFETTFMMmd6T1M4NU1qWXpNRE0zTWpnME16Z3l8YWJkOWM4MDVmYWFlM2I2M2VjYjdhMGM2MWE0N2U1ZmU4Z

Lawrence, X., Amidon, G., Khan, M., Hoag, S., Polli, J., Raju, G., & Woodcock, J. (2014). Understanding Pharmaceutical Quality by Design. *American Association of Pharmaceutical Scientists, 16*(4), 771-783. doi:https://doi.org/10.1208%2Fs12248-014-9598-3

Lee, Y., Kim, J., Han, J., Jeong, H., Woo, Y., & Chung, H. (2021). Axially slanted laser illumination scheme for direct and accurate Raman spectroscopic determination of gemcitabine concentration in freeze-dried gemcitabine injection powder housed in a glass container. *Analytica Chimica Acta, 1175*, 338-746. doi:https://doi.org/10.1016/j.aca.2021.338746

Lewis, I., & Edwards, H. (2001). *Handbook of Raman Spectroscopy.* New York: Marcel Dekker. doi:http://dx.doi.org/10.1201/9781420029253

Li Vigni, M., Durante, C., & Cocchi, M. (2013). Chapter 3 - Exploratory Data Analysis. In *Data Handling in Science and Technology* (pp. 55-126). Elsevier.

Lim, F., Sundaram, J., Sreedhara, A., & Lim, F. (2015). Application of Quality by Design Principles to the Drug Product Technology Transfer Process. In *Quality by Design for Biopharmaceutical Drug Product Development.* doi:http://dx.doi.org/10.1007/978-1-4939-2316-8_27

Liu, D., Ren, D., Huang, H., Dankberg, J., Rosenfeld, R., Cocco, M., . . . Remmele Jr., R. (2008). Structure and stability changes of human IgG1 Fc as a consequence of methionine oxidation. *Biochemistry, 47*(18), 5088-5100. doi:https://doi.org/10.1021/bi702238b

Liu, L., Randolph, T., & Carpenter, J. (2012). Particles shed from syringe filters and their effects on agitation-induced protein aggregation. *Journal of Pharmaceutical Sciences, 101*(8), 2952-2959. doi:https://doi.org/10.1002/jps.23225

Lopes, J., & Sarraguca, M. (2018). Data Processing in Multivariate Analysis of Pharmaceutical Processes. In *Multivariate Analysis in the Pharmaceutical Industry* (pp. 35-51). Elsevier.

Lu, H., Gaza-Bulseco, G., & Zhou, L. (2009). Mass spectrometry analysis of photo-induced methionine oxidation of a recombinant human monoclonal antibody. *Journal of the American Society for Mass Spectrometry, 20*(3), 525-528. doi:https://doi.org/10.1016/j.jasms.2008.11.011

Luis, L., Hu, Y., Zamiri, C., & et al. (2018). Determination of the Acceptable Ambient Light Exposure during Drug Product Manufacturing for Long Term Stability of Monoclonal Antibody. *PDA Journal of Pharmaceutical Science and Technology*, 1-33.

Luo, Q., Joubert, M., Stevenson, R., Ketchem, R., Narhi, L., & Wypych , J. (2011). Chemical modifications in therapeutic protein aggregates generated under different stress conditions. J. *Journal of Biological Chemistry, 286*(28), 25134-25144. doi:https://doi.org/10.1074/jbc.m110.160440

Luypaert, J., Massart, D., & Vander Heyden, Y. (2007). Near-infrared spectroscopy

applications in pharmaceutical analysis. *Talanta, 72*, 865-883.

Maa, Y., & Hsu, C. (1997). Protein denaturation by combined effect of shear and air-liquid interface. *Biotechnology Bioengineering, 54*(6), 503-512. doi:https://doi.org/10.1002/(sici)1097-0290(19970620)54:6%3C503::aid-bit1%3E3.0.co;2-n

MacGregor, J., & Kourti, T. (1995). Statistical Process Control of Multivariate Processes. *Control engineering practice, 3*(3), 403-414.

Mahar, P., & Verma, A. (2014). Pharmaceutical process validation: an overview. *International Journal of Pharmaceutical Research and bio-science, 3*(4), 243-262. Retrieved from https://www.researchgate.net/publication/264634497_PHARMACEUTICAL_PROCESS_VALIDATION_AN_OVERVIEW

Mainali, D., Li, J., Yehl, P., & Chetwyn, N. (2014). Development of a comprehensive near infrared spectroscopy calibration model for rapid measurements of moisture content in multiple pharmaceutical product. *Journal of Pharmaceutical and Biomedical Analysis, 95*, 169-175.

Makki, A., Massot, V., Byrne, H., Respaud, R., Bertrand, D., Mohammed, E., . . . Bonnier, F. (2021). Understanding the discrimination and quantification of monoclonal antibodies preparatios using Raman spectroscopy. *Journal of Pharmaceutical and Biomedical Analysis, 194*, 113734.

Marcato, A., Boccardo, G., & Marchisio, D. (2021). A computational workflow to study particle transport and filtration in porous media: coupling CFD and deep learning. *Chemical Engineering Journal, 413*, 128-936.

Martins, J., Guerra, R., Pires, R., Antunes, M., Panagopoulos, T., Brazio, A., . . . Cavaco, A. (2022). Spectranet-53: a deep residual learning architecture for predicting soluble solids content with VIS-NIR spectroscopy. *Computers and Electronics in Agriculture*.

Massart, D., Vandeginste, B., Buydens , L., Lewi, P., Smeyers-Verbeke, K., & De Long, S. (1998). *Handbook of Chemometrics and Qualimetrics.* United States: Elsevier Science Inc.

Massei, A., Falco, N., & Fissore, D. (2023). Use of machine learning tools and NIR

spectra to estimate residual moisture in freeze-dried products. *Spectrochimica Acta Part A: Molecular and Biomolecular Spectroscopy, 293*, 122-485. doi:https://doi.org/10.1016/j.saa.2023.122485

Massei, A., Falco, N., & Fissore, D. (2024). Use of Raman spectroscopy and PCA for quality evaluation and out-of-specification identification in biopharmaceutical products. *European Journal of Pharmaceutics and Biopharmaceutics, 200*, 114342. doi:https://doi.org/10.1016/j.ejpb.2024.114342

Massei, A., Falco, N., & Fissore, D. (2025). NIR-Based Real-Time Monitoring of Freeze-Drying Processes: Application to Fault and Endpoint Detection. *Processes*, 452.

McAvan, B., Bowsher, L., Powell, T., O'Hara, J., Spitali, M., & Goodacre, R. (2020). Raman Spectroscopy to Monitor Post-Translational Modifications and Degradation in Monoclonal Antibody Therapeutics. *Analytical Chemistry, 92*, 10381-10389.

McCreery, R. (2000). *Raman Spectroscopy for Chemical Analysis.* John Wiley & Sons. doi:10.1002/0471721646

Mensik, M., Frijlink, H., van der Voort Maarschalk, K., & Hinrichs, W. (2017). How sugars protect proteins in the solid state and during drying (review): Mechanisms of stabilization in relation to stress conditions. *European Journal of Pharmaceutics and Biopharmaceutics, 114*, 288-295. doi:https://doi.org/10.1016/j.ejpb.2017.01.024

Millrock Technology. (2016, jULY). *Some Common Methods Used to Detect the End of Primary Drying in Freeze Drying.* Retrieved from https://www.millrocktech.com/wp-content/uploads/2017/04/Tech-Note-Common-Methods-to-Detect-the-End-of-Primary-Drying.pdf

Minitab. (n.d.). *Overview for 2-Sample Equivalence Test*. Retrieved from https://support.minitab.com/en-us/minitab/help-and-how-to/statistics/equivalence-tests/how-to/2-sample-equivalence-test/before-you-start/overview/

Muller, A., & Guido, S. (2016). *Introduction to Machine Learning with Python - A guide for data scientists.* O'Reilly Inc.

Muller, J., Knop, K., Thies, J., Uerpmann, C., & Kleinebudde, P. (2010). Feasibility of

Raman Spectroscopy as PAT Tool in Active Coating. *Drug Development and Industrial Pharmacy, 36*, 234-243.

Nagy, B., Farkas, A., Borbas, E., Vass, P., Nagy, Z., & Marosi, G. (2018). Raman Spectroscopy for Process Analytical Technologies of Pharmaceutical Secondary Manufacturing. *American Association of Pharmaceutical Scientists., 20*(1), 1. doi:https://doi.org/10.1208/s12249-018-1201-2

Nayak, A., Colandene, J., Bradford, V., & Perkins, M. (2011). Characterization of subvisible particle formation during the filling pump operation of a monoclonal antibody solution. *Journal of Pharmaceutical Sciences, 100*(10), 4198-4204.

Nitika, N., Chhabra, H., & Rathore, A. (2021). Raman spectroscopy for in situ, real time monitoring of protein aggregation in lyophilized biotherapeutic products. *International journal of biological macromolecules, 15*(179), 309-313. doi:https://doi.org/10.1016/j.ijbiomac.2021.02.214

Nowak, C., Cheung, J., Dellatore, S., Katiyar, A., Bhat, R., Sun, J., . . . Liu, H. (2017). Forced degradation of recombinant monoclonal antibodies: A practical guide. *mAbs, 9*(8), 1217-1230. doi:https://doi.org/10.1080%2F19420862.2017.1368602

O'Connor, T., Yu, L., & Lee, S. (2016). Emerging technology: A key enabler for modernizing pharmaceutical manufacturing and advancing product quality. *International Journal of Pharmaceutics, 509*, 492-498. doi:https://doi.org/10.1016/j.ijpharm.2016.05.058

Oddone, I. (2015). *Vacuum Induced Nucleation as a method for freeze drying optimization, Ph.D. Thesis.* Torino: Politecnico di Torino.

Oddone, I., Barresi, A., & Pisano, R. (2017). Influence of controlled ice nucleation on the freeze-drying of pharmaceutical products: the secondary drying step. *International Journal of Pharmaceutics, 524*(1-2). doi:http://dx.doi.org/10.1016/j.ijpharm.2017.03.077

Parastar, H., van Kollenburg, G., Weesepoel, Y., van den Doel, A., Buydens, L., & Jansen, J. (2020). Integration of handheld NIR and machine learning to "Measure & Monitor" chicken meat authenticity. *Food Control, 112*, 107-149.

Patel, J., Kothari, R., Tunga, R., Ritter, N., & Tunga , B. (2011). *Stability Considerations for Biopharmaceuticals: Overview of Protein and Peptide Degradation*

Pathways. Retrieved from https://www.bioprocessintl.com/formulation/stability-considerations-for-biopharmaceuticals-overview-of-protein-and-peptide-degradation-pathways

Patel, S., Doen, T., & Pikal, M. (2010). Determination of End Point of Primary Drying in Freeze-Drying Process Control. *American Association of Pharmaceutical Scientists., 11*(1), 73-84. doi:https://doi.org/10.1208%2Fs12249-009-9362-7

Patel, S., Doen, T., & Pikal, M. (2010). Determination of End Point of Primary Drying in Freeze-Drying Processes. *AAPS PharmSciTech, 11*(1), 73-84. doi:https://doi.org/10.1208/s12249-009-9362-7

Patel, S., Nail , S., Pikal , M., Geidobler , R., Winter, G., Hawe, A., . . . Rambhatla Gupta, S. (2017). Lyophilized Drug Product Cake Appearance: What Is Acceptable? *Journal of Pharmaceutical Sciences, 106*(7), 1706-1721.

Patro, S., Freund, E., & Chang , B. (2002). Protein formulation and fill-finish operations. *Biotechnology Annual Review, 8*, 55-84. doi:https://doi.org/10.1016/s1387-2656(02)08004-3

Paudel, A., Raijada, D., & Rantanen, J. (2015). Raman Spectroscopy in Pharmaceutical Product Design. *Advanced Drug Delivery Reviews, 15*(89), 3-20. doi:https://doi.org/10.1016/j.addr.2015.04.003

Pieters, S., De Beer, T., & Vander Heyden, Y. (2012). Near-infrared and Raman spectroscopy: Potential tools for monitoring of protein conformational instability during freeze-drying processes. *American Pharmaceutical Review, 15*(1). Retrieved from https://www.americanpharmaceuticalreview.com/Featured-Articles/38367-Near-infrared-and-Raman-Spectroscopy-Potential-Tools-for-Monitoring-of-Protein-Conformational-Instability-during-Freeze-drying-Processes/

Pieters, S., De Beer, T., Kasper, J., Boulpaep, D., Waszkiewicz, O., Goodarzi, M., . . . Vander Heyden, Y. (2012). Near-Infrared Spectroscopy for In-Line Monitoring of Protein Unfolding and Its Interaction with Lyoprotectants during Freeze-Drying. *Analytical Chemistry, 84*(2), 947-955. doi:https://doi.org/10.1021/ac2022184

Pieters, S., Vander Heyden, Y., Roger, J., D'Hondt, M., Hansen, L., Palagos, B., . . . De Beer, T. (2013). Raman spectroscopy and multivariate analysis for the rapid

discrimination between native-like and non-native states in freeze-dried protein formulations. *European Journal of Pharmaceutics and Biopharmaceutics, 85*(2), 263-271. doi:https://doi.org/10.1016/j.ejpb.2013.03.035

Pikal, M., Roy, M., & Shah, S. (1984). Mass and heat transfer in vial freeze-drying of pharmaceuticals: role of the vial. *Journal of Pharmaceutical Sciences, 73*(9), 1224-1237. doi:https://doi.org/10.1002/jps.2600730910

Pisano, R., Fissore, D., & Barresi, A. (2011). Freeze-drying optimization using model predictive control techniques. *Ind. Eng. Chem. Res., 50*, 7363-7379.

Pisano, R., Fissore, D., & Barresi, A. (2011). Heat transfer in freeze-drying apparatus. In *Developments in Heat Transfer.* Rijeka:InTech.

Pisano, R., Fissore, D., & Barresi, A. (2011). Heat Transfer in Freeze-Drying Apparatus. In *Developments in Heat Transfer* (pp. 91-113). doi:http://dx.doi.org/10.5772/23799

Pramod, K., Tahir, M., Charoo, N., Ansari, S., & Ali, J. (2016). Pharmaceutical product development: A quality by design approach. *International Journal of Pharmaceutical Investigation, 6*(3), 129-138. doi:https://doi.org/10.4103%2F2230-973X.187350

Presser, I. (2003). *Innovative Online Measurement Procedures to Optimize Freeze-Drying Processes, Ph.D. Thesis.* Germany: University of Munich.

Prmod, K., Tahir, M., Charoo, N., Ansari, S., & Ali , J. (2016). Pharmaceutical product development: A quality by design approach. *International Journal of Pharmaceutical Investigation, 6*, 129-138.

Rajalahti, T., & Kvalheim, O. (2011). Multivariate data analysis in pharmaceutics: A tutorial review. *International Journal of Pharmaceutics, 417*, 280-290.

Rajniak, P., Tsinontides, S., Pham, D., Hunke, W., Reynolds, S., & Chern, R. (2008). Sterilizing filtration - Principles and practice for succesful scale-up to manufacturing. *Journal of Membrane Science, 325*, 223-237.

Rajniak, P., Tsinontides, S., Pham, D., Hunke, W., Reynolds, S., & Chern, R. (2008). Sterilizing filtration—Principles and practice for successful scale-up to manufacturing. *Journal of Membrane Science, 325*(1), 223-237. doi:https://doi.org/10.1016/j.memsci.2008.07.049

Rambhatla, S., & Pikal, M. (2003). Heat and mass transfer scale-up issues during freeze-drying. I: atypical radiation and the edge vial effect. *AAPS PharmSciTech, 4*(2), 111-120. doi:https://doi.org/10.1208/s12249-009-9362-7

Rantanen, J. (2007). Process Analytical Applications of Raman Spectroscopy. *Journal of Pharmacy and Pharmacology, 59*, 171-177.

Rathore, N., & Rajan, R. (2008). Current perspectives on stability of protein drug products during formulation, fill and finish operations. *Biotechnology Progress, 24*(3), 504-514.

Reich, G. (2005). Near-infrared spectroscopy and imaging: Basic principles and pharmaceutical applications. *Advanced Drug delivery Reviews, 57*(8), 1109-1143. doi:https://doi.org/10.1016/j.addr.2005.01.020

Remmele, R., Krishnan, S., & Callahan, W. (2012). Development of stable lyophilized protein drug products. *Current Pharmaceutical Biotechnology, 13*(3), 471-496. doi:https://doi.org/10.2174/138920112799361990

Richter, B., Rurik, M., Gurk, S., Kohlbacher, O., & Fischer, M. (2019). Food monitoring: screening of the geographical origin of white asparagus using FT-NIR and machine learning. *Food Control, 2019*, 318-325.

Rinnan, A., Norgaard, L., van den Berg, F., Thygesen, J., Bro, R., & Enelsen, S. (2009). Data Pre-processing. *Infrared Spectroscopy for Food Quality Analysis and Control*, 29-50.

Roberts, C. (2007). Non-native protein aggregation kinetics. *Biotechnology and Bioengineering, 98*(5), 927-938. doi:https://doi.org/10.1002/bit.21627

Rodrigues, M., Miller , M., Glass, M., Singh, S., & Johnston , K. (2011). Effect of freezing rate and dendritic ice formation on concentration profiles of proteins frozen in cylindrical vessels. *Journal of Pharmaceutical Sciences, 100*(4), 1316-1329. doi:https://doi.org/10.1002/jps.22383

Romero-Torres, S., Perez-Ramos, J., Morris, K., & Grant, E. (2005). Spectroscopic Measurements of Tablet-to-Tablet Coating Variability. *Journal of Pharmaceutical and Biomedical Analysis, 38*, 270-274.

Romero-Torres, S., Wikstrom, H., Grant, E., & Taylor, L. (2007). Monitoring of mannitol phase behavior during freeze-drying using non-invasive Raman spectroscopy.

PDA Journal of Pharmaceutical Science and Technology, 61(2), 131-145. Retrieved from https://pubmed.ncbi.nlm.nih.gov/17479721/

Rosas, J., de Waard, H., De Beer, T., Vervaet, C., Remon, J., Hinrichs, W., . . . Blanco, M. (2014). NIR spectroscopy for the in-line monitoring of a multicomponent formulation during the entire freeze-drying process. *Journal of Pharmaceutical and Biomedical Analysis, 97*, 39-46. doi:https://doi.org/10.1016/j.jpba.2014.04.010

Sandorfy, C., Buchet, R., & Lachenal, G. (2006). Principles of Molecular Vibrations for Near-Infrared Spectroscopy. In *Near-Infrared Spectroscopy in Food Science and Technology* (pp. 11-46). doi:http://dx.doi.org/10.1002/9780470047705.ch2

Sasic, S. (2008). *Pharmaceutical Applications of Raman Spectroscopy.* John Wiley & Sons. doi:10.1002/9780470225882

Savage, M., Torres, J., Franks, L., Masecar, B., & Hotta, J. (1998). Determination of Adequate Moisture Content for Efficient Dry-Heat Viral Inactivation in Lyophilized Factor VIII by Loss on Drying and by Near Infrared Spectroscopy. *Biologicals, 26*(2), 119-124. doi:https://doi.org/10.1006/biol.1998.0140

Schepers, U., & Watzig, H. (2006). Application of the equivalence test for analytical method transfers: Testing precision using the United States Pharmacopeia concept <1010> . *Journal of Pharmaceutical and Biodemical Analysis, 41*(1), 290-292.

Schneid, S., & Gieseler, H. (2008). Evaluation of a New Wireless Temperature Remote Interrogation System (TEMPRIS) to Measure Product Temperature During Freeze-Drying. *AAPS PharmSciTech, 9*(3), 729-739. doi:https://doi.org/10.1208/s12249-008-9099-8

Scott, C., & Ritter, N. (2021). *Stability Testing: Monitoring Biological Product Quality Over Time.* Retrieved from https://www.bioprocessintl.com/qa-qc/stability-testing-monitoring-biological-product-quality-over-time

Sharma, P., Kessler, W., Bogner, R., Thakur, M., & Pikal, M. (2019). Applications of the Tunable Diode Laser Absorption Spectroscopy: In-Process Estimation of Primary Drying Heterogeneity and Product Temperature During Lyophilization. *Journal of Pharmaceutical Sciences, 108*(1), 416-430. doi:https://doi.org/10.1016/j.xphs.2018.07.031

Shukla, M., Wilkes, P., Bargary, N., Meagher, K., Khamar, D., Bailey, D., & Hudson, S. (2023). Identification of monoclonal antibody drug substances using non-destructive Raman Spectroscopy. *Spectrochimica Acta Part A: Molecular and Biomolecular Spectroscopy, 299*, 1386-1425.

SIMCA Sartorius. (2020). *SIMCA® 15 User Guide*. Retrieved from https://www.sartorius.com/download/544940/simca-15-user-guide-en-b-00076-sartorius-data.pdf

Simpson , M. (2010). Near-Infrared Spectroscopy for Process Analytical Technology: theory, technology and implementation. In *Process Analytical Technology* (pp. 107-155). Bakeev: John Wiley & Sons.

Smith, E., & Dent, G. (2019). *Modern Raman Spectroscopy: A Pratical Approach.* Seiten: John Wiley & Sons. doi:10.1002/9781119440598

Soto , R., Meriage, D., Wagner, R., Wang, T., & Semin, D. (2021). Enabling rapid identification of biotherapeutic protein products using handled Raman spectrometers and principal component analysis. *Journal of Raman Spectroscopy, 52*, 1281-1293.

Tang, C., & Pikal, M. (2004). Design of Freeze-Drying Processes for Pharmaceuticals: Practical Advice. *Pharmaceutical Research, 21*(2), 191-200. doi:http://dx.doi.org/10.1023/B:PHAM.0000016234.73023.75

Telikepalli, S., Kumru, O., Kalonia, C., Esfandiary , R., Joshi, S., Middaugh, C., & Volkin, D. (2014). Structural characterization of IgG1 mAb aggregates and particles generated under various stress conditions. *Journal of Pharmaceutical Sciences, 103*(3), 796-809. doi:https://doi.org/10.1002/jps.23839

The business reasearch company. (n.d.). *Biologics Market by Tipes (Monoclonal antibodies, therapeutic proteins and vaccines) by trends, by regions and by key players. Global forecast to 2021.*

Thiagarajan, G., Widjaja, E., Heo, J., Cheung, J., Wabuyele, B., Mou, X., & Shameem, M. (2015). Use of Raman and Raman optical activity for the structural characterizaion of a therapeutic monoclonal antibody formulation subjected to heat stress. *Journal of Raman Spectroscopy, 46*, 531-536.

Van Buren, N., Rehder, D., Gadgil, H., Matsumura, M., & Jacob, J. (2009). Elucidation

of two major aggregation pathways in an IgG2 antibody. *Journal of Pharmaceutical Sciences, 98*(9), 3013-3030. doi:https://doi.org/10.1002/jps.21514

Vandenabeele, P. (2013). *Pratical Raman Spectroscopy - An Introduction.* John Wiley & Sons. doi:10.1002/9781119961284

Velardi, S., & Barresi, A. (2008). Development of simplified models for the freeze-drying. *Chemical Engineering Research and Design, 86*, 9-22. doi:10.1016/j.cherd.2007.10.007

Vergote, G., De Beer, T., Vervaet, C., Remon , J., Baeyens, W., Diericx, N., & Verpoort, F. (2004). In-line monitoring of a pharmaceutical blending process using FT-Raman spectroscopy. *European Journal of Pharmaceutical Sciences, 21*(4), 479-485. doi:https://doi.org/10.1016/j.ejps.2003.11.005

Vermeer, A., & Norde, W. (2000). The thermal stability of immunoglobulin: unfolding and aggregation of a multi-domain protein. *Biophysical Journal, 78*(1), 394-404. doi:https://doi.org/10.1016%2FS0006-3495(00)76602-1

Vuylsteke, B., Luyckx, I., & de Lannoy, G. (2019). The Diffusion of Hydrogen Peroxide Into the Liquid Product During Filling Operations Inside Vaporous Hydrogen Peroxide-Sterilized Isolators Can Be Predicted by a Mechanistic Model. *Journal of Pharmaceutical Sciences, 108*, 2527-2533.

Wang, Y., Muzzio, F., & Glasser, B. (2016). *Using multivariate analysis for pharmaceutical drug product development.*

Warne, N., & Mahler, H.-C. (2018). *Challenges in Protein Product Development* (Vol. 38). (Springer, Ed.) Cham, Switzerland: AAPS Advances in Pharmaceutical Sciences Series. doi:https://doi.org/10.1007/978-3-319-90603-4

Wei, B., Woon, N., Dai, L., fISH, r., Tai, M., Handagama, W., . . . et al. . (2022). Multi-Attribute Raman Spectroscopy (MARS) for Monitoring Product Quality Attributes in Formulated Monoclonal Antibody Therapeutics. *mAbs, 14*, 2007-2564.

Weiss 4th, W., Young, T., & Roberts, C. (2009). Principles, approaches, and challenges for predicting protein aggregation rates and shelf life. *Journal of Pharmaceutical Sciences, 98*(4), 1246-1277. doi:https://doi.org/10.1002/jps.21521

Wikström, H., Carroll, W., & Taylor, L. (2008). Manipulating Theophylline Mono-Hydrate Fromation during High-Shear Wet Granulation through Improved Understanding of the Role of Pharmaceutical Excipients. *Pharmaceutical Research, 25*, 923-935.

Wikström, H., Marsac, P., & Taylor, L. (2005). In-Line Monitoring of Hydrate Formation during Wet Granulation Using Raman Spectroscopy. *Journal of Pharmaceutical Sciences, 94*, 923-935.

Wold, S. (1992). Nonlinear partial least squares modelling II. Spline inner relation. *Chemometrics and Intelligent Laboratory Systems, 14*(1-3), 71-84.

Wold, S. (1995). Chemimetrics: what do we mean with it, and what do we want from it? *Chemometrics and Intelligent Laboratory Systems, 30*(1), 109-115.

Yu, L., Amidon, G., Khan, M., Hoag, S., Polli, J., Raju, G., & Woodcock, J. (2014). Understanding Pharmaceutical Quality by Design. *American Association of Pharmaceutical Scientists, 16*(4), 771-783.

Zahel, T., Marschall, L., Abad, S., Vasilieva, E., Maurer, D., Mueller, E., . . . Herwig, C. (2017). Workflow for Criticality Assessment Applied in Biopharmaceutical Process Validation Stage 1. *Bioengineering, 4*(4), 85. doi:https://doi.org/10.3390%2Fbioengineering4040085

Zhao, J., Tian, G., Qiu, Y., & Qu, H. (2021). Rapid quantification of active pharmaceutical ingredient for sugar-free Yangwei granules in commercial production using FT-NIR spectroscopy based on machine learning techniques. *Spectrochimica Acta, Part A: Molecular and Biomolecular Spectroscopy, 245*, 118-878.

Zhi-xiang, Y., Zenq-qiang, S., Hui, S., & Hong-fu, Y. (2016). Correction Multiplicative Effects in Raman Spectra through Vector Angle Transformation. *Spectroscopy and Spectral Analysis, 36*(2), 419-423. doi:10.3964/j.issn.1000-0593(2016)02-0419-05